UNIVERSITÉ DU LUXEMBOURG

PhD-FSTM-2026-001
The Faculty of Science, Technology and Medicine

DISSERTATION

Defence held on 15/01/2016 in Esch sur Alzette

to obtain the degree of

DOCTEUR DE L'UNIVERSITÉ DU LUXEMBOURG

EN BIOLOGIE

by

Kim Eiden

Born on 15th of March 1997 in Esch sur Alzette, (Luxembourg)

ELUCIDATING CELLULAR ADAPTATION MECHANISMS DURING NUCLEOTIDE INHIBITION

Dissertation defence committee

Dr Johannes Meiser, dissertation supervisor
Department Head, Department of Cancer Research, Luxembourg Institute of Health

Prof. Dr. Almut Schulze
Head of Division, Tumor Metabolism and Microenvironment, DKFZ, Heidelberg

Dr Marc Hennequart
Professor in Biochemistry and Cell biology, University of Namur

Dr Carole Linster, Chairman
Assoc. Professor in Biochemistry at the LCSB, University of Luxembourg

Dr Claude Haan, Vice Chairman
Research scientist, Department of Health, Medicine and Life Sciences, University of Luxembourg

UNIVERSITÉ DU LUXEMBOURG

Affidavit / Statement of originality

I declare that this thesis:

- is the result of my own work. Any contribution from any other party, and any use of generative artificial intelligence technologies have been duly cited and acknowledged;
- is not substantially the same as any other that I have submitted, and;
- is not being concurrently submitted for a degree, diploma or other qualification at the University of Luxembourg or any other University or similar institution except as specified in the text.

With my approval I furthermore confirm the following:

- I have adhered to the rules set out in the University of Luxembourg's Code of Conduct and the Doctoral Education Agreement (DEA)[1] , in particular with regard to Research Integrity.
- I have documented all methods, data, and processes truthfully and fully.
- I have mentioned all the significant contributors to the work.
- I am aware that the work may be screened electronically for originality. I acknowledge that if any issues are raised regarding good research practices based on the review of the thesis, the examination may be postponed pending the outcome of any investigation of such issues. If a degree was conferred, any such subsequently discovered issues may result in the cancellation of the degree.

Approved on 2025-10-27

If applicable (DEA is compulsory since August 2020)

UNIVERSITÉ DU LUXEMBOURG

Faculty of Science, Technology and Medicine

LUXEMBOURG INSTITUTE OF HEALTH

A PhD Dissertation by

Kim Eiden

Submitted to the University of Luxembourg

Elucidating Cellular Adaptation Mechanisms during Nucleotide Inhibition

Members of the thesis supervision committee (CET):

Dr. Johannes Meiser
(dissertation supervisor)

Department Head, Department of Cancer Research, Luxemburg Institute of Health, Luxembourg

Dr. Elisabeth Letellier

Assistant Professor, Department of Life Sciences and Medicine, University of Luxembourg, Luxembourg

Dr. Gerta Hoxhaj

Assistant Professor at Children's Research Institute at UT Southwestern Dallas, Texas, United States

Acknowledgements

I would like to start with expressing my deepest gratitude to my PhD supervisor Dr Johannes Meiser, I am extremely thankful for all the support you gave me throughout these 4 years. From the day I started, you did not only take on the role of guiding me through my research projects, you represented a role model and mentor, transmitting knowledge and sharing your passion for science and research. Thanks to the support and trust you put in me, I was able to grow professionally as a young scientist but also personally, gaining self-confidence and passion for the work we accomplish daily. You always remained approachable and easy to talk to, which is something I valued a lot.

Next, I am very thankful for the support I received within the CMG team. They made me feel welcomed instantly and even though the group has changed a lot throughout the years, there always remained a positive and supportive energy. I would like to especially thank Nicole and Laura, you helped me lot during my first steps in the lab, I could come to you with any question (I still do) and you would always try to help. Also, my office mate Lara, thank you for helping me with any IT issue and for all the laughter we shared together. Christina and Alina you were always there to discuss and exchange about experiments or organizational things in the lab and thank you Enzo for supporting me with the sphere assays. Moreover, as my PhD project involved a lot of metabolomics, I felt very lucky being able to make used of our Metabo platform at the LIH. Therefore, I would like to thank Dr Nathalie Legrave for all your efforts in running the platform and Monika and Francois for sneaking in small batches of me even when the booking schedule of the MS was tight.

As a PhD journey never goes straight, we were facing a standstill of our labs in 2022, lasting around 3 months, due to the move into our new building. However, I am very thankful that I was welcomed to join the lab of Dr Elisabeth Letellier at the University of Luxemburg during this period. One says there is always something good in every bad situation and this was actually true. I did not only perform my own experiments over there but also worked together with many nice people. Thank you Marianne for teaching me how to work with patient derived organoids and Fabien for your support in the lab.

Along these lines I would like to thank my CET committee, where Elisabeth was part of together with Johannes and Dr Gerta Hoxhaj form the Children's Medical Center Research Institute in Dallas. Once a year we would meet up and discuss about the progression of my PhD project, I appreciate all the useful input I received during each meeting.

Next, I would like to thank Dr Carole Linster, Dr Almut Schulze, Dr Marc Hennequart and Dr Claude Haan who made the effort to read my PhD thesis and agreed to be part of my thesis defense committee, I highly value your feedback and guidance.

During my time at the LIH I met a lot of inspiring people coming from many different places. Besides scientific collaborations or professional meetings there are sometimes also the real friendships that help you progress during your PhD. I am grateful for these connections, they represented an important mental support at work and I would like to thank Laura and Vanessa for always having an open ear. In that regard I would also like to thank a former PhD student from the Norlux team at LIH, Carina you were more that just the supervisor of my master thesis you gave me the inspiration and motivation to start a PhD myself and for that I am extremely grateful. Next, I really appreciated being part of the i2Tron DTU where I met many likeminded people with whom I could exchange about our projects and other experiences during our PhD. Thank you Vanessa and Elisa for making the i2Tron retreats so much more fun.

Of course, there are many people outside of the lab to whom I owe a big thank you. My roommate Julie, my friends from climbing Charel and Max, you helped me through stressful periods by simply distracting me and letting me switch off my mind for some time. Importantly, the people who believed in me the most, my family, my mom, dad and little sister Liz, you always made big efforts in trying to understand what exactly I am doing in the lab and supported me in every possible way. Finally, my partner Pascal, with you I shared every little thought that was lying on my mind, thank you for your warm words, hugs and all the cookies you have been baking for me, I am very grateful to have you by my side.

List of Publications

Manuscript I: "One-Carbon Metabolism in cancer"

RRCR Series - Fundamentals of Cancer Metabolism 2025

AUTHORS: **Kim Eiden**, Johannes Meiser

Personal contribution: All sections of this book chapter including the illustrations were done by myself. Johannes Meiser assisted with the "Plasticity of the One Carbon Metabolism" part and reviewed the final document.

Manuscript II: "Formate overflow drives toxic folate trapping in MTHFD1 inhibited cancer cells"

Nature Metabolism 2023

AUTHORS: Alanna C. Green, Petra Marttila, Nicole Kiweler, Christina Chalkiadaki, Elisée Wiita, Victoria Cookson, Antoine Lesur, **Kim Eiden**, François Bernardin, Karl S. A. Vallin, Sanjay Borhade, Maeve Long, Elahe Kamali Ghahe, Julio J. Jiménez-Alonso, Ann-Sofie Jemth, Olga Loseva, Oliver Mortusewicz, Marianne Meyers, Elodie Viry, Annika I. Johansson, Ondřej Hodek, Evert Homan, Nadilly Bonagas, Louise Ramos, Lars Sandberg, Morten Frödin, Etienne Moussay, Ana Slipicevic, Elisabeth Letellier, Jérôme Paggetti, Claus Storgaard Sørensen, Thomas Helleday, Martin Henriksson & Johannes Meiser

Personal contribution: I actively participated in the project meetings and generated the sphere growth data, which corresponds to Fig.5 a+b.

Manuscript III: "Purine inhibition affects redox state and activates compensatory mechanisms in cancer cells"

To be defined

AUTHORS: **Kim Eiden**, Nathalie Legrave, Christina Krötz, Johannes Meiser

Personal contribution: In this manuscript all the data corresponding to the main and the supplementary figures were generated by myself. The MS measurements have been performed by the LIH Metabolomics platform and the staff from the NCP platform assisted with the single cell soring for the CRISPR clones. This manuscript represents to the majority of my PhD work.

Manuscript IV: "Mitochondria preserve an autarkic one-carbon cycle to confer growth-independent cancer cell migration and metastasis"

Nature Communications 2022

AUTHORS: Nicole Kiweler, Catherine Delbrouck, Vitaly I. Pozdeev, Laura Neises, Leticia Soriano-Baguet, **Kim Eiden**, Feng Xian, Mohaned Benzarti, Lara Haase, Eric Koncina, Maryse Schmoetten, Christian Jaeger, Muhammad Zaeem Noman, Alexei Vazquez, Bassam Janji, Gunnar Dittmar, Dirk Brenner, Elisabeth Letellier & Johannes Meiser

Personal contribution: For this manuscript I performed a couple of migration assays corresponding to Fig.6 a-b,e and generated double MTHFD1L and ALDH1L2 KOs in MDA-MB-468 cells.

Manuscript V: "Protocol using ex vivo mouse brain slice culture mimicking in vivo conditions to study tumor growth and cell motility of glioblastoma cells"

STAR protocols 2024

AUTHORS: Laura Neises, Catherine Delbrouck, Anne Schuster, Mahsa Rezaipour, **Kim Eiden**, Anais Oudin, Carina Fabian, Simone P Niclou, Anna Golebiewska, Johannes Meiser

Personal contribution: For the STAR protocol, I created the graphical abstract and contributed to the revision of the article.

Abstract

Cancer cells dynamically rewire their metabolism according to changes in their environment or as a response to treatment. Such metabolic adaptations pose a challenge while targeting cancer cells, however they also represent potential metabolic vulnerabilities that can be exploited as secondary targets.

The one-carbon metabolism (OCM), is a metabolic pathway ensuring the transfer of one-carbon units via a number of biochemical reactions, serving a broad range of biological purposes. Cancer cells are highly reliant on the OCM as it confers the metabolic dynamism mentioned above, needed for tumor growth, homeostasis and progression. The activity of the OCM within cancer cells is exemplary for their metabolic plasticity and flexibility, as it covers the three main metabolic pillars in mammalian cells, namely: biosynthesis, redox homeostasis and bioenergetics. Since the 1950s, the OCM is successfully targeted for its biosynthetic potential, with methotrexate (MTX) being the first drug, targeting metabolism and eliminating cancer cells. However, the inhibition of the anabolic part of the OCM leads to the enhancement of the mitochondrial one-carbon cycle flux, supporting bioenergetics and subsequently supporting the metastatic potential of cancer cells.

On the one hand, we showed that inhibition of nucleotide biosynthesis while targeting the cytosolic OCM increases the risk of tumor spreading. On the other hand, we demonstrated that targeting the biosynthesis of nucleotides induces additional vulnerabilities. For instance, cancer cells become increasingly dependent on glutamine as a carbon source for TCA cycle activity, which represents a metabolic vulnerability in cancer cells treated with purine inhibitors. Additionally, they must dynamically adapt their ROS detoxification systems and show enhanced malic enzyme (ME) activity.

Importantly, cancer cells need to maintain their cofactor integrity to efficiently transfer one-carbon units via the OCM. We have identified a toxic folate trapping mechanism, resulting from cytosolic OCM inhibition and reduced purine nucleotide *de novo* synthesis. Due to limited free cofactor, namely THF, availability the genome stability is perturbed, leading to cancer cell toxicity.

The findings included in this thesis, illustrate the challenges and the opportunities while targeting the metabolism of cancer cells. Unravelling the mode of action of TH9619, helped to seek approval from the European Medicine Agency. TH9619 has entered the first round of clinical trial this year, highlighting the significance of fundamental mechanistic work to develop effective treatment strategies for cancer patients.

Aims and Objectives of the Thesis

The aims of this thesis are to:

1. give an extensive and comprehensive overview on the role of the OCM in tumor cells and the tumor microenvironment (TME).
2. study the efficacy and mode of action of specific OCM enzyme inhibitors that successfully eliminate cancer cells.
3. elucidate the adaptation mechanisms arising from these pharmacological interventions.

In sum, the objective of this study was to gain an in depth understanding on OCM in cancer cells with the aim to contribute to a more successful application of nucleotide inhibitors in treating cancer patients.

Methods

Method	Manuscript
Stable Isotope Tracing	IV, III, II
Metabolite extraction	IV, III, II
LC-MS measurements	IV, III, II
GC-MS measurements	IV
IC-MS measurements	III
YSI medium measurements	IV
DCF-DA ROS measurements with FACS	IV, III
AnnexinV-FITC/PI measurements with FACS	IV, III, II
CRISPR-Cas9 gene editing	IV, III, II
siRNA-mediated gene silencing	IV
Western Blot	IV, III, II
qPCR analysis	IV
Spheroid growth	III, II
Stable Isotope tracing, metabolite extraction and LC-MS measurements from Spheres	III
Proliferation Incucyte assay	IV, III, II
Resazurin cell viability assay	II
Mitochondrial membrane potential	II
Cellular thermal shift assay (CESTA)	II
Target engagement assay with using drug affinity responsive target stability (DARTS) assay	II
Formate derivatisation and quantification in medium by GC-MS	IV, II
10-formyl THF quantification	II
Cell cycle analysis by FACS	II
Seahorse measurements	IV
Scratch assay for migration	IV
Transwell assay for invasion and migration	IV
H&E staining	IV
Proteomics	IV

Animal model	Manuscript
Immunocompetent Balb/c mice Syngeneic 4T1 (SCR vs MTHFD1L KD) carcinoma cells, orthotopically implanted into the mammary fat pads (1 injection/mouse) Primary tumor growth was monitored between day 7 and day 35 of the experiment Examination of metastatic outgrowth after 6 weeks	IV

Table of Content

Affidavit / Statement of originality ... 2
Acknowledgements ... 4
List of Publications ... 6
Abstract ... 8
Aims and Objectives of the Thesis ... 9
Methods ... 10
1. Synopsis Introduction ... 14
1.1. Cancer ... 14
1.2. Cancer Metabolism a “Hallmark of Cancer” ... 14
1.3. Metabolic Plasticity and Flexibility of Cancer Cells ... 15
1.3.1. Examples of Metabolic Plasticity and Flexibility ... 16
1.3.1.1. Glutamine Metabolism ... 16
1.3.1.1.1. Targeting Glutamine Metabolism ... 17
1.3.1.2. Serine Metabolism ... 18
1.3.1.2.1. Serine Synthesis ... 19
1.3.1.2.2. Targeting Serine Metabolism ... 19
1.3.1.2.3. Serine feeds the OCM ... 21
1.3.1.2.4. Folate mediated serine catabolism and formate overflow ... 22
1.3.1.2.5. Targeting the folate mediated OCM and Metastasis ... 23
1.3.1.3. Purine Nucleotides ... 25
1.3.1.3.1. Targeting Purine Metabolism ... 26
1.3.1.4. NADPH ... 27
1.3.1.4.1. Compartmentalization of NADPH ... 28
2. Synopsis Results and Discussion ... 30
2.1. Manuscript II : “Formate overflow drives toxic folate trapping in MTHFD1-inhibited cancer cells” ... 30
2.1.1. Results of Manuscript II ... 30
2.1.1.1. TH9619 targets the DC function of MTHFD1 and not mitochondrial MTHFD2 ... 30
2.1.1.2. TH9619 blocks dTMP synthesis in WT cells ... 30
2.1.1.3. Hypoxanthine Enhances TH9619 Activity via Folate Trapping ... 31
2.1.1.4. Formate overflow drives TH9619-induced trapping of 10-CHO-THF ... 34
2.1.1.5. Treatment with TH9619 has differential biological outcomes depending on MTHFD2 status ... 34
2.1.2. Discussion of Manuscript II ... 35
2.2. Manuscript III : “Purine Inhibition affects Redox State and activates Compensatory Mechanisms in Persistent Cancer Cells” ... 36

2.2.1. Results of Manuscript III 36
2.2.1.1.Cell toxicity through dTMP depletion but not purine biosynthesis inhibition 36
2.2.1.2. Purine depletion disrupts the pentose phosphate pathway 37
2.2.1.3. Purine-Inhibited cancer cells shift towards glutamine-driven TCA cycle metabolism 38
2.2.1.4. Malic enzyme activity compensates for Redox stress following purine pathway blockade 39
2.2.1.5. Purines oppositely regulate ME and PEPCK activity under glucose limitation 40
2.2.2. Discussion of Manuscript III 40
2.3. Manuscript IV : “Mitochondria preserve an autarkic one-carbon cycle to confer growth-independent cancer cell migration and metastasis” 41
2.3.1. Results of Manuscript IV 41
2.3.1.1. Blocking anabolic pathways has distinct effects on the migratory capacity and the EMT phenotype of cancer cells 41
2.3.1.2. Mitochondrial OCM maintains serine catabolism upon cytosolic OCM inhibition after MTX treatment 42
2.3.1.3. Mitochondrial OCM supports cancer cell motility in dependence of serine and mitochondrial THF 43
2.3.2. Discussion of Manuscript IV 44
3. Conclusion and Perspectives 45
4. References 50
5. Abbreviations 57
6. Appendix of original publications 60

1. Synopsis Introduction

1.1. Cancer

Cancer represents a large group of diseases that can arise in any organ or tissue of the human body, though an abnormal and uncontrollable cell growth. Such characteristics usually develop due to changes, or mutations, in the cellular DNA. These mutations can affect genes that regulate cell growth and division, so called oncogenes, DNA repair mechanism and cell death or apoptosis. In 2022, an estimated number of 20 million new cancer cases were diagnosed worldwide, with approximately 10 million cancer related deaths were within the same year [1]. With that, cancer is the second leading cause of death globally, after cardiovascular diseases. The main characteristics of cancer cells are often referred to as “Hallmarks of cancer”, a concept introduced by researchers Hanahan and Weinberg, which describes the biological capabilities acquired during tumor development [2-4]. Among those are the ability to maintain proliferative signaling, resistance to growth inhibitory signals and programmed cell death, which together enhances uncontrolled cell division and tumor growth. Moreover, angiogenesis stimulates the formation of new blood vessel to ensure nutrient and oxygen supply within the tumor. Upon disease progression, cancer cells detach from the primary tumor and invade into the adjacent tissue, representing the onset of metastasis. Consequently, tumor cells can enter circulation and colonize distant organs, to form secondary tumors. Hence, tissue invasion and metastasis belong to the core hallmarks of cancer and represent the most important factor in determining patient prognosis. It is generally estimated that about 90% of cancer-related deaths are due to metastasis rather than the primary tumor itself [5, 6].

1.2. Cancer Metabolism a “Hallmark of Cancer”

In the updated version of 2011, "Deregulating Cellular Energetics" was added as an emerging hallmark of cancer [3]. Almost 100 years after Otto Warburg first discovered that cancer cells show abnormally high glucose consumption, linked to their inefficient way of producing energy through aerobic glycolysis known today as the “Warburg effect” [7]. This switch to high glycolytic activity, allows cancer cells to produce adenosine triphosphate (ATP) inefficiently but quickly. Warburg originally proposed that cancer cells have defective mitochondria, forcing them to rely on glycolysis for energy generation. However, we know now that this explanation is not universally true, in some tumors mitochondrial alterations or defects in the electron transport chain (ETC) may promote the Warburg effect, however in most cancers mitochondria are fully functional and even more proteome efficient than aerobic glycolysis in terms of ATP generation [8]. Moreover, high glucose dependency is not exclusively linked to increased glycolysis to generate ATP, cancer cells rely on glucose to fuel the anabolic needs for the biosynthesis of macromolecules such as amino acids, lipids and nucleotides. Additionally, glycolytic intermediates are connected to other metabolic pathways such as the pentose

phosphate pathway (PPP) and the serine synthesis pathway (SSP) [9, 10]. Besides, it has been shown as well that some tumors are more glycolytic, whereas others mainly depend on oxidative phosphorylation [11].

In a clinical context, the discovery of increased glucose uptake in tumors compared to healthy tissues, let to the development of diagnostic tools, exploiting this distinctive metabolic feature. The visualization of a glucose analog, 18F-fluorodeoxyglucose (18F-FDG) by positron emission tomography (PET)-based imaging, is successfully used in the clinic to assess treatment responsiveness [12]. However, the limitation of this method is that it only detects tissues with high glucose consumption, but does not inform about the rate of glycolysis nor the fate of glucose within the tumor cells.

Warburg's discoveries marked a new era within cancer research, as he has set the foundation to explore distinct metabolic features of cancer cells as therapeutic targets. However, besides a few successes such as the clinical introduction of antifolates through the work of Sidney Farber in the 1940's [13], the interest around cancer metabolism remained mediocre during the following years. It was only in the early 2000's where cancer metabolism reemerged as a hot topic for tumor research. The sequencing of the human genome [14] set a milestone for the research around tumor genetics, but also represented pioneering work for the discovery of metabolic enzymes such as PHGDH [15, 16] and MTHFD2 [17] overexpressed in human cancers.

The research around cancer cell metabolism has evolved tremendously during the last two decades, elucidating how metabolic reprogramming is crucial for cancer cell survival, growth, and proliferation. Highly proliferating tumor cells are forced to adapt their metabolism to maintain rapid cell division and meet the demands of increased biosynthesis of macromolecules such as nucleotides, proteins or lipids. Being metabolically flexible also allows tumor cell survival within a stressful environment, such as hypoxia, oxidative stress or nutrient depletion.

1.3. Metabolic Plasticity and Flexibility of Cancer Cells

The concept of metabolic plasticity and flexibility has been described in the context of the metastatic cascade and involves a switch between different metabolic pathways depending on the changing microenvironments while traveling to a distant organ. While metabolic plasticity means that a single nutrient can be metabolized for different purposes, metabolic flexibility represents the usage of multiple nutrients that are able to cover the same metabolic need (Fig. 1) [18]. Drivers of metabolic adaptations can be environmental factors within the TME, such as nutrient depletions or hypoxia, but they are also under genetic control. The uptake of metabolites as well as the activity of metabolic pathways such as fatty acid and nucleotide

1 here

synthesis, glutaminolysis and glycolysis can vary according to environmental conditions and are transcriptionally regulated [19-23]. Moreover, therapeutic pressure can also have an influence on the metabolism of cancer cells and metabolic rewiring is an important mechanism of adaptive chemoresistance [24]. However, the paradox metabolic flexibility creates is that it presents a challenge for treatment but also creates metabolic vulnerabilities and opportunities for combinatory therapies that target multiple pathways simultaneously. Hence, the goal is to on the one hand, identify the hardwired metabolic liabilities of cancer cells that can present a therapeutic target with high specificity to achieve a proper therapeutic index. On the other hand elucidate metabolic dependencies arising from therapies and explore their potential as secondary drug targets.

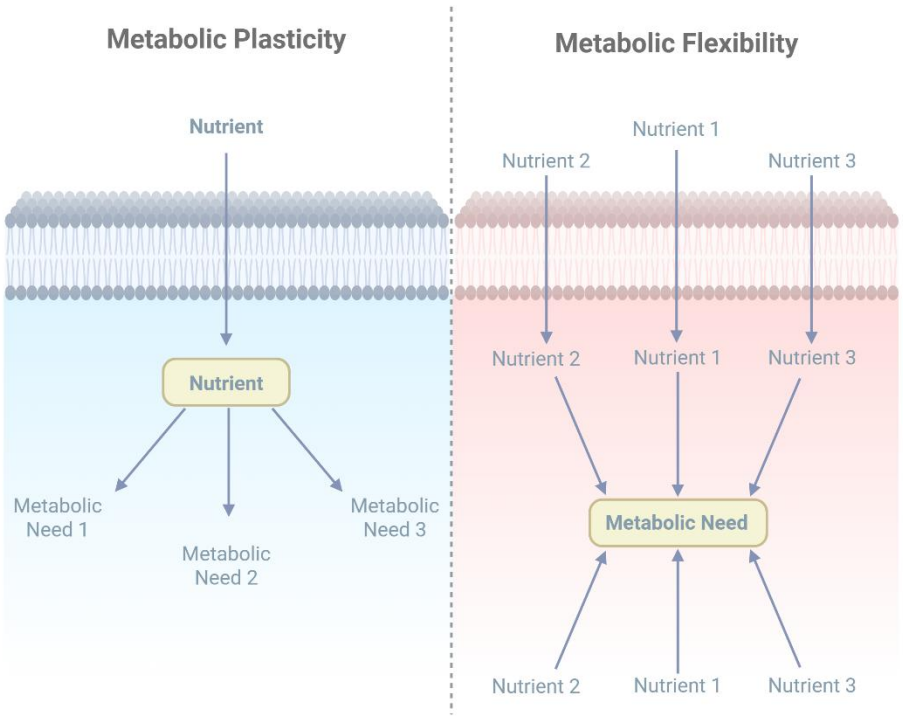

Figure 1: Schematic representation of metabolic plasticity: a single nutrient being able to cover multiple metabolic needs and metabolic flexibility: multiple nutrients supporting the same metabolic requirement

1.3.1. Examples of Metabolic Plasticity and Flexibility

1.3.1.1. Glutamine Metabolism

While many tumors rely heavily on glucose to fuel growth and proliferation, a subset of cancer cells develop a reliance on glutamine, also referred to as “glutamine addiction” [25]. Glutamine represents the most abundant amino acid in human plasma [26] and the second principal growth-supporting substrate for tumor cells [27]. Its catabolism can support many different cellular functions and is therefore exemplary for metabolic plasticity of cancer cells.

Glutamine acts as nitrogen donor for nucleotide and amino acid synthesis within the cytoplasm, but also represents an essential mitochondrial substrate, acting as carbon donor for TCA cycle activity, supporting energy production [28, 29]. In order to do so, glutamine is converted to glutamate by the enzyme glutaminase (GLS), which is further deaminated to α-ketoglutarate (α-KG). Importantly, glutamate has an essential non metabolic function, being a primary excitatory neurotransmitter, stimulating neurons in the central nervous system [30]. However, excessive glutamate secreted by brain tumor cells contributes to a pro-tumorigenic environment leading to excitotoxicity, causing damage to healthy tissue [31]. Moreover, the excretion of glutamate in exchange for cystine, also known as cystine/glutamate antiporter (xCT) ensures the import of cystine which can be further converted into cysteine, which together with glutamate and glycine represents an essential precursor for glutathione (GSH) synthesis, supporting the cellular antioxidant defense [32]. An overview of the metabolic functions covered by glutamine metabolism is summarized in Table 1.

Table 1: Summary of some key metabolic features covered by glutamine.

Metabolic need	**Role of glutamine**
Anaplerosis for the TCA cycle	*Glutamine replenishes TCA cycle intermediates via conversion to glutamate and α-ketoglutarate [28, 29]*
Reductive carboxylation and lipid biosynthesis	*In tumors with impaired mitochondria and oxidative TCA cycle function, glutamine supports lipid biosynthesis via reductive carboxylation [33]*
ATP Production	*Upon glucose limitation or impaired glycolysis, glutaminolysis can feed the TCA cycle to maintain ATP production [28, 29]*
Redox homeostasis	*Glutamine supplies glutamate, essential for GSH synthesis, buffering oxidative stress [34]*
Nucleotide biosynthesis	*Acts as nitrogen donor for the biosynthesis of purine and pyrimidine nucleotides [35]*
xCT transport	*Cystine/glutamate antiporter, importing cystine for GSH synthesis, is essential for cancer cells to counteract oxidative stress [32]*

1.3.1.1.1. Targeting Glutamine Metabolism

Besides tumor cells intrinsic metabolic needs, glutamine dependency can be induced by external factors such as changes within the TME or as a response to therapy. For instance, limited oxygen supply or reduced glucose availability pushes cancer cells towards an increased glutamine metabolism [36, 37]. Additionally, when mitochondrial pyruvate transport

is impaired, cancer cells become entirely dependent on glutamine in order to maintain cell growth [38]. In certain cancers, glutamine metabolism may support chemoresistance, as upregulation of glutamine transporters has been observed in cisplatin resistant cancer cells [39]. In **manuscript III** we show that cancer cells treated with purine nucleotide inhibitors increase their glutamine usage instead of glucose as a carbon source for TCA cycle activity. Interestingly, phosphoribosylpyrophosphate amidotransferase (PPAT) from the *de novo* purine biosynthesis pathway and GLS1 were shown to be reciprocally regulated during malignant progression. Depletion of one enzyme correlates with increased expression of the other and PPAT-GLS1 balance governs the fate of glutamine either entering the TCA cycle or nucleotide synthesis [40]. One could hypothesize that a dependency on GLS1 while purine biosynthesis is impaired, might increase the effectiveness of GLS inhibitors to target tumor progression.

However, GLS inhibitors like Telaglenastat (CB-839) are already being clinically tested as combinatory treatments, for example in combination with programmed cell death protein 1 (PD-1) or programmed cell death-ligand 1 (PD-L1) antibodies [41] as well as in combination with tyrosine-kinase inhibitor cabozantinib [42], or mTOR blocker everolimus [43]. Unfortunately, all combinations showed only low additive benefits for the patients. Most likely because of cancer cell flexibility, allowing tumors to bypass glutamine dependency by activating other metabolic pathways such as increased fatty acid oxidation or autophagy [44, 45]. A recent study also identified a unique capacity of serine synthesis enzyme phosphoserine aminotransferase (PSAT1) to sustain α-KG production (Fig. 2), when glutamine metabolism is impaired. Breast cancer cells resistant to GLS inhibition or glutamine starvation, showed an increased dependency on serine derived α-KG, which is another example of how metabolic adaptations can maintain tumor growth in a challenging nutrient environment [46].

1.3.1.2. Serine Metabolism

After glutamine, serine is usually the second most consumed amino acid in cancer cells. Serine plays a central role in cellular metabolism, particularly through its contribution to OCM, a network of reactions that transfer single carbon units for biosynthesis of nucleotides, amino acids, and other essential metabolites, and is involved in maintaining redox balance and epigenetic regulation. The OCM plays a crucial role in tumor growth and progression, which is described in more detail in **manuscript I**. Furthermore, serine supports the cellular antioxidant defense as it can be converted to glycine, needed for GSH generation. Finally, serine is a precursor of phosphatidylserine, an important component of cell membranes, serving as signaling molecule for apoptosis and currently explored as cancer biomarker and targeted drug delivery [47-49] (Fig.2).

Table 2: Metabolic needs supported by serine.

Metabolic need	Role of serine
Nucleotide Synthesis	*Donates one-carbon units, necessary for purine and thymidine synthesis [50]*
Redox homeostasis	*Serine is a precursor of glycin e, which, along with glutamate and cysteine forms GSH, protecting cancer cells from oxidative stress [50, 51]*
Lipid Synthesis	*Synthesis of phospholipid phosphatidylserine and contribution to sphingolipid metabolism, important in membrane dynamics and signaling [52, 53]*
Protein Synthesis	*Serine is incorporated into polypeptide chains during translation and, through its hydroxyl group, participates in various post-translational modifications that influence protein structure and function [54]*
Epigenetic Regulation	*Through the folate cycle, serine fuels SAM production, a methyl donor for DNA, RNA and histone methylation [50]*

1.3.1.2.1. Serine Synthesis

Cancer cells can import serine from the extracellular environment through solute carriers (SLCs), a family of transmembrane protein transporters, or synthesize it *de novo* from glucose via the serine synthesis pathway (SSP). This involves a sequence of three enzymatic reactions transforming the glycolytic intermediate 3-phosphoglycerate (3-PG) via phosphoglycerate dehydrogenase (PHGDH), PSAT1 and phosphoserine phosphatase (PSPH) [55] (Fig. 2). Upregulation of SSP genes occur in various cancer types, according to a TCGA dataset including mRNA levels of 33 different cancers, PHGDH expression is significantly higher in tumors compared to normal tissues [56] and correlates with a poor prognosis in cancer patients [56-60].

Moreover, serine plays an essential role during the formation of metastases. Several studies have elucidated a dependency on serine to sustain metastatic growth in secondary sites, supporting proliferative needs [61-64]. Hence, the development of therapeutic strategies targeting the serine metabolism is of strong interest.

1.3.1.2.2. Targeting Serine Metabolism

PHGDH is the rate-limiting enzyme of the *de novo* SSP and the discovery of PHGDH as oncogenic driver was made around 15 years ago, identifying PHGDH amplification and dependency in tumors [15, 16]. Demonstrating reduced cancer cell proliferation upon knockdown of PHGDH, established PHGDH as a metabolic target for cancer therapy. Later

studies showed that PHGDH depletion affects the OCM and disrupts nucleotide metabolism, which are essential for tumor growth, and also impacts other metabolic pathways such as the TCA cycle and cellular redox balance [65, 66].

Consequently, the development of inhibitors targeting PHGDH has been of major interest, with NCT-503 being the first reported selective PHGDH inhibitor, efficiently reducing serine synthesis and tumor growth in xenografts [67]. Unfortunately, many of the subsequently developed inhibitors such as CBR-5884, PH755 or BI-4924 show strong antiproliferative effects in PHGDH-high cancer cells *in vitro* [65, 68, 69]. However, their *in vivo* use remains challenging due to activation of resistance mechanisms, poor bioavailability or limited selectivity and potency *in vivo* [70]. Moreover, PHGDH expression only provides a growth advantage to tumors tissues with limited serine availability, otherwise the presence of serine in the TME can rescue the effect of PHGDH blockade [67, 71].

Nevertheless, PHGDH is not only supporting growth and proliferation in some cancers, but has also been associated with increased metastatic potential [58, 64, 72]. However, a challenge while targeting PHGDH in the context of metastasis remains its heterogeneity within the primary tumor. Paradoxically, lower PHGDH expression has been found in circulating tumor cells (CTCs) and early metastasis and low or heterogenic PHGDH expression was associated with a higher aggressiveness of the tumor. The authors concluded that although PHGDH favors cancer cell proliferation, its non-canonical function is associated with a reduction of dissemination and metastatic spread of the tumor [63]. In that case, high extracellular serine levels might help shaping the metastatic niche for PHGDH lo CTCs colonizing distant organs.

Therefore, another strategy implies the reduction of serine and glycine concentrations within the extracellular space, through dietary restrictions. Some promising outcomes have already been achieved in animal models where overall survival was increased through a serine/glycine restricted diet and trials in patients are currently explored [73, 74].

Additionally, targeting of both, the exogenous and endogenous serine source stand out as promising therapeutic approach to reduce tumor growth in preclinical mouse models [75]. Moreover, limited serine and glycine availability was shown to increase the sensitivity of PHGDH inhibition in brain metastasis [62]. Finally, combinations with other therapeutic agents such as antifolates or redox modulating agents might increase the therapeutic index of a serine/glycine restricted diet [65, 66]. Also the combination with radiation therapy sensitized different tumor types to a depletion in environmental serine and glycine [76].

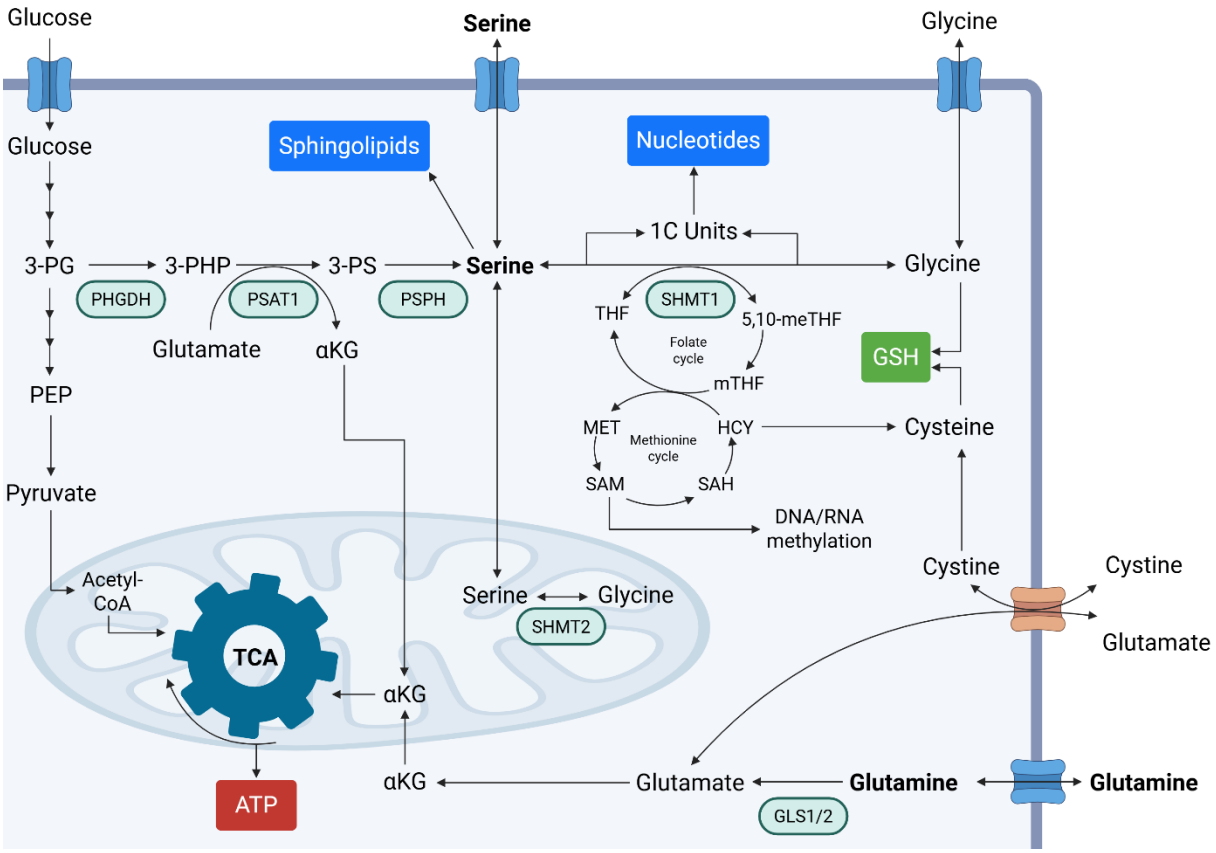

Figure 2: Role of serine and glutamine in metabolic processes: biosynthesis (blue), redox balance (green) and bioenergetics (red). 3-PG: 3-phosphoglycerate; PEP: phosphoenolpyruvate; PHGDH: 3-phosphoglycerate dehydrogenase; 3-PHP: 3-phosphohydroxypyruvate; PSAT: phosphoserine aminotransferase; 3PS: 3-phosphoserine; PSPH: phosphoserine phosphatase; SHMT1: serine hydroxymethyltransferase 1; 5,10-meTHF: 5,10-methylene tetrahydrofolate; mTHF: 5-methyl tetrahydrofolate; THF: tetrahydrofolate; GSH: reduced glutathione; MET; methionine; HCY: homocysteine; SAM: S-adenosyl methionine; SAH: S-adenosyl homocysteine

1.3.1.2.3. Serine feeds the OCM

One arm of serine metabolism leads into the OCM, where serine acts as a precursor for one-carbon units and unfolds its full potential as ambivalent metabolite, which supports cancer cell plasticity by contributing to a broad range of metabolic needs. The OCM encompasses three major metabolic pathways: the folate cycle, supporting nucleotide biosynthesis, redox balance and bioenergetics; the methionine cycle, providing methyl groups for DNA, RNA and histone methylation and the transsulfuration pathway, important for the cellular antioxidant defense. The function of the different OCM metabolic pathways and their relevance in cancer cells is highlighted in the book chapter on “One Carbon Metabolism in Cancer” referred to as **Manuscript I**.

1.3.1.2.4. Folate mediated serine catabolism and formate overflow

So far, we have been focusing on the metabolism of serine within the cytosol and highlighted its role in supporting tumor growth and dissemination, by covering various metabolic needs. However, serine catabolism via the folate mediated OCM is compartmentalized and supports the transfer of one carbon units within the cytosol as well as within the mitochondria. Serine entering the mitochondria is oxidized by serine hydroxymethyltransferase 2 (SHMT2) to form glycine and one carbon unit, which together with tetrahydrofolate (THF) forms 5,10-methylene-THF (5,10-CH2-THF). Subsequently 5,10-CH2-THF is converted to 10-formyl-THF (10-CHO-THF) in a NAD(P)+/NAD(P)H dependent reaction, catalyzed by methylenetetrahydrofolate dehydrogenase 2 (MTHFD2). Following the MTHFD2 mediated reaction, mitochondrial 10-CHO-THF is further metabolized at the metabolic fork, either via the action of aldehyde dehydrogenase 1 family member L2 (ALDH1L2) producing free THF and CO_2 or via methylenetetrahydrofolate dehydrogenase 1 like (MTHFD1L) generating THF and the one carbon molecule formate (Fig. 3). The fate of formate was long believed to mainly support biosynthesis of nucleotides, however it has been evidenced that the rate of serine derived formate exceeds the anabolic demands of cancer cells and is excreted into the extracellular space, referred to as “formate overflow [77]. Consequently, high levels of mitochondrial derived- as well as exogenous formate was shown to enhance cancer cell invasion, marking the onset of metastasis [78-81]. In **manuscript I** we are reviewing the role of the OCM and formate on cancer cells as well as on other cells within the TME. Current literature strongly encourages to further investigate the influence of formate not only on the cancer cells directly, but also on other cell types within the TME such as the immune cell compartment. Contrary to the observations stated above, displaying formate as a pro-tumor molecule, recent studies demonstrated that formate can enhance anti-tumor immunity, boosting CD8+ T-cell function and improving immune therapies, such as PD-1 checkpoint blockade [82, 83]. Moreover, orally administered formate was shown to reduce the metastatic potential of intravenously injected B16-F10 tumor cells in C57BL/6J mice [84]. Furthermore, the effects of microbiome-derived formate can also be differential as two independent studies, reported that formate produced by gut bacteria can have pro- as well as anti- metastatic effects [79, 84]. Taken together, these findings imply a context dependent effect of formate on cancer. Consequently, it is highly important to consider the immunological background, as well as the microbiome composition of the chosen *in vivo* tumor model, to investigate the impact of formate in tumors. The effects of formate on tumor growth and dissemination could potentially differ between high vs low immune cell infiltration or be dependent on the gut microbial composition.

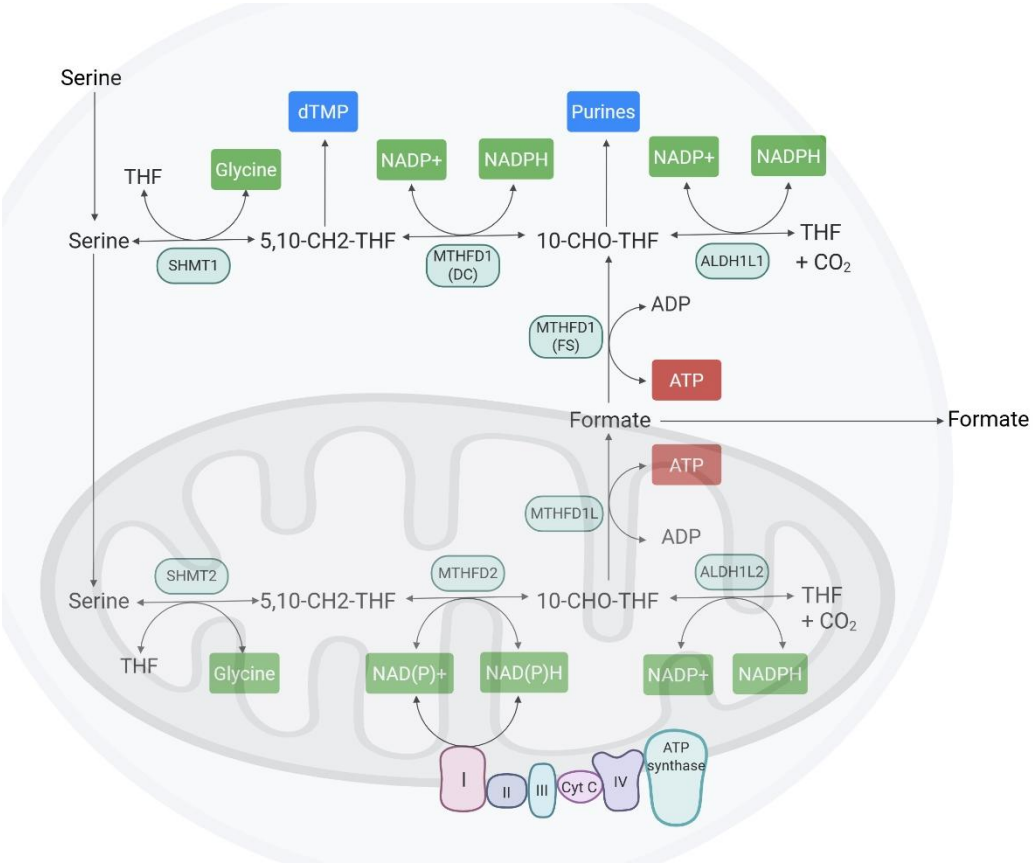

Figure 3: **Folate mediate OCM**: Schematic representation of serine entering the folates cycle to support the three major metabolic pillars biosynthesis (blue), redox balance (green) and bioenergetics (red). The key enzymes involved in the compartmentalized OCM are serine hydroxymethyltransferase 1/2 (SHMT1/2), methylenetetrahydrofolate dehydrogenase 2 (MTHFD2) trifunctional methylenetetrahydrofolate dehydrogenase, cyclohydrolase (DC) and formyltetrahydrofolate synthetase (FS) 1 (MTHFD1), methylenetetrahydrofolate dehydrogenase 1 like (MTHFD1/L) and aldehyde dehydrogenase 1 family member L1/L2 (ALDH1L1/2).

1.3.1.2.5. Targeting the folate mediated OCM and Metastasis

Targeting the folate mediated OCM for cancer therapy has been of interest early on. The work of Sydney Farber in the late 1940s, demonstrating that the antifolate aminopterin, induces remission in children with acute lymphoblastic leukemia (ALL) [13], set a landmark for the development of chemotherapeutics targeting cancer cell metabolism and especially the OCM. Until today, structural derivatives of these early folate antagonists—most notably MTX and pemetrexed (PEM)—remain a cornerstone of cancer chemotherapy and are used as first-line treatments across multiple malignancies, including acute lymphoblastic leukemia (ALL), breast cancer, bladder cancer, and lymphomas [85]. These drugs act by inhibiting human dihydrofolate reductase (DHFR), converting dihydrofolate (DHF) into tetrahydrofolate (THF),

thereby disrupting the OCM. In addition, pathways downstream of OCM emerged as therapeutic targets, for example thymidine synthase (TYMS). 5-fluorouracil (5-FU), a pyrimidine analogue inhibits TYMS, blocking the methylation of deoxyuridine monophosphate (dUMP) to deoxythymidine monophosphate (dTMP) and impairing DNA synthesis in cancer cells. As a standard-of-care treatment for multiple cancers, including advanced colorectal cancer, 5-FU potently inhibits folate-dependent dTMP synthesis and increases the overall survival of patients [86-89].

Currently, a lot of attention is drawn to MTHFD2 as a potential cancer target, as it has been identified as one of the most highly expressed enzymes among various human cancer types [17]. MTHFD2 is expressed in embryonic tissue but is absent in most healthy adult cells even the ones proliferating. High expression of MTHFD2 confers numerous advantages to tumor cells, supporting nucleotide biosynthesis, cellular respiration through its coupling to ETC, supporting redox balance and methylation reactions. Furthermore, MTHFD2 enhances chemoresistance and immune evasion in cancer cells [90-95]. Several compounds, targeting MTHFD2 have been developed [93], among them TH9619, first tested in acute myeloid leukemia (AML), causing DNA damage and cell death [96]. However, targeting MTHFD2 is challenging, as the drug needs to enter the mitochondrial compartment and selectively target MTHFD2. In **manuscript II** we investigated the mechanism of action of TH9619 in solid tumors and demonstrate that, contrary to what has been shown previously, the drug is unable to cross the inner mitochondrial membrane and therefore not reaching its target MTHFD2 due to high polarity and the presence of ionizable groups. Furthermore, we have demonstrated that high expression of MTHFD2 can paradoxically pose a metabolic vulnerability for cancer cells, as functional mitochondrial serine catabolism is required to increase the toxic effect of TH9619 [97].

Interestingly, even though mitochondrial enzymes such as MTHFD2 are among the most upregulated ones in cancer cells [17, 98], studies have shown that the mitochondrial OCM is dispensable for tumor proliferation as nucleotide synthesis can still be maintained due to the reversibility of the cytosolic OCM [99, 100]. In that regard, the question arises why MTHFD2 or mitochondrial metabolism generally is so well conserved, when tumor growth can be safeguarded without. One reason would be the support of growth independent functions related to the mitochondrial OCM, such as cancer cell motility and formation of metastasis. In **manuscript IV** we show that while inhibiting cancer cell proliferation by targeting nucleotide biosynthesis via the cytosolic OCM, the mitochondrial cycle keeps running independently, increases formate overflow, prompting cancer cell migration and metastasis [101]. However, the mechanism by which the mitochondrial OCM and formate affects metastasis formation remains to be elucidated.

1.3.1.3. Purine Nucleotides

As previously mentioned, the biosynthetic contribution of the OCM are dTMP and purines, which are essential for high proliferating cancer cells as they represent the building blocks for RNA and DNA. For the generation of purines, formate is incorporated from 10-CHO-THF, together with glutamine, glycine and aspartate to form the purine ring on top of a sugar backbone, derived from phosphoribosyl pyrophosphate (PRPP). This process is referred to as the *de novo* purine synthesis pathway, which is more energy costly as compared to the purine salvage pathway, where free purine bases namely adenine, guanine or hypoxanthine are converted to inosine monophosphate (IMP), the common precursor for both adenosine monophosphate (AMP) and guanosine monophosphate (GMP) (Figure 4). Although it was traditionally believed that mainly the *de novo* synthesis is the dominant source for purines in cancer cells, it has been evidenced that also the salvage pathway plays an essential role in maintaining the purine pools in tumor cells [102].

Besides serving as biosynthetic precursors for DNA and RNA, purines are crucial for energy metabolism and purinergic signaling. Moreover, purines play an essential role in the TME by influencing immune cell function and studies highlighted the effect of purines on tumor-specific immune regulation [103-105] and the potential of purine inhibitors as complementary strategies in cancer immunotherapy [106].

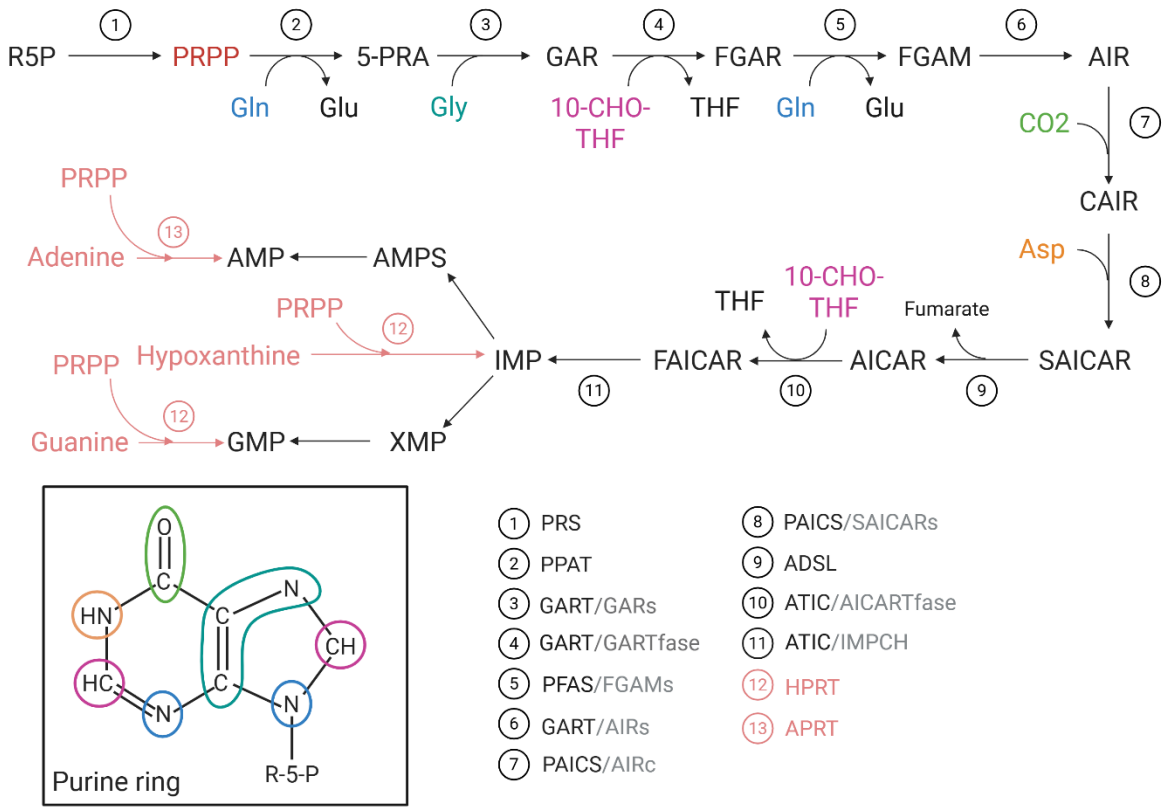

Figure 4: **Purine *de novo* synthesis**: Schematic representation of purine *de novo* biosynthesis (black) and simplified salvage pathway (red). Enzymes involved: phosphoribosylpyrophosphate synthetase (PRS), phosphoribosylpyrophosphate amidotransferase (PPAT), N-formylglycinamidine ribonucleotide synthase (PFAS), inosine monophosphate cyclohydrolase (IMPch), phosphoribosylaminoimidazole carboxylase/phosphoribosylaminoimidazole succinocarboxamide synthetase (PAICS), glycinamide ribonucleotide synthetase/glycinamide ribonucleotide transformylase/aminoimidazole ribonucleotide synthetase (GART), glycinamide ribonucleotide transformylase (GARt), glycinamide ribonucleotide synthetase (GARs), aminoimidazole-4-carboxamide ribonucleotide transformylase/inosine monophosphate cyclohydrolase (ATIC), aminoimidazole-4-carboxamide ribonucleotide transformylase (AICARt), adenylosuccinate lyase (ADSL), hypoxanthine-guanine phosphoribosyltransferase (HPRT), adenine phosphoribosyltransferase (APRT).

1.3.1.3.1. Targeting Purine Metabolism

The biosynthesis of purines is fundamentally altered in rapidly proliferating cancer cells as their need for nucleotide precursors is high compared to healthy differentiated cells. Many of the genes involved in purine biosynthesis are upregulated in tumors, making enzymes such as phosphoribosylaminoimidazole carboxylase/phosphoribosylaminoimidazole succinocarboxamide synthetase (PAICS), or glycinamide ribonucleotide

synthetase/glycinamide ribonucleotide transformylase/aminoimidazole ribonucleotide synthetase (GART), promising targets for cancer treatment [107-110].

Purine synthesis disrupting agents can act by mimicking purine nucleotides, which are so called purine analogues or directly inhibit key enzymes of the purine synthesis pathway, to interfere with DNA or RNA synthesis. 6-mercaptopurine or thioguanine are purine analogues that are already being used is the clinic to treat blood cancer patients [111, 112]. In contrast, the clinical success of specific purine *de novo* synthesis inhibitors remained moderate, with only a few entering clinical trials such as Lometrexol (LTX) a GART inhibitor. [113, 114].

So far, purine biosynthesis inhibitors have been scientifically promising, showing growth reduction of tumor growth in *in vitro* models [110, 115-117]. However, their clinical application remains challenging mainly due to toxicity to healthy cells or activation of resistance mechanisms. Moreover, a significant difference between targeting purine biosynthesis, compared to other therapeutic agents leading to genome instability, is that purine inhibitors lead to proliferation arrest but do not necessarily induce cancer cell toxicity (**Manuscript II and III**). An additional challenge while using purine inhibitors is that even though purine depletion efficiently reduces tumor growth, they can paradoxically prompt cancer cell migration and metastasis [101, 118]. Therefore, it is worth elucidating the metabolic adaptations occurring in cancer cells treated with purine inhibitors, which allow them to persist and even enhance their migratory potential. The goal is to detect metabolic vulnerabilities that could serve as potential secondary targets, leading to a more efficient elimination of the tumor cells. Hence, combinatory treatments could be an opportunity to increase the therapeutic index of purine inhibitors. Additionally, co-targeting of purines and their metabolic adaptations/vulnerabilities could possibly allow a lower dosage of the drug with less adverse effects. In **manuscript III** we aimed to investigate the changes in the metabolism in purine inhibited cancer cells and elucidate potential metabolic vulnerabilities.

1.3.1.4. NADPH

NADPH metabolism represents another paradigm of metabolic flexibility and plasticity of cancer cells. As a central cofactor required for maintaining redox balance, supporting reductive biosynthesis, and enabling nucleotide and lipid synthesis, NADPH is essential for tumor cell proliferation and survival. To meet these demands, cancer cells engage a variety of biochemical pathways that produce NADPH, adapting to changes in nutrient availability, oxygen concentrations, and oncogenic signals [119]. NADPH-producing pathways include the oxidative branch of the pentose phosphate pathway (PPP), cytosolic and mitochondrial isocitrate dehydrogenases (IDH1/2), malic enzymes (ME1/2/3), folate-dependent OCM via MTHFD1/2 and ALDH1L1/2, nicotinamide adenine dinucleotide kinase (NADK), converting

Typ12text

NAD+ to NADP+ and mitochondrial NADPH regeneration through nicotinamide nucleotide transhydrogenase (NNT) [92, 120-123].

Cancer cells dynamically regulate the activity and expression of these NADPH-generating enzymes in response to metabolic changes. For example, under glucose limitation, cells reduce their reliance on the PPP and instead increase NADPH production through glutamine metabolism via IDH1 or ME1 [124]. Moreover, oxidative PPP depletion increases the flux through of serine through the OCM as alternative NADPH-generating pathway [125]. In **manuscript III** we demonstrate that the dynamic switch between NADPH producing pathways can also be relevant in the context of chemotherapy, we show that upon purine depletion, the PPP becomes dysfunctional, hence activating ME as compensatory pathway.

1.3.1.4.1. Compartmentalization of NADPH

NADPH production in mammalian cells is highly compartmentalized, unlike NADH, which is primarily involved in mitochondrial oxidative phosphorylation, NADPH is not freely diffusible between organelles. As a result, cells maintain separate pools of NADPH in the cytosol, mitochondria, and other compartments, each serving unique biosynthetic and redox functions [126].

In the cytosol, the major NADPH source represents the oxidative branch of the PPP via glucose-6-phosphate dehydrogenase (G6PD) and 6-phosphogluconate dehydrogenase (6PGD). Other contributors of cytosolic NADPH are IDH1 and ME1, supporting biosynthesis of lipids and other biomolecules, and ROS detoxification. In parallel, mitochondrial NADPH is generated through enzymes, including mitochondrial IDH2, ME2/3, MTHFD2, ALDH1L2 and NNT, which uses the proton gradient to convert NADH and $NADP^+$ into NAD^+ and NADPH. This mitochondrial NADPH pool is critical for maintaining redox balance within the organelle, supporting mitochondrial biosynthetic processes including the OCM.

Compartmentalization enables cells to regulate NADPH supply in response to local metabolic needs and metabolic changes within cellular compartments. However, this spatial separation also poses a challenge to cancer cells to metabolically adapt, as the inability to directly shuttle NADPH across membranes limits compensatory fluxes between compartments. However, cells have evolved mechanisms to indirectly coordinate NADPH pools between organelles, for example by exchanging metabolites that fuel NADPH production like malate, citrate, and serine [127, 128]. In cancer, where both cytosolic and mitochondrial NADPH demands are elevated, tumors often upregulate multiple NADPH-generating pathways in parallel and redistribute metabolic fluxes to maintain compartment-specific redox homeostasis. This highlights the significance of considering subcellular localization when targeting NADPH metabolism therapeutically [129].

Overall, the versatility of NADPH-generating pathways exemplifies how cancer cells leverage metabolic plasticity to adapt to changing environmental and intracellular demands, and highlights NADPH homeostasis as a critical node of vulnerability in cancer metabolism.

Table 3: Enzymes involved in metabolic pathways, contributing to NADPH synthesis.

Source	Location	Major Functions
PPP; Glucose-6-phosphate dehydrogenase (G6PD), 6-phosphogluconate dehydrogenase (6PGD)	Cytosol	Primary NADPH source; Oxidative branch of PPP converts glucose-6-phosphate into ribulose-5-phosphate, generating 2 NADPH per glucose molecule
Malic Enzyme (ME1/2/3)	Cytosol/ Mitochondria	Provides NADPH through conversion of malate into pyruvate and CO_2. Supports TCA cycle function upon glucose limitation
Isocitrate Dehydrogenase (IDH1/2)	Cytosol/ Mitochondria	Links TCA cycle to NADPH generation; for redox balance but also important in fatty acid biosynthesis
Methylenetetrahydrofolate Dehydrogenase (MTHFD1/2/2L)	Cytosol/ Mitochondria/ Nucleus	Part of the OCM, supply NADPH and support nucleotide biosynthesis.
Aldehyde dehydrogenase 1 family member L1/L2 (ALDH1L1/2)	Cytosol/ Mitochondria	OCM enzyme generating NADPH and produce CO_2 and THF
Nicotinamide nucleotide transhydrogenase (NNT)	Mitochondria	Located in the inner mitochondrial membrane, converts NADH and $NADP^+$ into NAD^+ and NADPH
Nicotinamide adenine dinucleotide kinase (NADK/MNADK)	Cytosol/ Mitochondria	Converting NAD+ into NADP+ which can be further oxidized into NADPH

Type text here

2. Synopsis Results and Discussion

2.1. Manuscript II : "Formate overflow drives toxic folate trapping in MTHFD1-inhibited cancer cells"

In **manuscript II**, we identified a novel folate trapping mechanism, inducing a toxic buildup of 10-CHO-THF and a depletion of free THF. This leads to an inactivation of the enzymatic activity of SHMT1, utilizing THF as cofactor to bind one-carbon units. Consequently, dTMP synthesis by SHMT1 is blocked leading to DNA damage and cancer cell death.

2.1.1. Results of Manuscript II

2.1.1.1. TH9619 targets the DC function of MTHFD1 and not mitochondrial MTHFD2

Despite earlier assumptions, we demonstrated that TH9619 does not inhibit mitochondrial MTHFD2, as formate release was still maintained. Whereas in MTHFD2$^{-/-}$ cells, formate production was abolished entirely, cells treated with TH9619 were still able to produce formate at even higher rates compared to their control (Manuscript II, Fig. 1f). Therefore, we assumed that the inhibitor likely cannot cross the mitochondrial membrane, possibly due to low lipophilicity. Instead, TH9619 inhibits the dehydrogenase, cyclohydrolase (DC) domain of MTHFD1 in the cytosol, which leads to increased formate release from mitochondria, since downstream utilization is blocked. Interestingly, TH9619 stabilized nuclear MTHFD2 (Manuscript II, Fig. 1i), hinting to a potential regulatory role of TH9619 on MTHFD2's non catalytic activity at replication forks, however this is not explored in this study.

2.1.1.2. TH9619 blocks dTMP synthesis in WT cells

Given these observations, we wanted to further elucidate the mechanism of action of TH9619 and explored how the drug affects dTMP and purine synthesis. Hence, we conducted metabolic rescue experiments using thymidine, hypoxanthine and folic acid and compared the effects of TH9619 to other compounds: TH9975 (MTHFD1/2 inhibitor), DS18561882 (another MTHFD1/2 inhibitor), SHIN1 (SHMT1/2 inhibitor), MTX, and 5-FU. In colorectal cancer cell lines SW620 and HCT116, thymidine partially rescued cells from TH9619 toxicity, and full resistance occurred with thymidine plus hypoxanthine or folic acid. Interestingly, hypoxanthine alone increased sensitivity to TH9619. These patterns were not seen with the other compounds, the effects of DS18561882 and SHIN1 were only partially reversed by hypoxanthine, while MTX resistance required both thymidine and hypoxanthine. 5-FU's effects were unchanged by any additive (Manuscript II, Fig. 2a-f, Suppl. Data Fig. 2a-c). We also conducted a stable isotope tracing using [U-^{13}C]serine for purines and [2,3,3-^{2}H]serine for dTMP in WT and MTHFD2$^{-/-}$ SW620 cells. TH9619 slightly reduced ATP and ADP labeling in WT cells (Manuscript II, Fig 2i, j, Suppl. Data Fig. 2 d, e). In MTHFD2$^{-/-}$ however, treatment with

TH9619 completely blocked ATP and ADP synthesis (Manuscript II, Fig 2i, j, Suppl. Data Fig. 2 d, e) via the OCM confirming that blocking the DC function of MTHFD1 in cells lacking MTHFD2 disables both cytosolic and mitochondrial routes for serine-derived purine synthesis. We also traced dTMP synthesis using [2,3,3-^{2}H]serine, dTMP generated via the mitochondrial OCM becomes D+1 labelled and D+2 labeling occurs via the cytosolic route (Manuscript II, Fig. 2h). WT cells showed a high D+1/D+2 ratio, hence a strong mitochondrial flux, in contrast, MTHFD2$^{-/-}$ cells lacked the D+1 signal, regardless of treatment (Manuscript II, Fig. 2k). Treating WT cells with TH9619 removed the D+1 signal, showing that dTMP synthesis had shifted to a reverse flux through SHMT1 (Manuscript II, Fig. 2l). These findings suggest that TH9619 has a unique dual mechanism of action: it primarily causes thymidylate depletion and secondarily affects purine synthesis. Overall, these tracing studies revealed an unexpected mechanism by which TH9619 disrupts the OCM and causes cancer cell toxicity. Its main effect is to deplete dTMP by inhibiting the MTHFD1(DC) domain, which blocks the conversion of 10-CHO-THF to 5,10-CH2-THF. A secondary effect is purine deficiency. However, it was puzzling that thymidine alone could rescue resistance to TH9619, since SHMT1 in the cytosol should still support dTMP production. We therefore continued to investigate how exactly TH9619 causes dTMP depletion.

2.1.1.3. Hypoxanthine Enhances TH9619 Activity via Folate Trapping

Previous observations showed that adding hypoxanthine sensitized cancer cells to TH9619, while it lowered efficacy of other drugs. Which is surprising, given it's a purine analog. Up to that point, all experiments were done in RPMI-1640 medium with standard, heat-inactivated fetal bovine serum (FBS). RPMI without FBS, lacks purines and thymidine, however, addition of regular FBS containing around 95 µM hypoxanthine, translates into about 9.5 µM in RPMI containing 10% FBS. Full sensitization to TH9619 occurred between 1-5 µM hypoxanthine (Manuscript II, Fig. 3e, Suppl. Data Fig. 3a). To study the role of hypoxanthine more precisely, we switched to RPMI with dialyzed FBS (dFBS) which does not contain any purines and always supplemented with 50 µM hypoxanthine.

Interestingly, MTHFD2$^{-/-}$ cells are less sensitive to TH9619 in regular FBS. However, in dFBS, lacking the purine derivative hypoxanthine, TH9619 was dramatically more toxic to MTHFD2$^{-/-}$ cells (Manuscript II, Fig. 3g). Moreover, in WT cells, TH9619 did not affect serine-derived purine biosynthesis, however this pathway was strongly inhibited in MTHFD2$^{-/-}$ cells (Manuscript II, Fig. 4a,b; Suppl. Data Fig. 4a-d). Importantly, hypoxanthine completely suppressed purine synthesis from serine in both scenarios, meaning that cells switch towards the purine salvage pathway. Moreover, TH9619 or MTHFD2 loss impaired mitochondrial dTMP synthesis (D+1) and redirected one-carbon flux toward cytosolic synthesis (D+2) (Manuscript II, Fig. 4c).

In sum, TH9619 depleted dTMP in WT cells, an effect potentiated by hypoxanthine. In contrast, MTHFD2$^{-/-}$ cells experience purine synthesis blockade upon TH9619 treatment and showed drug resistance upon hypoxanthine supplementation.

The previous serine tracing confirmed that hypoxanthine inhibits *de novo* purine synthesis (Manuscript II, Fig. 4a), which reduces 10-CHO-THF consumption. In WT cells, mitochondrial formate production, drove the conversion of THF to 10-CHO-THF, causing its accumulation and the so called folate trapping. Indeed, we detected increased 10-CHO-THF levels after TH9619 treatment. This build-up was enhanced upon hypoxanthine supplementation (Manuscript II, Fig. 5d,e), suggesting that THF is sequestered as 10-CHO-THF, blocking SHMT1-driven dTMP synthesis. Notably, no 10-CHO-THF build-up occurred in MTHFD2$^{-/-}$ cells under conditions lacking formate overflow (Manuscript II, Fig. 5d,e). Therefore, WT cells die from dTMP depletion while MTHFD2$^{-/-}$ cells suffer from purine depletion upon TH9619 treatment.

The different scenarios are represented in figure 5.

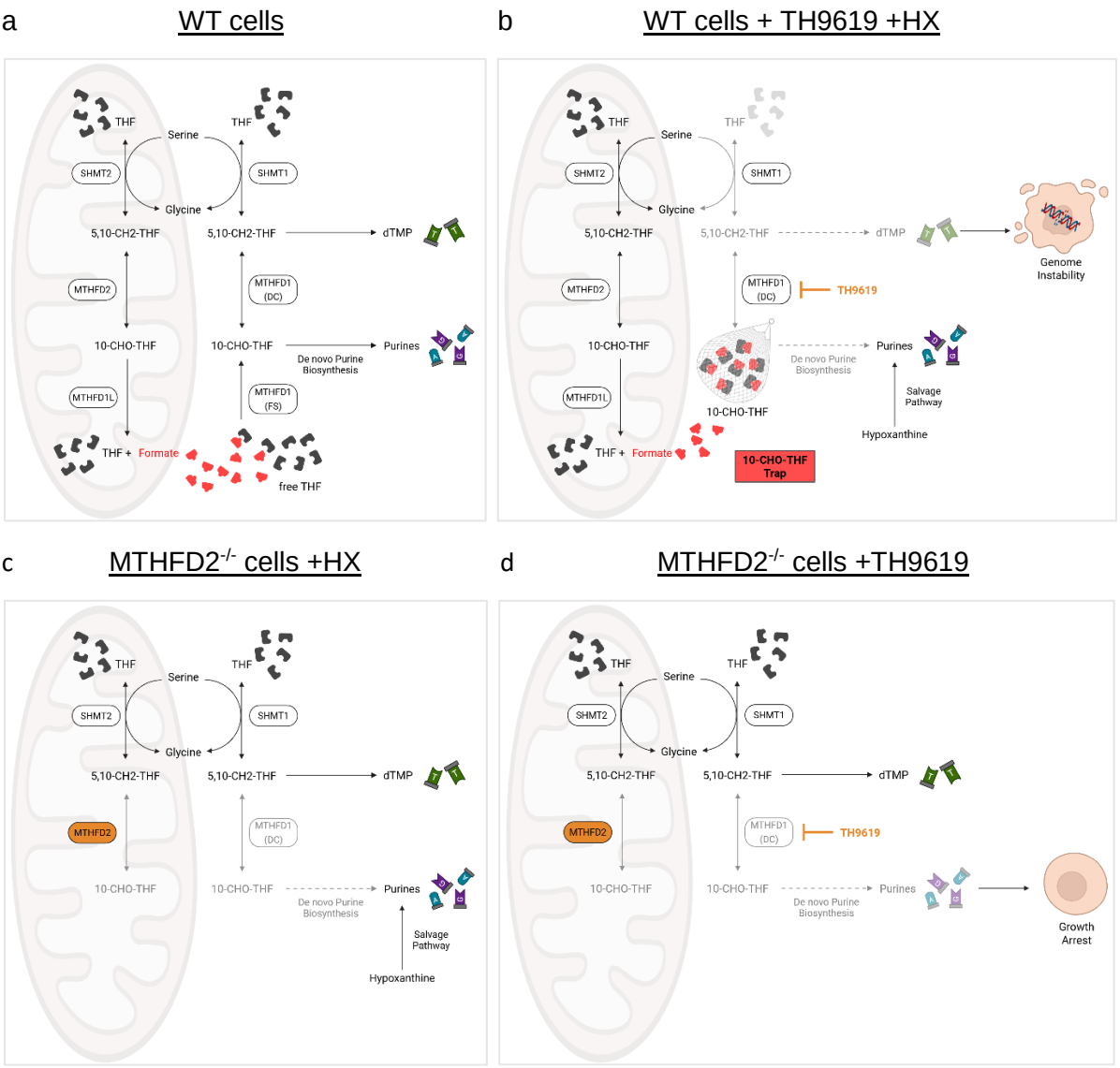

Figure 5: **Representation of the different scenarios** (a) OCM flux between mitochondria and cytosol, showing interconversion between the different folate species. (b) Folate trapping scenario in WT cells treated with TH9619 and hypoxanthine. Hypoxanthine (HX) feeds the purine salvage pathway, causing a negative feedback inhibition on the *de novo* synthesis of purines. In parallel, TH9619 inhibits the DC domain of MTHFD1 leading to a decreased consumption of 10-CHO-THF, hence free THF gets trapped and is no longer available for SHMT1 to support dTMP synthesis. (c) MTHFD2 deficient cells lack formate overflow. When treated with TH9619 and hypoxanthine they proliferate normaly as purines are synthesized via the salvage pathway and dTMP via SHMT1. (d) MTHFD2$^{-/-}$ cells treated with TH9619 develop purine defciency and only undergo proliferation arrest.

To validate physiological relevance, we tested drug responses in human-like plasma medium (HPLM) and the physiologically relevant Plasmax medium, which mimic human plasma and contain 5 respectively 10 µM hypoxanthine. SW620 WT cells cultured in HPLM remained

sensitive to TH9619 (Extended Data Fig. 5a), while MTX and DS18561882 lost potency (Manuscript II, Suppl. Data Fig. 5c,d). TH9619 also impaired tumor spheroid growth of SW620 and HCT116 in Plasmax (Manuscript II, Fig. 5a,b), suggesting clinical relevance.

2.1.1.4. Formate overflow drives TH9619-induced trapping of 10-CHO-THF

To determine whether formate release is necessary for triggering folate trapping and subsequent dTMP depletion, we investigated if one could sensitize MTHFD2 deficient cells, which lack mitochondrial formate production to TH9619, by supplementing them with exogenous formate and/or hypoxanthine. If our trapping hypothesis holds true, then co-treatment of MTHFD2$^{-/-}$ cells with TH9619, hypoxanthine, and formate should induce a similar toxic trapping of THF as 10-CHO-THF as in WT cells. Exogenous formate mimics mitochondrial overflow and combines with free THF to form 10-CHO-THF. Since hypoxanthine supplementation reduces *de novo* purine synthesis, 10-CHO-THF is no longer consumed in that pathway and instead accumulates (Manuscript II, Fig. 6b). This leads to a reduction in free THF, depriving SHMT1 of its substrate for producing 5,10-CH_2-THF, and ultimately impairing dTMP synthesis in MTHFD2$^{-/-}$ cells treated with TH9619.

Indeed, the combination of hypoxanthine and formate enhanced TH9619 toxicity in MTHFD2$^{-/-}$ cells (Manuscript II, Fig. 6c). Since purine levels were already replenished by hypoxanthine, the observed toxicity was attributable to dTMP deficiency and could be rescued by thymidine supplementation (Manuscript II, Fig. 6b). These findings point to a specific role for MTHFD1's DC domain inhibition and 10-CHO-THF accumulation in TH9619-mediated disruption of dTMP synthesis.

2.1.1.5. Treatment with TH9619 has differential biological outcomes depending on MTHFD2 status

Since TH9619 affects the OCM differently depending on MTHFD2 expression status, we investigated how these metabolic changes induced by TH9619 translate into cellular responses and whether hypoxanthine plays a role in modulating drug sensitivity.

TH9619 significantly reduced the proliferation of SW620 WT and MTHFD2$^{-/-}$ cells. In WT cells the anti-proliferative effect that was further enhanced by hypoxanthine but mitigated by thymidine (Manuscript II, Fig. 7b). In contrast, MTHFD2$^{-/-}$ cells were unresponsive to thymidine, though hypoxanthine partially restored their growth (Manuscript II, Fig. 7c). In WT cells, proliferation arrest was followed by apoptosis, which was intensified by hypoxanthine and rescued by thymidine (Manuscript II, Fig. 7f,g). In contrast, MTHFD2$^{-/-}$ cells exhibited minimal apoptosis under the same conditions (Manuscript II, Fig. 7f,g), indicating distinct modes of action depending on MTHFD2 status. In MTHFD2-deficient cells, TH9619 imposes a cytostatic effect by restricting purine synthesis, while in MTHFD2-expressing cells, it induces cytotoxicity

through dTMP depletion, likely due to DNA damage from uracil misincorporation. Importantly, co-supplementation with hypoxanthine and formate in MTHFD2$^{-/-}$ cells converted this cytostatic response into robust cell death (Manuscript II, Fig. 7h), consistent with the proposed folate-trapping model.

Altogether, these data demonstrate that TH9619 targets thymidylate biosynthesis in MTHFD2-expressing cells by inhibiting MTHFD1(DC), resulting in 10-CHO-THF trapping and depletion of THF. This mechanism was enhanced under physiological levels of hypoxanthine, which activate the purine salvage pathway and suppress *de novo* purine synthesis. In MTHFD2-deficient cells, the drug's effect is initially cytostatic due to purine depletion but becomes cytotoxic upon hypoxanthine and formate supplementation, which promote THF trapping. Given that formate levels may be elevated in some tumors *in vivo*, this metabolic context could enhance the therapeutic efficacy of TH9619.

2.1.2. Discussion of Manuscript II

In this study, we provided a deep mechanistic understanding of TH9619's mode of action in cancer cells overexpressing MTHFD2 and those with deficiencies in mitochondrial OCM. On the one hand, we found that TH9619 leads to dTMP deficiency and induces toxicity in MTHFD2 high tumors. Formate released from the mitochondria, is converted into 10-CHO-THF, this folate trap is enhanced by hypoxanthine as it further promotes 10-CHO-THF accumulation, leading to a depletion of free THF. Furthermore, we showed that thymidine is able to rescue the toxic effect of TH9619, suggesting dTMP synthesis is indeed blocked due to low free THF availability and impaired SHMT1 activity. On the other hand, we showed that in MTHFD2 deficient tumors TH9619 leads to an impairment of purine biosynthesis, which other than dTMP depletion does not induce cancer cell toxicity but rather puts them under growth arrest. The metabolic characterization of purine inhibited cancer cells will be explored further in **manuscript III**.

Importantly, formate overflow is considered a hallmark of cancer cell metabolism [78] and MTHFD2 is markedly overexpressed in many cancers [17]. Here, we showed that MTHFD2 enabling formate secretion, makes cancer cells particularly susceptible to MTHFD1(DC) inhibition by TH9619 and hypoxanthine.

Moreover, human plasma composition favors the effectiveness of TH9619 with hypoxanthine concentrations around 3-10 µM and very low thymidine levels. This is not the case for mouse plasma, containing high thymidine concentrations which could reduce sensitivity to TH9619. Therefore, *in vivo* studies with TH9619 in mice remain challenging.

Table 4: Concentrations of Folate, HX and Thymidine in different media and plasma: Folate, hypoxanthine and thymidine quantification in different cell culture media (DMEM F12 + 10% FBS, RPMI + 10 %FBS, RPMI, + 10% dFBS, DMEM + 10% FBS) as well as in mouse and human plasma.

	Folate	Hypoxanthine	Thymidine
DMEM F12 + 10% FBS	2,6 µM	16 µM	1 µM
RPMI +10% FBS	0,8 µM	9,5 µM	0,2 µM
RPMI + 10% dialFBS	0,8 µM	0,006 µM	0,2 µM
DMEM +10% FBS	3,5 µM	10 µM	0,2 µM
Mouse Plasma	NA	0,3 µM	7,7 µM
Human Plasma	NA	3-10 µM	< 1 µM

To conclude, we metabolically characterized TH9619 and confirmed its potential as a drug with high specificity that can kill MTHFD2 expressing cancer. This enlarges the therapeutic window of TH9616 tremendously. TH9619 is currently in phase 1/2 clinical trials in advanced solid tumours (NCT07151040).

2.2. Manuscript III : "Purine Inhibition affects Redox State and activates Compensatory Mechanisms in Persistent Cancer Cells"

2.2.1. Results of Manuscript III

2.2.1.1.Cell toxicity through dTMP depletion but not purine biosynthesis inhibition

In manuscript II we demonstrated that MTHFD2 deficient cancer cells treated with TH9619 leads to purine inhibition which reduced cell growth but had no toxic effect. Here, we wanted to look at metabolic adaptations in purine depleted cells allowing them to sustain. Moreover, we aimed to uncover metabolic vulnerabilities which would become potential secondary targets for a specific targeting and a more efficient killing of tumor cells.

To metabolically analyse purine depleted cancer cells we employed two cellular models: First, we used MTHFD2$^{-/-}$ cells treated with TH9619, and second, cancer cells treated with selective inhibitors targeting key enzymes in the purine de novo synthesis pathway; PAICS (inhibited by PAICSi) and GART (inhibited by GARTi) (Manuscript III, Fig. 1a). Both strategies, genetic knockout and pharmacological inhibition, led to a decrease in intracellular purine nucleotides (ATP and GTP) (Manuscript III, Fig. 1b). Supplying hypoxanthine completely restored nucleotide pools, demonstrating functional salvage compensation.

As shown previously, TH9619 induces cell death in WT cells through dTMP depletion. These findings were recapitulated using purine- and pyrimidine-targeting inhibitors. PEM and 5FU robustly reduced dTMP levels (Manuscript III, Fig. 1e), triggering both early and late-stage apoptosis (Manuscript III, Fig. 1f,g). However, PAICSi and GARTi, despite significantly reducing purine nucleotide levels, only induced cell cycle arrest without affecting cell survival (Manuscript III, Fig. 1f-h). Protein level analyses of DNA damage markers confirmed that only dTMP depletion—not purine depletion—elicits a DNA damage response (Manuscript III, Suppl. Fig. 1b).

At the signalling level, purine depletion was associated with inactivation of mTOR pathway (Manuscript III, Suppl. Fig. 1c), which likely promotes metabolic reprogramming and reduced growth. This is consistent with literature showing that mTORC1 activity depends on purine availability [130, 131]. Simultaneously, we observed AMPK activation, a cellular energy sensor that antagonizes mTOR and supports adaptation to metabolic stress by lowering energy expenditure (Manuscript III, Suppl. Fig. 1d).

Altogether, our data highlight a fundamental difference between purine and pyrimidine synthesis blockade. While pyrimidine (dTMP) depletion is lethal to cancer cells, purine inhibition only suppresses their proliferation (Manuscript III, Fig. 1g). This observation led us to further explore how cancer cells withstand purine limitation and adapt their metabolism accordingly.

2.2.1.2. Purine depletion disrupts the pentose phosphate pathway

Given that inhibition of purine biosynthesis led to cell cycle arrest without inducing cell death, we sought to identify intrinsic metabolic vulnerabilities that might emerge under these conditions. To this end, we performed metabolomic analyses to uncover changes in metabolic flux during purine depletion. Notably, we observed a marked reduction in key intermediates of the pentose phosphate pathway (PPP) (Manuscript III, Fig. 2a). Concurrently, phosphoribosyl pyrophosphate (PRPP) levels increased in MTHFD2$^{-/-}$ cells treated with TH9619 and WT cells treated with PAICSi or GARTi (Manuscript III, Fig. 2b,d). This accumulation is likely due to the reduced consumption of PRPP, which normally fuels purine biosynthesis.

PRPP has previously been shown to exert negative feedback on the non-oxidative arm of the PPP [132]. Our findings now extend this concept to intact cells. To further validate this regulatory mechanism, we supplemented WT SW620 cells with exogenous PRPP. Unexpectedly, S7P levels increased, while high intracellular PRPP showed the opposite. However, a closer examination of the oxidative branch of the PPP revealed that PRPP treatment decreased levels of glucose-6-phosphate (G6P) and fructose-6-phosphate (F6P) (Manuscript III, Suppl. Fig. 2a), indicating that PRPP accumulation might also perturb the

oxidative pathway. It is worth noting that, due to the absence of known PRPP transporters, intracellular uptake from the medium is likely limited. Thus, extracellular PRPP may not reach concentrations sufficient to fully suppress non-oxidative PPP activity. Or there might be other regulatory unknown mechanisms involved besides the feedback of PRPP. To directly assess the impact of purine synthesis inhibition on oxidative PPP function, we performed a [U-^{13}C]-glucose tracing time-course experiment in SW620 cells pre-treated with PAICSi (Manuscript III, Fig. 2f). As anticipated, total levels and ^{13}C labelling of G6P, F6P, and S7P were substantially reduced upon purine inhibition (Manuscript III, Fig. 2g).

The PPP operates alongside glycolysis, supplying ribose sugars and maintaining redox homeostasis through NADPH production. Despite its suppression under purine-depleted conditions, cancer cells continue to survive. This prompted us to explore how cells compensate metabolically and what alternative survival pathways may be activated under this stress.

2.2.1.3. Purine-inhibited cancer cells shift towards glutamine-driven TCA cycle metabolism

Following purine inhibition, cancer cells exhibit resilience despite a disturbance in glucose metabolism. Notably, both MTHFD2 knockout cells treated with TH9619 and cells exposed to PAICS and GART inhibitors displayed a metabolic shift, favouring glutamine over glucose as the primary carbon source (Manuscript III, Fig. 3a, b). Furthermore, [U-^{13}C]-glucose and [U-^{13}C]-glutamine stable isotope tracing showed an increase in glutamine-derived ^{13}C enrichment as opposed to a decrease in ^{13}C from the glucose tracer across all TCA intermediates in both purine inhibited models (Manuscript III, Fig. 3d,f, Suppl. Fig. 3a, b). Importantly, this metabolic reprogramming was specific to purine-depleted cells and was not observed following pyrimidine synthesis inhibition (Manuscript III, Suppl. Fig. 3b).

We showed that under purine depletion, cancer cells adapt to PPP dysfunction by shifting their carbon source from glucose to glutamine. This metabolic rewiring increases glutamine dependency and creates a potential vulnerability. To functionally validate this glutamine addiction, we deprived purine-inhibited cancer cells of glutamine and observed increased apoptosis when combined with PAICSi (Manuscript III, Fig. 3g, h), confirming glutamine availability as a key weakness.

Next, we tested whether co-targeting glutamine metabolism and purine biosynthesis would enhance cancer cell killing by combining PAICSi with the glutaminase 1 inhibitor (GLS1i), also known as telaglenastat (CB-839), blocking the conversion of glutamine to glutamate. Although apoptosis increased slightly compared to PAICSi alone, the effect was not significant (Manuscript III, Suppl. Fig. 3c). Stable-isotope tracing revealed that GLS1 inhibition did not fully block glutamine-to-glutamate conversion, as labelled TCA intermediates were still present

(Manuscript III, Suppl. Fig. 3d). This is likely due to residual GLS2 activity and the spontaneous degradation of glutamine to glutamate at 37 °C, both of which maintain TCA cycle function despite GLS1 inhibition.

In summary, purine-inhibited tumor cells respond to PPP blockade by reducing glucose use and increasing glutamine uptake to sustain the TCA cycle. This enhanced glutamine dependency supports metabolic flexibility but simultaneously exposes a therapeutic vulnerability.

2.2.1.4. Malic enzyme activity compensates for Redox stress following purine pathway blockade

Given the central role of the pentose phosphate pathway (PPP) in maintaining redox balance through NADPH production, we aimed to understand how cancer cells respond to PPP dysfunction triggered by purine synthesis inhibition. In SW620 cells exposed to PAICSi, cytosolic ROS levels rose significantly (Manuscript III, Fig. 4a). Simultaneously, we detected a notable drop in the NADH/NAD^+ ratio and a downward trend in NADPH/$NADP^+$, indicating a disrupted redox state (Manuscript III, Fig. 4b).

While tracing glutamine metabolism with [U-^{13}C]-glutamine, we found an accumulation of M+6 citrate and M+3 pyruvate indicating complete ^{13}C labelling (Manuscript III, Fig. 4c, d). This labelling pattern implies the activity of malic enzyme (ME), which decarboxylates malate to form pyruvate while generating NADPH (Manuscript III, Fig. 4e). Notably, the absence of labeled PEP (Manuscript III, Suppl. Fig. 4a) ruled out phosphoenolpyruvate carboxykinase (PEPCK) as potential pyruvate M+3 contributor. This shift in metabolism was not limited to a single cell line; increased ME activity was seen across multiple cancer models, including colorectal, lung, pancreatic, breast, and brain cancer cell lines, following PAICSi treatment, though not all changes reached statistical significance (Manuscript III, Fig. 4f, g).

As the PPP is disrupted, cells may increasingly depend on ME1 for cytosolic NADPH generation. To test this, we knocked out cytosolic ME1 and mitochondrial ME2 in SW620 cells using CRISPR, establishing two clonal lines per isoform (Manuscript III, Fig. 4h). Under purine-deprived conditions, ROS levels slightly increased only in ME1-deficient cells, not in ME2 knockouts (Manuscript III, Fig. 4i). This suggests that ME1 specifically mitigates oxidative stress in the cytosol, possibly together with other NADPH generating enzymes, in the absence of a functional PPP. However, the increase in ROS was not accompanied by a substantial rise in cell death, possibly due to compensatory redox systems, which may buffer redox pressure when ME1 is absent (Manuscript III, Fig. 4i).

Interestingly, previous work has shown that ATP binding can suppress ME function [133, 134], suggesting that ATP depletion under purine stress may lift this inhibition and promote ME activation. In this context, it would be interesting to investigate this regulatory mechanism further by introducing a point mutation in the ATP-binding site of ME.

Collectively, our results indicate that purine depletion indirectly activates ME1, likely via ATP reduction. In turn, ME1 helps sustain redox homeostasis in the absence of a functional PPP. This metabolic adaptation highlights a potential therapeutic vulnerability tied to NADPH production outside the PPP.

2.2.1.5. Purines oppositely regulate ME and PEPCK activity under glucose limitation

Cancer cells increase glutamine metabolism when glucose or pyruvate is scarce [36, 37, 135], requiring carbon flow from glutamine towards pyruvate and 3PG to sustain acetyl-CoA production and serine synthesis respectively [37]. This metabolic rewiring is controlled by both enzymes ME and PEPCK (Manuscript III, Fig. 5a). We found that after purine depletion, glutamine-addicted cancer cells relied entirely on ME but not PEPCK for generating pyruvate. To study this further, cells were treated with the PAICSi and cultured in galactose to mimick glucose limitation without complete deprivation [136]. [U-^{13}C]-glutamine tracing showed that PEPCK activity (PEP M+3) increased in galactose but was nearly abolished by PAICSi, while pyruvate M+3 remained largely intact (Manuscript III, Fig. 5d, e). This suggests that purines and their role as cofactors are essential for PEPCK activity under glucose restriction, shifting pyruvate production entirely to ME.

In sum, purine depletion, specifically GTP, suppresses PEPCK due to limited cofactor availability and shifts carbon flux through ME which oppositely becomes more active in the absence of ATP [133, 134], illustrating how metabolic flexibility allows cancer cells to adapt in a context of nutrient stress (Manuscript III, Fig. 5g).

2.2.2. Discussion of Manuscript III

Our study highlights how cancer cells dynamically rewire their metabolism in response to purine biosynthesis inhibitors. Besides depletion of the nucleotide pool, purine blockade disrupts redox balance by shutting down the PPP, a major source of NADPH. In turn, cells activate ME1 and increase glutamine uptake to support both redox homeostasis and TCA cycle function. Although other NADPH-generating enzymes like IDH1 or ALDH1L1 may also contribute, our tracing data pointed to ME as a key compensatory route. ME activity may be further enhanced by energy stress, given its regulation by ATP and AMPK signalling. In addition, we show that purines regulate the balance between ME and PEPCK activity, which

becomes relevant specifically under glucose-limited conditions. This elucidates the role of purines as metabolic regulators—not just as DNA precursors or energy carriers.

Functionally, we observed increased toxicity of purine inhibitors in combination with glutamine starvation, clearly depicting glutamine metabolism as a metabolic vulnerability of purine inhibited cancer cells and a potential secondary target. Furthermore, ME loss in addition to purine inhibition, showed only minor effects on cancer cell toxicity, therefore displaying ME as a secondary therapeutic target might seem slightly overestimated. Nevertheless, it would be worth investigating whether ME represents a therapeutic vulnerability, in cancers treated with purine inhibitors, having low ME expression. Moreover, stable ME knockouts may have adapted over time, masking acute dependencies. Hence, further studies are needed to explore this potential.

Finally, it would be worth investigating whether glutamine availability and/or ME activity confers selective advantages beyond persistence of purine inhibited cancer cells. In **manuscript IV** we show that tumor cell migration is increased upon nucleotide inhibition, hence it would be worth investigating the role of ME in supporting a pro-migratory phenotype.

2.3. Manuscript IV : "Mitochondria preserve an autarkic one-carbon cycle to confer growth-independent cancer cell migration and metastasis"

In **Manuscript IV** we identified a proliferation independent role of the mitochondrial OCM and showed that while blocking biosynthesis via the cytosolic OCM can induce the migratory potential of cancer cells. This study was published back to back with a story from another lab, referred to previously, elucidating that blocking specifically purine biosynthesis, can induce migration and metastasis [118].

2.3.1. Results of Manuscript IV

2.3.1.1. Blocking anabolic pathways has distinct effects on the migratory capacity and the EMT phenotype of cancer cells

We investigated how blocking major anabolic pathways influences the migration of cancer cells. To do so, breast cancer cells were treated with inhibitors of glycolysis, the mitochondrial electron transport chain (ETC), and lipid, protein, or nucleotide synthesis. As anticipated, all treatments reduced proliferation and affected cell cycle progression with minimal toxicity after 48 hours (Manuscript IV, Fig 1b,c). While inhibition of glycolysis, ETC, lipid, and protein synthesis markedly reduced cell migration, blocking nucleotide synthesis, despite strongly impairing cell proliferation, did not decrease migration (Manuscript IV, Fig 1d,e). In fact, some nucleotide synthesis inhibitors (MTX, PEM, hydroxyurea (HU), clofarabine (CLO)) even enhanced wound closure in migration assays (Manuscript IV, Fig 1g).

To explore the metabolic pathways that sustain cancer cell motility, we performed proteomics on breast cancer cells MDA-MB-468 and detected superoxide dismutase (SOD) as the most strongly induced protein (Manuscript IV, Fig. S2F). Indeed, previous studies confirmed MTX as a potent inducer of oxidative stress [137-139]. In line with this, we detected a moderate but significant increase in both mitochondrial and cytosolic reactive oxygen species (ROS) following MTX treatment, as well as in resistant cells (Manuscript IV, Fig. S2H–J). The increase in ROS observed under MTX treatment aligns with prior studies implicating oxidative stress in driving epithelial-mesenchymal transition (EMT) [140-143]. Consistently, we observed a time-dependent increase in the expression of EMT markers following MTX treatment and antioxidant N-acetyl cysteine (NAC) reduced both migratory and EMT phenotype (Manuscript IV, Fig. 2c-f). Thus, the moderate rise in ROS following MTX exposure likely provides a pro-migratory signal that underlies the observed persistence of cell migration.

2.3.1.2. Mitochondrial OCM maintains serine catabolism upon cytosolic OCM inhibition after MTX treatment

Beyond its effects on ROS and EMT, we exploited the sustained migratory phenotype under MTX treatment to uncover growth-independent metabolic features that may support cancer cell motility. Using a [U-^{13}C]-glucose and a [U-^{13}C]-glutamine tracer, we showed that MTX treated cancer cells remain metabolically active and maintain cellular respiration at levels similar to the untreated control (Manuscript IV, Fig. 3a-g). Surprisingly, cytosolic OCM ablated MDA-MB-468 cells increase their serine *de novo* synthesis, in conditions where their need for biosynthetic precursors is low (Manuscript IV, Fig. 3h). In parallel, the glucose derived formate release increased upon MTX treatment, hinting towards a potential independent activity of the mitochondrial (Manuscript IV, Fig. 3j) OCM cycle.

In order to monitor the fate of serine and substantiate our hypothesis, we supplemented MTX treated MDA-MB-468 cells with [U-^{13}C]-serine and detected an increase in labelled fomate (Manuscript IV, Fig. 4b), demonstrating that the majority of the released formate originates from [U-^{13}C]serine, rather than from alternative carbon sources that could generate formate upon cytosolic OCM block via MTX. To determine whether knockout of mitochondrial serine catabolism prevents formate overflow, we measured formate release upon MTX treatment in HAP1 cells lacking SHMT1 (cytosolic) or SHMT2 (mitochondrial). As expected, SHMT2 loss completely abolished formate overflow, whereas SHMT1 knockout led to an increase (Manuscript IV, Fig. 4h). We next validated this finding in MDA-MB-468 cells with MTHFD1L knockout, shRNA-mediated MTHFD2 knockdown, or MTHFD2 knockout (Manuscript IV, Fig. 4i, j, S4I–M). All genetic perturbations strongly suppressed formate overflow during MTX treatment, further supporting that the increased formate overflow upon MTX depends on mitochondrial serine catabolism (Manuscript IV, Fig. 4i, j, S4J, M). In summary, these results

demonstrate that mitochondria provide a protected environment enabling autonomous folate-mediated serine catabolism, independent of cytosolic folate metabolism.

2.3.1.3. Mitochondrial OCM supports cancer cell motility in dependence of serine and mitochondrial THF

Since we observed increased glucose-derived serine synthesis and its mitochondrial OCM catabolism, we tested whether blocking serine synthesis reduces sustained cell migration under cytosolic OCM inhibition. Indeed, PHGDH inhibition significantly reduced MTX-induced cell migration, an effect further enhanced by combined serine/glycine (S/G) starvation, which fully abolished migration (Manuscript IV, Fig. 5e,f, S5F). Since MTX already caused growth arrest (Manuscript IV, Fig. S5E), these findings indicate that mitochondrial OCM supports cell motility independently of serine's anabolic role. In summary, MTX as a tool compound revealed that serine is essential to sustain cancer cell migratory capacity independent of proliferation (Fig. 5j)

Interestingly, metformin treatment reduced migration of MTX-treated MDA-MB-468 cells (Manuscript IV, Fig. 6a), indicating that ETC activity supports motility. Targeting mitochondrial serine catabolism directly by MTHFD2 or MTHFD1L silencing, strongly reduced migration in MDA-MB-468 and 4T1 cells treated with MTX (Manuscript IV, Fig. 6b-e). Surprisingly, MTHFD1L loss did not impair migration of MTX-treated MDA-MB-468 cells (Manuscript IV, Fig. 6e). Further analysis revealed markedly higher ALDH1L2 expression in MDA-MB-468 compared to 4T1 cells, despite similar MTHFD1L levels (Manuscript IV, Fig. 6f,g). This reminded us that ALDH1L2 can compensate for MTHFD1L loss by oxidizing 10-CHO-THF to CO_2, thereby regenerating THF. In MDA-MB-468 cells, ALDH1L2 can oxidize 10-CHO-THF to CO_2, regenerating mitochondrial THF, whereas 4T1 cells rely on MTHFD1L. Thus, ALDH1L2 determines whether THF is available or trapped as 10-CHO-THF, affecting the mitochondrial cycle upon MTX (Manuscript IV, Fig. 6h). Supporting this hypothesis, combined depletion of MTHFD1L and ALDH1L2 in MDA-MB-468 cells reduced migration under MTX, similar to what we observed in 4T1 cells (Manuscript IV, Fig. 6i, S6K). In conclusion, these results suggested that free THF appears critical for the autarkic mitochondrial OCM cycle, and ALDH1L2 can compensate for MTHFD1L loss by regenerating THF.

For the in vivo validation of our findings, we used the 4T1 *wt* and *Mthfd1lL* KD cells and orthotopically implanted them in mice to monitor tumour growth and metastasis formation. In line with our hypothesis, we detected a reduction in lung metastasis with *Mthfd1l* KD cells (Manuscript IV, Fig.7 d-f) without affecting tumor size at endpoint (Manuscript IV, Fig.7 b,c), which strengthened the key relevance of the mitochondrial OCM in supporting metastasis formation independently of cancer cell proliferation.

2.3.2. Discussion of Manuscript IV

Our study reveals a growth-independent role of mitochondrial serine catabolism in supporting cancer cell motility. Using MTX to decouple migration from proliferation, we show that mitochondria sustain an autonomous OCM sufficient to maintain migratory capacity when the cytosolic OCM is inhibited. This autonomy is enabled by the MTHFD1L reaction, which releases one-carbon units without oxidizing THF, preserving the mitochondrial THF pool for SHMT2-dependent serine catabolism.

Polyglutamation of folates limits their transport across the mitochondrial membrane, trapping them inside the mitochondria. This compartmentalization provides a selective advantage under cytosolic OCM inhibition, allowing motility to continue. Moreover, increased extracellular formate upon MTX treatment may enhance invasiveness. Together, these findings establish mitochondrial OCM as a key driver of cancer cell motility, independent of proliferation.

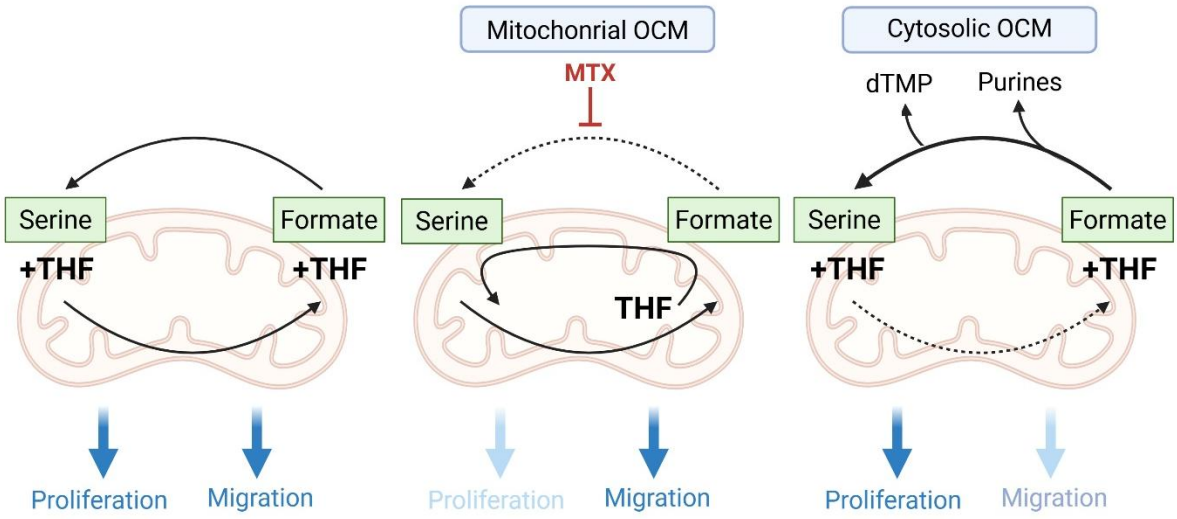

Figure 6: Illustration of the discrepancy between the mitochondrial and the cytosolic OCMs contribution to cancer cell migration and proliferation respectively.

3. Conclusion and Perspectives

Targeting nucleotide metabolism for cancer therapy comes along with successes but just as many challenges. One of the biggest challenges represents the capability of cancer cells to rapidly rewire their metabolism as a response to treatment, allowing them to sustain or even progress. We showed that reduction of tumor growth does not necessarily go along with less aggressiveness of the cancer, as targeting biosynthesis of nucleotides can result in enhanced migratory potential of tumor cells. Therefore, it is important to identify metabolic pathways that gain essentiality along this process and investigate whether these metabolic adaptions may represent vulnerabilities that could be exploited therapeutically.

One of these metabolic pathways we have been able to identify is the mitochondrial OCM, which gains an autarkic mode of function upon interference with the cytosolic part via MTX treatment. The mitochondrial OCM running independently, leads to enhanced formate overflow, which is a characteristic of many oxidative cancers and known to enhance cancer cell invasion [77, 78, 80]. However, a high mitochondrial OCM activity can paradoxically emerge as metabolic vulnerability. Formate excreted from the mitochondria reacts with free THF to form 10-CHO-THF, leading to the described trapping of free folate, which sensitizes cancer cells to TH9619 treatment. Addition of HX further potentiates the toxic effect of TH9619 as the purine analogue decreases the dependency on *de novo* purine biosynthesis, which could restore the free THF pool. Consequently, it is the inability to produce thymidine via the THF-dependent SHMT1 reaction, that leads to cancer cell death. We showed that loss of dTMP induces DNA damage, through the incorporation of uracil instead of thymidine into newly synthesized DNA, which becomes a self-destructive mistake. This displays how what seems to be a metabolic advantage at first can be exploited as metabolic vulnerability in a context dependent manner.

Interestingly, we observed a fundamental difference between targeting dTMP compared to purine nucleotides. While cancer cells lacking dTMP are unable to survive, this is different for cells depleted in purines for DNA synthesis. We observed that even though inhibition of purine biosynthesis efficiently reduces cell growth, cancer cells remain metabolically active, allowing them to sustain and even progress. However, they have to deal with increased intracellular ROS levels due to PPP dysfunction, a major NADPH generating pathway. Moreover, we saw that regardless of their critical metabolic state, purine inhibited cancer cells are able to shift towards an EMT phenotype, accompanied with an enhanced migratory potential. Increased migration and metastatic colonization after treatment with purine inhibitors has been demonstrated in parallel by other research group [118].

Hence, a question arising is what are possible factors supporting the metastasizing potential of purine depleted cancer cells. Firstly, as mentioned above, we showed that blocking nucleotide via interference with the cytosolic OCM leads to an uncoupling of the mitochondrial OCM and enhanced formate secretion. In previous studies formate was shown to promote an invasive phenotype of cancer cells as well as enhance their seeding capacity though increased expression of matrix metalloproteinases (MMPs) and via interfering with lipid metabolism [80]. Additionally, formate increases formyl-methionine (fMet) levels, needed for mitochondrial translation but also for formyl-peptide receptor (FPR)-dependent signalling, promoting cell migration and metastasis [81].

Moreover, we observed an enhanced glutamine dependency in purine inhibited cancer cells, which potentially supports their metastatic potential. Glutamine metabolism has been extensively studied in proliferating cancer cells and growing evidence indicates it also supports metastasis formation. *In vitro*, invasive ovarian cancer cells but not their non-invasive counterparts were highly dependent on glutamine availability [135]. Also melanoma cells display an increased dependency on glutamine metabolism to maintain their metastatic phenotype [144]. Furthermore, GLS1 is required for cancer cell migration under hypoxia and high GLS1 mRNA expression correlates with lymph node metastasis of colorectal cancer [145]. Glutamine-derived glutamate can be exported through the cystine/glutamate antiporter xCT. Notably, xCT expression has been identified as a predictive marker for tumor invasion in colorectal cancer patients [146]. In the scope of our study we have not investigated the impact of glutamine depletion in addition to purine inhibition on cancer cell migration but have planned to do so. However, we performed cell death assays combining glutamine starvation with PAICS inhibition and observed an increased percentage of apoptotic cells. In parallel, we assessed cell toxicity of purine inhibition in combination with a GLS1 inhibitor and observed a trend towards increased cell death however not significant. Importantly, our tracing data suggests that there is no complete inhibition of GLS1 through the inhibitor. Moreover, serine derived α-KG could potentially compensate for the inhibition of glutamine metabolism [46]. In this context it would be worth considering a combination of PHGDH and GLS1 inhibition to enhance toxicity.

Next, we believe it would be worth considering the significance of ROS during cancer progression, as we observed that purine inhibited cancer cells deal with an increase of oxidative stress. The role of ROS during tumor progression is extensively studied, but its role in metastasis formation remains ambiguous. When cancer cells enter circulation, the ability to efficiently induce antioxidant mechanisms is crucial for cell survival [147, 148]. Moreover, NADPH-generating enzymes in the folate metabolism are essential to reduce oxidative stress in circulating melanoma cells, as knockdown of ALDH1L2 or MTHFD1, suppressed distant

melanoma metastases without significantly affecting primary tumor growth in mice [149]. These observations stand in contrast to the previously cited study, showing an enhanced metastatic burden upon ALDH1L2 loss [81], which is just one example of the fact that ROS can be involved in promoting or limiting metastasis [150].

Interestingly and relevant for our study is the observation that ROS induced cell detachment can occur as a consequence of decreased glucose uptake and lower flux into the oxidative PPP [151]. We showed that purine inhibition decreases glucose consumption and PPP activity in cancer cells, consequently activating ME, which possibly compensates for NADPH generation. Importantly and in line with the findings from the previous studies, we observed enhanced migration upon PAICS and GART inhibition in SW620 and LN229 cells, during ongoing experiments. Hence, we started hypothesizing that the activity of ME confers the ability to maintain intracellular ROS levels in a tolerable range but still high enough to function as a pro-migratory signal. In addition, several studies have shown that ME supports redox balance and promotes metastasis [152-155]. Ongoing experiments are currently performed to evaluate the involvement of ME in conferring metastatic potential to purine depleted tumor cells.

Lastly, we demonstrated that purine levels influence enzyme activity but also affect signalling pathways such as the metabolic checkpoint guardian AMP-activated protein kinase (AMPK) and mammalian target of rapamycin (mTOR), a central regulator of cell growth and proliferation. Both AMPK and mTOR illustrate a “tug of war” over cell growth and metabolism as they can act as tumor suppressors as well as tumor supporters, in a context dependent manner. Even though they are functionally opposite, they are closely connected and constantly influencing each other, with AMPK acting as inhibitior of mTOR when cellular energy is low. The concept of mTOR mediated purine sensing is not new, it has been demonstrated by several studies that purine availability regulates the activity of mTORC1 and depletion of purine nucleotides inhibits mTORC1 signalling [130, 131, 156, 157]. We showed that purine depletion activates AMPK, but also inhibits mTOR signalling, thereby reducing cancer cell proliferation without inducing cell death. The loss of mTOR activity triggers catabolic processes, including autophagy, which support cell survival under nutrient-poor conditions [158]. We hypothesized that the persistence of purine depleted cancer cells might be supported due to low mTOR signal allowing them to sustain in the absence of purine nucleotides as building blocks for DNA. Hence, something we think is worth testing is whether activation of mTOR together with purine inhibition might drive cancer cells into a critical situation in which they keep trying to proliferate and produce biomass, but lacking purine building block leads them into a fatal trap. Unfortunately, we have not been able to confirm the functionality of our mTOR activator (3BDO, MVE 890405-51-3) and therefore did not obtain conclusive results yet.

Nevertheless, we still believe that the role of the mTOR pathway is relevant for our study, as it has been shown that in some cancers mTOR inhibition can promote the metastatic potential of cancer cells. Although mTORC1 inhibition has therapeutic potential as a cancer treatment, it can paradoxically promote metastasis in certain settings. This effect may arise from feedback activation of alternative signaling pathways, such as PI3K/AKT, which enhance cell survival and migration [159]. Moreover, in some cancer cells, mTORC1 inhibition can induce epithelial-mesenchymal transition (EMT) to facilitate metastatic spread. Suppression of mTOR downstream target, 4E-BP1 was shown to induce EMT and metastasis, while activated 4E-BP1 reduces cell migration and invasion [160, 161]. Moreover, inhibition of PI3K/mTOR results in growth arrest but induces EMT in intestinal epithelial cells [160]. Considering these findings, we believe that they are of interest in order to understand the migratory phenotype of purine inhibited cancer cells, however activating mTOR to reduce metastasis upon nucleotide inhibition, may not be the key solution as most likely this intervention comes along with numerous side effects.

Overall, we confirmed that targeting the OCM mediated nucleotide synthesis remains a promising approach to target cancer cells. However, we also elucidated some challenges that come along with inhibiting the anabolic part of the OCM, especially purine nucleotide biosynthesis. Those being the persistence of purine inhibited cancer cells and the ability to maintain their migratory potential. Moreover, we identified potential vulnerabilities in purine inhibited cancer cells, namely increased glutamine dependency and ME activity, which might serve as secondary targets and a more efficient elimination of the tumor cells. Furthermore, we identified formate overflow as another metabolic vulnerability, as high formate release enhances the toxic folate trap and sensitizes tumor cells to TH9619 treatment. The introduction of TH9619 in the first round of clinical trials elucidates the importance of depicting fundamental metabolic mechanism for the development of novel therapeutics. Moreover, there remains therapeutic potential of purine nucleotide inhibitors in combination with immunotherapy. Inhibiting purine metabolism in parallel to immune checkpoints is highly investigated and may serve as promising complementary strategy to enhance the efficacy of immune checkpoint blockade [106, 162-164]. Finally, we hope that our findings provide a deeper mechanistic understanding on how cancer cells respond to nucleotide inhibition, and may contribute to a clinical success in the future.

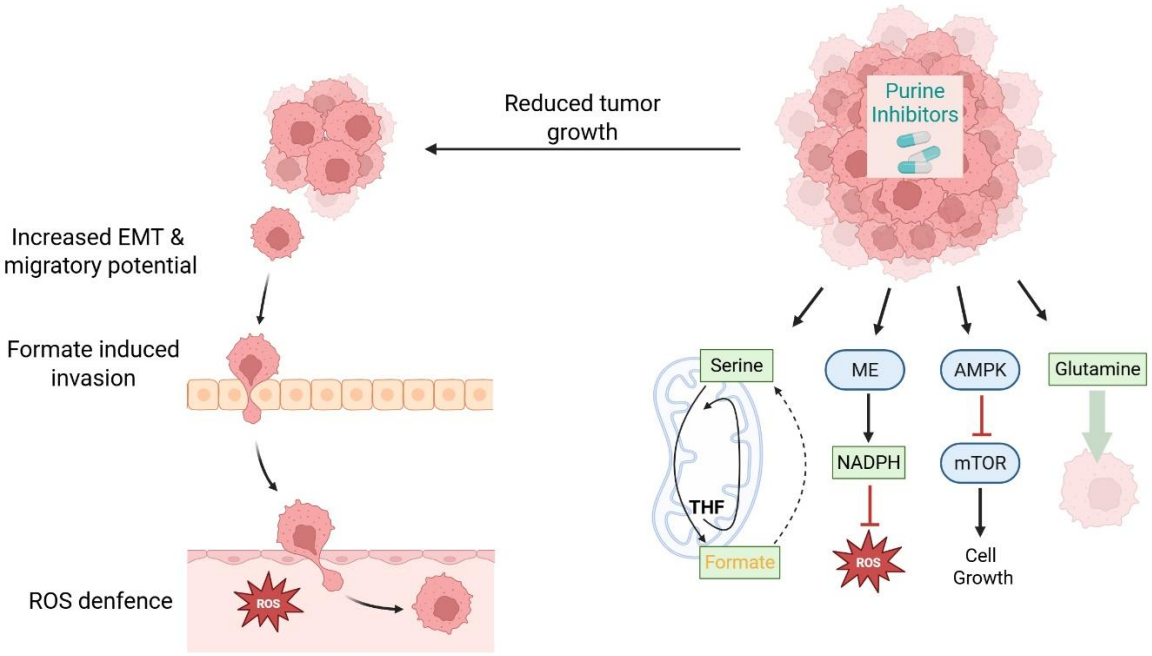

Figure 7: **Graphical abstract**, illustrating the key findings of the studies included in this thesis. Purine nucleotide inhibition leads to an increased dependency on glutamine as a carbon source as well as ME activity for ROS defense. Furthermore, purine depletion activates AMPK and deactivated mTOR signaling in parallel. Treatment, with MTX inhibits purine biosynthesis and activates an autarkic mitochondrial OCM flux resulting in formate overflow. All of these metabolic features contribute in one or the other way to a reduction in tumor growth but also to increase metastatic potential of the cancer cells.

4. References

1. Bray, F., et al., *Global cancer statistics 2022: GLOBOCAN estimates of incidence and mortality worldwide for 36 cancers in 185 countries.* CA Cancer J Clin, 2024. **74**(3): p. 229-263.
2. Hanahan, D. and R.A. Weinberg, *The hallmarks of cancer.* Cell, 2000. **100**(1): p. 57-70.
3. Hanahan, D. and R.A. Weinberg, *Hallmarks of cancer: the next generation.* Cell, 2011. **144**(5): p. 646-74.
4. Hanahan, D., *Hallmarks of Cancer: New Dimensions.* Cancer Discov, 2022. **12**(1): p. 31-46.
5. Sporn, M.B., *The war on cancer.* Lancet, 1996. **347**(9012): p. 1377-81.
6. Gupta, G.P. and J. Massagué, *Cancer metastasis: building a framework.* Cell, 2006. **127**(4): p. 679-95.
7. Warburg, O., F. Wind, and E. Negelein, *THE METABOLISM OF TUMORS IN THE BODY.* J Gen Physiol, 1927. **8**(6): p. 519-30.
8. Shen, Y., et al., *Mitochondrial ATP generation is more proteome efficient than glycolysis.* Nat Chem Biol, 2024. **20**(9): p. 1123-1132.
9. Vander Heiden, M.G., L.C. Cantley, and C.B. Thompson, *Understanding the Warburg effect: the metabolic requirements of cell proliferation.* Science, 2009. **324**(5930): p. 1029-33.
10. Locasale, J.W., *Serine, glycine and one-carbon units: cancer metabolism in full circle.* Nat Rev Cancer, 2013. **13**(8): p. 572-83.
11. Griguer, C.E., C.R. Oliva, and G.Y. Gillespie, *Glucose metabolism heterogeneity in human and mouse malignant glioma cell lines.* J Neurooncol, 2005. **74**(2): p. 123-33.
12. Vansteenkiste, J., et al., *Positron-emission tomography in prognostic and therapeutic assessment of lung cancer: systematic review.* Lancet Oncol, 2004. **5**(9): p. 531-40.
13. Farber, S. and L.K. Diamond, *Temporary remissions in acute leukemia in children produced by folic acid antagonist, 4-aminopteroyl-glutamic acid.* N Engl J Med, 1948. **238**(23): p. 787-93.
14. Lander, E.S., et al., *Initial sequencing and analysis of the human genome.* Nature, 2001. **409**(6822): p. 860-921.
15. Possemato, R., et al., *Functional genomics reveal that the serine synthesis pathway is essential in breast cancer.* Nature, 2011. **476**(7360): p. 346-50.
16. Locasale, J.W., et al., *Phosphoglycerate dehydrogenase diverts glycolytic flux and contributes to oncogenesis.* Nat Genet, 2011. **43**(9): p. 869-74.
17. Nilsson, R., et al., *Metabolic enzyme expression highlights a key role for MTHFD2 and the mitochondrial folate pathway in cancer.* Nat Commun, 2014. **5**: p. 3128.
18. Bergers, G. and S.M. Fendt, *The metabolism of cancer cells during metastasis.* Nat Rev Cancer, 2021. **21**(3): p. 162-180.
19. Stine, Z.E., et al., *MYC, Metabolism, and Cancer.* Cancer Discov, 2015. **5**(10): p. 1024-39.
20. Son, J., et al., *Glutamine supports pancreatic cancer growth through a KRAS-regulated metabolic pathway.* Nature, 2013. **496**(7443): p. 101-5.
21. Elstrom, R.L., et al., *Akt stimulates aerobic glycolysis in cancer cells.* Cancer Res, 2004. **64**(11): p. 3892-9.
22. Saxton, R.A. and D.M. Sabatini, *mTOR Signaling in Growth, Metabolism, and Disease.* Cell, 2017. **168**(6): p. 960-976.
23. Cairns, R.A., I.S. Harris, and T.W. Mak, *Regulation of cancer cell metabolism.* Nat Rev Cancer, 2011. **11**(2): p. 85-95.
24. Zaal, E.A. and C.R. Berkers, *The Influence of Metabolism on Drug Response in Cancer.* Front Oncol, 2018. **8**: p. 500.
25. Wise, D.R. and C.B. Thompson, *Glutamine addiction: a new therapeutic target in cancer.* Trends Biochem Sci, 2010. **35**(8): p. 427-33.
26. Cruzat, V., et al., *Glutamine: Metabolism and Immune Function, Supplementation and Clinical Translation.* Nutrients, 2018. **10**(11).
27. Pavlova, N.N. and C.B. Thompson, *The Emerging Hallmarks of Cancer Metabolism.* Cell Metab, 2016. **23**(1): p. 27-47.

28. Reitzer, L.J., B.M. Wice, and D. Kennell, *Evidence that glutamine, not sugar, is the major energy source for cultured HeLa cells.* J Biol Chem, 1979. **254**(8): p. 2669-76.
29. Yoo, H.C., et al., *A Variant of SLC1A5 Is a Mitochondrial Glutamine Transporter for Metabolic Reprogramming in Cancer Cells.* Cell Metab, 2020. **31**(2): p. 267-283.e12.
30. Curtis, D.R. and J.C. Watkins, *The excitation and depression of spinal neurones by structurally related amino acids.* J Neurochem, 1960. **6**: p. 117-41.
31. Moriarty, C., N. Gupta, and D. Bhattacharya, *Role of Glutamate Excitotoxicity in Glioblastoma Growth and Its Implications in Treatment.* Cell Biol Int, 2025. **49**(5): p. 421-434.
32. Conrad, M. and H. Sato, *The oxidative stress-inducible cystine/glutamate antiporter, system x (c) (-) : cystine supplier and beyond.* Amino Acids, 2012. **42**(1): p. 231-46.
33. Brose, S.A., A.L. Marquardt, and M.Y. Golovko, *Fatty acid biosynthesis from glutamate and glutamine is specifically induced in neuronal cells under hypoxia.* J Neurochem, 2014. **129**(3): p. 400-12.
34. Whillier, S., et al., *Glutamine and α-ketoglutarate as glutamate sources for glutathione synthesis in human erythrocytes.* Febs j, 2011. **278**(17): p. 3152-63.
35. Cory, J.G. and A.H. Cory, *Critical roles of glutamine as nitrogen donors in purine and pyrimidine nucleotide synthesis: asparaginase treatment in childhood acute lymphoblastic leukemia.* In Vivo, 2006. **20**(5): p. 587-9.
36. Le, A., et al., *Glucose-independent glutamine metabolism via TCA cycling for proliferation and survival in B cells.* Cell Metab, 2012. **15**(1): p. 110-21.
37. Benzarti, M., et al., *PKM2 diverts glycolytic flux in dependence on mitochondrial one-carbon cycle.* Cell Rep, 2024. **43**(3): p. 113868.
38. Yang, C., et al., *Glutamine oxidation maintains the TCA cycle and cell survival during impaired mitochondrial pyruvate transport.* Mol Cell, 2014. **56**(3): p. 414-424.
39. Yang, S.M., et al., *Regulation of glucose and glutamine metabolism to overcome cisplatin resistance in intrahepatic cholangiocarcinoma.* BMB Rep, 2023. **56**(11): p. 600-605.
40. Kodama, M., et al., *A shift in glutamine nitrogen metabolism contributes to the malignant progression of cancer.* Nat Commun, 2020. **11**(1): p. 1320.
41. Gouda, M.A., et al., *A phase I/II study of the safety and efficacy of telaglenastat (CB-839) in combination with nivolumab in patients with metastatic melanoma, renal cell carcinoma, and non-small-cell lung cancer.* ESMO Open, 2025. **10**(5): p. 104536.
42. Tannir, N.M., et al., *Efficacy and Safety of Telaglenastat Plus Cabozantinib vs Placebo Plus Cabozantinib in Patients With Advanced Renal Cell Carcinoma: The CANTATA Randomized Clinical Trial.* JAMA Oncol, 2022. **8**(10): p. 1411-1418.
43. Lee, C.H., et al., *Telaglenastat plus Everolimus in Advanced Renal Cell Carcinoma: A Randomized, Double-Blinded, Placebo-Controlled, Phase II ENTRATA Trial.* Clin Cancer Res, 2022. **28**(15): p. 3248-3255.
44. Long, B., et al., *Quantitative proteomics analysis reveals glutamine deprivation activates fatty acid β-oxidation pathway in HepG2 cells.* Amino Acids, 2016. **48**(5): p. 1297-307.
45. Fares, H.M., et al., *Autophagy in cancer: The cornerstone during glutamine deprivation.* Eur J Pharmacol, 2022. **916**: p. 174723.
46. Qiu, Y., et al., *The unique catalytic properties of PSAT1 mediate metabolic adaptation to glutamine blockade.* Nat Metab, 2024. **6**(8): p. 1529-1548.
47. Kaynak, A., et al., *Phosphatidylserine: The Unique Dual-Role Biomarker for Cancer Imaging and Therapy.* Cancers (Basel), 2022. **14**(10).
48. Martín-Otal, C., et al., *Phosphatidylserine as a tumor target for CAR-T cell therapy.* J Immunother Cancer, 2025. **13**(2).
49. Budhu, S., et al., *Targeting Phosphatidylserine Enhances the Anti-tumor Response to Tumor-Directed Radiation Therapy in a Preclinical Model of Melanoma.* Cell Rep, 2021. **34**(2): p. 108620.
50. Yang, M. and K.H. Vousden, *Serine and one-carbon metabolism in cancer.* Nat Rev Cancer, 2016. **16**(10): p. 650-62.

51. Engel, A.L., et al., *Correction: Serine-dependent redox homeostasis regulates glioblastoma cell survival.* Br J Cancer, 2021. **125**(7): p. 1030.
52. Gatti, C., M. Brunetti, and A. Gaiti, *Serine incorporation into phospholipids in vivo and serine phosphoglyceride metabolic transformations in cerebral areas from adult and aged rats.* Neurobiol Aging, 1989. **10**(3): p. 241-5.
53. Hirabayashi, Y. and S. Furuya, *Roles of l-serine and sphingolipid synthesis in brain development and neuronal survival.* Prog Lipid Res, 2008. **47**(3): p. 188-203.
54. Shu, M., Y. Liu, and J. Wang, *Protein post-translational modifications in serine synthetic pathway: functions and molecular mechanisms.* Cell Commun Signal, 2025. **23**(1): p. 311.
55. Li, L., Y. Qin, and Y. Chen, *The enzymes of serine synthesis pathway in cancer metastasis.* Biochim Biophys Acta Mol Cell Res, 2024. **1871**(4): p. 119697.
56. Zhang, H., et al., *Comprehensive analysis of PHGDH for predicting prognosis and immunotherapy response in patients with endometrial carcinoma.* BMC Med Genomics, 2023. **16**(1): p. 29.
57. Jia, X.Q., et al., *Increased Expression of PHGDH and Prognostic Significance in Colorectal Cancer.* Transl Oncol, 2016. **9**(3): p. 191-6.
58. Song, Z., et al., *PHGDH is an independent prognosis marker and contributes cell proliferation, migration and invasion in human pancreatic cancer.* Gene, 2018. **642**: p. 43-50.
59. Bi, F., et al., *PHGDH Is Upregulated at Translational Level and Implicated in Platin-Resistant in Ovarian Cancer Cells.* Front Oncol, 2021. **11**: p. 643129.
60. Geeraerts, S.L., et al., *The ins and outs of serine and glycine metabolism in cancer.* Nat Metab, 2021. **3**(2): p. 131-141.
61. Pollari, S., et al., *Enhanced serine production by bone metastatic breast cancer cells stimulates osteoclastogenesis.* Breast Cancer Res Treat, 2011. **125**(2): p. 421-30.
62. Ngo, B., et al., *Limited Environmental Serine and Glycine Confer Brain Metastasis Sensitivity to PHGDH Inhibition.* Cancer Discov, 2020. **10**(9): p. 1352-1373.
63. Rossi, M., et al., *PHGDH heterogeneity potentiates cancer cell dissemination and metastasis.* Nature, 2022. **605**(7911): p. 747-753.
64. Samanta, D., et al., *Correction: PHGDH Expression Is Required for Mitochondrial Redox Homeostasis, Breast Cancer Stem Cell Maintenance, and Lung Metastasis.* Cancer Res, 2022. **82**(6): p. 1153.
65. Pacold, M.E., et al., *A PHGDH inhibitor reveals coordination of serine synthesis and one-carbon unit fate.* Nat Chem Biol, 2016. **12**(6): p. 452-8.
66. Reid, M.A., et al., *Serine synthesis through PHGDH coordinates nucleotide levels by maintaining central carbon metabolism.* Nat Commun, 2018. **9**(1): p. 5442.
67. Mullarky, E., et al., *Identification of a small molecule inhibitor of 3-phosphoglycerate dehydrogenase to target serine biosynthesis in cancers.* Proc Natl Acad Sci U S A, 2016. **113**(7): p. 1778-83.
68. Weinstabl, H., et al., *Intracellular Trapping of the Selective Phosphoglycerate Dehydrogenase (PHGDH) Inhibitor BI-4924 Disrupts Serine Biosynthesis.* J Med Chem, 2019. **62**(17): p. 7976-7997.
69. Chen, C., et al., *Identification of a novel PHGDH covalent inhibitor by chemical proteomics and phenotypic profiling.* Acta Pharm Sin B, 2022. **12**(1): p. 246-261.
70. Wang, Q., et al., *Rational Design of Selective Allosteric Inhibitors of PHGDH and Serine Synthesis with Anti-tumor Activity.* Cell Chem Biol, 2017. **24**(1): p. 55-65.
71. Sullivan, M.R., et al., *Increased Serine Synthesis Provides an Advantage for Tumors Arising in Tissues Where Serine Levels Are Limiting.* Cell Metab, 2019. **29**(6): p. 1410-1421.e4.
72. Liu, X., et al., *PHGDH activation fuels glioblastoma progression and radioresistance via serine synthesis pathway.* J Exp Clin Cancer Res, 2025. **44**(1): p. 99.
73. Maddocks, O.D., et al., *Serine starvation induces stress and p53-dependent metabolic remodelling in cancer cells.* Nature, 2013. **493**(7433): p. 542-6.

74. Maddocks, O.D.K., et al., *Modulating the therapeutic response of tumours to dietary serine and glycine starvation.* Nature, 2017. **544**(7650): p. 372-376.
75. Tajan, M., et al., *Serine synthesis pathway inhibition cooperates with dietary serine and glycine limitation for cancer therapy.* Nat Commun, 2021. **12**(1): p. 366.
76. Falcone, M., et al., *Sensitisation of cancer cells to radiotherapy by serine and glycine starvation.* Br J Cancer, 2022. **127**(10): p. 1773-1786.
77. Meiser, J., et al., *Serine one-carbon catabolism with formate overflow.* Sci Adv, 2016. **2**(10): p. e1601273.
78. Meiser, J., et al., *Increased formate overflow is a hallmark of oxidative cancer.* Nat Commun, 2018. **9**(1): p. 1368.
79. Ternes, D., et al., *The gut microbial metabolite formate exacerbates colorectal cancer progression.* Nat Metab, 2022. **4**(4): p. 458-475.
80. Delbrouck, C., et al., *Formate promotes invasion and metastasis in reliance on lipid metabolism.* Cell Rep, 2023. **42**(9): p. 113034.
81. Hennequart, M., et al., *ALDH1L2 regulation of formate, formyl-methionine, and ROS controls cancer cell migration and metastasis.* Cell Rep, 2023. **42**(6): p. 112562.
82. Xu, X., et al., *One-carbon unit supplementation fuels purine synthesis in tumor-infiltrating T cells and augments checkpoint blockade.* Cell Chem Biol, 2024. **31**(5): p. 932-943.e8.
83. Rowe, J.H., et al., *Formate Supplementation Enhances Antitumor CD8+ T-cell Fitness and Efficacy of PD-1 Blockade.* Cancer Discov, 2023. **13**(12): p. 2566-2583.
84. Phelps, C.M., et al., *Exercise-induced microbiota metabolite enhances CD8 T cell antitumor immunity promoting immunotherapy efficacy.* Cell, 2025. **188**(20): p. 5680-5700.e28.
85. Koźmiński, P., et al., *Overview of Dual-Acting Drug Methotrexate in Different Neurological Diseases, Autoimmune Pathologies and Cancers.* Int J Mol Sci, 2020. **21**(10).
86. Diasio, R.B. and B.E. Harris, *Clinical pharmacology of 5-fluorouracil.* Clin Pharmacokinet, 1989. **16**(4): p. 215-37.
87. Spears, C.P., et al., *In vivo kinetics of thymidylate synthetase inhibition of 5-fluorouracil-sensitive and -resistant murine colon adenocarcinomas.* Cancer Res, 1982. **42**(2): p. 450-6.
88. Afzal, S., et al., *MTHFR polymorphisms and 5-FU-based adjuvant chemotherapy in colorectal cancer.* Ann Oncol, 2009. **20**(10): p. 1660-6.
89. Folprecht, G., et al., *Efficacy of 5-fluorouracil-based chemotherapy in elderly patients with metastatic colorectal cancer: a pooled analysis of clinical trials.* Ann Oncol, 2004. **15**(9): p. 1330-8.
90. Mo, J., et al., *Targeting mitochondrial one-carbon enzyme MTHFD2 together with pemetrexed confers therapeutic advantages in lung adenocarcinoma.* Cell Death Discov, 2022. **8**(1): p. 307.
91. Shang, M., et al., *The folate cycle enzyme MTHFD2 induces cancer immune evasion through PD-L1 up-regulation.* Nat Commun, 2021. **12**(1): p. 1940.
92. Mo, H.Y., et al., *MTHFD2-mediated redox homeostasis promotes gastric cancer progression under hypoxic conditions.* Redox Rep, 2024. **29**(1): p. 2345455.
93. Pardo-Lorente, N. and S. Sdelci, *MTHFD2 in healthy and cancer cells: Canonical and non-canonical functions.* NPJ Metab Health Dis, 2024. **2**(1): p. 3.
94. Liu, J., et al., *MTHFD2 Enhances cMYC O-GlcNAcylation to Promote Sunitinib Resistance in Renal Cell Carcinoma.* Cancer Res, 2025. **85**(6): p. 1113-1129.
95. Yao, S., et al., *MTHFD2 marks pemetrexed resistance in pulmonary adenocarcinoma with EGFR wild type.* Discov Oncol, 2025. **16**(1): p. 581.
96. Bonagas, N., et al., *Pharmacological targeting of MTHFD2 suppresses acute myeloid leukemia by inducing thymidine depletion and replication stress.* Nat Cancer, 2022. **3**(2): p. 156-172.
97. Green, A.C., et al., *Formate overflow drives toxic folate trapping in MTHFD1 inhibited cancer cells.* Nat Metab, 2023. **5**(4): p. 642-659.
98. Jain, M., et al., *Metabolite profiling identifies a key role for glycine in rapid cancer cell proliferation.* Science, 2012. **336**(6084): p. 1040-4.

99. Ducker, G.S., et al., *Reversal of Cytosolic One-Carbon Flux Compensates for Loss of the Mitochondrial Folate Pathway.* Cell Metab, 2016. **24**(4): p. 640-641.
100. Lee, W.D., et al., *Tumor Reliance on Cytosolic versus Mitochondrial One-Carbon Flux Depends on Folate Availability.* Cell Metab, 2021. **33**(1): p. 190-198.e6.
101. Kiweler, N., et al., *Mitochondria preserve an autarkic one-carbon cycle to confer growth-independent cancer cell migration and metastasis.* Nat Commun, 2022. **13**(1): p. 2699.
102. Tran, D.H., et al., *De novo and salvage purine synthesis pathways across tissues and tumors.* Cell, 2024. **187**(14): p. 3602-3618.e20.
103. Kumar, V., *Adenosine as an endogenous immunoregulator in cancer pathogenesis: where to go?* Purinergic Signal, 2013. **9**(2): p. 145-65.
104. Muller-Haegele, S., L. Muller, and T.L. Whiteside, *Immunoregulatory activity of adenosine and its role in human cancer progression.* Expert Rev Clin Immunol, 2014. **10**(7): p. 897-914.
105. Antonioli, L., et al., *Immunity, inflammation and cancer: a leading role for adenosine.* Nat Rev Cancer, 2013. **13**(12): p. 842-57.
106. Keshet, R., et al., *Targeting purine synthesis in ASS1-expressing tumors enhances the response to immune checkpoint inhibitors.* Nat Cancer, 2020. **1**(9): p. 894-908.
107. Hung, M.H., et al., *Purine anabolism creates therapeutic vulnerability in hepatocellular carcinoma through m 6 A-mediated epitranscriptomic regulation.* Hepatology, 2023. **78**(5): p. 1462-1477.
108. Chakravarthi, B.V., et al., *Expression and Role of PAICS, a De Novo Purine Biosynthetic Gene in Prostate Cancer.* Prostate, 2017. **77**(1): p. 10-21.
109. Chakravarthi, B., et al., *A Role for De Novo Purine Metabolic Enzyme PAICS in Bladder Cancer Progression.* Neoplasia, 2018. **20**(9): p. 894-904.
110. Huo, A. and X. Xiong, *PAICS as a potential target for cancer therapy linking purine biosynthesis to cancer progression.* Life Sci, 2023. **331**: p. 122070.
111. Chen, L., et al., *Clinical efficacy and safety of 6-thioguanine in the treatment of childhood acute lymphoblastic leukemia: A protocol for systematic review and meta-analysis.* Medicine (Baltimore), 2020. **99**(18): p. e20082.
112. Gehan, E.A. and E.J. Freireich, *The 6-MP versus placebo clinical trial in acute leukemia.* Clin Trials, 2011. **8**(3): p. 288-97.
113. Laohavinij, S., et al., *A phase I clinical study of the antipurine antifolate lometrexol (DDATHF) given with oral folic acid.* Invest New Drugs, 1996. **14**(3): p. 325-35.
114. Roberts, J.D., et al., *Weekly lometrexol with daily oral folic acid is appropriate for phase II evaluation.* Cancer Chemother Pharmacol, 2000. **45**(2): p. 103-10.
115. Chong, Y.C., et al., *Targeted Inhibition of Purine Metabolism Is Effective in Suppressing Hepatocellular Carcinoma Progression.* Hepatol Commun, 2020. **4**(9): p. 1362-1381.
116. Agarwal, S., et al., *PAICS, a De Novo Purine Biosynthetic Enzyme, Is Overexpressed in Pancreatic Cancer and Is Involved in Its Progression.* Transl Oncol, 2020. **13**(7): p. 100776.
117. Singh, S.X., et al., *Purine Synthesis Inhibitor L-Alanosine Impairs Mitochondrial Function and Stemness of Brain Tumor Initiating Cells.* Biomedicines, 2022. **10**(4).
118. Soflaee, M.H., et al., *Purine nucleotide depletion prompts cell migration by stimulating the serine synthesis pathway.* Nat Commun, 2022. **13**(1): p. 2698.
119. Ju, H.Q., et al., *NADPH homeostasis in cancer: functions, mechanisms and therapeutic implications.* Signal Transduct Target Ther, 2020. **5**(1): p. 231.
120. TeSlaa, T., et al., *The pentose phosphate pathway in health and disease.* Nat Metab, 2023. **5**(8): p. 1275-1289.
121. Li, S., et al., *Nicotinamide nucleotide transhydrogenase-mediated redox homeostasis promotes tumor growth and metastasis in gastric cancer.* Redox Biol, 2018. **18**: p. 246-255.
122. Ducker, G.S. and J.D. Rabinowitz, *One-Carbon Metabolism in Health and Disease.* Cell Metab, 2017. **25**(1): p. 27-42.

123. Ju, H.Q., et al., *Modulation of Redox Homeostasis by Inhibition of MTHFD2 in Colorectal Cancer: Mechanisms and Therapeutic Implications.* J Natl Cancer Inst, 2019. **111**(6): p. 584-596.
124. Ying, M., et al., *Lactate and glutamine support NADPH generation in cancer cells under glucose deprived conditions.* Redox Biol, 2021. **46**: p. 102065.
125. Lan, T., et al., *Glucose-6-phosphate dehydrogenase maintains redox homeostasis and biosynthesis in LKB1-deficient KRAS-driven lung cancer.* Nat Commun, 2024. **15**(1): p. 5857.
126. Lewis, C.A., et al., *Tracing compartmentalized NADPH metabolism in the cytosol and mitochondria of mammalian cells.* Mol Cell, 2014. **55**(2): p. 253-63.
127. Zhang, Z., et al., *Serine catabolism generates liver NADPH and supports hepatic lipogenesis.* Nat Metab, 2021. **3**(12): p. 1608-1620.
128. Palmieri, E.M., et al., *Acetylation of human mitochondrial citrate carrier modulates mitochondrial citrate/malate exchange activity to sustain NADPH production during macrophage activation.* Biochim Biophys Acta, 2015. **1847**(8): p. 729-38.
129. Pramono, A.A., et al., *NAD- and NADPH-Contributing Enzymes as Therapeutic Targets in Cancer: An Overview.* Biomolecules, 2020. **10**(3).
130. Emmanuel, N., et al., *Purine Nucleotide Availability Regulates mTORC1 Activity through the Rheb GTPase.* Cell Rep, 2017. **19**(13): p. 2665-2680.
131. Hoxhaj, G., et al., *The mTORC1 Signaling Network Senses Changes in Cellular Purine Nucleotide Levels.* Cell Rep, 2017. **21**(5): p. 1331-1346.
132. Hosomi, S., et al., *Inhibitory effect of 5-phosphoribosyl 1-pyrophosphate and ADP on the nonoxidative pentose phosphate pathway activity.* Biochem Med Metab Biol, 1989. **42**(1): p. 52-9.
133. Yang, Z., C.W. Lanks, and L. Tong, *Molecular mechanism for the regulation of human mitochondrial NAD(P)+-dependent malic enzyme by ATP and fumarate.* Structure, 2002. **10**(7): p. 951-60.
134. Hung, H.C., et al., *Functional roles of ATP-binding residues in the catalytic site of human mitochondrial NAD(P)+-dependent malic enzyme.* Biochemistry, 2005. **44**(38): p. 12737-45.
135. Yang, L., et al., *Metabolic shifts toward glutamine regulate tumor growth, invasion and bioenergetics in ovarian cancer.* Mol Syst Biol, 2014. **10**(5): p. 728.
136. Frey, P.A., *The Leloir pathway: a mechanistic imperative for three enzymes to change the stereochemical configuration of a single carbon in galactose.* Faseb j, 1996. **10**(4): p. 461-70.
137. García-Sánchez, A., A.G. Miranda-Díaz, and E.G. Cardona-Muñoz, *The Role of Oxidative Stress in Physiopathology and Pharmacological Treatment with Pro- and Antioxidant Properties in Chronic Diseases.* Oxid Med Cell Longev, 2020. **2020**: p. 2082145.
138. Babiak, R.M., et al., *Methotrexate: pentose cycle and oxidative stress.* Cell Biochem Funct, 1998. **16**(4): p. 283-93.
139. Phillips, D.C., K.J. Woollard, and H.R. Griffiths, *The anti-inflammatory actions of methotrexate are critically dependent upon the production of reactive oxygen species.* Br J Pharmacol, 2003. **138**(3): p. 501-11.
140. Benzarti, M., et al., *Metabolic Potential of Cancer Cells in Context of the Metastatic Cascade.* Cells, 2020. **9**(9).
141. Nguyen, H.L., et al., *Oxidative stress and prostate cancer progression are elicited by membrane-type 1 matrix metalloproteinase.* Mol Cancer Res, 2011. **9**(10): p. 1305-18.
142. Porporato, P.E., et al., *A mitochondrial switch promotes tumor metastasis.* Cell Rep, 2014. **8**(3): p. 754-66.
143. Chen, D., et al., *MiR-373 drives the epithelial-to-mesenchymal transition and metastasis via the miR-373-TXNIP-HIF1α-TWIST signaling axis in breast cancer.* Oncotarget, 2015. **6**(32): p. 32701-12.
144. Rodrigues, M.F., et al., *Enhanced OXPHOS, glutaminolysis and β-oxidation constitute the metastatic phenotype of melanoma cells.* Biochem J, 2016. **473**(6): p. 703-15.

145. Xiang, L., et al., *Glutaminase 1 expression in colorectal cancer cells is induced by hypoxia and required for tumor growth, invasion, and metastatic colonization.* Cell Death Dis, 2019. **10**(2): p. 40.
146. Sugano, K., et al., *Expression of xCT as a predictor of disease recurrence in patients with colorectal cancer.* Anticancer Res, 2015. **35**(2): p. 677-82.
147. Elia, I., G. Doglioni, and S.M. Fendt, *Metabolic Hallmarks of Metastasis Formation.* Trends Cell Biol, 2018. **28**(8): p. 673-684.
148. Faubert, B., A. Solmonson, and R.J. DeBerardinis, *Metabolic reprogramming and cancer progression.* Science, 2020. **368**(6487).
149. Piskounova, E., et al., *Oxidative stress inhibits distant metastasis by human melanoma cells.* Nature, 2015. **527**(7577): p. 186-91.
150. Cheung, E.C. and K.H. Vousden, *The role of ROS in tumour development and progression.* Nat Rev Cancer, 2022. **22**(5): p. 280-297.
151. Schafer, Z.T., et al., *Antioxidant and oncogene rescue of metabolic defects caused by loss of matrix attachment.* Nature, 2009. **461**(7260): p. 109-13.
152. Liao, R., et al., *ME1 promotes basal-like breast cancer progression and associates with poor prognosis.* Sci Rep, 2018. **8**(1): p. 16743.
153. Lu, Y.X., et al., *ME1 Regulates NADPH Homeostasis to Promote Gastric Cancer Growth and Metastasis.* Cancer Res, 2018. **78**(8): p. 1972-1985.
154. Liu, C., et al., *Malic Enzyme 1 Indicates Worse Prognosis in Breast Cancer and Promotes Metastasis by Manipulating Reactive Oxygen Species.* Onco Targets Ther, 2020. **13**: p. 8735-8747.
155. Hu, W.C., et al., *Overexpression of malic enzyme is involved in breast cancer growth and is correlated with poor prognosis.* J Cell Mol Med, 2024. **28**(6): p. e18163.
156. Zarou, M.M., et al., *Inhibition of mitochondrial folate metabolism drives differentiation through mTORC1 mediated purine sensing.* Nat Commun, 2024. **15**(1): p. 1931.
157. Benjamin, D. and M.N. Hall, *mTORC1 Controls Synthesis of Its Activator GTP.* Cell Rep, 2017. **19**(13): p. 2643-2644.
158. Laplante, M. and D.M. Sabatini, *mTOR signaling in growth control and disease.* Cell, 2012. **149**(2): p. 274-93.
159. Wei, F., et al., *mTOR inhibition induces EGFR feedback activation in association with its resistance to human pancreatic cancer.* Int J Mol Sci, 2015. **16**(2): p. 3267-82.
160. Shao, J., B.M. Evers, and H. Sheng, *Roles of phosphatidylinositol 3'-kinase and mammalian target of rapamycin/p70 ribosomal protein S6 kinase in K-Ras-mediated transformation of intestinal epithelial cells.* Cancer Res, 2004. **64**(1): p. 229-35.
161. Cai, W., Q. Ye, and Q.B. She, *Loss of 4E-BP1 function induces EMT and promotes cancer cell migration and invasion via cap-dependent translational activation of snail.* Oncotarget, 2014. **5**(15): p. 6015-27.
162. Yang, L., et al., *Blockade of purine metabolism reverses macrophage immunosuppression and enhances anti-tumor immunity in non-small cell lung cancer.* Drug Resist Updat, 2025. **78**: p. 101175.
163. Fathi, M., et al., *Combined cancer immunotherapy based on targeting adenosine pathway and PD-1/PDL-1 axis.* Expert Opin Ther Targets, 2024. **28**(9): p. 757-777.
164. Wu, H.L., et al., *Targeting nucleotide metabolism: a promising approach to enhance cancer immunotherapy.* J Hematol Oncol, 2022. **15**(1): p. 45.

5. Abbreviations

ATP	Adenosine triphosphate
TME	Tumor microenvironment
18F-FDG	18F-fluorodeoxyglucose
PET	Positron emission tomography
EAA	Essential amino acids
TCA	Tricarboxylic acid
xCT	cystine/glutamate antiporter
GSH	Glutathione
GLS	Glutaminase
PD-1	Programmed cell death protein 1
PD-L1	Programmed cell death-ligand 1
OCM	One-carbon metabolism
SAM	S-adenosylmethionine
TNBC	Triple-negative breast cancers
MM	Multiple myeloma
GBM	Glioblastoma
RCC	Renal cell carcinoma
NSCLC	Non-small-cell lung cancer
SSP	Serine synthesis pathway
3-PG	3-phosphoglycerate
PEP	Phosphoenolpyruvate
CTCs	Circulating tumor cells
PHGDH	3-phosphoglycerate dehydrogenase
PSAT	Phosphoserine aminotransferase
PSPH	Phosphoserine phosphatase

SHMT	Serine hydroxymethyltransferase
MTHFD	Methylenetetrahydrofolate Dehydrogenase
ALDH	Aldehyde Dehydrogenase
SAM	S-adenosyl methionine
SAH	S-adenosyl homocysteine
WT	Wild-type
dTMP	Thymidylate
FBS	Fetal bovine serum
dFBS	dialyzed fetal bovine serum
PPP	Pentose phosphate pathway
PRPP	Phosphoribosylpyrophosphate
ADSL	Adenylosuccinate lyase;
AICARt	Aminoimidazole-4-carboxamide ribonucleotide transformylase;
ATIC	Aminoimidazole-4-carboxamide ribonucleotide transformylase/inosine monophosphate cyclohydrolase;
GARs	Glycinamide ribonucleotide synthetase;
GARt	Glycinamide ribonucleotide transformylase;
GART	Glycinamide ribonucleotide synthetase/glycinamide ribonucleotide transformylase/aminoimidazole ribonucleotide synthetase;
IMPch	Inosine monophosphate cyclohydrolase
PAICS	Phosphoribosylaminoimidazole carboxylase/phosphoribosylaminoimidazole succinocarboxamide synthetase
PFAS	N-formylglycinamidine ribonucleotide synthase;
PPAT	Phosphoribosylpyrophosphate amidotransferase
PRS	Phosphoribosylpyrophosphate synthetase
IMP	Inosine monophosphate
AMP	Adenosine monophosphate

GMP	Guanosine monophosphate
ME	Malic Enzyme
IDH	Isocitrate Dehydrogenase
NADK	Nicotinamide adenine dinucleotide kinase
NNT	Nicotinamide nucleotide transhydrogenase
NAD(P)H	Nicotinamide adenine dinucleotide (phosphate)
MTX	Methotrexate
PEM	Pemetrexed
HU	Hydroxyurea
CLO	Clofarabine
ETC	Electron transport Chain
SOD	Superoxide dismutase
EMT	Epithelial to mesenchymal transition
NAC	N-acetyl cysteine

6. Appendix of original publications

One-Carbon Metabolism in Cancer

Kim Eiden[1,2], Johannes Meiser[1#]

[1]Cancer Metabolism Group, Department of Cancer Research, Luxembourg Institute of Health, Luxembourg, Luxembourg.

[2]Faculty of Science, Technology and Medicine, University of Luxembourg, 2 avenue de Université, Esch-sur-Alzette, Luxembourg.

Contact: Johannes.meiser@lih.lu

Abstract:

In the following chapter we are highlighting the various roles of the one carbon metabolism (OCM) in cancer progression. The OCM is a critical metabolic pathway that facilitates nucleotide synthesis, amino acid metabolism, and epigenetic modifications, while also playing a role in redox balance and energy production. Cancer cells exploit OCM to meet their high proliferative demands, making its enzymes attractive therapeutic targets. The plasticity of OCM allows cancer cells to adapt dynamically to metabolic needs, supporting proliferation, migration, and survival under stress. Formate, a product of OCM, serves as both a one-carbon source for biosynthetic needs and a signalling molecule that influences cancer cell invasion, metastasis, and interactions within the tumor microenvironment. The OCM also affects immune responses, influencing T cell function and macrophage polarization. Understanding the OCM's context-dependent roles in cancer could lead to novel, more effective therapeutic strategies beyond traditional antifolate treatments.

Keywords:

One-carbon metabolism, Compartmentalization, Metabolic plasticity, Tumor microenvironment, Formate

1 Introduction

The OCM is an essential metabolic pathway mediating the transfer of one carbon-units through various biochemical reactions to provide biosynthetic precursors for nucleotide synthesis, amino acid metabolism and epigenetic modifications. Yet, the role of OCM goes beyond the provision of building units for biosynthesis. It supports other pillars of metabolism including redox balance within cellular compartments and bioenergetics by generating ATP [1, 2]. In the context of cancer, the OCM becomes particularly important, due to the high proliferative demands of cancer cells and their need to constantly adapt to changing microenvironments. Upregulation of OCM enzymes is observed across various cancer types supporting tumour growth and progression, making them attractive targets for cancer therapy. [3-5]. Here we are providing an overview on the latest findings on OCM in cancer and presenting a conceptual view on how the OCM can be hijacked by cancer cells in a context dependent manner to support cell proliferation, survival and disease progression.

2 Components of the One-Carbon Metabolism

Folate Cycle

The backbone of the OCM is folate, also known as vitamin B9, which cannot be produced by eukaryotic cells but needs to be supplied by dietary intake. Folate is essential for embryonic development and deficiency during pregnancy is leading to neural tube defects (NTDs) in infants [6]. Therefore, folic acid is provided as a supplement to pregnant women and is added to grain and cereal products within the United States and Canada. In many cancer types, folate metabolism plays a crucial role, as it is not only supporting nucleotide biosynthesis for proliferating tumour cells, but also contributes to antioxidant defence and the formation of metastasis. Consequently, enzymes of the folate metabolism became promising therapeutic targets and circulating folate cycle metabolites such as formate could potentially serve as biomarkers for cancer detection [7].

After cellular uptake, folate is reduced via dihydrofolate reductase (DHFR) to its biologically active form tetrahydrofolate (THF) which serves as a one-carbon carrier along the OCM. THF accepts one-carbon units and acts as cofactor for OCM enzymes

to produce different folate species carrying and redistributing the one-carbon units for biological processes. The major substrate feeding the OCM is the non-essential amino acid serine. In a first reaction, carbon three of serine is oxidised and transferred to THF by serine hydroxymethyltransferase (SHMT) forming 5,10-CH_2-THF (5,10-methylene-THF). Subsequently, 5,10-methylene-THF is oxidised in a two-step reaction to 10-CHO-THF (10-formyl-THF) by the bifunctional enzyme methylenetetrahydrofolate dehydrogenase/cyclohydrolase 2 (MTHFD2) in the mitochondria or by the trifunctional methylenetetrahydrofolate dehydrogenase/cyclohydrolase/formyltetrahydrofolate synthetase 1 (MTHFD1) in the cytoplasm (Fig.1). The cytosolic OCM provides the building units for nucleotides required for DNA and RNA biosynthesis. 10-formyl-THF derived carbons are incorporated into the purine ring and 5,10-methylene-THF provides the methyl group to form deoxythymidine monophosphate (dTMP) via thymidylate synthase (TYMS). In the mitochondria, 10-formyl-THF is further processed by methylenetetrahydrofolate dehydrogenase 1-like (MTHFD1L) to THF formate in a reaction that also generates one mole of ATP. Alternatively, aldehyde dehydrogenase 1 family member L2 (ALDH1L2) converts 10-formyl-THF to THF and CO_2 in an $NADP^+$-dependent reaction [8] (Fig.1).

Methionine Cycle

The methionine cycle allows the integration of one-carbon units that are predominantly used as methyl groups for DNA, RNA, and protein methylation. Methionine, an essential amino acid, is converted to the universal methyl group donor S-adenosyl-methionine (SAM), which upon donation of its methyl group is converted to S-adenosyl-homocysteine (SAH). The methionine and the folate cycle are closely linked. Methylenetetrahydrofolate reductase (MTHFR) reduces 5,10-methylene-THF to 5-CH_3-THF (5-methyl-THF). Cobalamin (vitamin B12) serves as cofactor for methionine synthase (MS) to transfer methyl groups from 5-methyl-THF to homocysteine, producing methionine and free THF (Fig.1). Vitamin B12 deficiency results in elevated methylmalonic acid and homocysteine levels causing anaemia and developmental disorders. Additionally, inactivation of MS due to vitamin B12 deficiency results in accumulation of 5-methyl-THF. This “dead-end” of the folate cycle, known as “folate-trap” [9], can lead to folate deficiency, thereby inhibiting the OCM (Fig.3). Methionine can alternatively be recycled from the SAM-dependent polyamine biosynthesis by-product, methylthioadenosine (MTA), which is further used by the enzyme

methylthioadenosine phosphorylase (MTAP) via the methionine salvage pathway, or it can be generated by betaine-homocysteine methyltransferase (BHMT) which converts betaine to dimethylglycine (DMG) (Fig.1). However, BHMT activity is not sufficient to prevent homocystinuria during vitamin B12 deficiency [10, 11]. Cancer-specific alterations in methionine consumption have their relevance as a diagnostic marker in the clinic. Intratumoural methionine uptake measured by positron emission tomography (PET) imaging of ^{11}C-methionine serves as indicator for therapeutic response and overall survival in hematologic malignancies and brain tumours [12, 13].

Transsulfuration Pathway

The transsulfuration pathway serves as an important route to retain systemic homocysteine at a low level. The enzymes cystathionine-β-synthase (CBS) and cystathionine γ-lyase (CSE) catalyse the conversion of homocysteine to cysteine through the intermediate metabolite cystathionine, in two vitamin B6 dependent reactions (Fig.1). The production of cysteine via the transsulfuration pathway is important for cellular antioxidant defence as it is incorporated in the tripeptide and antioxidant molecule glutathione (GSH; L-γ-glutamyl-L-cysteinylglycine). The cysteine side chain carries the reducing power as a transferable electron on the thiol (-SH). In protein biosynthesis, cysteine allows the generation of disulphide bonds, essential for protein folding, structure and stability [14, 15]. A by-product of this pathway is alpha-ketobutyrate which can be further converted to propionyl-coA. Subsequently, propionyl-coA is converted via methylmalonyl-coA (MMA) to succinyl-coA feeding the tricarboxylic acid (TCA) cycle. Propionate metabolism has been shown to promote cancer cell invasion and tumor progression [16].. MMA mutase is the second mammalian enzyme that uses vitamin B12 as a cofactor and low vitamin B12 levels result in MMA accumulation, which often increasedwith age and can drive tumour progression [17]. An additional product of the transsulfuration pathway is the gaseous signalling molecule hydrogen sulphide (H_2S) which has gained increasing attention in the context of cancer biology [18].

3 Sources of one-carbon units

The major one-carbon donor entering the folate cycle is the non-essential amino acid serine, it can be taken up extracellularly or synthesized *de novo* via the serine synthesis pathway (SSP), which is mediated by the enzymes phosphoglycerate dehydrogenase (PHGDH), phosphoserine aminotransferase 1 (PSAT1) and phosphoserine phosphatase (PSPH) (Fig.1). Serine is cleaved to glycine which is another one-carbon source by itself, as glycine can be catabolized to CO_2 and 5,10-methylene-THF via the glycine cleavage system (GCS) [19]. Choline catabolism generates one carbon and sarcosine, which itself can donate another carbon to THF to form 10-formyl-THF. Additional one-carbon sources are betaine, histidine, tryptophan and demethylation reactions. Lastly, the small carboxylic acid formate can serve as a carbon molecule to support anabolic processes. A broader overview on one-carbon sources is provided in recent reviews [7, 20]. Overall, it remains important to remember that this list of one-carbon sources is a theoretical list, meaning that often only certain sources contribute to the cellular one-carbon pool while other pathways remain inactive. The glycine-cleavage system for example is mainly active in liver and kidney and tryptophan catabolism can be upregulated during inflammation but remains at very low rate under homeostatic conditions [21]. In sum, serine represents the major source but other metabolites can also contribute to OCM in a tissue and context dependent manner.

4 Compartmentalization of OCM

OCM is highly compartmentalized, the major folate pools are found in the cytoplasm and the mitochondria but also the nucleus contains folates and OCM activity [22, 23]. Serine-derived one-carbon units for nucleotide biosynthesis can be generated via either the mitochondrial or the cytosolic OCM. The mitochondrial OCM enzymes are among the most upregulated enzymes in cancer cells [3-5]. Indeed, most proliferative cells rely predominantly on the mitochondrial production of one-carbon units, shown by Ducker et al. using a [2,3,3-^{2}H]serine isotopic tracer approach. High mitochondrial flux resulted in M+1 labelled deoxythymidine triphosphate (dTTP), seen in a majority

of cancer cell lines. However, upon loss of mitochondrial OCM activity in genetically MTHFD2-ablated xenografts, cytosolic flux can compensate, still enabling tumour growth [24]. In contrast, upon inhibition of cytosolic OCM, the mitochondria can preserve an autarkic one-carbon cycle that can run independent of the cytosolic OCM. In a recent study, we have demonstrated that in presence of the antifolate methotrexate, growth-arrested cancer cells retain the ability to catabolize serine through the mitochondrial one-carbon route sustaining formate release into the extracellular space. At a mechanistic level, this independent OCM cycling is possible because MTHFD1L dependent formate production regenerates free THF, which can readily accept another one-carbon unit within the SHMT2 dependent step (Fig. 1). Consequently, in contrast to the cytosol, mitochondria do not rely on DHFR to regenerate THF. Interestingly, we and others observed that such antifolate-treated, growth-arrested cancer cells gained increased motility potential in dependence on mitochondrial OCM [25, 26].

In addition to the classical view where one-carbon units are predominantly generated through the mitochondrial pathway it has been shown that, depending on the intracellular folate concentrations, some cancer cells rely more on cytosolic OCM. High folate uptake favours the mitochondrial pathway activity, whereas physiological folate increases cytosolic OCM flux [27]. In this study, the authors also showed that the reduced folate carrier (RFC) SLC19A1 regulates folate availability and cancers with low SLC19A1 expression become highly dependent on cytosolic SHMT1 to support tumour growth [27].

Whether cells rely more on cytosolic or mitochondrial OCM is potentially linked to the cancer cell's tissue of origin. While expression of SHMT2 is ubiquitous across most tissues, cytosolic SHMT1 is predominantly expressed in the kidney and the liver [28, 29]. In parallel, liver and kidney express lower amounts of mitochondrial OCM enzymes MTHFD2 and MTHFD1L [30] (Fig.2). This phenomenon may be linked to the fact that kidney and liver serve as detoxification organs. Similar to hepatic lactate recycling through gluconeogenesis, kidney and liver recycle glycine and formate to serine by "reversing" OCM directionality. Simultaneously, hepatic gluconeogenesis can serve as a major pathway for serine disposal under certain circumstances providing a rationale to couple these two pathways within the same organ [31]. This reversal of OCM is crucial to control systemic serine, glycine and one-carbon homeostasis [32]. In

summary, the cancer cell's tissue of origin might have direct implications on the directionality of OCM enzyme fluxes (Fig.2).

5 Folate transport and folate homeostasis

The predominant form of dietary folate is 5-methyl-THF and folic acid, which are also the only folate species normally found within the circulation [33]. In mammalian cells, free folates are imported via transporters that are either carrier mediated, proton coupled (PCFT) or controlled by folate receptor (Fra-FOLR1, Frb-FOLR2, and Frg-FOLR3). In humans, the most extensively studied transporter is the bidirectional anion antiporter, reduced folate carrier (RFC), encoded by the *SLC19A1* gene. Its maximal activity is at physiological pH of 7.2, below pH 6.5 the transporter remains inactive. RFC is a major determinant of antifolate sensitivity and its dysregulation can lead to antifolate therapy resistance, within different cancer types [34, 35]. Furthermore, RFC serves as a biomarker to predict responsiveness to antifolate treatment [36, 37].

The mitochondrial folate carrier is encoded by the *SLC25A32* gene and facilitates the transfer of free folates across the mitochondrial membrane. Genetic ablation of *SLC25A32* results in full ablation of mitochondrial OCM suggesting that no other transporters can compensate for it [38].

Folate transporters only carry free folates without glutamate tails, therefore folylpolyglutamate synthetase (FPGS) is expressed in both cytosol and mitochondria and catalyses the addition of glutamate moieties. This step is essential for cellular folate homeostasis as the glutamate tails retain the folate species within cellular compartments making them more efficient substrates for OCM enzymes [39, 40]. This compartmentalization of the intracellular folate pools also provides further rationale for the existence of an independent mitochondrial OCM cycle during antifolate treatment, as elaborated earlier [25].

Since glutamylated folates cannot cross the mitochondrial membrane, communication between the two compartments is mediated via exchange of serine or formate. Excessive amounts of 10-formyl-THF can be converted into 5-formyl-THF, a storage form, as free folates are unstable and can be degraded under production of toxic formaldehyde [38, 41]. Interestingly, in addition to folate storage as 5-formyl-THF,

excessive amounts of one-carbon units can also be excreted from cancer cells. In previous work, we elucidated that the amount of formate released by the mitochondria, often exceeds the biosynthetic needs of cancer cells resulting in significant formate release, a phenomenon we termed “formate overflow” [42]. In order to ensure cellular free folate availability, mitochondrial formate release serves as a carbon outlet to balance the ratio of free folates to folates covalently bound to one-carbon units (Fig.3). Imbalance in free THF levels affects folate homeostasis and has detrimental effects on cells. The trapping of folate as 5-methyl-THF has been described earlier as a physiological response to vitamin B12 deficiency [9, 43, 44], resulting in impaired thymidine biosynthesis and genome instability. The 10-formyl-THF trap has been described as a consequence of partial MTHFD1 inhibition. Dysfunction of the dehydrogenase–cyclohydrolase (DC) activity of MTHFD1 prevents the carbon shuffling from 10-formyl-THF to 5,10-methylene-THF. The accumulation of 10-formyl-THF is further potentiated through a high mitochondrial MTHFD2 flux and formate release as well as through the use of the purine salvage pathway instead of *de novo* synthesis. Consequently, the trapped THF is no longer available for SHMT1 to produce dTMP, which results in cell death due do thymidine depletion [45] (Fig.3). This highlights the importance of cellular folate homeostasis for normal cell function and survival.

Finally, folate homeostasis can also be genetically controlled, as both mTORC1 and mTORC2 were shown to be responsive to folate availability, hence acting as folate sensors. Downstream targets of mTOR remain inactive under low folate conditions, whereas mTOR signalling is activated upon re-supplementation with folate [46]. Moreover, transcriptional control of folate enzymes and transporters by ATF4, NRF2, MYC and KRAS have been described in various studies [46-53].

6 Plasticity of One Carbon Metabolism

The OCM can contribute to different essential cellular processes related to the three major metabolic pillars: anabolism, catabolism and redox homeostasis. Given its compartmentalisation and the specific functions of OCM enzymes, the OCM can contribute to these metabolic requirements in a highly dynamic way (Fig.4). In the following section, we will elaborate how OCM can be polarized towards one of these

three pillars to illustrate its plasticity, which can be exploited by cancer cells in a rapid and flexible manner.

Anabolic functions

All proliferating cells, including cancer cells, have high biosynthetic demands in order to increase the synthesis of the major cellular building blocks: proteins, lipids and nucleotides. From a quantitative point of view, protein biosynthesis is the largest biosynthetic sink, followed by lipid and nucleotide synthesis. Amongst the essential nucleotides, purine molecules, in particular adenine, represent the largest sink, since cellular ATP concentrations are generally within the millimolar range. In addition to the energetic aspect related to ATP, nucleotides are essential for DNA and RNA synthesis. Contrary to adenosine, which represents the largest cellular nucleoside pool, dTMP synthesis represents the smallest biosynthetic nucleotide flux. Yet, it is essential for *de novo* DNA synthesis and deficiency in dTMP leads to DNA damage and cell death [54]. Although salvage pathways can help to sustain intracellular nucleotide pools, *de novo* synthesis via the OCM becomes particularly important during cell proliferation [55, 56]. In addition to nucleotide synthesis, serine, glycine and cysteine are also needed for protein biosynthesis, GSH, heme or sphingolipid synthesis [57]. In sum, targeting OCM can affect all major anabolic processes (protein, lipid and nucleotide synthesis). Not surprisingly, antifolates inhibiting nucleotide biosynthesis belong to the first drugs that have been developed as anticancer treatment. The discovery of antifolates (i.e. Methotrexate, Pemetrexed, Pralatrexate) for cancer therapy has been a major breakthrough and became one of the first chemotherapeutic drugs used in the early 1950s, after curing children with acute lymphoblastic leukaemia [58]. Shortly after, Methotrexate was also shown to be effective in solid tumours [59]. Since then, antifolates are used as a first line chemotherapy in hematologic cancers and solid tumours [60, 61]. The challenges thereby are the rather large underlying side effects of classical antifolate therapies. Hence, developing more targeted approaches against OCM holds promise to increase therapeutic efficacy.

Even though the first inhibitors have been developed decades ago, recent advances in genome analyses revealing amplification of OCM genes, such as *MTHFD2*, across a wide range of different cancer types, have put OCM once more into the spotlight [3, 62]. In this context, MTHFD2 could potentially serve as a promising candidate to inhibit

nucleotide synthesis specifically in cancer cells, as it is only sparsely expressed in the majority of healthy adult tissues [3]. Many studies have shown the relevance of MTHFD2 in cancer development, tumour growth and metastasis, hence targeting this enzyme for cancer therapy is of major interest [63-67].

Redox functions

One consequence of mitochondrial respiration is the production of reactive oxidative species (ROS) by the electron transport chain (ETC) [68]. In cancer, metabolic alterations, gene mutations or a hypoxic tumour microenvironment (TME) can lead to oxidative stress and consequently, increase the need for efficient ROS detoxification mechanisms [69]. The OCM is actively involved in controlling ROS and maintaining cellular redox balance, by generating glycine from SHMT-mediated serine catabolism and cysteine from the transsulfuration pathway. Both amino acids serve as building units for GSH, a major cellular antioxidant. The re-generation of GSH from GSSG requires the reduction of the sulphur groups of GSSG and the electrons for this redox reaction are provided by NADPH, acting as cofactor for glutathione reductase. In addition to GSH homeostasis, maintenance of the reduced THF pool requires constant DHFR dependent NADPH consumption (Fig. 1). Thus, OCM activity does not only provide NADPH but also requires NADPH for its own functionality. However, recent reports indicate that OCM contributes to NADPH homeostasis and oxidative stress management, suggesting a net production of NADPH [70-72].

The OCM can generate NADPH via the activity of dehydrogenase 1 family member L1 (ALDH1L1) (cytosolic) or ALDH1L2 (mitochondrial). Both enzymes use 10-formyl-THF and oxidize formate to CO_2 thereby generating one mole of NADPH. Consequently, ALDH1L1/2 dependent NADPH production comes at the expense of formate oxidation which otherwise could be used for nucleotide synthesis. However, during ROS stress, cells may likely undergo growth arrest and the cellular need for NADPH becomes more important than providing building blocks for nucleotide synthesis. Interestingly, it has been observed that ALDH1L1 is often epigenetically silenced in cancer cells, while ALDH1L2 is upregulated in some but not all cancers [73]. Most likely, downregulation of cytosolic ALDH1L1 provides an advantage to cancer cells by safeguarding one-carbon units required for nucleotide synthesis, while mitochondrial ALDH1L2 derived NADPH can help to control ETC derived ROS stress. ALDH1L2 can be upregulated in a dynamic manner during stress conditions [74] and depletion of ALDH1L2 increases

mitochondrial ROS, without affecting overall ROS levels [75]. In principle, mitochondrial 10-formyl-THF can have two fates: either the formyl moiety is fully oxidized to CO_2 via ALDH1L2 or it is hydrolysed via MTHFD1L and free formate is subsequently released into the cytoplasm (Fig.1). Both reactions release free THF, which can readily serve again as a co-factor for SHMT2. Dynamic regulation of ALDH1L2 can thus control NADPH production and cytosolic one-carbon unit availability. Interestingly, depletion of ALDH1L2 promotes mitochondrial formate production and enhances cell migration and breast cancer metastasis [75]. On the other hand, it was found that upregulation of ALDH1L2 is essential for disseminating melanoma cells to survive ROS stress along the metastatic cascade [76]. These different reports suggest that ALDH1L2 expression and ROS have context dependent roles, as ROS often acts as a double edged sword: too little ROS, but also too high steady-state ROS levels can negatively affect tumour progression and metastasis [77]. In sum, a balanced NADPH/$NADP^+$ ratio is essential for cellular homeostasis and supports cancer cell survival and persistence in a dynamic manner that can quickly adapt to changes within the TME. Likely, the interplay of OCM, NADPH homeostasis and ROS management is tumour type and context dependent making it hard to develop tailored therapies that target cellular redox homeostasis.

An important aspect of NADPH homeostasis is the strict compartmentalisation of NADPH pools. In contrast to NAD(H), NADP(H) cannot cross the inner mitochondrial membrane resulting in separation of cytosolic and mitochondrial pools that are independently regulated [78]. There is evidence that folate mediated OCM has particular importance in maintaining mitochondrial redox balance. For example, endoplasmic reticulum (ER) stress results in a strong upregulation of mitochondrial one-carbon cycle genes including enhanced ALDH1L2 expression [74]. Under standard cell culture conditions and in most tissues, serine catabolism results in secretion of glycine and formate [42]. Interestingly, we observed that ER stress results in a switch from glycine release to glycine consumption, despite a concomitant increase in serine consumption and serine *de novo* synthesis [74]. Apparently, ER stress represents a distinct metabolic state where serine derived glycine production cannot satisfy the cellular glycine demand and therefore cells need to consume additional glycine from the extracellular space [74]. In an independent study, it was found that loss of mitochondrial fumarate hydratase results in metabolic stress and an

increased glycine uptake occurred as a consequence of the integrated stress response and ATF4 activation [79]. In summary, this glycine switch represents another excellent example of OCM's plasticity to cope with current cellular needs.

Catabolic functions and Formate Overflow

Following the catabolic concept, serine catabolism with glycine and formate release leads to zero carbon gain but generation of NADH and ATP [2]. Thus, the selective advantage of this process is not towards the generation of biomass but to provide co-factors and energy to the cell. Interestingly, we have observed that energy limitation can increase the rate of serine catabolism and formate overflow [42, 80]. Furthermore, we have identified that increasing extracellular formate concentrations promote the invasiveness and the rate of metastasis in different cancer models [25, 81-83]. Silencing of MTHFD1L prevents formate release without reducing proliferation rates but reduces metastasis in murine models of breast cancer [25, 83]. Using different genetically engineered mouse models and orthotopic implantation models, we and others have demonstrated that the rate of serine catabolism to formate is increased in cancer cells, leading to strong accumulation of formate within the TME compared to plasma [75, 81, 82]. Moreover, mitochondrial formate production and thus, formate overflow depends on active mitochondrial respiration and ETC function [25, 42] and is affected by external factors such as hypoxia or inflammation but also by the intracellular NADH/NAD^+ balance [84]. NADH acts as an essential redox cofactor transferring the electrons from the TCA cycle to the ETC. However, the TCA cycle is not the only source of NADH, the mitochondrial OCM enzyme MTHFD2 also reduces NAD^+ during 5,10-methylene-THF oxidation and feeds the ETC [85]. Hence, direct inhibition of the ETC inhibits both TCA cycle activity and formate overflow [25, 42, 81]. Similarly, mitochondrial formate production is also altered under low oxygen conditions, suggesting that hypoxic tumour regions are formate overflow negative [81].

While the cytosolic part of OCM can compensate for loss of mitochondrial OCM activity to sustain nucleotide synthesis and thus, proliferation [14], it cannot compensate for formate overflow because the MTHFD1 formyl THF synthetase (FS) reaction is irreversible (Fig.1). Based on the data indicating that serine and oxygen are required for formate overflow, one can speculate that only specific regions within a tumour are formate overflow positive (i.e. the outer vascularised regions) while other parts, such as the inner hypoxic and nutrient scarce regions, are formate overflow negative. Given

the implication of formate in cancer cell invasion, current working models propose that in regions with increased formate concentrations, tumour cells become more invasive and more prone to escape from the primary tumour to form metastases at distant sites. Since chemotherapies such as antifolate treatments increase formate release rates [25, 26], it is suggested that this metabolic alteration may promote cancer cell escape and onset of metastasis. Following the plasticity concept, the high mitochondrial one-carbon flux can quickly be redirected through ALDH1L2 in times of increased oxidative stress to survive stressful conditions during the dissemination process, while at secondary sites, when anabolic programs need to be prioritized to support metastatic outgrowth, generated one-carbon units may primarily fuel nucleotide synthesis.

7 Formate as Stress Signal

As the smallest carboxylic acid, formate was formed as one of the first metabolites on earth and is evolutionary conserved as an essential one-carbon molecule in all living systems [86, 87]. As illustrated so far, the function of formate goes far beyond serving as a building block for anabolic processes. At first glance, the excessive release of formate by cancer cells appears like a carbon wasting phenotype (similar to the Warburg effect) but we speculate that it can serve as a signalling molecule, promoting invasiveness by a yet undescribed mechanism. One potential mechanism could be the increased formation of formylated peptides such as formyl-methionine (fMET), which can act in an autocrine manner on formyl peptide receptors to increase invasion via activation of a MAPK pathway [75].

Another interesting observation is that the rate of formate overflow is often increased during cellular stress conditions, giving further rational on speculating that formate may act as a mitochondrial derived stress signal. This has been shown in cell culture conditions where glucose is replaced by galactose, mimicking a nutrient depleted environment. The switch from glucose to galactose was shown to cause metabolic stress and reduce proliferation rates, whereas it promotes mitochondrial metabolism and formate overflow [80]. Interestingly, even though formate excretion was increased, serine consumption remained constant. Meaning that under energy stress cells would continue to catabolize serine, but instead of incorporating the carbons into purines they rather release them as free formate [42, 80]. Another form of metabolic stress is caused

by treatment with the antifolate Methotrexate, putting the cells into proliferation arrest and ablating the cytosolic OCM activity but sustaining serine catabolism via the mitochondrial OCM, which results in formate overflow [25, 81]. Both examples clearly demonstrate that cellular stress leading to growth arrest can trigger mitochondrial formate release. The existence of mitochondria-derived metabolic signals is not novel and represents an evolutionary conserved mechanism [88]. Following these lines, formate may be an under-appreciated member of such metabolic signalling molecules. Given its conserved nature across the kingdom of life, it may have broad implications in health and disease that need to be further explored.

8 OCM in the Tumour Microenvironment

The tumour microenvironment (TME) is a complex system composed of diverse cell types, including cancer, immune and stromal cells. Furthermore, the chemical composition of interstitial space is often very distinct (tumour specific) and different from the surrounding tissue of origin [89, 90]. For instance, intra-tumoural formate concentrations can be up to 20 times higher compared to circulating plasma levels [75, 82]. A constant crosstalk among the different components of the TME dictates tumour growth and dissemination. In particular, the immune response and angiogenesis have a high influence on tumour development and progression. The TME is commonly acidic, hypoxic and/or nutrient depleted, requiring a high degree of metabolic flexibility and plasticity of cancer cells to be able to survive, proliferate and disseminate [91]. Importantly, different and distinct metabolic niches exist within the same tumour as oxygen and nutrient distribution across the tumour tissue is not uniform. As elaborated in previous paragraphs, the OCM confers metabolic flexibility and plasticity to cells within the TME and OCM-derived metabolites are shaping metabolic niches. Furthermore, different cell types within the TME compete for the same nutrients and influence each other by releasing different metabolites and cytokines into the extracellular space.

Immune Cells

Immune cells are a critical component of the TME, their interaction with cancer cells is a highly dynamic process, which can either suppress or promote tumour growth. Immune cells are categorized into two major populations, the innate and the adaptive

immune cells. Macrophages, neutrophils and dendritic cells belong to the innate subclass whereas T cells, B cells and natural killer T cells (NK-T) are mediators of the adaptive immune response [92]. Here we will highlight the relevance of the OCM mainly in T cells and in macrophages.

T-Cells - T lymphocytes are defined by the surface expression of their T cell receptor (TCR) which is specific to one antigen. T cells that express CD8 are cytotoxic T cells that detect tumour antigens and get primed to eliminate the cancer cells. CD4 expressing T cells can differentiate into either pro-inflammatory helper T cells (Th cells) that secrete cytokines to guide the immune response or regulatory T cells (Tregs) that dampen the antitumour immune response [93].

The OCM has been identified as the most induced mitochondrial pathway upon T cell activation [90]. Mitochondrial SHMT2 is crucial for T cell expansion, providing the building blocks for nucleotides and ROS defence. SHMT2 downregulation in T cells causes nucleotide imbalance and DNA damage, which could not be rescued by purine salvage or through cytosolic one-carbon cycle flux. Also, formate alone did not rescue SHMT2 deficient T cell proliferation, but only did so in combination with antioxidants, such as NAC [94], highlighting the plasticity of the OCM. Interestingly, inhibition of SHMT1/2 only impaired T cell proliferation but had no effect on the expression of activation markers (CD25 and CD44) nor the production of cytokines in CD4+ and CD8+ T cells [95]. In contrast, MTHFD2 deficiency promoted Treg differentiation by inducing the expression of FOXP3, which could be rescued by formate supplementation [96]. One explanation could be that the expression of OCM enzymes differs throughout the stages of T cell development.

T cells are also armed with a range of immunological safety controls such as surface expression of programmed death-1 (PD-1) or cytotoxic T-lymphocyte antigen-4 (CTLA-4), known as “immune checkpoints”. Checkpoint inhibitors are used as immunotherapy for numerous cancer types, they allow a more efficient recognition between T cells and cancer cells. Formate supplementation improved anti-PD-1 therapy and increased tumour infiltrating CD8+ T cells [97]. Moreover, the response of T cells to checkpoint blockade can be hindered by insufficient incorporation of circulating one-carbon units [98], which is the case in serine depleted tumours. In MC38, colorectal tumours, safe doses of methanol were used as formate prodrug to raise circulating formate

concentrations and provide one-carbon units to T cells. In the absence of PD-1 checkpoint inhibition, methanol had no impact on tumour growth while in combination with anti-PD-1, methanol augmented tumour suppression and synergized with checkpoint blockade [98]. This suggests that pharmacological one-carbon supplementation could improve the clinical outcome of immune checkpoint blockade in cancers. (Fig.5).

At first sight, the observations that formate enhances immune cell function appears in contrast to earlier observations that clearly revealed formate enrichment as a hallmark of oxidative tumours. A possible explanation may come from the fact that TMEs can be very diverse. Poorly vascularized tumour regions lead to nutrient and oxygen depletion, including a scarcity of one-carbon units. Consequently, the effectiveness of formate supplementation to improve immune checkpoint therapy depends on the formate status of the tumour itself: when formate is depleted, supplementation can help to improve T cell function, however in tumours that are formate overflow positive, the additive effects on immune cells might be minor. Additionally, potential adverse effects related to relapse and metastasis have not been investigated so far. In conclusion, the metabolic landscape including formate concentrations are tumour specific and require in-depth understanding to design appropriate therapies.

Macrophages - Macrophages are tissue resident phagocytic cells, which originate from circulating monocytes and can be polarized towards inflammatory M1 macrophages and immunosuppressive M2 macrophages. Up to 50 percent of the tumour mass can be composed of tumour associated macrophages (TAMs) with the M2 phenotype being predominant and often associated with a poor disease outcome, as they dampen the antitumour immune response and support the formation of new blood vessels [92, 99]. Macrophages are terminally differentiated and do not have the same biosynthetic needs as proliferative cancer cells or T cells [100]. For instance, nucleotide *de novo* synthesis runs at very low rates in activated macrophages. Instead, nitric oxide (NO), an important effector molecule in stimulated macrophages, diverts the flux to purine nucleotide salvaging. Additional supplementation with THF and formate was not able to restore nucleotide *de novo* synthesis [101]. Whereas T cells rely on nucleotide biosynthesis mainly for proliferation, this is different for macrophages (Fig.5). In non-proliferative immune cells, nucleotide metabolism, especially the uptake and release of purines, has a significant impact on autocrine and paracrine signalling

during the immune response [102]. Macrophages also rely on one-carbon flux for SAM generation upon inflammation. A high SAM/SAH ratio is essential to maintain key histone methylation marks during LPS-induced inflammation that transcriptionally activate the production of pro-inflammatory cytokines such as IL-1β [103]. Furthermore, the OCM plays an essential role during the inflammatory response by supporting cytokine synthesis (Fig.5). LPS induced inflammation commonly increases ROS levels in macrophages, consequently GSH is needed to control oxidative stress. Serine flux through the folate OCM is enhanced upon inflammatory stimuli and LPS-driven ROS increased the incorporation of serine-derived carbons into GSH. Serine starvation led to a decrease in LPS-induced IL-1β production, which could not be rescued by formate, suggesting that this phenotype is not related to the production of one-carbon units but rather to glycine, which is incorporated into GSH [104]. However, formate was identified as an important signalling molecule to regulate macrophage polarization. Transcriptional activation of MTHFD1L is favoured in M2 macrophages, causing accumulation of intracellular formate. Depletion of MTHFD1L promoted the LPS/IFN-γ-induced M1 phenotype and the secretion of numerous pro-inflammatory cytokines, which could be rescued by formate supplementation. Interestingly, formate stimulation alone significantly inhibited the expression of M1-related genes, highlighting a potential role of formate as anti-inflammatory molecule in the TME [105].

Taken together the plasticity of the OCM is a key feature to support immune cell function and contributes to the shaping of the TME. Targeting the OCM offers promising strategies for cancer therapy, particularly in combination with immunotherapy.

9 Conclusion

In summary, this chapter highlights the plasticity of OCM and how it is exploited by different cells within the TME. The outputs of the OCM can be tailored according to the cellular needs, along the various stages of tumour development and progression. Targeting OCM for cancer therapy remains highly attractive, but the context dependency of the different functions of OCM intermediates makes it important to design the right intervention at a specific stage of the disease and for the right tumour. Conclusively, by increasing our in-depth knowledge on these aspects, there is a lot of

potential for the development of more targeted and more effective anticancer strategies as an alternative to classical antifolates.

Competing interest:

The authors declare no competing interests.

Acknowledgements:

Co-funded by the European Union (ERC, 4M8, Project Number: 101124557) (J.M.). Views and opinions expressed are however those of the authors only and do not necessarily reflect those of the European Union or the European Research Council. Neither the European Union nor the granting authority can be held responsible for them. Additional funding through FNR-CORE (C21/BM/15718879) (J.M.) and FNR-PRIDE i2Tron (PRIDE19/14254520) (K.E.).

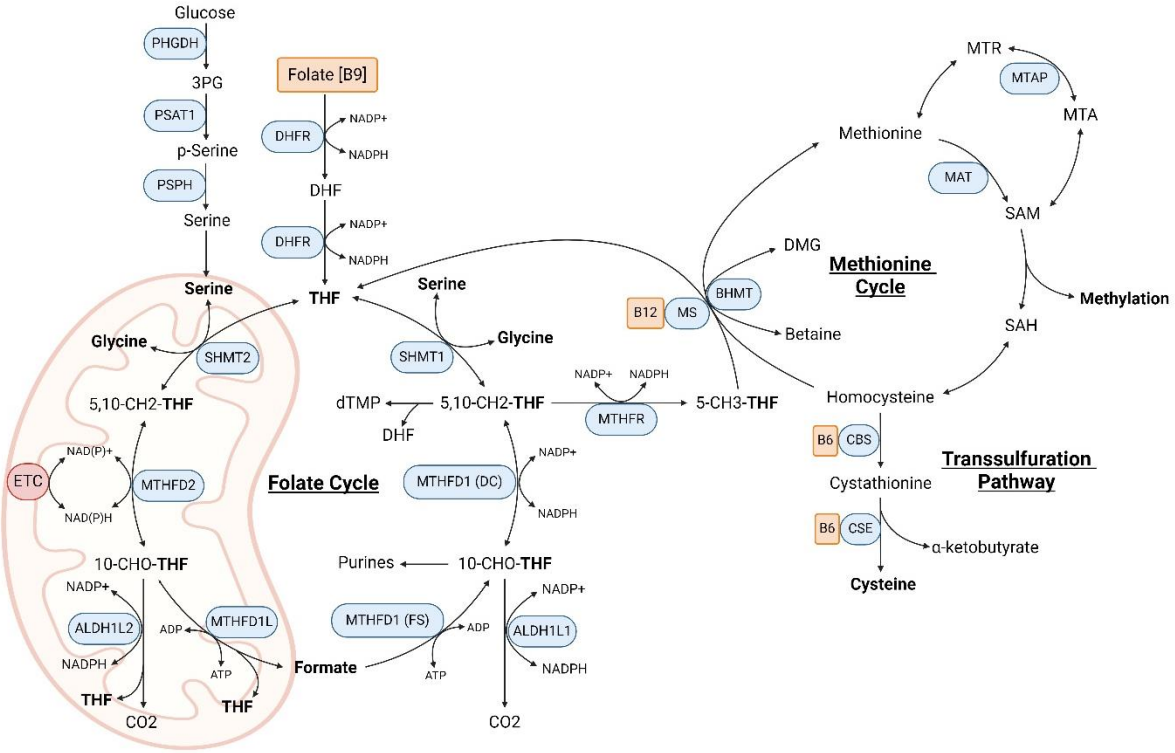

Figure 1: Overview of the folate cycle, the methionine cycle and the transsulfuration pathway

Interconnection between the folate cycle, the methionine cycle and the transsulfuration pathway. Serine is the major one-carbon donor and can be taken up from the extracellular space or synthesized from glucose by the enzymes phosphoglycerate dehydrogenase (PHGDH), phosphoserine aminotransferase 1 (PSAT1) and phosphoserine phosphatase (PSPH). Tetrahydrofolate (THF) acts as a cofactor for the transfer of one-carbon units within the folate cycle and is derived from dietary folate (vitamin B9) via dihydrofolate reductase (DHFR). The carbons are shuffled through various biochemical reactions, catalysed by different OCM enzymes. Methionine synthase (MS) creates the link between the folate and the methionine cycle by remethylation of homocysteine to methionine using methyl-groups from 5-CH_3-THF. The OCM also involves the B-vitamins cobalamin (vitamin B12) and pyridoxine (vitamin B6) in the methionine cycle and the transsulfuration pathway, respectively.

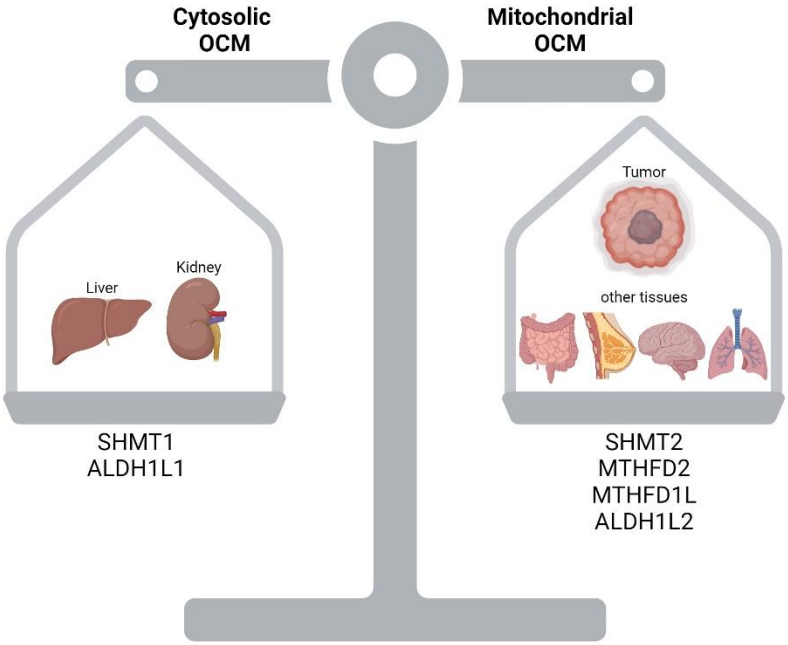

Figure 2: Tissue-specific OCM activity

Tissue-specific expression of OCM enzymes. Cytosolic serine hydroxymethyltransferase 1 (SHMT1) and aldehyde dehydrogenase 1 family member L1 (ALDH1L1) show increased expression in liver and kidney. In contrast, mitochondrial serine hydroxymethyltransferase 2 (SHMT2), methylenetetrahydrofolate dehydrogenase/cyclohydrolase 2 (MTHFD2), methylenetetrahydrofolate dehydrogenase 1-like (MTHFD1L) and aldehyde dehydrogenase 1 family member L2 (ALDH1L2) are highly expressed in various tumours. Additionally, other healthy organs show a higher mitochondrial OCM cycle activity, which overall is still lower compared to tumour tissue due to the reduced biosynthetic needs of differentiated, non-proliferative tissues.

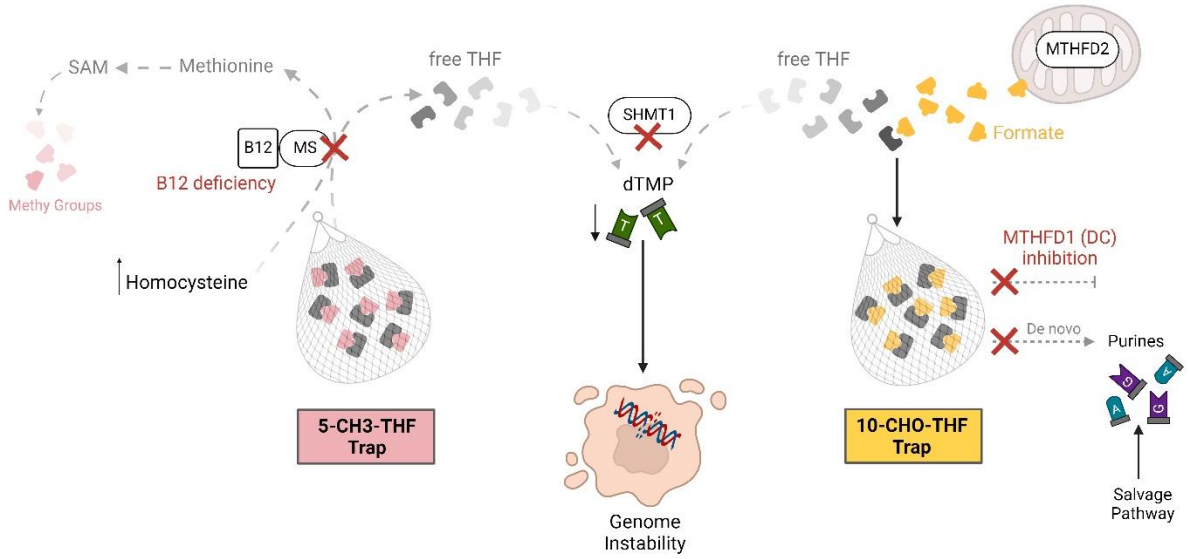

Figure 3: The folate traps

Both, the 5-methyl-THF (5-CH_3-THF) and the 10-formyl-THF (10-CHO-THF) trap lead to a reduction of the free folate pool, which negatively affects the folate mediated OCM and the activity of serine hydroxymethyltransferase 1 (SHMT1) for the generation of thymidylate (dTMP). 5-CH_3-THF gets trapped as a consequence of vitamin B12 deficiency whereas 10-CHO-THF trapping occurs due to inhibition of the dehydrogenase/cyclohydrolase (DC) function of methylenetetrahydrofolate dehydrogenase 1 (MTHFD1) in combination with enhanced purine salvage activity. In both cases, dTMP deficiency results in genome instability and cell death due to thymidine depletion.

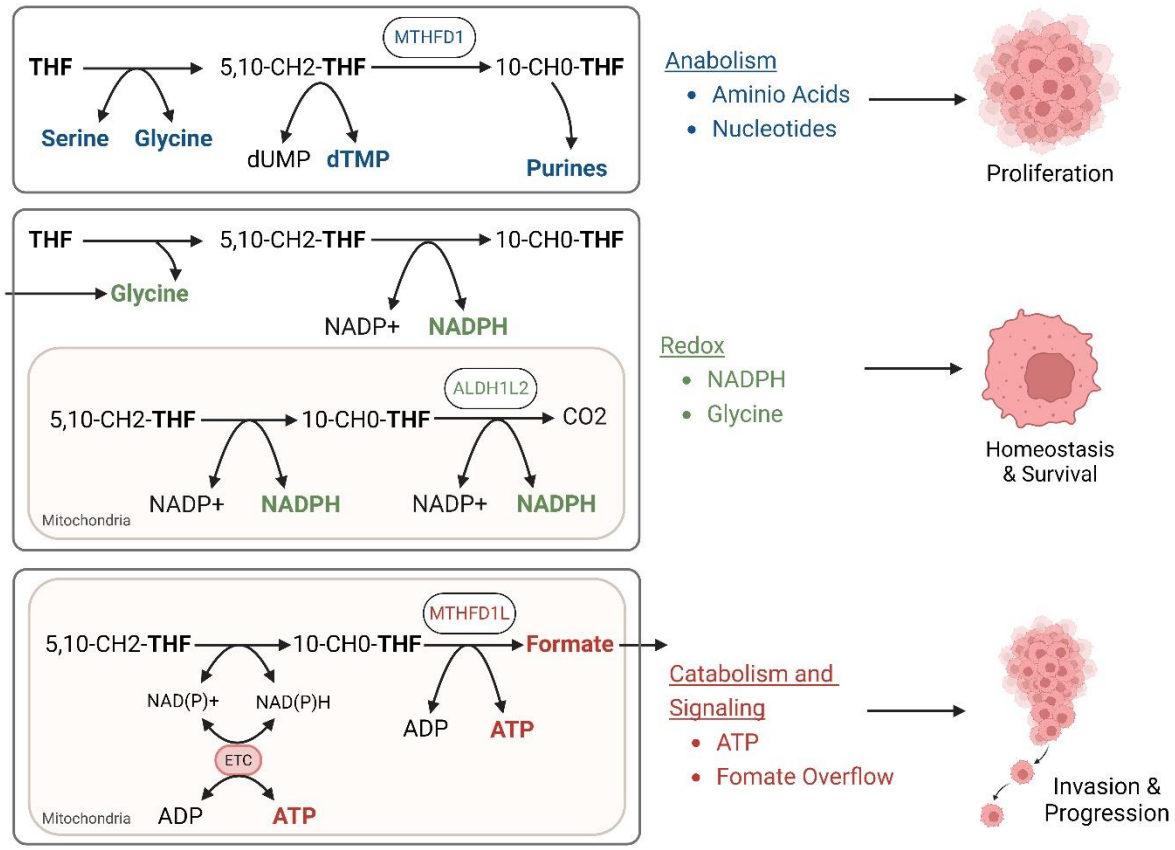

Figure 4: OCM plasticity in cancer cells

The OCM covers the three major metabolic pillars namely anabolism, redox homeostasis and catabolism, which are essential for cancer cell proliferation, homeostasis and progression, respectively. See details in text.

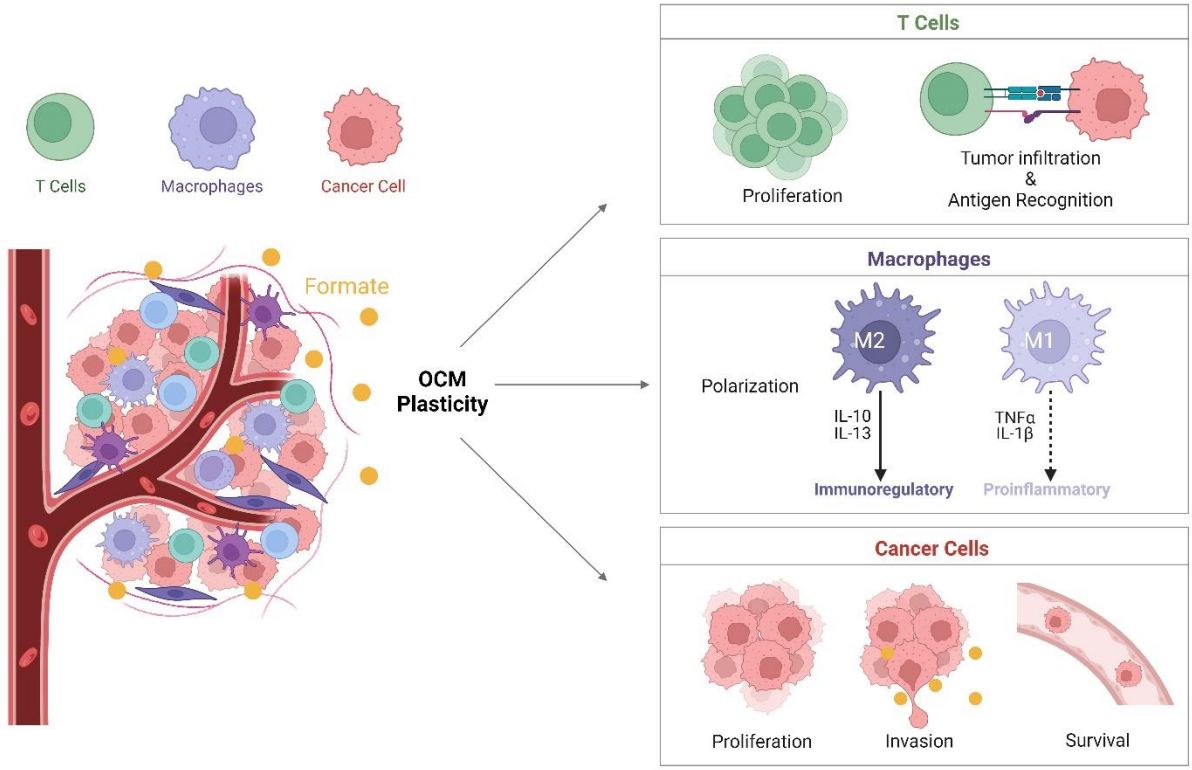

Figure 5: OCM in the tumour microenvironment

The OCM and formate play an essential role within the tumour microenvironment (TME) and cover the biological needs of not only cancer but also immune cells. T cells and cancer cells are highly proliferative, hence they rely on the anabolic function of OCM. The OCM also supports tumour infiltration of T cells and increases the therapeutic impact of immune checkpoint blockade. In addition, differentiated macrophages rely on the OCM for cytokine release during their activation and polarization phase. Furthermore, excessive formate concentrations can prime cancer cells and drive the onset of metastasis. In conclusion, a context-dependent understanding of OCM is crucial to direct the right intervention at the right time of the disease.

References

1. Locasale, J.W., *Serine, glycine and one-carbon units: cancer metabolism in full circle.* Nat Rev Cancer, 2013. **13**(8): p. 572-83.
2. Benzarti, M., et al., *Metabolic Potential of Cancer Cells in Context of the Metastatic Cascade.* Cells, 2020. **9**(9).
3. Nilsson, R., et al., *Metabolic enzyme expression highlights a key role for MTHFD2 and the mitochondrial folate pathway in cancer.* Nat Commun, 2014. **5**: p. 3128.
4. Li, A.M., et al., *Metabolic Profiling Reveals a Dependency of Human Metastatic Breast Cancer on Mitochondrial Serine and One-Carbon Unit Metabolism.* Mol Cancer Res, 2020. **18**(4): p. 599-611.
5. Liu, C., et al., *Cytoplasmic SHMT2 drives the progression and metastasis of colorectal cancer by inhibiting β-catenin degradation.* Theranostics, 2021. **11**(6): p. 2966-2986.
6. Smithells, R.W., S. Sheppard, and C.J. Schorah, *Vitamin deficiencies and neural tube defects.* Arch Dis Child, 1976. **51**(12): p. 944-50.
7. Lee, Y., K.H. Vousden, and M. Hennequart, *Cycling back to folate metabolism in cancer.* Nat Cancer, 2024. **5**(5): p. 701-715.
8. Tibbetts, A.S. and D.R. Appling, *Compartmentalization of Mammalian folate-mediated one-carbon metabolism.* Annu Rev Nutr, 2010. **30**: p. 57-81.
9. Palmer, A.M., et al., *Folate rescues vitamin B(12) depletion-induced inhibition of nuclear thymidylate biosynthesis and genome instability.* Proc Natl Acad Sci U S A, 2017. **114**(20): p. E4095-e4102.
10. Cantoni, G.L., *THE NATURE OF THE ACTIVE METHYL DONOR FORMED ENZYMATICALLY FROM L-METHIONINE AND ADENOSINETRIPHOSPHATE1,2.* Journal of the American Chemical Society, 1952. **74**(11): p. 2942-2943.
11. Sanderson, S.M., et al., *Methionine metabolism in health and cancer: a nexus of diet and precision medicine.* Nat Rev Cancer, 2019. **19**(11): p. 625-637.
12. Glaudemans, A.W., et al., *Value of 11C-methionine PET in imaging brain tumours and metastases.* Eur J Nucl Med Mol Imaging, 2013. **40**(4): p. 615-35.
13. Lückerath, K., et al., *11C-Methionine-PET: a novel and sensitive tool for monitoring of early response to treatment in multiple myeloma.* Oncotarget, 2015. **6**(10): p. 8418-29.
14. Ducker, G.S. and J.D. Rabinowitz, *One-Carbon Metabolism in Health and Disease.* Cell Metab, 2017. **25**(1): p. 27-42.
15. Eriksson, S., et al., *Dietary methionine can sustain cytosolic redox homeostasis in the mouse liver.* Nat Commun, 2015. **6**: p. 6479.
16. Gomes, A.P., et al., *Altered propionate metabolism contributes to tumour progression and aggressiveness.* Nat Metab, 2022. **4**(4): p. 435-443.
17. Gomes, A.P., et al., *Age-induced accumulation of methylmalonic acid promotes tumour progression.* Nature, 2020. **585**(7824): p. 283-287.
18. Kabil, O., et al., *The quantitative significance of the transsulfuration enzymes for H2S production in murine tissues.* Antioxid Redox Signal, 2011. **15**(2): p. 363-72.
19. Kikuchi, G., *The glycine cleavage system: composition, reaction mechanism, and physiological significance.* Mol Cell Biochem, 1973. **1**(2): p. 169-87.
20. Pietzke, M., J. Meiser, and A. Vazquez, *Formate metabolism in health and disease.* Mol Metab, 2020. **33**: p. 23-37.
21. Newman, A.C., et al., *Immune-regulated IDO1-dependent tryptophan metabolism is source of one-carbon units for pancreatic cancer and stellate cells.* Mol Cell, 2021. **81**(11): p. 2290-2302.e7.
22. Field, M.S., et al., *Nuclear enrichment of folate cofactors and methylenetetrahydrofolate dehydrogenase 1 (MTHFD1) protect de novo thymidylate biosynthesis during folate deficiency.* J Biol Chem, 2014. **289**(43): p. 29642-50.
23. Field, M.S., et al., *Nuclear Folate Metabolism.* Annu Rev Nutr, 2018. **38**: p. 219-243.

24. Ducker, G.S., et al., *Reversal of Cytosolic One-Carbon Flux Compensates for Loss of the Mitochondrial Folate Pathway.* Cell Metab, 2016. **23**(6): p. 1140-1153.
25. Kiweler, N., et al., *Mitochondria preserve an autarkic one-carbon cycle to confer growth-independent cancer cell migration and metastasis.* Nat Commun, 2022. **13**(1): p. 2699.
26. Soflaee, M.H., et al., *Purine nucleotide depletion prompts cell migration by stimulating the serine synthesis pathway.* Nat Commun, 2022. **13**(1): p. 2698.
27. Lee, W.D., et al., *Tumor Reliance on Cytosolic versus Mitochondrial One-Carbon Flux Depends on Folate Availability.* Cell Metab, 2021. **33**(1): p. 190-198.e6.
28. Girgis, S., et al., *Molecular cloning, characterization and alternative splicing of the human cytoplasmic serine hydroxymethyltransferase gene.* Gene, 1998. **210**(2): p. 315-24.
29. Wei, J., et al., *Identification of AGXT2, SHMT1, and ACO2 as important biomarkers of acute kidney injury by WGCNA.* PLoS One, 2023. **18**(2): p. e0281439.
30. Shin, M., et al., *Mitochondrial MTHFD2L is a dual redox cofactor-specific methylenetetrahydrofolate dehydrogenase/methenyltetrahydrofolate cyclohydrolase expressed in both adult and embryonic tissues.* J Biol Chem, 2014. **289**(22): p. 15507-17.
31. Handzlik, M.K., et al., *Insulin-regulated serine and lipid metabolism drive peripheral neuropathy.* Nature, 2023. **614**(7946): p. 118-124.
32. McBride, M.J., C.J. Hunter, and J.D. Rabinowitz, *Glycine homeostasis requires reverse SHMT flux.* bioRxiv, 2023.
33. Pietrzik, K., L. Bailey, and B. Shane, *Folic acid and L-5-methyltetrahydrofolate: comparison of clinical pharmacokinetics and pharmacodynamics.* Clin Pharmacokinet, 2010. **49**(8): p. 535-48.
34. Kobayashi, H., Y. Takemura, and T. Ohnuma, *Variable expression of RFC1 in human leukemia cell lines resistant to antifolates.* Cancer Lett, 1998. **124**(2): p. 135-42.
35. O'Connor, C., et al., *Folate transporter dynamics and therapy with classic and tumor-targeted antifolates.* Sci Rep, 2021. **11**(1): p. 6389.
36. Alvarez-Fernandez, C., et al., *Reduced folate carrier (RFC) as a predictive marker for response to pemetrexed in advanced non-small cell lung cancer (NSCLC).* Invest New Drugs, 2014. **32**(2): p. 377-81.
37. Ifergan, I., et al., *Reduced folate carrier protein expression in osteosarcoma: implications for the prediction of tumor chemosensitivity.* Cancer, 2003. **98**(9): p. 1958-66.
38. Burgos-Barragan, G., et al., *Mammals divert endogenous genotoxic formaldehyde into one-carbon metabolism.* Nature, 2017. **548**(7669): p. 549-554.
39. Cook, R.J. and J.A. Blair, *The distribution and chemical nature of radioactive folates in rat liver cells and rat liver mitochondria.* Biochem J, 1979. **178**(3): p. 651-9.
40. Lawrence, S.A., et al., *Mammalian mitochondrial and cytosolic folylpolyglutamate synthetase maintain the subcellular compartmentalization of folates.* J Biol Chem, 2014. **289**(42): p. 29386-96.
41. Zheng, Y., et al., *Mitochondrial One-Carbon Pathway Supports Cytosolic Folate Integrity in Cancer Cells.* Cell, 2018. **175**(6): p. 1546-1560.e17.
42. Meiser, J., et al., *Serine one-carbon catabolism with formate overflow.* Sci Adv, 2016. **2**(10): p. e1601273.
43. Scott, J.M. and D.G. Weir, *The methyl folate trap. A physiological response in man to prevent methyl group deficiency in kwashiorkor (methionine deficiency) and an explanation for folic-acid induced exacerbation of subacute combined degeneration in pernicious anaemia.* Lancet, 1981. **2**(8242): p. 337-40.
44. Scott, J. and D. Weir, *Folate/vitamin B12 inter-relationships.* Essays Biochem, 1994. **28**: p. 63-72.
45. Green, A.C., et al., *Formate overflow drives toxic folate trapping in MTHFD1 inhibited cancer cells.* Nat Metab, 2023. **5**(4): p. 642-659.
46. Rosario, F.J., T.L. Powell, and T. Jansson, *mTOR folate sensing links folate availability to trophoblast cell function.* J Physiol, 2017. **595**(13): p. 4189-4206.

47. Ben-Sahra, I., et al., *mTORC1 induces purine synthesis through control of the mitochondrial tetrahydrofolate cycle.* Science, 2016. **351**(6274): p. 728-733.
48. Adams, C.M., *Role of the transcription factor ATF4 in the anabolic actions of insulin and the anti-anabolic actions of glucocorticoids.* J Biol Chem, 2007. **282**(23): p. 16744-53.
49. Białopiotrowicz, E., et al., *Serine Biosynthesis Pathway Supports MYC-miR-494-EZH2 Feed-Forward Circuit Necessary to Maintain Metabolic and Epigenetic Reprogramming of Burkitt Lymphoma Cells.* Cancers (Basel), 2020. **12**(3).
50. DeNicola, G.M., et al., *NRF2 regulates serine biosynthesis in non-small cell lung cancer.* Nat Genet, 2015. **47**(12): p. 1475-81.
51. Nikiforov, M.A., et al., *A functional screen for Myc-responsive genes reveals serine hydroxymethyltransferase, a major source of the one-carbon unit for cell metabolism.* Mol Cell Biol, 2002. **22**(16): p. 5793-800.
52. Moran, D.M., et al., *KRAS mutation status is associated with enhanced dependency on folate metabolism pathways in non-small cell lung cancer cells.* Mol Cancer Ther, 2014. **13**(6): p. 1611-24.
53. Li, G., et al., *p53 deficiency induces MTHFD2 transcription to promote cell proliferation and restrain DNA damage.* Proc Natl Acad Sci U S A, 2021. **118**(28).
54. Kuong, K.J. and A. Kuzminov, *Stalled replication fork repair and misrepair during thymineless death in Escherichia coli.* Genes Cells, 2010. **15**(6): p. 619-34.
55. Wu, Z., et al., *Electron transport chain inhibition increases cellular dependence on purine transport and salvage.* Cell Metab, 2024. **36**(7): p. 1504-1520.e9.
56. Tran, D.H., et al., *De novo and salvage purine synthesis pathways across tissues and tumors.* Cell, 2024. **187**(14): p. 3602-3618.e20.
57. Reina-Campos, M., M.T. Diaz-Meco, and J. Moscat, *The complexity of the serine glycine one-carbon pathway in cancer.* J Cell Biol, 2020. **219**(1).
58. Farber, S. and L.K. Diamond, *Temporary remissions in acute leukemia in children produced by folic acid antagonist, 4-aminopteroyl-glutamic acid.* N Engl J Med, 1948. **238**(23): p. 787-93.
59. Li, M.C., R. Hertz, and D.M. Bergenstal, *Therapy of choriocarcinoma and related trophoblastic tumors with folic acid and purine antagonists.* N Engl J Med, 1958. **259**(2): p. 66-74.
60. Schweitzer, B.I., A.P. Dicker, and J.R. Bertino, *Dihydrofolate reductase as a therapeutic target.* Faseb j, 1990. **4**(8): p. 2441-52.
61. Wood, G.S. and J. Wu, *Methotrexate and Pralatrexate.* Dermatol Clin, 2015. **33**(4): p. 747-55.
62. Locasale, J.W., et al., *Phosphoglycerate dehydrogenase diverts glycolytic flux and contributes to oncogenesis.* Nat Genet, 2011. **43**(9): p. 869-74.
63. Liu, F., et al., *Increased MTHFD2 expression is associated with poor prognosis in breast cancer.* Tumour Biol, 2014. **35**(9): p. 8685-90.
64. Gustafsson Sheppard, N., et al., *The folate-coupled enzyme MTHFD2 is a nuclear protein and promotes cell proliferation.* Sci Rep, 2015. **5**: p. 15029.
65. Ju, H.Q., et al., *Modulation of Redox Homeostasis by Inhibition of MTHFD2 in Colorectal Cancer: Mechanisms and Therapeutic Implications.* J Natl Cancer Inst, 2019. **111**(6): p. 584-596.
66. Wang, J., et al., *Identification of MTHFD2 as a novel prognosis biomarker in esophageal carcinoma patients based on transcriptomic data and methylation profiling.* Medicine (Baltimore), 2020. **99**(37): p. e22194.
67. Shi, Y., et al., *MTHFD2 promotes tumorigenesis and metastasis in lung adenocarcinoma by regulating AKT/GSK-3β/β-catenin signalling.* J Cell Mol Med, 2021. **25**(14): p. 7013-7027.
68. Zhao, R.Z., et al., *Mitochondrial electron transport chain, ROS generation and uncoupling (Review).* Int J Mol Med, 2019. **44**(1): p. 3-15.
69. Perillo, B., et al., *ROS in cancer therapy: the bright side of the moon.* Exp Mol Med, 2020. **52**(2): p. 192-203.
70. Lewis, C.A., et al., *Tracing compartmentalized NADPH metabolism in the cytosol and mitochondria of mammalian cells.* Mol Cell, 2014. **55**(2): p. 253-63.

71. Fan, J., et al., *Quantitative flux analysis reveals folate-dependent NADPH production.* Nature, 2014. **510**(7504): p. 298-302.
72. Ye, J., et al., *Serine catabolism regulates mitochondrial redox control during hypoxia.* Cancer Discov, 2014. **4**(12): p. 1406-17.
73. Krupenko, S.A. and N.I. Krupenko, *Loss of ALDH1L1 folate enzyme confers a selective metabolic advantage for tumor progression.* Chem Biol Interact, 2019. **302**: p. 149-155.
74. Becker, B., et al., *Serine metabolism is crucial for cGAS-STING signaling and viral defense control in the gut.* iScience, 2024. **27**(3): p. 109173.
75. Hennequart, M., et al., *ALDH1L2 regulation of formate, formyl-methionine, and ROS controls cancer cell migration and metastasis.* Cell Rep, 2023. **42**(6): p. 112562.
76. Piskounova, E., et al., *Oxidative stress inhibits distant metastasis by human melanoma cells.* Nature, 2015. **527**(7577): p. 186-91.
77. DeBerardinis, R.J. and N.S. Chandel, *Fundamentals of cancer metabolism.* Sci Adv, 2016. **2**(5): p. e1600200.
78. Niu, X., et al., *Cytosolic and mitochondrial NADPH fluxes are independently regulated.* Nat Chem Biol, 2023. **19**(7): p. 837-845.
79. Ryan, D.G., et al., *Disruption of the TCA cycle reveals an ATF4-dependent integration of redox and amino acid metabolism.* Elife, 2021. **10**.
80. Benzarti, M., et al., *PKM2 diverts glycolytic flux in dependence on mitochondrial one-carbon cycle.* Cell Rep, 2024. **43**(3): p. 113868.
81. Meiser, J., et al., *Increased formate overflow is a hallmark of oxidative cancer.* Nat Commun, 2018. **9**(1): p. 1368.
82. Ternes, D., et al., *The gut microbial metabolite formate exacerbates colorectal cancer progression.* Nat Metab, 2022. **4**(4): p. 458-475.
83. Delbrouck, C., et al., *Formate promotes invasion and metastasis in reliance on lipid metabolism.* Cell Rep, 2023. **42**(9): p. 113034.
84. Vercellino, I. and L.A. Sazanov, *The assembly, regulation and function of the mitochondrial respiratory chain.* Nat Rev Mol Cell Biol, 2022. **23**(2): p. 141-161.
85. Shin, M., J. Momb, and D.R. Appling, *Human mitochondrial MTHFD2 is a dual redox cofactor-specific methylenetetrahydrofolate dehydrogenase/methenyltetrahydrofolate cyclohydrolase.* Cancer Metab, 2017. **5**: p. 11.
86. Schwander, L., et al., *Serpentinization as the source of energy, electrons, organics, catalysts, nutrients and pH gradients for the origin of LUCA and life.* Front Microbiol, 2023. **14**: p. 1257597.
87. Drysdale, G.R., G.W. Plaut, and H.A. Lardy, *The relationship of folic acid to formate metabolism in the rat; formate incorporation into purines.* J Biol Chem, 1951. **193**(2): p. 533-8.
88. Picard, M. and O.S. Shirihai, *Mitochondrial signal transduction.* Cell Metab, 2022. **34**(11): p. 1620-1653.
89. Sullivan, M.R., et al., *Quantification of microenvironmental metabolites in murine cancers reveals determinants of tumor nutrient availability.* Elife, 2019. **8**.
90. Abbott, K.L., et al., *Metabolite profiling of human renal cell carcinoma reveals tissue-origin dominance in nutrient availability.* bioRxiv, 2024.
91. Bergers, G. and S.M. Fendt, *The metabolism of cancer cells during metastasis.* Nat Rev Cancer, 2021. **21**(3): p. 162-180.
92. Anderson, N.M. and M.C. Simon, *The tumor microenvironment.* Curr Biol, 2020. **30**(16): p. R921-r925.
93. He, X. and C. Xu, *Immune checkpoint signaling and cancer immunotherapy.* Cell Res, 2020. **30**(8): p. 660-669.
94. Ron-Harel, N., et al., *Mitochondrial Biogenesis and Proteome Remodeling Promote One-Carbon Metabolism for T Cell Activation.* Cell Metab, 2016. **24**(1): p. 104-17.

95. Ma, E.H., et al., *Serine Is an Essential Metabolite for Effector T Cell Expansion.* Cell Metab, 2017. **25**(2): p. 345-357.
96. Sugiura, A., et al., *MTHFD2 is a metabolic checkpoint controlling effector and regulatory T cell fate and function.* Immunity, 2022. **55**(1): p. 65-81.e9.
97. Rowe, J.H., et al., *Formate Supplementation Enhances Antitumor CD8+ T-cell Fitness and Efficacy of PD-1 Blockade.* Cancer Discov, 2023. **13**(12): p. 2566-2583.
98. Xu, X., et al., *One-carbon unit supplementation fuels purine synthesis in tumor-infiltrating T cells and augments checkpoint blockade.* Cell Chem Biol, 2024. **31**(5): p. 932-943.e8.
99. Vinogradov, S., G. Warren, and X. Wei, *Macrophages associated with tumors as potential targets and therapeutic intermediates.* Nanomedicine (Lond), 2014. **9**(5): p. 695-707.
100. Davies, L.C. and P.R. Taylor, *Tissue-resident macrophages: then and now.* Immunology, 2015. **144**(4): p. 541-8.
101. John, S.V., et al., *Macrophages undergo functionally significant reprograming of nucleotide metabolism upon classical activation.* bioRxiv, 2023.
102. Linden, J., F. Koch-Nolte, and G. Dahl, *Purine Release, Metabolism, and Signaling in the Inflammatory Response.* Annu Rev Immunol, 2019. **37**: p. 325-347.
103. Yu, W., et al., *One-Carbon Metabolism Supports S-Adenosylmethionine and Histone Methylation to Drive Inflammatory Macrophages.* Mol Cell, 2019. **75**(6): p. 1147-1160.e5.
104. Rodriguez, A.E., et al., *Serine Metabolism Supports Macrophage IL-1β Production.* Cell Metab, 2019. **29**(4): p. 1003-1011.e4.
105. Zhu, W., et al., *The SMYD3-MTHFD1L-formate metabolic regulatory axis mediates mitophagy to inhibit M1 polarization in macrophages.* Int Immunopharmacol, 2022. **113**(Pt A): p. 109352.

nature metabolism

Article

https://doi.org/10.1038/s42255-023-00771-5

Formate overflow drives toxic folate trapping in MTHFD1 inhibited cancer cells

Received: 12 August 2022

Accepted: 28 February 2023

Published online: 3 April 2023

Check for updates

Alanna C. Green[1,14], Petra Marttila[2,14], Nicole Kiweler[3,14], Christina Chalkiadaki[2], Elisée Wiita[2], Victoria Cookson[1], Antoine Lesur[3], Kim Eiden[3], François Bernardin[3], Karl S. A. Vallin[2,4], Sanjay Borhade[2,5], Maeve Long[2], Elahe Kamali Ghahe[6], Julio J. Jiménez-Alonso[2,7], Ann-Sofie Jemth[2], Olga Loseva[2], Oliver Mortusewicz[2], Marianne Meyers[8], Elodie Viry[9], Annika I. Johansson[10], Ondřej Hodek[11], Evert Homan[2], Nadilly Bonagas[2], Louise Ramos[1], Lars Sandberg[12], Morten Frödin[6], Etienne Moussay[9], Ana Slipicevic[2,13], Elisabeth Letellier[8], Jérôme Paggetti[9], Claus Storgaard Sørensen[6], Thomas Helleday[1,2,15] ✉, Martin Henriksson[2,15] ✉ & Johannes Meiser[3,15] ✉

Cancer cells fuel their increased need for nucleotide supply by upregulating one-carbon (1C) metabolism, including the enzymes methylenetetrahydrofolate dehydrogenase–cyclohydrolase 1 and 2 (MTHFD1 and MTHFD2). TH9619 is a potent inhibitor of dehydrogenase and cyclohydrolase activities in both MTHFD1 and MTHFD2, and selectively kills cancer cells. Here, we reveal that, in cells, TH9619 targets nuclear MTHFD2 but does not inhibit mitochondrial MTHFD2. Hence, overflow of formate from mitochondria continues in the presence of TH9619. TH9619 inhibits the activity of MTHFD1 occurring downstream of mitochondrial formate release, leading to the accumulation of 10-formyl-tetrahydrofolate, which we term a 'folate trap'. This results in thymidylate depletion and death of MTHFD2-expressing cancer cells. This previously uncharacterized folate trapping mechanism is exacerbated by physiological hypoxanthine levels that block the de novo purine synthesis pathway, and additionally prevent 10-formyl-tetrahydrofolate consumption for purine synthesis. The folate trapping mechanism described here for TH9619 differs from other MTHFD1/2 inhibitors and antifolates. Thus, our findings uncover an approach to attack cancer and reveal a regulatory mechanism in 1C metabolism.

One-carbon (1C) metabolism is central to the supply of nucleotides for DNA synthesis and repair. Without sufficient nucleotide supply to meet the proliferative demands, cells undergo cell cycle arrest or cell death due to replication stress and genomic instability[1–3]. Enzymes involved in the 1C metabolism pathway are commonly upregulated in cancer to produce nucleotides and amino acids required for rapid proliferation[4–6].

The 1C metabolism is predominantly fuelled by the non-essential amino acid serine, which can be generated from the glycolytic intermediate 3-phosphoglycerate or supplied from the extracellular space[7]. Catabolism of serine via folate-dependent 1C metabolism is required for nucleotide synthesis. It is mediated by four reversible enzymatic reactions that occur in the mitochondria and cytosol (Fig. 1a).

A full list of affiliations appears at the end of the paper. ✉e-mail: thomas.helleday@scilifelab.se; martin.henriksson@scilifelab.se; Johannes.Meiser@lih.lu

Serine hydroxymethyl transferase (SHMT) transfers a hydroxymethyl group from serine to tetrahydrofolate (THF) to generate 5,10-methylenetetrahydrofolate (CH_2-THF) and glycine. Methylenetetrahydrofolate dehydrogenase–cyclohydrolase (MTHFD) oxidizes and hydrolyses CH_2-THF to 10-formyl-tetrahydrofolate (10-CHO-THF), which is then hydrolysed to THF and formate by formyl THF synthetase. In the cytosol, these reactions are catalysed by SHMT1 and the tri-functional MTHFD1, which comprises two distinct domains, the dehydrogenase–cyclohydrolase (DC) domain and the formyl THF synthetase (FS) domain. In the mitochondrion, the same reactions are catalysed by SHMT2, bifunctional MTHFD2 (DC activity) and MTHFD1L (FS activity) (Fig. 1a)[8]. Although variations exist[9], the canonical directionality of the pathway follows serine catabolism and 1C unit oxidation via the mitochondrion, while cytosolic 1C units follow a reductive (reverse) route that is driven by a high cytosolic NADPH:$NADP^+$ ratio[8,10–12]. This way, the 1C metabolism forms a cycle that is spread between mitochondrion and cytoplasm. Due to the reversibility of the SHMT1 and MTHFD1 catalysed reactions, loss of mitochondrial 1C metabolism can be compensated via the cytosolic route[13].

Recently, the mitochondrial enzyme MTHFD2 has gained increasing attention, as it has been identified as one of the most highly upregulated genes in cancer[6,14,15]. A large body of validation work of MTHFD2 as an anticancer target has been ongoing in recent years, demonstrating that MTHFD2 RNA interference depletion or inhibition can kill cancer cells of diverse origin such as acute myeloid leukaemia (AML)[16,17], breast cancer[18] and colorectal cancer[19]. This work contrasts CRISPR–Cas9 knockout results demonstrating *MTHFD2*$^{-/-}$ cancer cell lines are mostly alive[20], and further research is required to understand these discrepancies.

We recently developed nanomolar, small-molecule MTHFD2 inhibitors (MTHFD2i). Owing to similar active sites in both enzymes, the inhibitors also target the DC domain of MTHFD1 (ref. 16). Here, we expand on our previous findings and revisit the mechanism of action of TH9619, and find that the compound does not enter mitochondria to target mitochondrial MTHFD2. Instead, we show that TH9619 targets MTHFD2-expressing cancer cells by inhibiting MTHFD1(DC). This phenomenon occurs because TH9619 requires MTHFD2 activity to cause thymidylate deficiency and cell toxicity. TH9619 inhibition of MTHFD1(DC) causes accumulation of the 1C intermediate 10-CHO-THF in MTHFD2-expressing cancer cells (a mechanism we term 'folate trapping'). The subsequent depletion of free cytosolic THF starves SHMT1 of its substrate and prevents downstream thymidylate synthesis. Moreover, we show that the purine-derivative hypoxanthine is a strong potentiator of this mechanism. Hypoxanthine contributes to folate trapping through exogenous supply of purines, providing feedback inhibition on de novo purine synthesis. Without consumption of 10-CHO-THF for de novo purine synthesis, folate trapping is potentiated and thymidylate synthesis is blocked. In addition to its toxicity in MTHFD2-expressing cancers, we also discover that TH9619 has a potent antitumorigenic effect on cancers deficient in mitochondrial 1C enzymes (MTHFD2 and MTHFD1L) by blocking purine synthesis. In summary, we detail the complex metabolic pathway that contributes to efficient cancer-specific killing with TH9619, a prerequisite to translate TH9619 into the clinic. In wider terms, the obtained knowledge vastly improves our understanding of how to effectively target 1C metabolism to induce cytotoxicity in cancer cells.

Results

TH9619/TH9975 target MTHFD1(DC) but not mitochondrial MTHFD2

In our recent study, we demonstrated that loss of MTHFD2 caused resistance to TH9619, validating MTHFD2 as a target of TH9619 (ref. 16). Yet, we showed that the effect of TH9619 is metabolically rescued by addition of thymidine, but not with hypoxanthine. This was surprising given that SHMT1 can support thymidylate synthesis independently of the MTHFD enzymes[13]. Thus, we wanted to further investigate whether TH9619 directly targets MTHFD2 and/or MTHFD1 with the aim to better understand the mode of action of MTHFD1/2i.

MTHFD2 and MTHFD1L normally produce formate in the mitochondria, which is then consumed by cytosolic 1C metabolism to produce thymidylate and purines (Fig. 1a)[13]. If TH9619 inhibits mitochondrial MTHFD2, this would block mitochondrial production of formate, and presumably exogenous addition of formate should overcome inhibitor activity. However, addition of 1 mM sodium formate did not rescue viability on TH9619 treatment, and had no additional effect when combined with thymidine, indicating formate depletion is not responsible for TH9619 toxicity (Fig. 1b). Similarly, formate did not rescue the effect of TH9975 (Fig. 1c), another MTHFD1/2i from the same series (Extended Data Fig. 1a,b). This contrasts with the previously described 1C metabolism inhibitors DS18561882 (ref. 18) (MTHFD1/2i, ref. 16) and SHIN1 (ref. 21) (SHMT1/2i), which were both partially rescued by addition of sodium formate (Fig. 1d,e).

We previously demonstrated that cancer cells generate formate in excess of the anabolic demand resulting in formate excretion (formate overflow)[22,23]. This formate overflow specifically depends on active mitochondrial 1C metabolism[24]. Thus, formate overflow can be used as a readout to assess the activity of mitochondrial 1C metabolism. To investigate this further, formate release rates from cells were measured by gas chromatography–MS. As expected, *MTHFD2*$^{-/-}$ cells had no formate release (Fig. 1f). In contrast, TH9619 and TH9975 did not impair formate release in wild-type (WT) or CRISPR–Cas9 generated *SHMT1*$^{-/-}$ SW620 cells (Fig. 1f and Extended Data Fig. 1c,d). In fact, TH9619 increased formate release rates of SW620 WT, most probably as a result of MTHFD1(DC) inhibition that prevents thymidylate synthesis and recycling of mitochondrial-derived formate. A similar phenomenon has previously been reported for methotrexate (MTX), which inhibits dihydrofolate reductase but does not impair mitochondrial 1C metabolism[24], and served as a positive control in our

Fig. 1 | TH9619 and TH9975 target MTHFD1(DC) but not mitochondrial MTHFD2. a, 1C metabolism flux between mitochondria and cytosol/nucleus. **b**–**e**, Dose–response curves of SW620 cells treated for 96 h with TH9619 (**b**), TH9975 (**c**), DS18561882 (**d**) or SHIN1 (**e**) in the presence of 50 µM thymidine, 1 mM sodium formate or vehicle (cultured in RPMI-FBS), means ± s.d. ($n = 3$). **f**, [U-^{13}C]serine-derived formate release rate of SW620 WT, *MTHFD2*$^{-/-}$ and *SHMT1*$^{-/-}$ cells treated for 24 h with the indicated concentrations of TH9619 and TH9975 or 50 nM MTX (cultured in RPMI-FBS), means ± s.d. ($n = 3$ for control and TH9619, $n = 2$ for TH9975, $n = 1$ for MTX); one-way ANOVA (analysis of variance) with Tukey's multiple comparisons test. **g**, Quantification of mitochondrial membrane potential in SW620 WT cells treated with 1 µM of TH9619 or TH9975 or 0.5 µM MTX for 48 h. FCCP was used as positive control. Data are displayed as means ± s.d. ($n = 4$, $n = 5$ for FCCP); one-way ANOVA with Dunnett's test for multiple comparisons. **h**,**i**, CETSA analysis of MTHFD2 stabilization in SW620 WT cells treated for 3 h with 10 µM TH9619 or vehicle. MTHFD2 stabilization was assessed by western blot by normalizing remaining MTHFD2 signal to HSP60 in the mitochondrial fractions (**h**) or lamin A/C in the nuclear fractions (**i**). **j**, Representative immunoblots of one out of two independent experiments. **k**, DARTS analysis of MTHFD1 stabilization in SW620 lysates that were incubated with 10 µM TH9619 or vehicle for 30 min, followed by protein digestion at increasing pronase concentration and assessment of MTHFD1 degradation by western blot. MTHFD1 signal was normalized to SOD1. Shown is a representative out of three independent experiments. **l**, Mean pIC_{50} (−log of half-maximum inhibitory concentration) values for indicated MTHFD1/2 inhibitors assessed for their inhibitory activity against MTHFD1(DC) WT or MTHFD1(DC) mutant (Q100A), mean (from left to right $n = 4, 9, 2, 19, 5, 15, 5, 6, 4, 8$); unpaired, two-tailed *t*-test. **m**, CRISPR-Select cassette for MTHFD1-Q100A was delivered to SW620 cells. The graph shows the ratio of MTHFD1-Q100A versus WT on day 2 and day 25 of 10 µM TH9619 treatment normalized to day 2 value, means ± s.d. ($n = 4$); paired, two-tailed *t*-test.

https://doi.org/10.1038/s42255-023-00771-5

experimental setup (Fig. 1f). Furthermore, mitochondrial membrane potential was not impaired, but TH9619 and TH9975 caused a slight hyperpolarization after 48 h (Fig. 1g). This hyperpolarization may be a secondary effect, caused by small changes in nucleotide balances, rather than direct effects of TH9619 and TH9975 on mitochondrial function. Together, this indicates that TH9619 and TH9975 are not inhibiting mitochondrial MTHFD2.

The metabolic data and the functional assay indicating that TH9619 does not directly inhibit MTHFD2 (Fig. 1b–g) contrast with our previous study showing that TH9619 binds and stabilizes MTHFD2

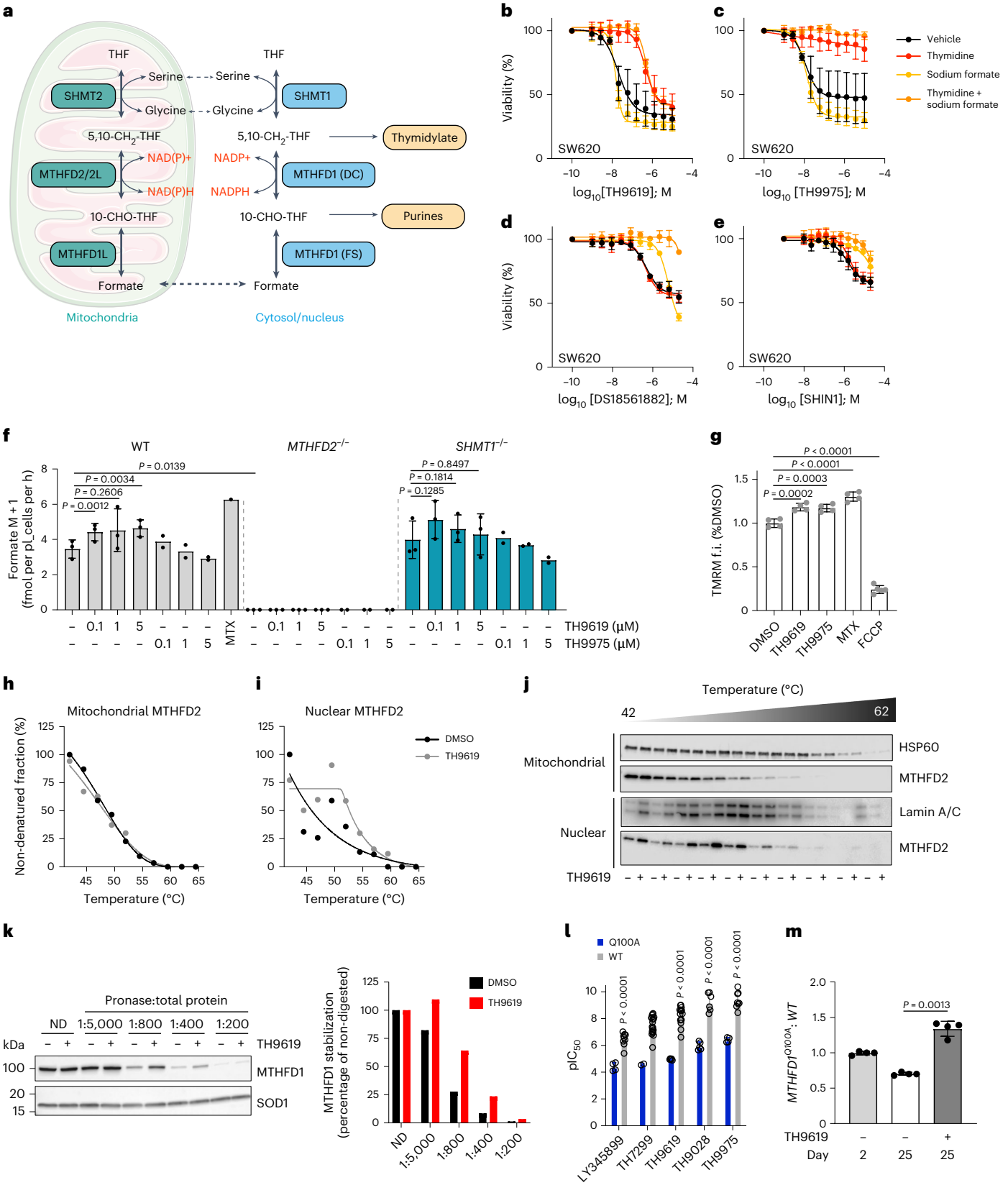

in whole cells and cell lysates from leukaemic HL-60 cells using a cellular thermal shift assay (CETSA)[16]. MTHFD2 is located both in the mitochondria and in the nucleus[25], meaning that the stabilization we observed could be due to MTHFD2 stabilization in either of these organelles. Therefore, we performed CETSA on purified subcellular fractions of mitochondria and nuclei (Extended Data Fig. 1e). Indeed, while TH9619 stabilized nuclear MTHFD2, there was no stabilization of mitochondrial MTHFD2 (Fig. 1h–j), supporting the notion that TH9619 does not inhibit mitochondrial MTHFD2. Since its physicochemical properties prohibit passive membrane permeation, we propose that TH9619 is not a substrate for the mitochondrial folate transporter (SLC25A32) and hence cannot enter the mitochondria to engage with MTHFD2. In contrast, DS18561882 inhibits formate release and ATP biosynthesis, while increasing intracellular serine levels, indicating mitochondrial MTHFD2 inhibition (Extended Data Fig. 1f–i). DS18561882 is much more lipophilic than TH9619 and likely to passively diffuse across membranes, thus not requiring SLC25A32 to reach mitochondrial MTHFD2.

Owing to technical limitations, we had not previously been able to determine whether TH9619 binds to MTHFD1 in cells by CETSA. Here, we used a drug affinity responsive target stability (DARTS)[26] assay and found that TH9619 was able to stabilize MTHFD1 in lysates and whole cells (Fig. 1k and Extended Data Fig. 1j), suggesting MTHFD1 may play a role in TH9619 toxicity despite of a lack of resistance in *MTHFD1*^{KD} cells. We also found that DS18561882 (MTHFD1/2i) engaged MTHFD1 in lysates (Extended Data Fig. 1k). To explore whether targeting MTHFD1 is important for toxicity, we generated a MTHFD1(DC) mutant that is resistant to TH9619 and other compounds in this series (TH7299, ref. 16; TH9028, ref. 16 and TH9975) but is still enzymatically active. Using the crystal structure of MTHFD2 bound to an inhibitor (TH7299)[16], which resembles MTHFD1(DC), we predicted that exchanging glutamine for an alanine at position 100 (Q100A) would drastically reduce the affinity for MTHFD1/2i, without majorly affecting the catalytic activity of the enzyme (Extended Data Fig. 1l). Hence, this could prompt a resistance mutation to the drugs. To test this, we purified *MTHFD1*^{Q100A} and determined its biochemical activity. While the mutant showed comparable enzymatic activity to the WT enzyme (Extended Data Fig. 1m), we found, as expected, that the Q100A mutation led to an increased resistance to all the inhibitors in the series (Fig. 1l). To confirm involvement of MTHFD1, we used the recently developed technique CRISPR-Select[27], to introduce the *MTHFD1*^{Q100A} mutation into cells. *MTHFD1*^{Q100A} cells accumulated roughly 1.9-fold compared to WT cells in the cell population over the 25-day experiment (Fig. 1m), demonstrating that the Q100A mutation increases cell proliferation and confers partial resistance to TH9619. This indicates that toxicity to TH9619 is at least partially due to targeting of MTHFD1(DC).

Together, these data along with our previous findings[16], reveal that both MTHFD1(DC) and MTHFD2 are required for TH9619 mechanism of action, but that the drug toxicity is not due to TH9619 directly targeting mitochondrial MTHFD2. Given the surmounting evidence for a potentially non-catalytic role of MTHFD2 in the nucleus[25,28], and for a stabilization of nuclear MTHFD2 by TH9619, TH9619 may also play a role in regulating nuclear MTHFD2 activity at replication forks. Whereas this role merits further investigation in future studies, here we focus on the metabolic effects of 1C metabolism to explain the potent, cancer-specific toxicity of TH9619.

TH9619 primarily inhibits thymidylate synthesis in WT cells

The 1C units for purine and thymidylate synthesis can be generated from serine by cytosolic or mitochondrial 1C metabolism (Fig. 1a)[13]. Given that MTHFD2 expression sensitizes to TH9619, but that mitochondrial MTHFD2 is not directly inhibited and that TH9619 also targets MTHFD1(DC), we further investigated the impact of TH9619 on thymidylate and purine synthesis. We performed metabolic rescue experiments with thymidine, hypoxanthine, folinic acid and folic acid, and compared TH9619 to TH9975 (MTHFD1/2i), DS18561882 (ref. 18) (MTHFD1/2i, ref. 16), SHIN1[21] (SHMT1/2i), MTX and 5-fluorouracil (5-FU).

SW620 and HCT116 colorectal cancer cells became partially resistant to TH9619 in the presence of thymidine, and fully resistant in the presence of thymidine plus hypoxanthine (Fig. 2a and Extended Data Fig. 2a) or with thymidine and folinic acid or folic acid (Extended Data Fig. 2b,c). Resistance to TH9975 toxicity was obtained by addition of thymidine (Fig. 2b and Extended Data Fig. 2a). Hypoxanthine moderately increased the sensitivity to TH9619 and TH9975 (Fig. 2a,b). This contrasts to all other compounds (Fig. 2c–f and Extended Data Fig. 2a,c). Instead, the effects of DS18561882 and SHIN1 were both partially reversed in the presence of hypoxanthine (Fig. 2c,d). Response also differed when treating with existing antifolates, as MTX resistance was induced by the combination of thymidine and hypoxanthine, but by neither alone, and no change was detected in response to 5-FU with any of the additives (Fig. 2e,f). This highlights that TH9619 has a unique mechanism of action that involves a primary toxicity due to thymidylate depletion, as well as a secondary toxicity due to purine deficiency.

To explore this further, we performed isotope tracing using [U-^{13}C] serine and [2,3,3-^{2}H]serine and measured newly synthesized purines (Fig. 2g) and thymidine (Fig. 2h), respectively, in response to TH9619 and TH9975 in SW620 WT, *MTHFD2*$^{-/-}$ and *SHMT1*$^{-/-}$ cells. Newly synthesized purines can be identified by the incorporation of [U-^{13}C] serine-derived glycine and formate, which increases their mass (that is, M + 1, M + 2, M + 3, M + 4) due to incorporation of single or multiple ^{13}C atoms from [U-^{13}C]serine (Fig. 2g). To evaluate purine de novo synthesis rates during TH9619 and TH9975 treatment, we thus inspected the relative mass isotopomer distribution (MID) of these higher mass isoptopologues of ATP and ADP. SW620 WT cells showed a small reduction of ATP and ADP synthesis in response to TH9619 and TH9975 (Fig. 2i and Extended Data Fig. 2d). Untreated *SHMT1*$^{-/-}$ cells were still able to synthesize purines in a similar capacity to SW620 WT cells and showed a modest reduction in isotope labelling compared to WT cells (Fig. 2i and Extended Data Fig. 2d) in response to TH9619 and TH9975

Fig. 2 | TH9619 primarily inhibits thymidylate biosynthesis in SW620 WT cells and purine biosynthesis in *MTHFD2*$^{-/-}$ cells. a–f, Dose–response curves of SW620 WT cells treated for 96 h with TH9619 (**a**), TH9975 (**b**), DS18561882 (**c**), SHIN1 (**d**), MTX (**e**) or 5-FU (**f**) in the presence of 50 µM thymidine, 250 µM hypoxanthine or vehicle (cultured in RPMI-FBS), means ± s.d. ($n = 3$). **g**, 1C metabolism labelling derived from [U-^{13}C] serine tracer with red dots indicating ^{13}C atoms in individual metabolites. 5,10-CH_2-THF, 5,10-methylenetetrahydrofolate; 10-CHO-THF, 10-formyl tetrahydrofolate; MTHFD1/1L/2/2L, methylenetetrahydrofolate dehydrogenase 1/1L/2/2L. **h**, 1C metabolism labelling derived from [2,3,3-^{2}H]serine tracer with coloured dots indicating cytosol and mitochondrial-derived ^{2}H atoms in individual metabolites. **i**, [U-^{13}C]serine-derived MID of ATP in SW620 WT, *MTHFD2*$^{-/-}$ and *SHMT1*$^{-/-}$ cells treated for 24 h with the indicated concentrations of TH9619 and TH9975 in µM or 50 nM MTX (cultured in RPMI-FBS), mean ± s.d. ($n = 3$ for untreated and TH9619, $n = 2$ for TH9975, $n = 1$ for MTX); one-way ANOVA with Tukey's multiple comparisons test for M + 0. *P* values indicate comparisons to untreated control of each cell line. **j**, ATP level normalized to PCV in SW620 WT, *MTHFD2*$^{-/-}$ and *SHMT1*$^{-/-}$ cells treated for 24 h with the indicated concentrations of TH9619 and TH9975 in µM (cultured in RPMI-FBS), means ± s.d. ($n = 3$ for untreated and TH9619, $n = 2$ for TH9975); one-way ANOVA with Dunnett's test for multiple comparisons. *P* values indicate comparisons to the untreated control. **k**, Ratio of the [2,3,3-^{2}H]serine-derived M + 1 to M + 2 isotopologues of dTMP in SW620 WT and *MTHFD2*$^{-/-}$ cells treated for 24 h with 1 µM TH9619 and TH9975 (cultured in RPMI-FBS), means ± s.d. ($n = 3$ for untreated and TH9619, $n = 2$ for TH9975); one-way ANOVA with Tukey's multiple comparisons test. **l**, Relative enrichment of [2,3,3-^{2}H]serine-derived M + 1 to M + 2 isotopologues of dTMP in SW620 WT and *MTHFD2*$^{-/-}$ cells treated for 24 h with 1 µM TH9619 and TH9975 (cultured in RPMI-FBS), means ± s.d. ($n = 3$ for untreated and TH9619, $n = 2$ for TH9975); one-way ANOVA with Tukey's multiple comparisons test for D + 1 isotopologue of dTMP.

https://doi.org/10.1038/s42255-023-00771-5

treatment. Owing to the reversibility of the cytosolic 1C cycle, untreated *MTHFD2*$^{-/-}$ cells also retained the ability to synthesize purines in the absence of TH9619 or TH9975 treatments (Fig. 2i and Extended Data Fig. 2d). In stark contrast to WT and *SHMT1*$^{-/-}$ cells, *MTHFD2*$^{-/-}$ cells were, however, unable to synthesize ATP from the 1C cycle in response to TH9619 or TH9975 at all tested concentrations (Fig. 2i and Extended

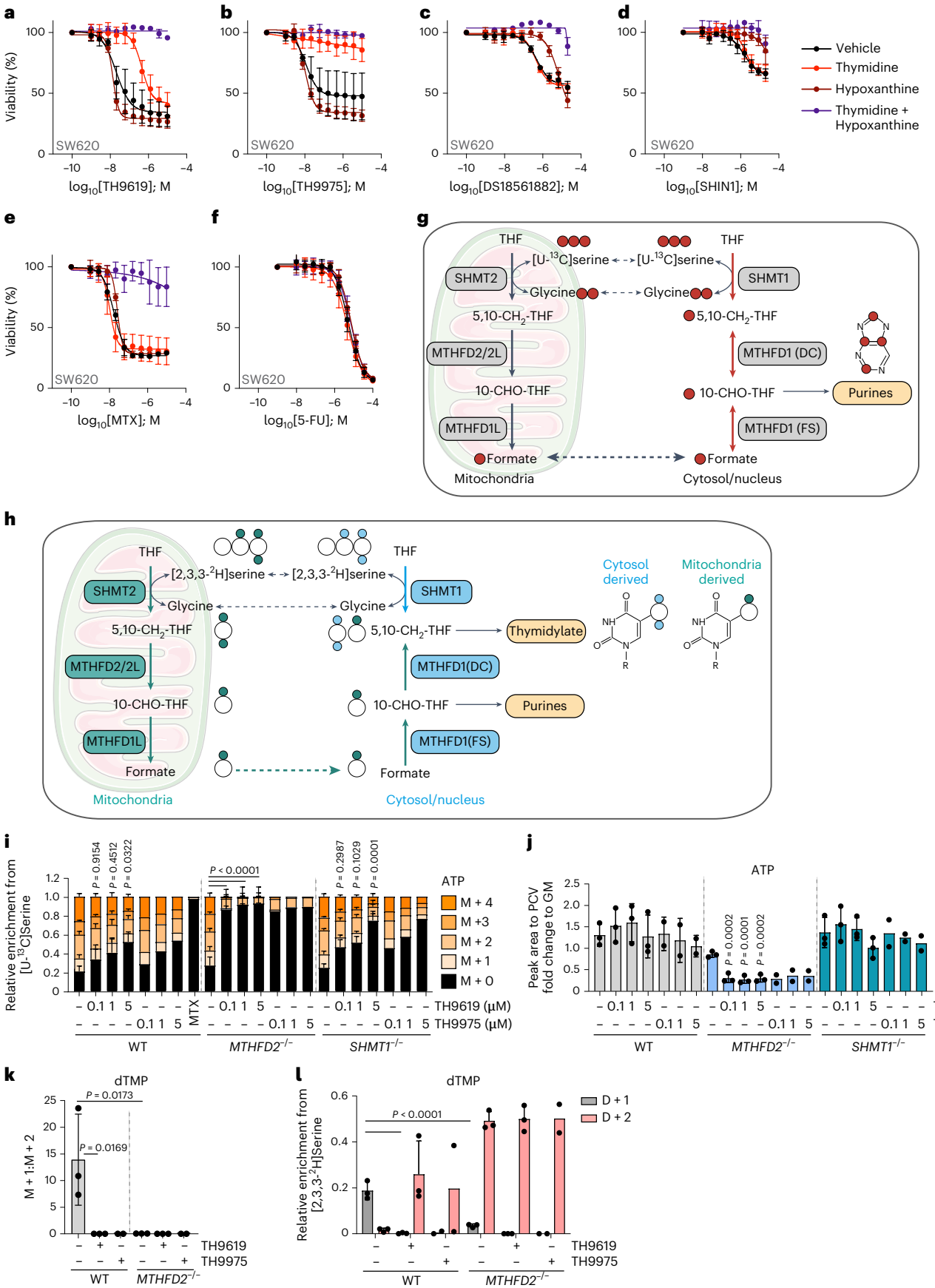

Data Fig. 2d). This loss of de novo purine synthesis was also reflected in a drop in total ATP and ADP levels (Fig. 2j and Extended Data Fig. 2e). This result is in line with our observation that TH9619 inhibits the DC domain of MTHFD1 as it shows that *MTHFD2*$^{-/-}$ cells can neither use the mitochondrial nor the cytosolic route of 1C metabolism to synthesize purines from [U-^{13}C]serine when treated with TH9619 or TH9975.

Deuterium (^{2}H) labelling with [2,3,3-^{2}H]serine allows the tracking of the origin of the methylene-THF that is used for thymidylate synthesis (Fig. 2h). The cytosolic or nuclear route produces thymidylate with two deuterium atoms (D + 2) and the mitochondrial route produces thymidylate with one deuterium atom (D + 1)[13,29,30]. SW620 WT cells showed a high mitochondrial flux through MTHFD2 indicated by high D + 1/D + 2 ratio (Fig. 2k). Compared to WT cells, *MTHFD2*$^{-/-}$ cells showed (independent of treatment) a near complete lack of the dTMP+1 isotopologue (Fig. 2l). Treatment of WT cells with TH9619 or TH9975 resulted in a loss of dTMP+1, indicating a reversal of the 1C flux with CH_2-THF for dTMP synthesis being mainly derived via SHMT1. These results further indicate that TH9619 and TH9975 inhibit the DC domain activity of MTHFD1 and thus prevent incorporation of formate produced by the mitochondria into dTMP.

The metabolic tracing experiments revealed an interesting and unexpected mechanism of TH9619 in altering 1C metabolism flux and subsequent toxicity to cancer cells. The primary mechanism of TH9619 toxicity in SW620 WT cells is through thymidylate depletion because TH9619 inhibits the MTHFD1(DC) domain activity and thereby prevents the conversion of 10-CHO-THF to 5,10-CH_2-THF for thymidylate biosynthesis. At this stage, it remained enigmatic to us why thymidine induced resistance to TH9619 and TH9975, given that SW620 WT cells should still be able to compensate for thymidylate synthesis through cytosolic SHMT1. We therefore further investigated how TH9619 and TH9975 cause thymidylate depletion.

Hypoxanthine potentiates TH9619 by folate trapping

In early experiments, we noted that some cells were sensitized to TH9619 and TH9975 by the addition of hypoxanthine (Fig. 2a,b and Extended Data Fig. 2a). Until this point our experiments were performed in Roswell Park Memorial Institute (RPMI)-1640 culture media supplemented with normal, heat-inactivated foetal bovine serum (FBS). RPMI medium does not contain thymidine or purines, which can alter the sensitivity to our inhibitors, but normal FBS contains hypoxanthine. In our hands, normal FBS contains roughly 95 µM hypoxanthine (equating to 9.5 µM in RPMI + 10% FBS) and full sensitization to TH9619 occurs somewhere between 1 and 5 µM hypoxanthine (Fig. 3e and Extended Data Fig. 3a). Hence, to better understand the role of hypoxanthine, we performed subsequent experiments using media supplemented with dialysed FBS (dFBS) ± addition of 50 µM hypoxanthine.

When viability assays were repeated in RPMI supplemented with dFBS (RPMI-dFBS) lacking hypoxanthine, the toxicity in dose–response assays to TH9619 and TH9975 in SW620 WT cells was lost, and sensitivity was restored with supplementation of 50 µM hypoxanthine (Fig. 3a,b). In contrast, in RPMI-dFBS media SW620 cells were sensitized to MTX and DS18561882 (Fig. 3c,d), further suggesting a different mode of action of TH9619. Moreover, other purines including adenine, adenosine and guanosine increased the toxicity to TH9619 and TH9975, but partially rescued the toxicity of MTX and DS18561882 (Extended Data Fig. 3b). We also identified a key difference in sensitivity to TH9619 between WT and *MTHFD2*$^{-/-}$ cells in FBS versus dFBS. As we reported previously[16], compared to WT cells, *MTHFD2*$^{-/-}$ cells display a decreased sensitivity to TH9619 in FBS (Fig. 3f). In stark contrast, TH9619 was several orders of magnitude more effective at reducing the viability of *MTHFD2*$^{-/-}$ cells in dFBS compared to FBS (Fig. 3g). This suggested that the mechanism of TH9619 differs in cells with deficient or intact mitochondrial 1C metabolism.

We then performed metabolic rescue experiments with 50 µM thymidine, 50 µM hypoxanthine or 1 mM sodium formate using RPMI-dFBS in SW620 WT cells and in cells deficient in mitochondrial 1C metabolism: SW620 *MTHFD2*$^{-/-}$ cells and MTHFD1L-defective PA-TU-8988T pancreatic cancer cells[13] (Fig. 3h–o and Extended Data Fig. 3c–e). In SW620 WT cells, simultaneous supplementation of thymidine together with hypoxanthine caused resistance to TH9619 or TH9975 (Fig. 3h,i). In contrast, hypoxanthine mildly desensitized cells to MTX and provided resistance to DS18561882 (Fig. 3j,k). Moreover, the impact on cell viability in dFBS occurs downstream of mitochondrial formate production because sodium formate was unable to rescue the effect of TH9619 in WT cells (Extended Data Fig. 3c).

In contrast to WT cells, *MTHFD2*$^{-/-}$ cells were resistant to TH9619 and TH9975 in the presence of hypoxanthine or sodium formate, but thymidine had no effect (Fig. 3l,m and Extended Data Fig. 3d). Similar results were obtained using PA-TU-8988T cells that are defective in MTHFD1L (ref. 13) (Extended Data Fig. 3e). Thus, in cells with defective mitochondrial 1C metabolism, the reduced viability is due to purine deficiency. This further supports our model that TH9619 causes toxicity by inhibiting the DC domain of MTHFD1.

This prompted us to investigate whether TH9619 and TH9975 effects on 1C-dependent nucleotide synthesis changed by culturing in RPMI-dFBS, thus we repeated [U-^{13}C]serine and [2,3,3-^{2}H]serine tracing in dFBS. In dFBS, de novo purine synthesis (ATP, guanosine monophosphate (GMP), inosine monophosphate (IMP)) from serine appeared mostly unaffected in SW620 WT cells following treatment with 1 µM TH9619 or TH9975 (Fig. 4a and Extended Data Fig. 4a–d). By contrast, serine-dependent de novo purine synthesis was severely impaired with TH9619 and TH9975 in *MTHFD2*$^{-/-}$ cells (Fig. 4a and Extended Data Fig. 4a–d), which is reflected in lower total levels of ATP, GMP and IMP (Fig. 4b and Extended Data Fig. 4b,d). The addition of exogenous hypoxanthine caused a complete block in serine-derived de novo purine synthesis in both WT and *MTHFD2*$^{-/-}$ cells (Fig. 4a and Extended Data Fig. 4a,c).

Similar to tracing experiments in FBS, in dFBS treatment with TH9619 or TH9975, or depletion of MTHFD2 prevented mitochondrial production of dTMP (D + 1) and reversed 1C flux to produce dTMP via the cytosol (D + 2) (Fig. 4c). *MTHFD2*$^{-/-}$ cells treated with TH9619 or TH9975 displayed only a moderate reduction of total dTMP levels (Fig. 4d), while dTMP levels and de novo dTMP synthesis from serine in WT cells were strongly reduced (Fig. 4d,e). In line with dTMP synthesis inhibition, we observed a stark accumulation of dUMP, the precursor for dTMP synthesis in WT cells (Fig. 4f). This effect was much less pronounced in *MTHFD2*$^{-/-}$ cells.

In summary, our data indicate that in cells with intact mitochondrial 1C metabolism, TH9619 and TH9975 cause thymidylate depletion and that this toxicity is dependent on hypoxanthine. By contrast, *MTHFD2*$^{-/-}$ cells treated with TH9619 and TH9975 suffer from loss of purine synthesis and are resistant when cultured with hypoxanthine.

These findings also highlight the importance of cell culture media formulations in studies of 1C metabolism[31,32]. To ensure that these findings are clinically relevant, we compared drug responses in human plasma-like medium (HPLM)[32] and Plasmax[31] that have been developed to contain levels of nutrients comparable to human plasma, including 10 µM (HPLM) or 5 µM (Plasmax) hypoxanthine. SW620 WT cells were highly sensitive to TH9619 and TH9975 when cultured in HPLM, identical to RPMI-dFBS + 10 µM hypoxanthine (Extended Data Fig. 5a,b). In contrast, the presence of hypoxanthine in HPLM provided a slight resistance to MTX and several orders of magnitude lower sensitivity to DS18561882 (Extended Data Fig. 5c,d). Similarly, TH9619 reduced SW620 and HCT116 spheroid growth in physiological Plasmax medium (Fig. 5a,b). This supports that TH9619 is likely to be effective under human physiological conditions.

We proposed that the hypoxanthine-induced inhibition of de novo purine synthesis may be an important contributor to the mechanism of TH9619 and TH9975. In the purine salvage pathway, hypoxanthine is converted to IMP by hypoxanthine phosphoribosyltransferase 1 (HPRT1).

https://doi.org/10.1038/s42255-023-00771-5

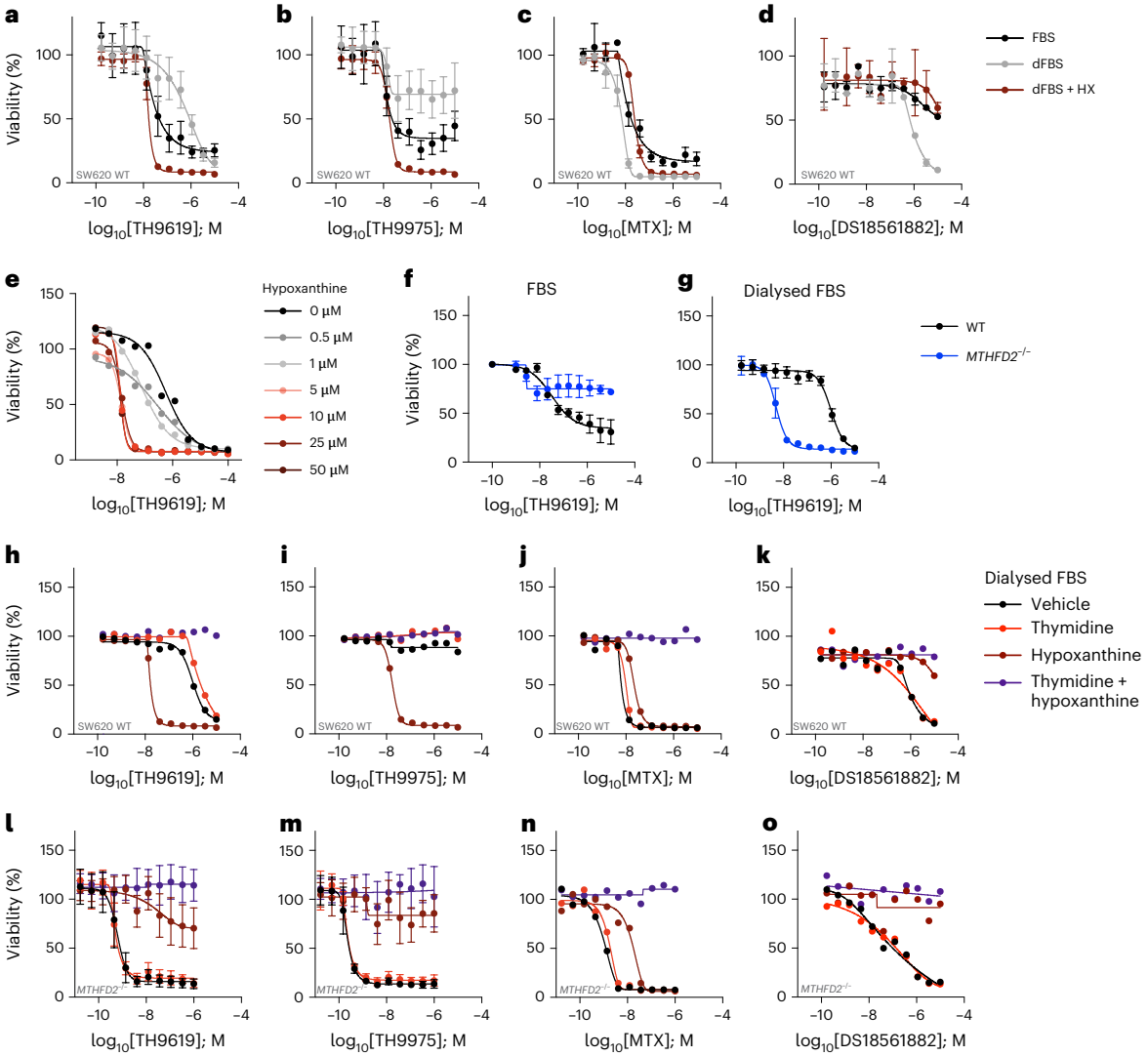

Fig. 3 | Hypoxanthine potentiates TH9619-induced thymidylate depletion. **a**–**d**, Cell viability dose–response curves of SW620 WT cells treated for 96 h with TH9619 (**a**), TH9975 (**b**), MTX (**c**) or DS18561882 (**d**), and cultured in RPMI-FBS, RPMI-dFBS or RPMI-dFBS supplemented with 50 μM hypoxanthine, means ± s.d. ($n = 8$ independent cell cultures for TH9619 and TH9975, $n = 4$ for MTX and DS18561882). **e**, Titration of hypoxanthine at indicated doses in SW620 WT cells treated for 96 h with TH9619 (cultured in RPMI-dFBS). Data are displayed as means ($n = 2$ independent cell cultures). **f**,**g**, Dose–response curves of SW620 WT and *MTHFD2*$^{-/-}$ cells treated for 96 h with TH9619 and cultured in RPMI-FBS (**f**) or RPMI-dFBS (**g**), means ± s.d. ($n = 3$ independent cell cultures). **h**–**k**, Cell viability dose–response curves of SW620 WT cells treated for 96 h with TH9619 (**h**), TH9975 (**i**), MTX (**j**) or DS18561882 (**k**) and 50 μM thymidine, 50 μM hypoxanthine or vehicle (cultured in RPMI-dFBS), means ($n = 2$ independent cell cultures). **l**–**o**, Cell viability dose–response curves of SW620 *MTHFD2*$^{-/-}$ cells treated for 96 h with TH9619 (**l**), TH9975 (**m**), MTX (**n**) or DS18561882 (**o**) and 50 μM thymidine, 50 μM hypoxanthine or vehicle (cultured in RPMI-dFBS), means ± s.d. ($n = 4$ independent cell cultures for TH9619 and TH9975, $n = 2$ for MTX and DS18561882).

IMP and its downstream products AMP and GMP are in turn inhibitors of phosphoribosyl pyrophosphate amidotransferase (PPAT), the first enzyme in the de novo purine synthesis pathway[33,34]. A reduced flow through de novo purine synthesis would lead to a reduced consumption of 10-CHO-THF because 10-CHO-THF is a cofactor for enzymes in the de novo purine synthesis pathway; glycinamide ribonucleotide transformylase and 5-amino-4-imidazolecarboxamide ribonucleotide transformylase (AICAR Tfase). In addition, if MTHFD1(DC) is inhibited by TH9619 or TH9975, this would prevent 10-CHO-THF consumption for both purine and thymidylate synthesis and block the re-synthesis of serine from glycine (Fig. 5c). Simultaneously, we have observed that formate continues to be produced from the mitochondria (Fig. 1f) and high formate concentrations will push the THF:10-CHO-THF equilibrium towards 10-CHO-THF. This scenario with a high synthesis and a small consumption of 10-CHO-THF could lead to a trapping of 10-CHO-THF and depletion of free THF (Fig. 5c). Measuring folate intermediates is inherently challenging, however, we managed to detect 10-CHO-THF by scaling up experiments, adapting previously published protocols and using a modified derivatization method (Extended Data Fig. 6a). Indeed, we observed an increase in 10-CHO-THF levels with TH9619, which was further increased on addition of hypoxanthine (Fig. 5d,e), indicating that 10-CHO-THF is accumulating. Since THF is a substrate for SHMT1, this trapping of THF as 10-CHO-THF would explain why SHMT1 cannot support dTMP synthesis on MTHFD1(DC) inhibition. Of note, there was no accumulation of 10-CHO-THF in *MTHFD2*$^{-/-}$ cells in the absence of formate overflow (Fig. 5d,e). Our previous [U-^{13}C] serine tracing experiments using exogenous, unlabelled hypoxanthine further confirm this 10-CHO-THF trapping model. If hypoxanthine fuels the cellular purine pool via the salvage pathway, and thereby prevents de novo synthesis from serine, we expect a loss of the ^{13}C-labelled purine isotopologues coming from [U-^{13}C]-serine tracer. Indeed, addition of hypoxanthine to WT cells strongly reduced the ^{13}C-labelled fraction in

https://doi.org/10.1038/s42255-023-00771-5

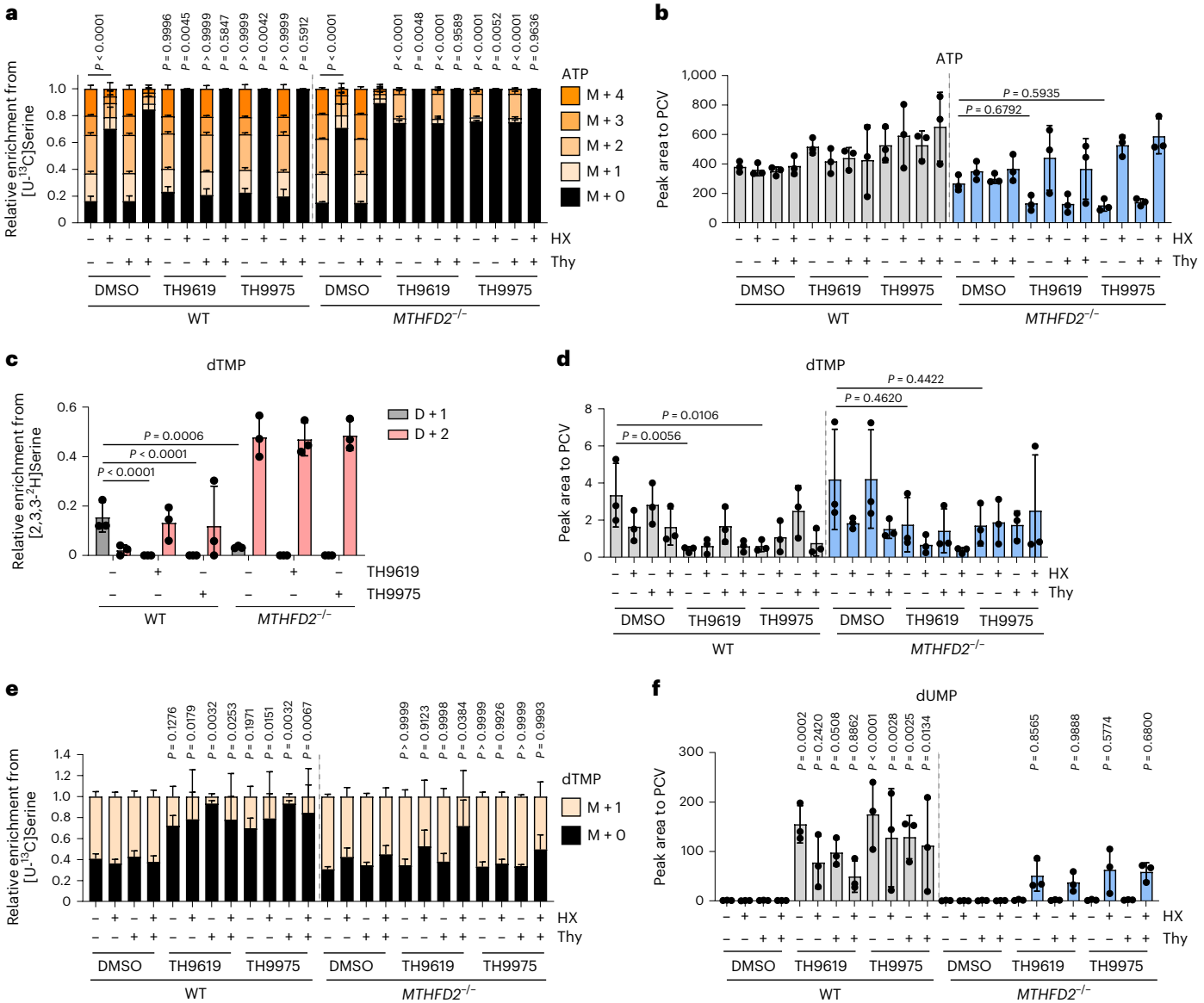

Fig. 4 | Metabolic tracing confirms potentiation of TH9619-induced thymidylate depletion by hypoxanthine. a, [U-^{13}C]serine- derived MID of ATP in SW620 WT and *MTHFD2*$^{-/-}$ cells treated for 24 h with 1 μM TH9619 or TH9975, 50 μM hypoxanthine and 50 μM thymidine (cultured in RPMI-dFBS), means ± s.d. ($n = 3$); one-way ANOVA with Šídák's multiple comparisons test for M + 0. *P* values indicate comparisons to DMSO controls of each cell line. **b**, ATP levels normalized to PCV in SW620 WT and *MTHFD2*$^{-/-}$ cells treated for 24 h with 1 μM TH9619 or TH9975, 50 μM hypoxanthine and 50 μM thymidine (cultured in RPMI-dFBS), means ± s.d. ($n = 3$); one-way ANOVA with Šídák's multiple comparisons test. **c**, Relative enrichment of [2,3,3-^{2}H]serine-derived M + 1 to M + 2 isotopologues of dTMP in SW620 WT and *MTHFD2*$^{-/-}$ cells treated for 24 h with 1 μM TH9619 and TH9975 (cultured in RPMI-dFBS), means ± s.d. ($n = 3$); one-way ANOVA with Tukey's multiple comparisons test. **d**, dTMP levels normalized to PCV in SW620 WT and *MTHFD2*$^{-/-}$ cells treated for 24 h with 1 μM TH9619 or TH9975, 50 μM hypoxanthine and 50 μM thymidine (cultured in RPMI-dFBS), means ± s.d. ($n = 3$); one-way ANOVA with Šídák's multiple comparisons test. **e**, [U-^{13}C]serine-derived MID of dTMP in SW620 WT and *MTHFD2*$^{-/-}$ cells treated for 24 h with 1 μM TH9619 or TH9975, 50 μM hypoxanthine and 50 μM thymidine (cultured in RPMI-dFBS), means ± s.d. ($n = 3$); one-way ANOVA with Šídák's multiple comparisons test for M + 0. *P* values indicate comparisons to respective DMSO controls of each cell line. **f**, dUMP levels normalized to PCV in SW620 WT and *MTHFD2*$^{-/-}$ cells treated for 24 h with 1 μM TH9619 or TH9975, 50 μM hypoxanthine and 50 μM thymidine (cultured in RPMI-dFBS), means ± s.d. ($n = 3$); one-way ANOVA with Šídák's multiple comparisons test. *P* values indicate comparisons to respective DMSO controls of each cell line.

ATP and on combined TH9619 or TH9975 treatment, the ^{13}C-labelled fraction completely vanished (Fig. 4a). We also tested and could exclude a role for hypoxanthine in potentiating TH9619 response due to inhibition of uridine monophosphate synthase (Extended Data Fig. 5e–k and Supplementary Discussion)[32].

Mitochondrial formate release drives TH9619 trapping of 10-CHO-THF

We next wanted to confirm that formate overflow was required to feed this folate trap and to cause thymidylate depletion. To investigate this, we tested whether a comparable toxic trapping of THF in the form of 10-CHO-THF could also be induced in *MTHFD2*$^{-/-}$ cells that are unable to synthesize formate via the mitochondrial route (Fig. 6a). Supplementation of hypoxanthine or formate allowed *MTHFD2*$^{-/-}$ cells to overcome purine deficiency by using hypoxanthine for purine synthesis or restoring formate, respectively (Fig. 3l,m and Extended Data Fig. 3d). If the trapping hypothesis is correct, the combination of TH9619, hypoxanthine and formate in *MTHFD2*$^{-/-}$ would lead to trapping of 10-CHO-THF and thymidylate deficiency. Exogenous formate would mimic formate overflow and would be converted with free THF to 10-CHO-THF.

https://doi.org/10.1038/s42255-023-00771-5

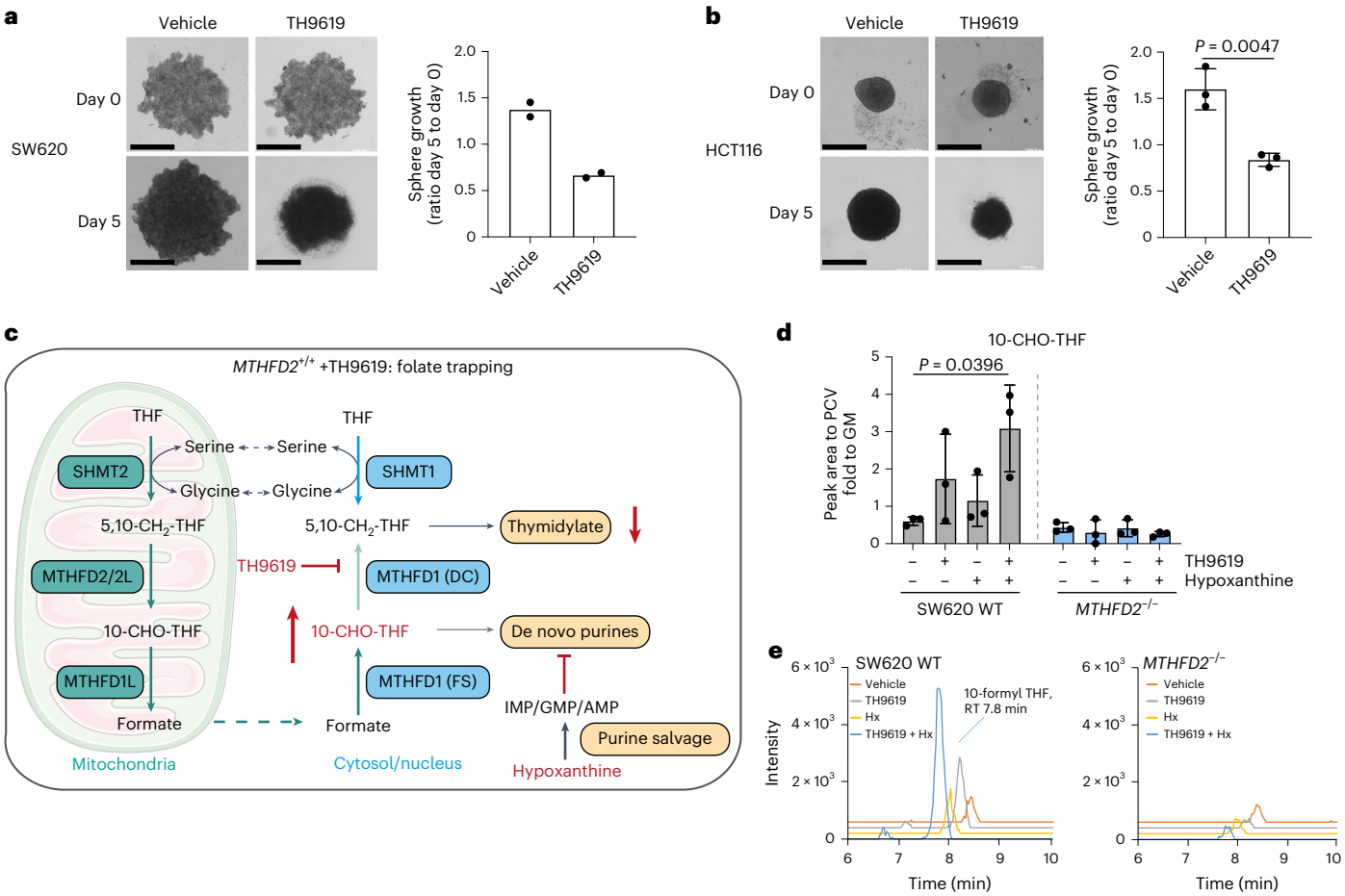

Fig. 5 | TH9619 and hypoxanthine causes 10-CHO-THF accumulation. **a**,**b**, HCT116 (**a**) and SW620 (**b**) cells were grown as spheroid cultures in three dimensions. Proliferation was measured as spheroid area from day 0 to 5 on 1 µM TH9619 or vehicle, means ± s.d. ($n = 3$ for HCT116 and $n = 2$ for SW620). Representative pictures shown for both cell lines. Scale bars, 500 µm. **c**, In the folate trapping model, hypoxanthine is converted to IMP, GMP or AMP by purine salvage, causing feedback inhibition on de novo purine synthesis. Simultaneously, TH9619 inhibits MTHFD1(DC), which together blocks consumption of 10-CHO-THF, creating a folate trap and preventing thymidylate synthesis due to exhaustion of THF. **d**, 10-CHO-THF levels normalized to PCV in SW620 WT and *MTHFD2*$^{-/-}$ cells treated for 24 h with 1 µM TH9619 and 50 µM hypoxanthine (cultured in RPMI-dFBS), means ± s.d. ($n = 3$); one-way ANOVA with Tukey's multiple comparisons test. **e**, LC–MS chromatograms for one representative experiment of **d**. RT, retention time.

10-CHO-THF would now also accumulate in TH9619-treated *MTHFD2*$^{-/-}$ cells because it is not being consumed for purine synthesis in the presence of hypoxanthine (Fig. 6b). The consequential depletion of free THF means that there is now also in *MTHFD2*$^{-/-}$ cells no substrate available for SHMT1 and thymidylate production. In line with this hypothesis, a combination of hypoxanthine and formate induced TH9619 and TH9975 toxicity in *MTHFD2*$^{-/-}$ cells (Fig. 6c,d). This toxicity was no longer due to purine deficiency, but instead caused by thymidylate deficiency and could thus be rescued by thymidine addition (Fig. 6b–d). The TH9619 and TH9975 toxicity in *MTHFD2*$^{-/-}$ cells in the presence of hypoxanthine and formate in dFBS (TH9619 half-maximum effective concentration (EC_{50}) of 11.6 nM, TH9975 EC_{50} = 10.7 nM) resembled that of SW620 WT cells when cultured in dFBS plus hypoxanthine (TH9619 EC_{50} = 16.5 nM, TH9975 EC_{50} = 17.4 nM) (Figs. 3a,b and 6c,d and Supplementary Table 1). This phenomenon may also exist with DS18561882 at much higher concentrations, but does not occur with MTX or SHIN1 (Fig. 6e–g). This suggests that inhibition of the DC domain of MTHFD1 and accumulation of 10-CHO-THF in a folate trap is key to the mechanism behind TH9619-dependent inhibition of thymidylate synthesis.

We were also interested to see whether a conversion of 10-CHO-THF to THF could save SW620 WT cells from toxicity caused by TH9619 or TH9975 plus hypoxanthine. We reasoned that because hypoxanthine leads to IMP-mediated inhibition of PPAT[33,34], the synthesis of AICAR in de novo purine synthesis pathway would decrease (Fig. 6h). Since AICAR Tfase uses AICAR as a substrate and 10-CHO-THF as a cofactor, the 10-CHO-THF consumption decreases and results in further 10-CHO-THF trapping. Therefore, toxicity caused by TH9619 combined with hypoxanthine should be saved by addition of membrane permeable 5-amino-4-imidazolecarboxamide ribonucleoside (AICAr), which is intracellularly converted to AICAR by adenosine kinase. On hypoxanthine-mediated PPAT inhibition, such AICAr supplementation would thus increase the conversion of 10-CHO-THF to THF and the liberated THF can be used by SHMT1 to synthesize 5,10-CH_2-THF that is required for dTMP synthesis. Indeed, AICAr dose-dependently reduced the toxicity of TH9619 or TH9975 in combination with hypoxanthine (Fig. 6i,j). The ability of combined hypoxanthine and formate treatment to trigger TH9619 or TH9975 toxicity via thymidylate deficiency in *MTHFD2*$^{-/-}$ cells, along with AICAr rescue in SW620 WT cells strongly supports that 10-CHO-THF trapping causes toxicity due to thymidylate depletion. In comparison, MTX was unaffected by supplementation of AICAr (Fig. 6k), indicating that 10-CHO-THF trapping is a mechanism unique to this class of 1C inhibitors.

We have previously shown that formate overflow is a common trait in cancer cells that requires mitochondrial 1C metabolism[22–24]. We here propose that MTHFD2 supports formate overflow in cancer cells (as in

https://doi.org/10.1038/s42255-023-00771-5

Fig. 1f) rendering them sensitive to MTHFD1(DC) inhibition by TH9619. Indeed, we found that TH9619 and TH9975 increase formate overflow in SW620 WT cells and that this effect is most pronounced when either drug is combined with hypoxanthine, regardless of the presence of exogenous thymidine (Fig. 6l).

dTMP depletion induces cell death and purine depletion is cytostatic

Thymidylate and purine biosynthesis are both essential for maintaining genomic integrity and supporting the high proliferative demands in cancer cells. As TH9619 exerts different effects on 1C metabolism flux

Fig. 6 | Formate release by mitochondrial 1C flux is required for TH9619-mediated trapping of 10-CHO-THF. a, TH9619 blocks purine synthesis in *MTHFD2*$^{-/-}$ cells. **b**, Exogenous supply of sodium formate and hypoxanthine can induce the TH9619 folate trapping mechanism and block thymidylate synthesis in *MTHFD2*$^{-/-}$ cells. **c**–**g**, Cell viability dose–response curves of SW620 *MTHFD2*$^{-/-}$ cells treated for 96 h with TH9619 (**c**), TH9975 (**d**), MTX (**e**), DS18561882 (**f**) or SHIN1 (**g**) and 50 µM hypoxanthine, 1 mM sodium formate, 50 µM thymidine or vehicle (cultured in RPMI-dFBS), two representative experiments displayed as means ± s.d. ($n = 4$ independent cell cultures). **h**, Hypoxanthine and TH9619 cause folate trapping in WT cells. Treatment with AICAr bypasses the block in de novo purine synthesis and releases the folate trap by AICAR Tfase consumption of 10-CHO-THF. **i**–**k**, Cell viability dose–response curves of SW620 WT cells treated for 96 h with TH9619 (**i**), TH9975 (**j**) or MTX (**k**) and vehicle or increasing AICAr concentrations (cultured in RPMI-dFBS), two representative experiments are shown as means ± s.d. ($n = 4$ independent cell cultures for TH9619 and TH9965, $n = 2$ for MTX). **l**, [U-^{13}C]serine-derived formate release rate of SW620 WT cells treated for 24 h with 1 µM TH9619 or TH9975, 50 µM hypoxanthine and 50 µM thymidine (cultured in RPMI-dFBS), means ± s.d. ($n = 3$); one-way ANOVA with Dunnett's multiple comparisons test. *P* values indicate comparisons to the DMSO control.

in MTHFD2-expressing versus null cancers, we next explored whether these distinct metabolic changes also result in different biological effects in these cells and how hypoxanthine contributes to sensitization.

We found that TH9619 and TH9975 impaired proliferation in SW620 WT and *MTHFD2*$^{-/-}$ cells cultured in RPMI-FBS over a 96 h time course (Fig. 7a). Similarly, WT cells cultured in RPMI-dFBS exhibited reduced proliferation in response to TH9619 and TH9975 treatment, which was exacerbated by hypoxanthine while resistance was increased by the addition of thymidine (Fig. 7b). This contrasts with *MTHFD2*$^{-/-}$ cells, which did not proliferate following TH9619 or TH9975 treatment and did not show resistance in response to thymidine supplementation, but in which proliferation could be restored with hypoxanthine supplementation (Fig. 7c).

The impaired proliferation in SW620 WT cells corresponded to cell cycle arrest in S-phase after 48 h of TH9619 treatment in cells cultured in RPMI-FBS with or without hypoxanthine supplementation (Fig. 7d). S-phase arrest also occurred in SW620 WT cells cultured in RPMI-dFBS, although this was slightly less pronounced (Fig. 7e). Cell cycle arrest could be rescued by the addition of thymidine to WT cells cultured in media with either FBS or dFBS (Fig. 7d,e). Similarly, *MTHFD2*$^{-/-}$ cells also exhibited S-phase arrest in response to TH9619 when cultured in RPMI-FBS combined with hypoxanthine (Fig. 7d), but the S-phase arrest was less pronounced in RPMI-dFBS-hypoxanthine cultures (Fig. 7e).

In SW620 WT cells, cell cycle arrest was followed by induction of apoptosis on TH9619 and TH9975 treatment, which was exacerbated with hypoxanthine and rescued with thymidine irrespective of culturing with FBS or dFBS (Fig. 7f,g). This is in stark contrast to *MTHFD2*$^{-/-}$ cells, which showed minimal induction of apoptosis following TH9619 or TH9975 treatment (Fig. 7f,g). This revealed that the reduced viability in resazurin assays following TH9619 treatment is caused by distinct biological mechanisms in WT and *MTHFD2*$^{-/-}$ cells (Fig. 3h,i,l,m), depending on the drugs' impact on 1C metabolism. TH9619 imposes a cytostatic effect on cancer cells with low MTHFD2 expression by restricting the pool of purines available for DNA synthesis. In comparison, thymidylate deficiency caused by TH9619 in SW620 WT cells with high MTHFD2 expression induces cell death, presumably due to induction of DNA damage by uracil misincorporation[5]. Finally, and in accordance with the folate trapping model, simultaneous addition of hypoxanthine and formate sensitized *MTHFD2*$^{-/-}$ cells to TH9619 and TH9975 and resulted in a very strong induction of cell death (Fig. 7h).

To ensure that the described mechanism is also consistent across a broader panel of cell lines, we aimed to verify the effects of TH9619 treatment in breast cancer cell lines with different expression levels of MTHFD2. We confirmed different MTHFD2 protein expression in MDA-MB-231 (low MTHFD2 expression), MDA-MB-468 WT (high MTHFD2 expression) and MDA-MB-468 *MTHFD2*$^{-/-}$ (no MTHFD2 expression) cells compared to SW620 WT cells (Fig. 7i and Extended Data Fig. 6b,c). Furthermore, MTHFD2 expression levels are reflected in different formate release rates (Fig. 7j). We found that TH9619 slowed proliferation in MDA-MB-468 WT, *MTHFD2*$^{-/-}$ cells and MDA-MB-231 cells (Fig. 7k). In line with results in SW620 cells, proliferation of MDA-MB-468 WT cells was further reduced on combined treatment with hypoxanthine, while hypoxanthine addition restored proliferation in *MTHFD2*$^{-/-}$ cells (Fig. 7b,c,k and Extended Data Fig. 6d). Of note, simultaneous supplementation of hypoxanthine and formate in TH9619-treated MDA-MB-468 *MTHFD2*$^{-/-}$ cells caused an increase in cell size but not absolute cell numbers (Extended Data Fig. 6d), explaining the increase in confluency observed in the proliferation assay in these conditions (Fig. 7k). Comparable to SW620 cells, TH9619 toxicity in MDA-MB-468 WT cells was increased with hypoxanthine addition and unaltered by additional formate treatment (Fig. 7g,h,l). Moreover, similar to SW620 *MTHFD2*$^{-/-}$ cells, TH9619 alone had minimal effects on apoptosis in MDA-MB-468 *MTHFD2*$^{-/-}$ cells, while simultaneous addition of formate and hypoxanthine potently induced TH9619-dependent apoptosis (Fig. 7h,l).

Together, this indicates that TH9619 causes thymidylate deficiency in MTHFD2-expressing cancer cells by inhibiting MTHFD1(DC), leading to 10-CHO-THF trapping and depletion of THF. This mechanism relies on physiological levels of hypoxanthine to activate the purine salvage pathway and feedback inhibition of de novo purine synthesis. The drug effect in *MTHFD2*$^{-/-}$ cells can be switched from cytostatic purine depletion to toxic inhibition of thymidylate biosynthesis by inducing 10-CHO-THF trapping on combinatorial hypoxanthine and formate supplementation. Given that formate levels are likely to be increased in certain tumours in vivo[22], this may increase the pharmaceutical potential of TH9619. This will be important to ensure sensitivity

Fig. 7 | Depletion of dTMP induces cell death while inhibition of purine synthesis induces growth and cell cycle arrest. a–**c**, Proliferation of (**a**,**b**) SW620 WT and (**c**) *MTHFD2*$^{-/-}$ cells measured as fold change of cell confluence after (**a**) 1 µM TH9619 or TH9975 (**b**,**c**) with or without 50 µM hypoxanthine and 50 µM thymidine (cultured in RPMI-FBS or RPMI-dFBS). AUC of proliferation curves is shown as means ± standard error ((**a**) $n = 3$ for WT, $n = 4$ for *MTHFD2*$^{-/-}$ (**b**,**c**) $n = 4$); one-way ANOVA with (**a**) Šídák's multiple comparisons test or (**b**,**c**) Tukey's multiple comparisons test. **d**,**e**, Cell cycle analysis of SW620 WT and *MTHFD2*$^{-/-}$ cells treated with TH9619, 50 µM thymidine (T), 250 µM hypoxanthine (H) or vehicle (cultured in (**d**) RPMI-FBS or (**e**) RPMI-dFBS), means ± s.d. ($n = 3$); one-way ANOVA with Tukey's multiple comparisons test for S-phase. **f**–**h**, Cell death analysis by annexinV/PI staining of SW620 WT and *MTHFD2*$^{-/-}$ cells after 96 h treatment with 1 µM TH9619 or TH9975 and (**f**,**g**) 50 µM hypoxanthine (H) and 50 µM thymidine (T) cultured in (**f**) RPMI-FBS or (**g**) RPMI-dFBS, or (**h**) treated with T and 1 mM formate (F) cultured in RPMI-dFBS, means ± s.d. ($n = 3$); one-way ANOVA analysis with Tukey's multiple comparisons test for pooled early and late apoptotic populations. **i**, MTHFD2 protein levels in SW620, MDA-MB468 and MDA-MB-231 cells normalized to β-actin, means ± s.d. ($n = 3$); one-way ANOVA analysis with Tukey's multiple comparisons test. **j**, Formate release rates of SW620, MDA-MB-468 and MDA-MB-231 cells, means ± s.d. ($n = 7$ for SW620, $n = 12$ for MDA-MB-468 and $n = 3$ for MDA-MB-231). **k**, Proliferation of MDA-MB-468 WT and *MTHFD2*$^{-/-}$ cells and MDA-MB-231 cells measured as fold change of cell confluence in response to 1 µM TH9619 and 50 µM hypoxanthine and 1 mM sodium formate (cultured in RPMI-dFBS). AUC of curves is shown as means ± s.e. ($n = 3$ for MDA-MB-468 and $n = 4$ for MDA-MB-231); one-way ANOVA with Tukey's multiple comparisons test. **l**, Cell death analysis of MDA-MB-468 WT and *MTHFD2*$^{-/-}$ cells after 96 h treatment with 1 µM TH9619 and 50 µM hypoxanthine (H) and 1 mM formate (F) (cultured in RPMI-dFBS), means ± s.d. ($n = 4$); one-way ANOVA analysis with Tukey's multiple comparisons test for pooled early and late apoptotic populations.

https://doi.org/10.1038/s42255-023-00771-5

of human tumours, given that physiological levels of purines may dampen the response to 1C drugs that work by primarily inhibiting purine synthesis[35].

Discussion

We previously developed inhibitors towards MTHFD2, such as TH9619, which turned out to be equipotent MTHFD1 and MTHFD2L inhibitors

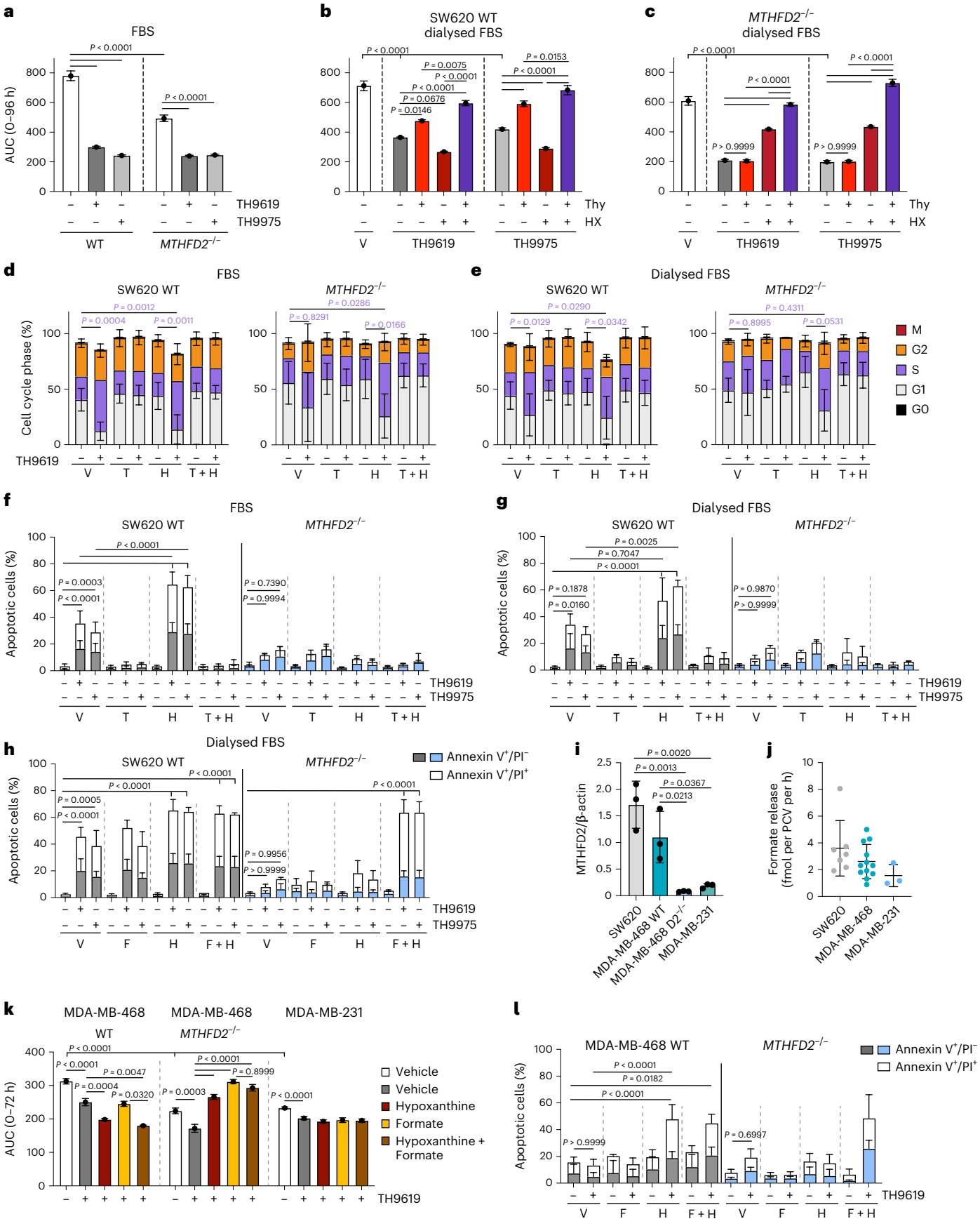

because of the considerable similarities of the active sites of these isoenzymes[16,36]. In this study, we reveal the complex biological mechanism of action behind TH9619 (and related TH9975) and show how it can be exploited to target both, MTHFD2-overexpressing cancers and cancers deficient in mitochondrial 1C metabolism.

We found that inhibition of the DC domain of MTHFD1 by TH9619 causes thymineless death specifically in MTHFD2-expressing cancer cells (Fig. 7f,g). This cell death induction occurs when MTHFD2-dependent formate is released from mitochondria and converted to 10-CHO-THF by the FS domain of MTHFD1. The 10-CHO-THF cannot be subsequently converted to 5,10-CH_2-THF because the MTHFD1(DC) activity is inhibited by TH9619. This generates a 'folate trap' and 10-CHO-THF accumulates (Fig. 5c–e). At the same time, free THF is consumed and SHMT1 becomes starved of its THF substrate, which blocks thymidylate synthesis. This folate trap (10-CHO-THF accumulation) is dependent on physiological levels of hypoxanthine as hypoxanthine inhibition of de novo purine synthesis in conjunction with TH9619 inhibition of MTHFD1(DC), further prevents consumption of 10-CHO-THF. The reduced thymidine levels after hypoxanthine and TH9619 treatment suggest that SHMT1 activity and generation of 5,10-CH_2-THF is impaired. We furthermore clearly demonstrate that treatment with TH9619 results in purine loss in *MTHFD2*$^{-/-}$ cells (Fig. 2i,j) because 5,10-CH_2-THF generated by SHMT1 cannot be converted to 10-CHO-THF and used for purine synthesis when TH9619 inhibits MTHFD1(DC) activity. Cytostatic effects of TH9619 in *MTHFD2*$^{-/-}$ cells due purine depletion are fully rescued with either hypoxanthine or sodium formate but not with thymidine (Fig. 3l and Extended Data Fig. 3d) as SHMT1 upholds thymidine supply in *MTHFD2*$^{-/-}$ cells. We were able to induce cytotoxic folate trapping in *MTHFD2*$^{-/-}$ cells by combining TH9619 with sodium formate and hypoxanthine (Figs. 6c,d and 7h). This switched the mode of action from cytostatic purine deficiency to cytotoxic thymidylate deficiency and cell death, which could then be rescued with thymidine addition (Fig. 6c,d). These experiments neatly illustrate the folate trapping model and provide evidence for the mode of action of TH9619 and TH9975.

Previously, we reported that *MTHFD2*$^{-/-}$, but not *MTHFD1*^{KD}, cells were highly resistant to TH9619 treatment[16], which suggested MTHFD2 rather than MTHFD1 was the drug target. This was not the case. Instead, we here show that mitochondrial MTHFD2 is not a drug target but that the observed resistance to TH9619 in *MTHFD2*$^{-/-}$ cells is due to the lack of mitochondrial formate release. As a consequence, *MTHFD2*$^{-/-}$ cells cannot feed the folate trap. As MTHFD1 is essential in many cancer cell lines[20], the surviving MTHFD1 clones in our previous work may have had marginal expression of MTHFD1 (as detected by faint bands on western blots[16]). Resistance to TH9619 in *MTHFD1*^{KD} cells was not observed because they still express MTHFD2 and, as we now know, can thus generate a toxic folate trap. This is a lesson learned to exercise caution in CRISPR–Cas9 target validation, as in our case CRISPR–Cas9 deletion of the MTHFD2 protein (that is, node removal) resulted in an edgetic perturbation[37] that changed the metabolic phenotype (that is, loss of mitochondrial formate release) of these cells. It was this change in phenotype, rather than the removal of the drug target, that made *MTHFD2*$^{-/-}$ cells resistant to TH9619. Together this reveals that while MTHFD1(DC) is the drug target, it is formate overflow driven by MTHFD2 that sensitizes cells to thymidylate depletion and cell death upon TH9619 treatment. The lack of inhibition of mitochondrial MTHFD2 is probably due to the physicochemical properties of TH9619 and TH9975, which as other folate-like compounds require active transport over membranes by mitochondrial folate transporter. Instead, we found that it is nuclear MTHFD2 that is stabilized by TH9619. There may also be important roles for TH9619 interfering with nuclear functions of MTHFD2, but this is a topic for future studies.

Although TH9619 is highly effective in killing HL-60 cancer cell in vitro (EC_{50} = 11 nM), only a marginal anticancer effect was observed in vivo, even with validation of in vivo target engagement in the tumour[16]. This is because the 1C metabolite levels in mice do not model the physiological levels in humans. In mice, thymidine (roughly 100-fold) and folate (roughly 100-fold) levels are much higher while hypoxanthine is 100–1,000-fold lower than in humans[32,38]. A slightly better effect was observed by using low-folate diet, which assisted in reducing murine THF levels and hence reduced the ability of SHMT1 to use abundant THF as a substrate for thymidylate synthesis on TH9619 treatment. However, low-folate diet does not reduce high thymidine levels in mouse plasma[16]. Furthermore, with the gained mechanistic insights we now have, the poor efficacy of TH9619 in mice is probably also explained by low plasma levels of hypoxanthine in mice (roughly 0.02 μM)[32], which is insufficient to inhibit the de novo purine pathway to support folate trapping. Therefore, mouse in vivo cancer models are probably unsuitable to predict TH9619 efficacy in humans. As such, a lack of appropriate animal models remains a limitation of this study.

Earlier, we reported that TH9619 and related compounds were highly toxic to cancer cells, while sparing non-malignant cells in vitro, demonstrating an impressive therapeutic index[16]. The reasoning was that MTHFD2 is an oncofetal protein, highly expressed during embryogenesis, largely silenced in adult cells and then re-expressed in cancer[6]. We have now discovered that the large therapeutic index is due to formate overflow, which we previously showed is a hallmark of cancer cells and requires mitochondrial 1C metabolism[22–24]. Without MTHFD2-driven formate release from mitochondria in cancer cells, the THF pool will not be depleted and 10-CHO-THF is not trapped (Extended Data Fig. 7). This is exemplified by the resistance of *MTHFD2*$^{-/-}$ cells to TH9619 in the presence of hypoxanthine, resembling non-transformed cells with low levels of MTHFD2 expression. It is also important to note that in cell lysates TH9619 is also able to inhibit MTHFD2L. MTHFD2L is expressed in both, normal and cancer cells, albeit at lower levels than MTHFD2 (ref. 39). Owing to the structural similarity of both isozymes it may be challenging to develop a highly specific MTHFD2 inhibitor[36]. However, in the case of TH9619, the lack of effect on mitochondrial 1C metabolism means that side effects caused by targeting MTHFD2L are highly unlikely. Moreover, the folate trapping mechanism now provides an incentive for developing MTHFD1(DC)-specific inhibitors to treat MTHFD2-expressing cancers. Last, the cancer selectivity of TH9619 is also probably explained by increased target engagement with TH9619 in cancer cells as compared to non-transformed cells[16]. This is due to active uptake of folate-like compounds such as TH9619 in cancer cells through folate transporters to support the increased folate demand in cancer cells to drive biomass generation for rapid proliferation.

In conclusion, we describe a previously uncharacterized folate (specifically 10-CHO-THF) trapping mechanism, that is generated by inhibition of MTHFD1(DC) activity by TH9619 and related compounds. We demonstrate a mechanism of action distinct from other MTHFD1/2 inhibitors (DS18561882, ref. 18), traditional antifolates (MTX) or antimetabolites targeting TYMS (5-FU). We propose that cancer selectivity of TH9619 is related to the MTHFD2-dependent release of mitochondrial formate, which is a hallmark of cancer cells. Future work should be devoted to identifying the nuclear function of MTHFD2 through development of MTHFD1 and MTHFD2-selective chemical probes, identifying TH9619 transporters, response biomarkers and analysis of primary patients' material under human physiological conditions to assist future clinical development. This study discovered that drugs targeting MTHFD1 can kill cancer cells that have upregulated MTHFD2, revealing cancer vulnerabilities that can be exploited for drug development.

Methods

Chemicals

Thymidine, hypoxanthine, sodium formate, adenine, adenosine, guanosine, deoxyuridine, H_2O_2 and pyrazofurin are from Sigma Aldrich. AICAr is from Chemtronica. Febuxostat is from Stratech Scientific Ltd. Allopurinol and Uric acid were from Merck Life Science UK.

Cell culture

SW620 (CLL-227), HCT116 (CLL-247), MDA-MB-468 (HTB-132) and MDA-MB-231 (HTB-26) cells were from ATCC. PA-TU-8988T cells were from DSMZ (ACC162). SW620 and HCT116 WT cells were authenticated by short-tandem repeat analysis. SW620 *MTHFD2*$^{-/-}$ and SW620 *SHTM1*$^{-/-}$ cells were purchased from Synthego using single-guide RNA sequences targeting exon 2 (5′-CGCCAACCAGGAUCACACUC-3′ for *MTHFD2*$^{-/-}$)[17] or exon 4 (5′-UCAGGUGGCCCCCAUCCGGA-3′ for *SHMT1*$^{-/-}$). MDA-MB-468 *MTHFD2*$^{-/-}$ cells were generated as described previously[24]. All cell lines were cultured in RPMI GlutaMAX (Life Technologies), except for PA-TU-8988T cells that were maintained in DMEM GlutaMAX (Life Technologies). Unless otherwise specified, all media were supplemented with 10% heat-inactivated FBS (Life Technologies), 100 U ml^{-1} penicillin and 100 µg ml^{-1} streptomycin (Life Technologies). Cell lines were maintained at 37 °C in 5% CO_2 humidified incubators, and routinely tested for mycoplasma using MycoAlertTM Kit (Lonza). HPLM was supplemented with 5% dFBS (Thermo Fisher Scientific). For experiments, 5 or 10% heat-inactivated or dFBS was used as indicated.

Resazurin cell viability

Inhibitors were dissolved in dimethylsulfoxide (DMSO) at 10 mM and dispensed to final concentrations in 384-well plates (Corning) using Echo 550 Liquid handler (Labcyte) or D300e digital dispenser (Tecan). Cells were seeded at 1,000 (SW620) and 500 (HCT116) cells per well in 50 µl of complete medium. Plates were incubated in a humidified chamber for 96 h at 37 °C and 5% CO_2. Cell viability was determined by adding 10 µg ml^{-1} resazurin (Sigma Aldrich) and measuring conversion to resorufin after 5 h. Fluorescence at 595 nm was measured with Hidex Sense reader and Hidex Sense Software v.1.0 (Hidex Oy) or SpectraMax iD5 reader (Molecular Devices). Half-maximal effective concentration (EC_{50}) was calculated with logistic nonlinear regression in Prism v.9.3.1 (GraphPad).

Mitochondrial membrane potential

SW620 cells were seeded at 5,000 per well in 96-well plates in complete medium 2–3 days before imaging. The next day, cells were treated with compounds for 48 h. Before imaging, cells were washed with PBS and incubated with 20 nM tetramethylrhodamine methyl ester (TMRM) (Molecular Probes) and 10 µM verapamil (Sigma Aldrich) for 30 min at 37 °C. Carbonyl cyanide p-trifluoromethoxyphenylhydrazone (FCCP, 20 µM, Sigma Aldrich) was used as a positive control. Cells were imaged live withSpark Cyto (Tecan) reader. TMRM fluorescence analysis in mitochondrial regions of interest was performed using CellProfiler.

Mitochondrial isolation and CETSA

Here, 2.5 × 10^6 SW620 cells were seeded on 150 mm dishes and grown for 4 days, followed by treatment for 3 h at 37 °C and 5% CO_2 in a humidified incubator. Mitochondria were isolated using Qproteome Mitochondria Isolation Kit (Qiagen, catalogue no. 37612), and mitochondrial material from two fractionations were pooled before proceeding to CETSA. Briefly, cells were gathered and normalized to cell count. Cells were washed in 0.9% NaCl and lysed for 10 min in 1 ml lysis buffer with protease inhibitors. To isolate cytosolic protein from mitochondria and nuclei, cells were centrifuged at 1,000*g*, 4 °C for 10 min. Pellet was resuspended in 1 ml disruption buffer with protease inhibitors and passed ten times through a 21-gauge needle, followed by centrifugation at 1,000*g*, 4 °C for 10 min. The supernatant, containing mitochondria, was saved and mitochondria were re-extracted from the pellet by resuspending in 500 µl disruption buffer, passing through a needle and centrifuging at 1,000*g*, 4 °C for 10 min. Mitochondrial supernatants were then centrifuged at 6,000*g*, 4 °C for 10 min. Mitochondrial pellets were washed in 1 ml mitochondrial storage buffer and centrifuged at 6,000*g*, 4 °C for 20 min. For CETSA, mitochondria were resuspended in 360 µl 1× TBS (50 mM Tris-HCl, 150 mM NaCl, pH 7.6) with protease inhibitors (Roche) and divided into 30 µl aliquots. Mitochondria were heated in a Veriti Thermal Cycles (Applied Biosystems) for 3 min at indicated temperatures (temperature interval of 2.5 °C increases, from 42 to 62 °C) and cooled for 5 min at room temperature for precipitation of denatured proteins. Disruption of mitochondrial membrane was achieved by 4× freeze–thaw cycle in dry ice for 3 min and 37 °C for 3 min. Samples were cleared at 17,000*g*, 4 °C for 20 min. Supernatant was prepared for western blot analysis.

DARTS

Target engagement was determined using DARTS assay as previously described[16,26,40]. SW620 cells in logarithmic growth phase were collected by trypsinization and lysed 10 min on ice in M-PER buffer (Thermo Fisher Scientific) with protease inhibitors (Roche). Lysates were centrifuged at 16,000*g*, 4 °C for 10 min. Protein concentration was determined by Bradford method with Pierce Coomassie Plus Assay Reagent (Thermo Fisher Scientific). Samples were diluted in 1× TN buffer (50 mM Tris-HCl pH 8.0, 50 mM NaCl) and treated as indicated for 30 min at room temperature. Treated cell lysates were aliquoted into 20 µg protein aliquots and digested with pronase (Roche) at the indicated pronase to total protein ratios for 30 min at room temperature. Reaction was stopped by 4× Laemmli sample buffer (BioRad) with 100 mM dithiothreitol and boiling at 95 °C for 5 min. Protein stabilization was analysed by western blot.

For target engagement in intact cells, SW620 cells were treated in culture with indicated compounds for 3 h before collection, lysis and pronase treatment performed as described above.

Production of MTHFD1-Q100A

Complementary DNA encoding human MTHFD1-Q100A was ordered from Thermo Fisher Scientific and subcloned into pET22b using NdeI and SalI restriction enzymes and the bacterial expression vector pET22b-GFP-CPDSalI (kind gift from M. Bogyo and A. Shen; Addgene, 38257). Expression results in MTHFD1-Q100A C-terminally fused to cysteine protease domain (CPD) with C-terminal hexahistidin-tag[37]. MTHFD1-Q100A expression vector was transformed into *Escherichia coli* BL21 DE3 (Millipore, D48406). Bacterial culture was grown to an optical density (OD_{600}) of 0.6 when expression was induced by 1 mM isopropyl-β-D-thiogalactoside (Sigma Aldrich, I6758). Bacteria were cultured at 16 °C for 20 h and centrifuged at 5,000*g* for 20 min. Bacteria were lysed using BugBuster (Millipore, D48832) with complete protease inhibitor cocktail (Roche, 11697498001), Benzonase nuclease (Millipore, D48913, 2.5 mU ml^{-1}) and lysozyme (Sigma, L6876, 0.25 mg ml^{-1}). After rotation for 30 min at room temperature, lysate was cleared at 16,000*g*. Lysate was loaded onto 5 ml HisTrap HP column (GE Healthcare) equilibrated with buffer A (50 mM Tris-HCl pH 7.8, 250 mM NaCl, 5% glycerol) and washed with buffer A with 10 mM imidazole. Bound proteins were eluted with 40–500 mM imidazole gradient in buffer A. Fractions were analysed using SDS–PAGE and Coomassie G-250 colloidal staining. Fractions containing MTHFD1 DCQ100A were pooled and dialysed against buffer B (50 mM Tris-HCl pH 8.0, 150 mM NaCl, 10% glycerol, 1 mM TCEP) over night and incubated with 300 µM phytic acid ($InsP_6$) for 3 h at 5 °C to cleave CPD-tag. The His-tagged CPD protein was removed by passing over a 5 ml HisTrap column equilibrated with buffer B. The flow through fractions were collected and analysed using SDS–PAGE with Coomassie G-250 staining. Fractions with pure MTHFD1 DCQ100A were pooled and the concentration was determined using the Coomassie Plus Protein Kit (Thermo Scientific) using bovine serium albumin as a standard. Glycerol was added to 40% and protein was kept as aliquots at −20 °C.

MTHFD1 and MTHFD1-Q100A inhibition assay

Inhibition assay of MTHFD1 and MTHFD1-Q100A mutant was performed as described previously[16,40]. Assay buffer consisted of 25 mM MOPS (pH 7.3), 0.5 mM TCEP, 400 µM $NADP^+$ and 0.005% TritonX100. $NADP^+$ was purchased from Sigma (N5755). Working solution of

folitixorin (1.2% DMSO) was 60 µM in assay buffer. MTHFD1 WT and MTHFD1-Q100A mutant were diluted 0.5 nM in the assay buffer. Assay was performed as for MTHFD2 described in detail previously[40], but using white Non-Binding Surface 384-well plates (Corning, 3824) and with 1 µl of 2.75 mM Menadione (Sigma, M5625) in 20% DMSO 10 min before reading. The final concentration in 5 µl was 30 µM folitixorin, 400 µM $NADP^+$, 0.25 nM MTHFD1 WT or MTHFD1-Q100A.

TYMS, SHMT1 and SHMT2 inhibition assay

Inhibition of TYMS, SHTM1 and SHMT2 was measured as previously described[40].

CRISPR-Select

We carried out CRISPR-Select analysis as described previously[27]. SW620 cells were nucleofected with CRISPR-Select cassette composed of: (1) Alt-R SpCas9 Nuclease V3 with target specific genomic RNA (synthetic crRNA–tracrRNA duplex; Integrated DNA Technologies), (2) a single-stranded oligodeoxynucleotide (ssODN) repair template containing MTHFD1-Q100A and (3) an identical ssODN repair template containing a synonymous MTHFD1-Q100Q internal normalization mutation (WT′) (both Ultramer DNA oligonucleotides; Integrated DNA Technologies). Nucleofection was performed in a Lonza 4D-Nucleofectorwith SF Cell Line 4D-Nucleofector X Kit S and CM-130 pulse program. On day 2 postnucleofection, cell population was split in two and cultured with and without 10 µM TH9619. Medium was changed every 3 days and cells were split to roughly 20% when 70–80% confluency was reached. On day 25, 100 ng genomic DNA was used as template to PCR amplify and sequence MTHFD1 genomic target site by amplicon Next Generation Sequencing using the MiSeq Reagent Kit v.2 (Illumina) and MiSeq instrument (Illumina) according to manufacturer´s instructions. Data were analysed by CRISPResso2 online tool using default settings (https://crispresso.pinellolab.partners.org/submission) to determine frequencies of MTHFD1-Q100A and MTHFD1-Q100Q alleles in cell populations.

Stable isotope tracing

Experiments with [U-^{13}C]-serine and [2,3,3-^{2}H]-serine (Cambridge Isotope Laboratories) were performed in customized serine-, glycine- and glutamine-free RPMI-1640 (Cell Culture Technologies, Switzerland) with 0.4 mM glycine, 2 mM glutamine, 0.4 mM serine tracer and 10% FBS (or dFBS). Then 200,000 cells were seeded in 500 µl medium in 24-well plates in triplicates for each condition and in parallel triplicates for cell count and volume determination (to calculate the packed cell volume (PCV)). The day after, medium was replaced by 500 µl tracer medium with and without treatment. Three untreated wells per cell line were counted for start PCV. After 24 h of culture, one set of triplicate wells per condition were counted for end PCV. A parallel set of triplicate wells was used to collect medium for formate release rates and to preform metabolite extraction for liquid chromatography–mass spectrometry (LC–MS) analysis.

Formate release rates

Formate extraction, derivatization and quantification in medium from stable isotope tracing experiments was performed as described previously[23].

LC–MS analysis of metabolite levels and mass isotopologue distribution

We carried out LC–MS analysis as described previously[23]. Cells in 24-well plates were washed with 500 µl cold PBS and extracted with 200 µl extraction solvent (MeOH:acetonitrile:H_2O, 50:30:20) for 5 min at 4 °C under agitation. Solvent was centrifuged full speed, 10 min at 4 °C and supernatant was submitted for analysis. The LC–MS setup consisted in a Vanquish Flex (Thermo Scientific) LC system configured in binary gradient and coupled with a Q-Exactive Plus mass spectrometer (Thermo Scientific) and piloted by Xcalibur software (v.4.4.16.14, Thermo Scientific). The column was a SeQuant ZIC-pHILIC (Merck) (2.1 × 150 mm, 5 µm) with a guard column (2.1 × 20 mm) and was heated at 45 °C in the column oven. Solvent A is 20 mM ammonium carbonate pH 9.2 with 5 µM of medronic acid. Solvent B is pure acetonitrile. Samples were eluted by linear gradient from 80% B to 20% B in 15 min at constant flow rate of 200 µl min^{-1}. MS acquisition was performed with a polarity switch between positive and negative electrospray ionization modes. Full MS spectra were acquired from 75 to 1,000 *m/z* at 70,000 resolution (at 200 *m/z*) with an automatic gain control set to 1×10^6 charges and a maximum ion trap fill time of 250 ms. Data were analysed with TraceFinder (v.4.1, Thermo Scientific) and Skyline software (v.21.2). Data normalization and natural isotope subtraction were performed using in house scripts as previously reported[23].

Analysis of dTMP deuterium labelling

Data were acquired with the above described LC–MS system in negative polarity using targeted selected ion monitoring (tSIM) method. Ions were filtered by the quadrupole with an isolation window of 8 Da centred on 323.061 *m/z* and accumulated in C-trap for a maximum of 250 ms and a maximum of 5×10^5 charges. Ions were analysed by the orbitrap at a resolution of 140,000 (at 200 *m/z*). Data were analysed with TraceFinder (v.4.1) using a 30 ppm mass tolerance for data processing. Natural isotope subtraction using in house scripts as described previously[23] was used to correct deuterium labelling for ^{13}C natural isotope abundance.

Quantification of hypoxanthine in FBS

Heat-inactivated FBS and dFBS were precipitated by a tenfold dilution in the extraction buffer (MeOH:acetonitrile:H_2O, 50:30:20). Samples were further diluted 1:1 by hypoxanthine standard solution to yield seven calibration points from 0 to 30 nM of added hypoxanthine. Endogenous concentration of the hypoxanthine was calculated as the absolute value of the *x* intercept of the linear regression curve. FBS samples were diluted 1,000 times more than dFBS to match concentration range. Data were acquired with the above described LC–MS system but using parallel reaction monitoring acquisition. Hypoxanthine protonated cation was selected at unit resolution by the quadrupole, fragmented with a normalized collision energy of 40. Maximum ion accumulation time was set to 220 ms and resulting fragment ions were analysed by the orbitrap at a resolution of 70,000 (at 200 *m/z*). The tandem MS (MS/MS) signal of the hypoxanthine's fragment ions 119.0353, 110.0350, 94.0400, 82.0400, 67.0292 and 55.0294 *m/z* was extracted and summed with Skyline software (v.21.2)[41].

Quantification of 10-formyl THF

Sample preparation was adapted from Schittmayer et al.[42] and Chen et al.[43] Here, 11×10^6 SW620 WT and *MTHFD2*$^{-/-}$ cells were seeded in 10 ml culture medium in 75 cm^2 flasks. 24 h after seeding, medium was exchanged to 10 ml of RPMI-1640 with 10% dFBS and cells were treated as indicated for 24 h. Then $15–30 \times 10^6$ cells were collected by trypsination and pellets were washed with PBS. Solution in PBS was counted to determine cell count and size for PCV normalisation. Then 500 µl of ice-cold derivatization buffer (80% methanol, 30 mM NaB_2H_3CN, 0.2% $^{13}CO_2H_2$ and 0.1% acetic acid) was added to cell pellets and incubated on ice for 60 min. After centrifugation, supernatant was collected and evaporated in vacuum centrifuge. Samples were suspended in 450 µl aqueous buffer (50 mM K_2HPO_4, 0.5% 2-mercaptoethanol pH 7.0), mixed with 25 µl of charcoal purified rat serum and incubated for 2 h at 37 °C to cleave poly-glutamate tails. Samples were acidified with 3.5 µl of formic acid and purified using Bond Elute-PH SPE columns (Agilent). Columns were conditioned with 1 ml of MeOH and 1 ml of 25 mM of ammonium acetate pH 4.0. Samples were loaded onto the columns, washed with 1 ml of 25 mM ammonium acetate pH 4 and eluted in 400 µl elution buffer (50% methanol, 0.5% 2-mercaptoethanol, 49.5%

25 mM ammonium acetate at pH 7.0). Eluates were evaporated and resuspended in 50 µl of 80% MeOH with 0.5% acetic acid for analysis by LC–MS. Data were acquired with the above described LC–MS system in parallel reaction monitoring acquisition mode with positive ionization. The derivatized precursor ion of 10-formyl THF (492.211 *m*/*z*) was selected by the quadrupole at unit resolution and fragmented at a normalized collision energy of 20. The resulting fragment ions were accumulated for up to 1,000 ms, with a maximum number 1×10^6 charges and analysed by the orbitrap at a resolution of 140,000 (at 200 *m*/*z*). The MS/MS signal fragment-ion 317.1629 *m*/*z* was used for quantification as described by Schittmayer et al.[42]. The absence of interference with 5-formyl THF was controlled using pure standard solutions for 10-formyl-THF and 5-formyl THF. MS data were processed with Skyline software (v.22.2) with a 5 ppm mass error tolerance on the centroid signal.

Proliferation

Cells were seeded at low density in 96-well plates in 4–8 technical replicates per condition. Cell proliferation was determined as cell confluence using the IncuCyte Live-Cell Analysis system and IncuCyte ZOOM 2021C and 2018A software (Essen Bioscience). Area under curve (AUC) of cell confluence curves from 0 to 96 h were calculated in GraphPad v.9 and displayed as means ± s.e.

Cell cycle analysis by flow cytometry

SW620 cells were cultured for 48 h in RPMI containing 10% FBS or dFBS and treated as indicated. Cells were collected, washed and resuspended in PBS. Cells were resuspended in fixation/permeabilization buffer and washed in permeabilization buffer (Thermo Fisher Scientific). Cells were stained with Ki-67 eFluor 506 (1:20, BioLegend) and p-Histone H3 AlexaFluor488 (1:50, BioLegend) or isotype controls in permeabilization buffer at 4 °C in the dark. Cells were washed twice in permeabilization buffer then resuspended in 100 µl PBS containing 10 µg ml^{-1} Hoechst 33342 (Life Technologies) and 100 µg ml^{-1} RNaseA[5] (Thermo Scientific) and incubated for 15 min at room temperature in the dark. Samples were analysed on a BD LSRII with BD FACSDiva software (BD Biosciences) and data analysed in FlowJo (v.10.7.2, BD).

Cell death measurement using annexinV-PI staining

Cells were seeded at 100,000 cells per well in 1 ml in 12-well plates and treated the subsequent day as indicated. After 96 h, samples were collected and stained as previously[24]. Measurement was done at NovoCyte Quanteon (Agilent) with NovoExpress software (Agilent, v.1.5.0). Analysis was conducted in FlowJo (v.10.6.2, BD).

Sphere growth assay

Cells were cultured in Ultra Low Attachment Flasks, collected in a 50 ml Falcon and centrifuged at 300*g* for 5 min. Pellet was resuspended in 1 ml of TripLE and incubated 5 min at 37 °C. Culture medium was added to deactivate TripLE (Thermo Fisher). Cell suspension was centrifuged 5 min at 300*g*, pellet was resuspended in 1 ml of Plasmax (custom made) and counted with CEDEX XS (INNOVATIS). Here 5,000 cells were seeded in each well of a 96-well, cell repellent-treated, U-shaped-bottom microplate (Greiner). The plate was centrifuged at 300*g* for 5 min and incubated for 2 days at 37 °C to allow sphere formation. Spheres were treated with 1 µM TH9619 and imaged on Cytation5 (Agilent) on day 0 and day 5 after treatment. Sphere size and area was measured using binary pictures and particle analysis in ImageJ.

Western blot

Cell pellets were incubated for 30 min on ice in lysis buffer (150 mM NaCl, 1 mM EDTA, 50 mM Tris-HCl, 1% NP-40) and sonicated. Lysates were centrifuged at 13,000*g*, 10 min 4 °C. Supernatant was collected and stored at −80 °C. Protein concentration was determined by Bradford assay. 15–30 µg of total protein were loaded on RunBlue 4–12% Bis-Tris gels (Westburg) using 4× NuPage LDS Sample buffer (Thermo Fisher Scientific) with 10 mM DTT (Sigma Aldrich) and blotted onto nitrocellulose membrane according to standard protocols. Membranes were blocked with 5% milk-powder in tris-buffered saline with Tween and incubated with primary antibodies over night at 4 °C. Incubation with secondary antibody was performed light-protected for 2 h at room temperature. Detection was done with Odyssey CLx Infrared Imaging System (LI-COR). ImageStudioLite v.5.2 (LI-COR) was used for analysis.

Antibodies

Antibodies used for western blotting were: rabbit anti-MTHFD1 (Thermo Fisher Scientific, PA5-42825; 1:1,000), rabbit anti-MTHFD1 (Atlas Antibodies, HPA-000704; 1:500), rabbit anti-MTHFD1L (Proteintech, 16113-1-AP; 1:1,000), rabbit anti-MTHFD2 (Cell Signaling Technology, 41377, D8W9U; 1:1,000), mouse anti-MTHFD2 (Abcam, ab56772; 1:500), rabbit anti-SHMT1 (Sigma Aldrich, HPA023314; 1:1,000), rabbit anti-SHMT2 (Sigma Aldrich, HPA020549; 1:1,000), rabbit anti-HSP60 (Abcam, ab46798; 1:1,000), rabbit anti-Vinculin (Cell Signaling Technology, 4650; 1:1,000), rabbit anti-Lamin A/C (Cell Signaling Technology, 2032; 1:1,000), mouse anti-α-Tubulin (Abcam, ab7291; 1:20,000), mouse anti-ATP synthase beta (Invitrogen, A21351; 1:1,000), rabbit anti-TOM20 (Proteintech, 11802-1-AP-150; 1:1,000), mouse anti-β-actin (Cell Signaling Technology, 3700, clone 8H10D10; 1:3,000) and mouse anti-SOD1 (Santa Cruz Biotechnology, sc-17767; 1:1,000). Secondary antibodies were: IRDye 680RD Goat Anti-Mouse IgG (H+L) (Li-Cor Biosciences, 926-68070; 1:10,000), IRDye 800CW Donkey Anti-Mouse IgG (H+L) (Li-Cor Biosciences, 926-32212; 1:5,000), IRDye 800CW Donkey Anti-Rabbit IgG (H+L) (Li-Cor Biosciences, 926-32213; 1:5,000 or 1:10,000), Peroxidase AffiniPure Donkey Anti-Rabbit IgG (Jackson ImmunoResearch, 711-035-152; 1:5,000) and Peroxidase AffiniPure Donkey Anti-Mouse IgG (Jackson ImmunoResearch, 715-035-150; 1:5,000).

Chemical synthesis of TH9975

Please see the Supplementary Information for a detailed protocol.

Quantification and statistical analysis

All data were plotted and statistical analysis was carried out in Prism v.9.3.1 (GraphPad Software). Data are plotted as means ± standard deviation (s.d.) or means ± standard error (AUC plots) as indicated in the figure legends. Standard deviation is indicated for all cases where $n \geq 3$. The number of replicates (n) corresponds to the number of independent experiments or independent cell cultures and is indicated in the figure legends.

Reporting summary

Further information on research design is available in the Nature Portfolio Reporting Summary linked to this article.

Data availability

All data generated or analysed during the present study, including source data, can be found in the article, Extended Data or Supplementary Information. Source data are provided with this paper.

References

1. Bester, A. C. et al. Nucleotide deficiency promotes genomic instability in early stages of cancer development. *Cell* **145**, 435–446 (2011).
2. Helleday, T. & Rudd, S. G. Targeting the DNA damage response and repair in cancer through nucleotide metabolism. *Mol. Oncol.* **16**, 3792–3810 (2022).
3. Henriksson, S., Groth, P., Gustafsson, N. & Helleday, T. Distinct mechanistic responses to replication fork stalling induced by either nucleotide or protein deprivation. *Cell Cycle* **17**, 568–579 (2018).

4. Locasale, J. W. Serine, glycine and one-carbon units: cancer metabolism in full circle. *Nat. Rev. Cancer* **13**, 572–583 (2013).
5. Yang, M. & Vousden, K. H. Serine and one-carbon metabolism in cancer. *Nat. Rev. Cancer* **16**, 650–662 (2016).
6. Nilsson, R. et al. Metabolic enzyme expression highlights a key role for MTHFD2 and the mitochondrial folate pathway in cancer. *Nat. Commun.* **5**, 3128–3128 (2014).
7. Newman, A. C. & Maddocks, O. D. K. Serine and functional metabolites in cancer. *Trends Cell Biol.* **27**, 645–657 (2017).
8. Tibbetts, A. S. & Appling, D. R. Compartmentalization of mammalian folate-mediated one-carbon metabolism. *Annu. Rev. Nutr.* **30**, 57–81 (2010).
9. Lee, W. D. et al. Tumor reliance on cytosolic versus mitochondrial one-carbon flux depends on folate availability. *Cell Metab.* **33**, 190–198.e196 (2021).
10. Ducker, G. S. & Rabinowitz, J. D. One-carbon metabolism in health and disease. *Cell Metab.* **25**, 27–42 (2017).
11. Meiser, J. & Vazquez, A. Give it or take it: the flux of one-carbon in cancer cells. *FEBS J.* **283**, 3695–3704 (2016).
12. Pietzke, M., Meiser, J. & Vazquez, A. Formate metabolism in health and disease. *Mol. Metab.* **33**, 23–37 (2019).
13. Ducker, G. S. et al. Reversal of cytosolic one-carbon flux compensates for loss of the mitochondrial folate pathway. *Cell Metab.* **23**, 1140–1153 (2016).
14. Jain, M. et al. Metabolite profiling identifies a key role for glycine in rapid cancer cell proliferation. *Science* **336**, 1040–1044 (2012).
15. Dekhne, A. S., Hou, Z., Gangjee, A. & Matherly, L. H. Therapeutic targeting of mitochondrial one-carbon metabolism in cancer. *Mol. Cancer Ther.* **19**, 2245–2255 (2020).
16. Bonagas, N. et al. Pharmacological targeting of MTHFD2 suppresses acute myeloid leukemia by inducing thymidine depletion and replication stress. *Nat. Cancer* **3**, 156–172 (2022).
17. Pikman, Y. et al. Targeting MTHFD2 in acute myeloid leukemia. *Blood* **126**, 443–443 (2015).
18. Kawai, J. et al. Discovery of a potent, selective, and orally available MTHFD2 inhibitor (DS18561882) with in vivo antitumor activity. *J. Med. Chem.* **62**, 10204–10220 (2019).
19. Ju, H. Q. et al. Modulation of redox homeostasis by inhibition of MTHFD2 in colorectal cancer: mechanisms and therapeutic implications. *J. Natl Cancer Inst.* **111**, 584–596 (2019).
20. Tsherniak, A. et al. Defining a cancer dependency map. *Cell* **170**, 564–576 e516 (2017).
21. Ducker, G. S. et al. Human SHMT inhibitors reveal defective glycine import as a targetable metabolic vulnerability of diffuse large B-cell lymphoma. *Proc. Natl Acad. Sci USA* **114**, 11404–11409 (2017).
22. Meiser, J. et al. Increased formate overflow is a hallmark of oxidative cancer. *Nat. Commun.* **9**, 1368 (2018).
23. Meiser, J. et al. Serine one-carbon catabolism with formate overflow. *Sci. Adv.* **2**, e1601273 (2016).
24. Kiweler, N. et al. Mitochondria preserve an autarkic one-carbon cycle to confer growth-independent cancer cell migration and metastasis. *Nat. Commun.* **13**, 2699 (2022).
25. Gustafsson Sheppard, N. et al. The folate-coupled enzyme MTHFD2 is a nuclear protein and promotes cell proliferation. *Sci. Rep.* **5**, 15029 (2015).
26. Huang, L., Wang, D. & Zhang, C. Drug affinity responsive target stability (DARTS) assay to detect interaction between a purified protein and a small molecule. *Methods Mol. Biol.* **2213**, 175–182 (2021).
27. Niu, Y. et al. Multiparametric and accurate functional analysis of genetic sequence variants using CRISPR-Select. *Nat. Genet.* **54**, 1983–1993 (2022).
28. Li, G., Wu, J., Li, L. & Jiang, P. p53 deficiency induces MTHFD2 transcription to promote cell proliferation and restrain DNA damage. *Proc. Natl Acad. Sci. USA* **118**, e2019822118 (2021).
29. Herbig, K. et al. Cytoplasmic serine hydroxymethyltransferase mediates competition between folate-dependent deoxyribonucleotide and S-adenosylmethionine biosyntheses. *J. Biol. Chem.* **277**, 38381–38389 (2002).
30. Lewis, C. A. et al. Tracing compartmentalized NADPH metabolism in the cytosol and mitochondria of mammalian cells. *Mol. Cell* **55**, 253–263 (2014).
31. Vande Voorde, J. et al. Improving the metabolic fidelity of cancer models with a physiological cell culture medium. *Sci. Adv.* **5**, eaau7314 (2019).
32. Cantor, J. R. et al. Physiologic medium rewires cellular metabolism and reveals uric acid as an endogenous inhibitor of UMP synthase. *Cell* **169**, 258–272 e217 (2017).
33. Henderson, J. F. & Khoo, K. Y. On the mechanism of feedback inhibition of purine biosynthesis de novo in ehrlich ascites tumor cells in vitro. *J. Biol. Chem.* **240**, 3104–3109 (1965).
34. An, S., Kumar, R., Sheets, E. D. & Benkovic, S. J. Reversible compartmentalization of de novo purine biosynthetic complexes in living cells. *Science* **320**, 103–106 (2008).
35. Hennequart, M. et al. The impact of physiological metabolite levels on serine uptake, synthesis and utilization in cancer cells. *Nat. Commun.* **12**, 6176 (2021).
36. Scaletti, E. et al. The first structure of human MTHFD2L and its implications for the development of isoform-selective inhibitors. *Chem. Med. Chem.* **17**, e202200274 (2022).
37. Zhong, Q. et al. Edgetic perturbation models of human inherited disorders. *Mol. Syst. Biol.* **5**, 321 (2009).
38. Leamon, C. P. et al. Impact of high and low folate diets on tissue folate receptor levels and antitumor responses toward folate-drug conjugates. *J. Pharmacol. Exp. Ther.* **327**, 918–925 (2008).
39. Nilsson, R., Nicolaidou, V. & Koufaris, C. Mitochondrial MTHFD isozymes display distinct expression, regulation, and association with cancer. *Gene* **716**, 144032 (2019).
40. Bonagas, N. et al. Supplementary methods for 'Pharmacological targeting of MTHFD2 suppresses acute myeloid leukemia by inducing thymidine depletion and replication stress'. *Protocol Exchange* https://doi.org/10.21203/rs.3.pex-1730/v1 (2022).
41. Adams, K. J. et al. Skyline for small molecules: a unifying software package for quantitative metabolomics. *J. Proteome Res.* **19**, 1447–1458 (2020).
42. Schittmayer, M., Birner-Gruenberger, R. & Zamboni, N. Quantification of cellular folate species by LC-MS after stabilization by derivatization. *Anal. Chem.* **90**, 7349–7356 (2018).
43. Chen, L., Ducker, G. S., Lu, W., Teng, X. & Rabinowitz, J. D. An LC-MS chemical derivatization method for the measurement of five different one-carbon states of cellular tetrahydrofolate. *Anal. Bioanal. Chem.* **409**, 5955–5964 (2017).

Acknowledgements

We thank the members of the Helleday laboratory for fruitful discussions. We also thank M. Benzarti from the Cancer Metabolism Group at the Luxembourg Institute of Health and F. Rodriguez from the Molecular Disease Mechanisms Group at University of Luxembourg for their technical assistance and C. Jäger from the LCSB Metabolomics Platform at University of Luxembourg for providing technical and analytical support. This project is supported by the Weston Park Cancer Centre and the University of Sheffield (A.C.G. and T.H.), a DFG fellowship (no. KI 2508/1-1, N.K.), the Mobility programme for the FPU predoctoral fellowship from Ministerio de Universidades of the Spanish Government (grant no. FPU17/02185, J.J.J.-A.), the Helleday Foundation (P.M., C.C., S.B. and M.L.), Karolinska Institute's KID funding

for doctoral students (N.B.), the Novo Nordisk Foundation (grant no. 17OC0029972, T.H.), the Swedish Cancer Society (grant nos. 2018/600, 2021/1490, T.H.), the Swedish Children's Cancer Foundation (grant nos. 2018-0095, 2021-0030, T.H.), the Swedish Research Council (grant nos. 2015-00162, 2017-06095, T.H.), Vinnova (grant nos. 2018-00257, 2021-04817, T.H.), Torsten and Ragnar Söderberg Foundation (T.H.), the Luxembourg National Research Fund (FNR) and Fondation Cancer (grant nos. C20/BM/14582635, E.M. and C20/BM/14592342, J.P.), the FNRS-Télévie (grant nos. 7.4509.20 and 7.4572.22, E.V.), the FNR-ATTRACT programme (A18/BM/11809970, J.M.), a FNR-CORE grant (no. C21/BM/15718879, J.M.) and the FNR-PRIDE i2Tron (grant no. PRIDE19/14254520, K.E.) programme.

Author contributions

Conceptualization was done by A.C.G., T.H., M.H. and J.M. Chemical synthesis was carried out by M.H., K.S.A.V. and S.B. Biology experiments were carried out by A.C.G., P.M., N.K., C.C., E.W., V.C., K.E., F.B., M.L., E.K.G., J.J.J.-A., E.V., M.M., A.I.J., O.H., N.B., L.S. and L.R. Biochemistry experiments and protein production were carried out by E.W., A.-S.J. and O.L. Methodology, investigation and formal analysis were carried out by A.C.G., P.M., N.K., C.C., E.W., V.C., A.L., K.E., K.S.A.V., S.B., M.L., E.K.G., J.J.J.-A., A.I.J., A.-S.J., O.L., O.H., A.L., N.B., L.R., L.S., E.H. and M.H. The original draft was written by A.C.G., P.M., N.K., M.H., T.H. and J.M. Review and editing of the draft were conducted by A.C.G., P.M., N.K., M.H., A.S., T.H. and J.M. Data curation was carried out by A.C.G., P.M. and N.K. Visualization was carried out by A.C.G., P.M., N.K. and T.H. A.C.G., P.M., O.M., E.H., M.F., E.M., J.P., E.L., C.S.S., A.S., T.H., M.H. and J.M. supervised the project. Funding and resources were acquired by A.C.G., T.H. and J.M.

Competing interests

MTHFD1/2 inhibitors are developed toward the clinic by the company One-Carbon Therapeutics AB. A.S. is an employee of One-Carbon Therapeutics AB. T.H. owns shares in One-Carbon Therapeutics AB and P.M., E.W., S.B., A.-S.J., O.L., O.M., E.H., N.B. and M.H. have rights to One-Carbon Therapeutics AB. The remaining authors declare no competing interests.

Additional information

Extended data is available for this paper at https://doi.org/10.1038/s42255-023-00771-5.

Supplementary information The online version contains supplementary material available at https://doi.org/10.1038/s42255-023-00771-5.

Correspondence and requests for materials should be addressed to Thomas Helleday, Martin Henriksson or Johannes Meiser.

Peer review information *Nature Metabolism* thanks Deepak Nagrath, Kim Kampen and the other, anonymous, reviewer(s) for their contribution to the peer review of this work. Primary Handling Editor: Alfredo Gimenez-Cassina, in collaboration with the *Nature Metabolism* team.

Reprints and permissions information is available at www.nature.com/reprints.

Publisher's note Springer Nature remains neutral with regard to jurisdictional claims in published maps and institutional affiliations.

Open Access This article is licensed under a Creative Commons Attribution 4.0 International License, which permits use, sharing, adaptation, distribution and reproduction in any medium or format, as long as you give appropriate credit to the original author(s) and the source, provide a link to the Creative Commons license, and indicate if changes were made. The images or other third party material in this article are included in the article's Creative Commons license, unless indicated otherwise in a credit line to the material. If material is not included in the article's Creative Commons license and your intended use is not permitted by statutory regulation or exceeds the permitted use, you will need to obtain permission directly from the copyright holder. To view a copy of this license, visit http://creativecommons.org/licenses/by/4.0/.

© The Author(s) 2023

[1]Weston Park Cancer Centre and Mellanby Centre for Musculoskeletal Research, Department of Oncology and Metabolism, The Medical School, University of Sheffield, Sheffield, UK. [2]Science for Life Laboratory, Department of Oncology-Pathology, Karolinska Institutet, Solna, Sweden. [3]Cancer Metabolism Group, Department of Cancer Research, Luxembourg Institute of Health, Luxembourg, Luxembourg. [4]RISE Research Institutes of Sweden, Södertälje, Sweden. [5]RedGlead Discover, Lund, Sweden. [6]Biotech Research and Innovation Centre, University of Copenhagen, Copenhagen, Denmark. [7]Department of Pharmacology, Faculty of Pharmacy, University of Seville, Seville, Spain. [8]Faculty of Science, Technology and Medicine, Department of Life Sciences and Medicine, Molecular Disease Mechanisms Group, University of Luxembourg, Esch-sur-Alzette, Luxembourg. [9]Tumor Stroma Interactions, Department of Cancer Research, Luxembourg Institute of Health, Luxembourg, Luxembourg. [10]Swedish Metabolomics Centre, Department of Plant Physiology, Umeå University, Umeå, Sweden. [11]Department of Forest Genetics and Plant Physiology, Swedish University of Agricultural Sciences, Umeå, Sweden. [12]Drug Discovery and Development Platform, Science for Life Laboratory, Department of Organic Chemistry, Stockholm University, Solna, Sweden. [13]One-carbon Therapeutics AB, Stockholm, Sweden. [14]These authors contributed equally: Alanna C Green, Petra Marttila, Nicole Kiweler. [15]These authors jointly supervised this work: Thomas Helleday, Martin Henriksson, Johannes Meiser. ✉e-mail: thomas.helleday@scilifelab.se; martin.henriksson@scilifelab.se; Johannes.Meiser@lih.lu

https://doi.org/10.1038/s42255-023-00771-5

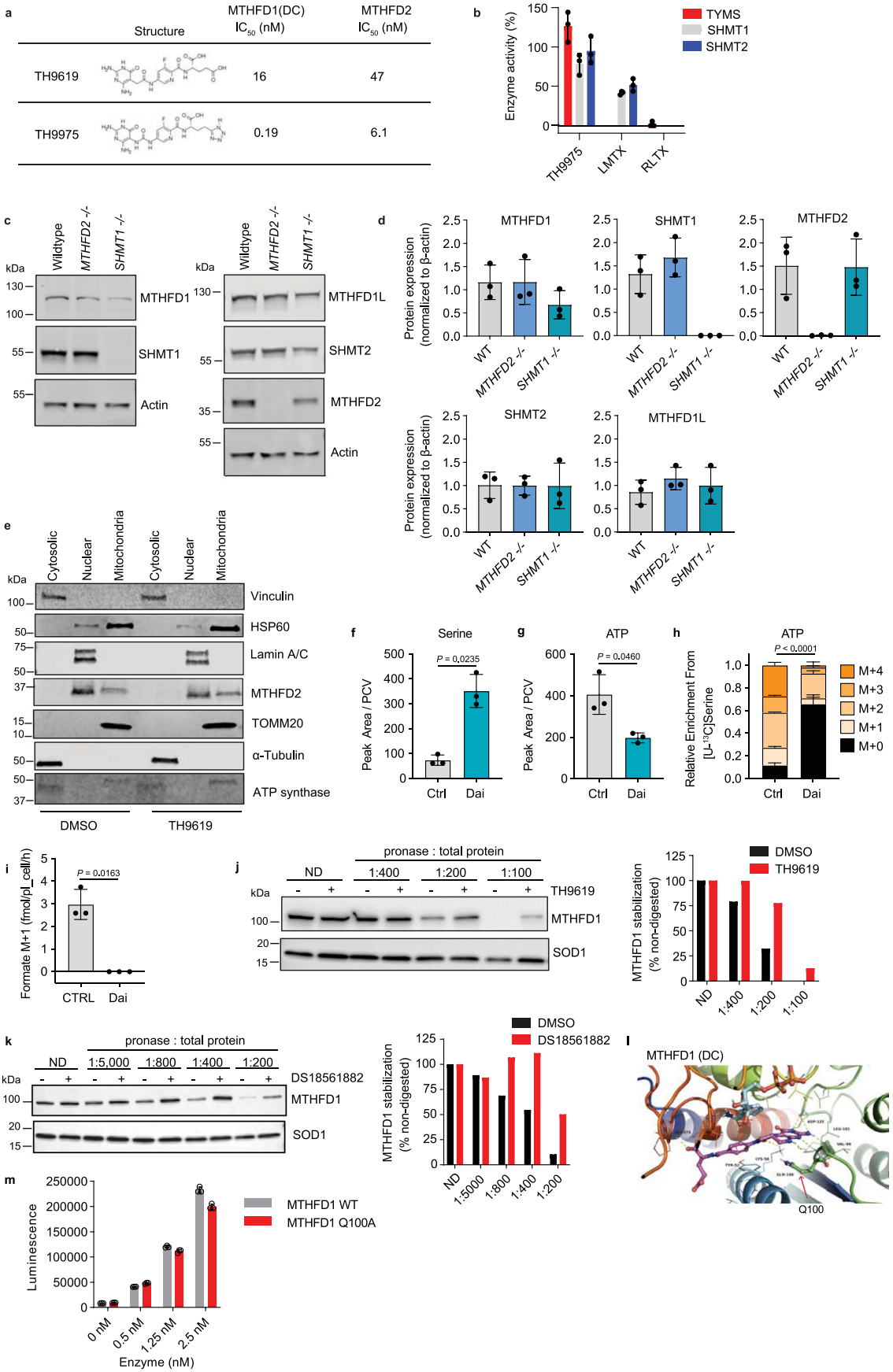

Extended Data Fig. 1 | See next page for caption.

https://doi.org/10.1038/s42255-023-00771-5

Extended Data Fig. 1 | TH9619 and TH9975 are inhibitors of MTHFD1(DC) *in vitro*. (**a**) Chemical structures of MTHFD1/2 inhibitors TH9619 and TH9975 and IC_{50} values for inhibition of MTHFD1(DC) and MTHFD2 enzymatic activities for each inhibitor. (**b**) Enzymatic activity of TYMS, SHMT1 and SHMT2 upon incubation with 100 µM TH9975 compared to their known inhibitors lometrexol (LMTX) and raltitrexed (RLTX), means ± SD (n = 3). (**c**, **d**) Expression of the indicated proteins was analyzed by Western Blot in SW620 WT, *MTHFD2*$^{-/-}$ and *SHMT1*$^{-/-}$ cells. β-actin served as loading control. Immunoblots are representative of 3 independent repeats. Signal intensity was quantified and normalized to loading control and global mean, means ± SD (n = 3). (**e**) Verification of the purity of mitochondrial and nuclear fractions for CETSA analysis. Shown are representative immunoblots of one out of two independent experiments. (**f**, **g**) Serine and ATP levels normalized to packed cell volume (PCV) in SW620 WT cells treated for 24 h with 10 µM DS18561882, mean ± SD (n = 3); paired, two-tailed t-test. (**h**) [U-^{13}C]serine-derived MID of ATP in SW620 WT cells treated for 24 h with 10 µM DS18561882, mean ± SD (n = 3); one-way ANOVA with Šídák's multiple comparison test for M + 0. (**i**) [U-^{13}C]serine-derived release rate of formate M + 1 isotopologue from SW620 WT cells treated for 24 h with 10 µM DS18561882, mean ± SD (n = 3); paired, two-tailed t-test. (**j**, **k**) DARTS analysis of MTHFD1 stabilization in SW620 cells upon TH9619 (**j**) or DS18561882 (**k**) treatment. Intact cells (**j**) or cell lysates (**k**) were incubated with 10 µM TH9619 or vehicle for 3 h (**j**) or 30 min (**k**), followed by protein digestion at increasing pronase concentration and assessment of MTHFD1 degradation by Western blot. MTHFD1 intensities were normalized to SOD1; one representative immunoblot of two independent experiments. (**l**) Design of MTHFD1/2 inhibitor resistant MTHFD1 protein based on the crystal structure of structurally similar MTHFD2 bound to LY345899 (PDB ID: 5TC4). Highlighted is the residue Q100 that was mutated to alanine (Q100A) and tested in downstream biochemical assays. (**m**) Enzymatic activity of purified MTHFD1(DC) WT and MTHFD1(DC) mutant (Q100A), means ± SD (n = 3).

https://doi.org/10.1038/s42255-023-00771-5

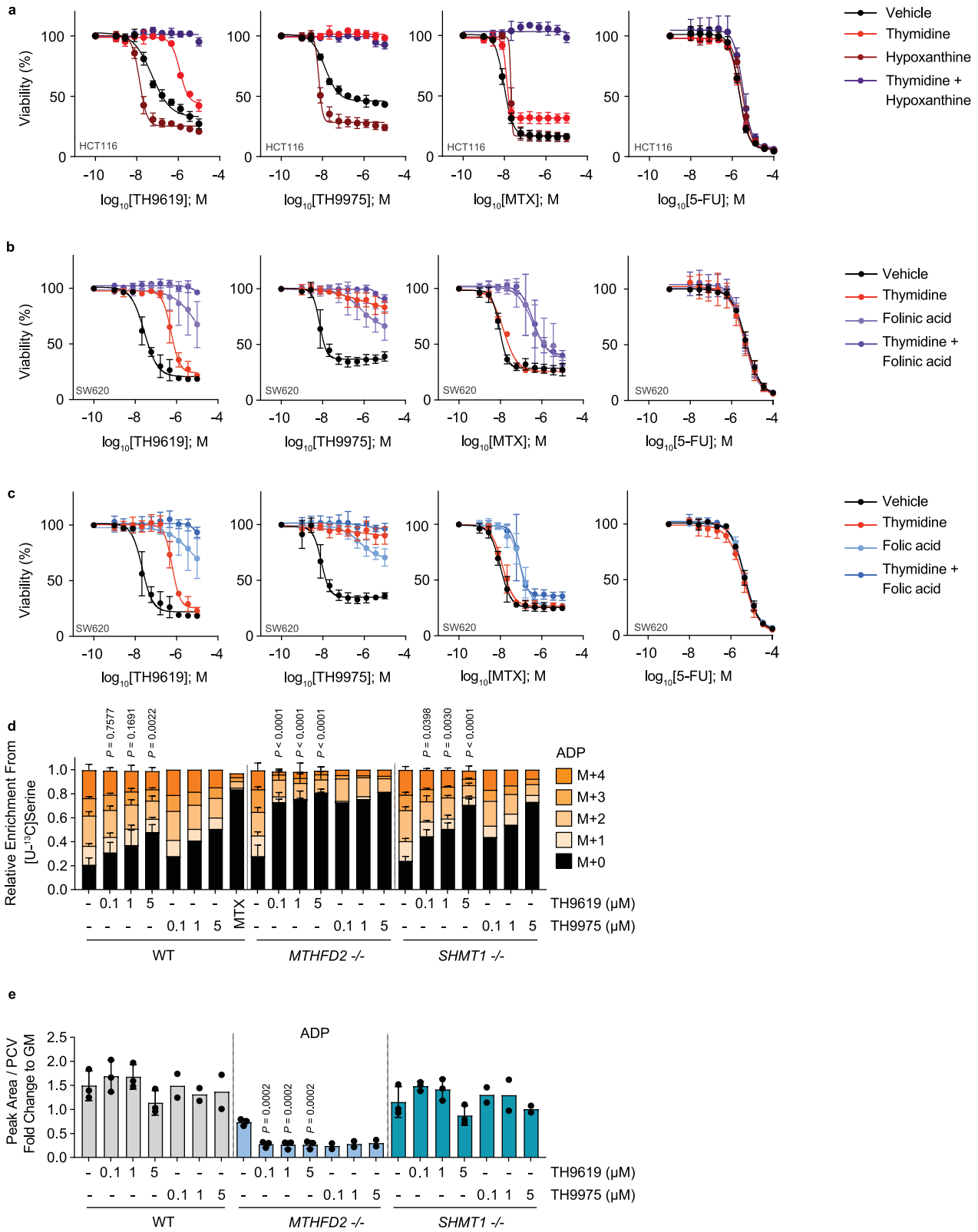

Extended Data Fig. 2 | See next page for caption.

https://doi.org/10.1038/s42255-023-00771-5

Extended Data Fig. 2 | Thymidine and folinic acid or folic acid rescue TH9619 and TH9975 toxicity in SW620 WT cells. (**a**) Dose-response curves of HCT116 cells treated for 96 h with TH9619, TH9975, methotrexate (MTX) or 5-fluorouracil (5-FU) and 50 µM thymidine, 250 µM hypoxanthine or vehicle (cultured in RPMI-FBS), means ± SD (n = 3). (**b**) Dose-response curves of SW620 cells treated for 96 h with TH9619, TH9975, MTX or 5-FU and 50 µM thymidine, 1 µM folinic acid or vehicle (cultured in RPMI-FBS), means ± SD (n = 3). (**c**) Dose-response curves of SW620 cells treated for 96 h with TH9619, TH9975, MTX or 5-FU and 50 µM thymidine, 250 µM folic acid or vehicle (cultured in RPMI-FBS), means ± SD (n = 3). (**d**) [U-^{13}C]serine- derived MID of ADP in SW620 WT, *MTHFD2*$^{-/-}$ and *SHMT1*$^{-/-}$ cells treated for 24 h with the indicated concentrations of TH9619 and TH9975 in µM or 50 nM MTX (cultured in RPMI-FBS), means ± SD (n = 3 for untreated and TH9619, n = 2 for TH9975, n = 1 for MTX); one-way ANOVA with Tukey's multiple comparisons test for M + 0. *P*-values indicate comparisons to the untreated control of each cell line. (**e**) ADP levels normalized to packed cell volume (PCV) in SW620 WT, *MTHFD2*$^{-/-}$ and *SHMT1*$^{-/-}$ cells treated for 24 h with the indicated concentrations of TH9619 and TH9975 in µM (cultured in RPMI-FBS), mean ± SD (n = 3 for untreated and TH9619, n = 2 for TH9975); one-way ANOVA with Dunnett's test for multiple comparisons. *P*-values indicate comparisons to the untreated control.

https://doi.org/10.1038/s42255-023-00771-5

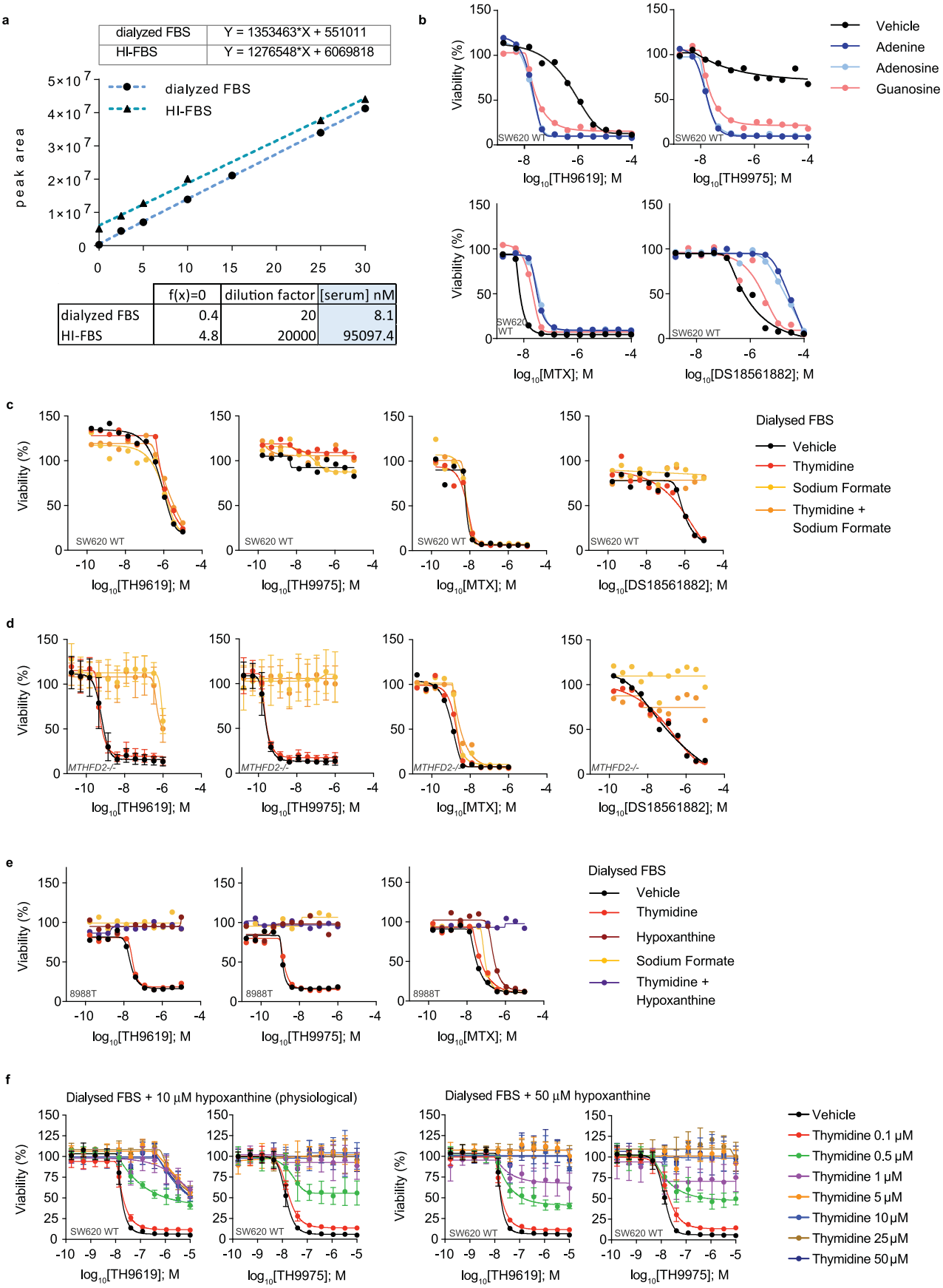

Extended Data Fig. 3 | See next page for caption.

https://doi.org/10.1038/s42255-023-00771-5

Extended Data Fig. 3 | External supply of sodium formate rescues viability of cells with impaired mitochondrial 1C folate cycle. (**a**) HX concentration in HI-FBS and dialyzed FBS was determined by titration with HX standard of known concentration. Linear regression of the standard curve was used to calculate y-intercept and corresponding HX concentration in nM in pure HI-FBS or dialyzed FBS. (**b**) Dose-response curves of SW620 WT cells treated for 96 h with TH9619, TH9975, methotrexate (MTX) or DS18561882 and 50 µM adenine, 50 µM adenosine, 50 µM guanosine or vehicle (cultured in RPMI-dFBS), means (n = 2 independent cell cultures). (**c**) Dose-response curves of SW620 WT cells treated for 96 h with TH9619, TH9975, MTX or DS18561882 and 50 µM thymidine, 1 mM sodium formate or vehicle (cultured in RPMI-dFBS), means (n = 2 independent cell cultures). (**d**) Dose-response curves of SW620 *MTHFD2*$^{-/-}$ cells treated as in (**c**). Means ± SD (n = 4 independent cell cultures for TH9619 and TH9975, n = 2 for MTX and DS18561882). (**e**) Cell viability dose-response curves of PA-TU-8988T cells treated for 96 h with TH9619, TH9975 or MTX and 50 µM thymidine, 50 µM hypoxanthine, 1 mM sodium formate or vehicle (cultured in DMEM-dFBS), means (n = 2 independent cell cultures). (**f**) Dose-response curves of SW620 WT cells treated for 96 h with TH9619 or TH9975 and increasing doses of thymidine. Cells were cultured in media containing dFBS and 10 or 50 µM hypoxanthine, means ± SD (n = 4).

https://doi.org/10.1038/s42255-023-00771-5

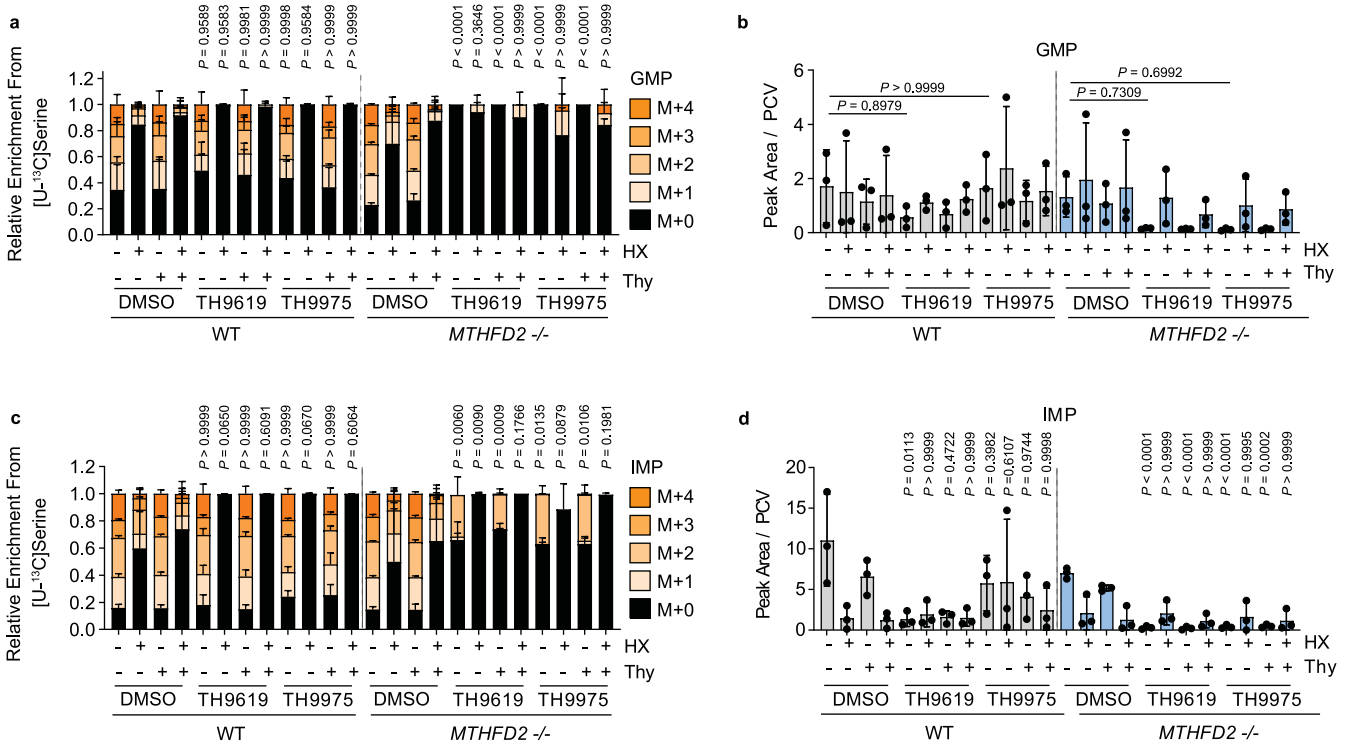

Extended Data Fig. 4 | TH9619 and TH9975 impair GMP synthesis in SW620 *MTHFD2-/-* cells and reduce IMP levels in SW620 WT and *MTHFD2-/-* cells. (**a**–**d**) [U-^{13}C]serine- derived MID of GMP (**a**) and IMP (**c**) and levels of GMP (**b**) and IMP (**d**) normalized to packed cell volume (PCV) in SW620 WT and *MTHFD2*$^{-/-}$ cells treated for 24 h with 1 µM TH9619 or TH9975, 50 µM hypoxanthine and 50 µM thymidine (cultured in RPMI-dFBS), means ± SD (n = 3); one-way ANOVA with Šídák's multiple comparisons test. For panels a and c, statistical analysis was performed for M + 0. *P*-values indicate comparisons to respective DMSO controls.

https://doi.org/10.1038/s42255-023-00771-5

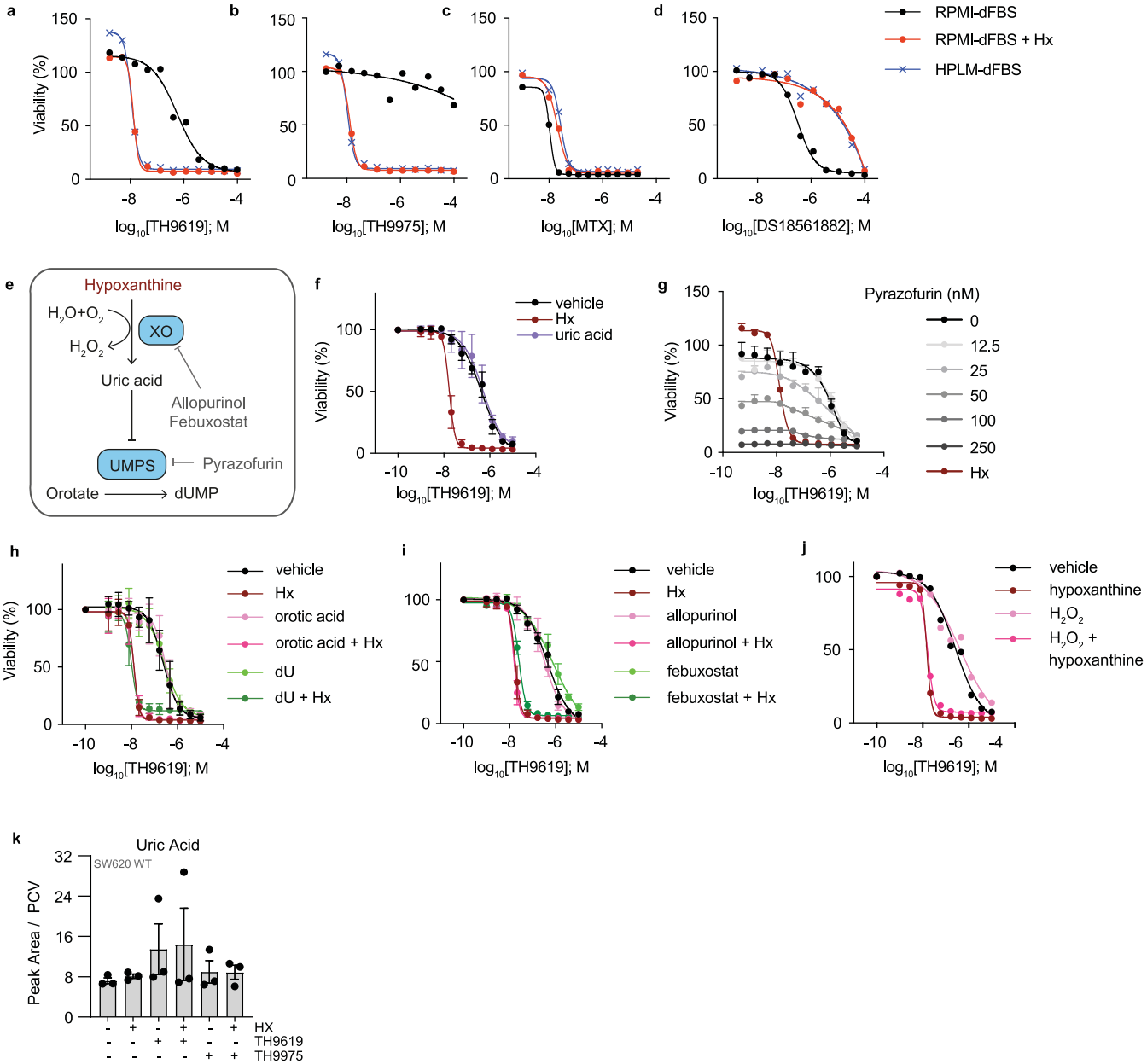

Extended Data Fig. 5 | Inhibition of UMPS is not a major contributor to MTHFD1/2i toxicity. (**a**–**d**) Dose-response curves of SW620 cells treated for 96 h with TH9619, TH9975, methotrexate (MTX) or DS18561882 (cultured in RPMI-dFBS, RPMI-dFBS with 50 µM hypoxanthine or HPLM-dFBs), one representative experiment displayed as means (n = 2 independent cell cultures). (**e**) Hypothesis that hypoxanthine converts to uric acid to inhibit UMPS. (**f**) Dose-response curves of SW620 cells treated for 96 h with TH9619, 50 µM hypoxanthine, 350 µM uric acid or vehicle (cultured in RPMI-dFBS), means ± SD (n = 3). (**g**) Dose-response curves of SW620 cells treated for 96 h with TH9619, pyrazofurin or 50 µM hypoxanthine (cultured in RPMI-dFBS), means ± SD (n = 3 independent cell cultures). (**h**) Dose-response curves of SW620 cells treated for 96 h with TH9619, 50 µM hypoxanthine, 1 mM orotic acid, 500 µM deoxyuridine (dU) or vehicle (cultured in RPMI-dFBS), means ± SD (n = 3). (**i**) Dose-response curves of SW620 cells treated for 96 h with TH9619, 50 µM hypoxanthine (Hx), 10 µM allopurinol, 10 µM febuxostat or vehicles (cultured in RPMI-dFBS), means ± SD (n = 3). (**j**) Dose-response curves of SW620 cells treated for 96 h with TH9619 and 50 µM hypoxanthine, 100 µM H_2O_2 or vehicle (cultured in RPMI-dFBS), means (n = 2). (**k**) Uric acid levels normalized to PCV in SW620 WT cells treated for 24 h with 1 µM TH9619 or TH9975 and 50 µM hypoxanthine (cultured in RPMI-dFBS), means ± SD (n = 3).

https://doi.org/10.1038/s42255-023-00771-5

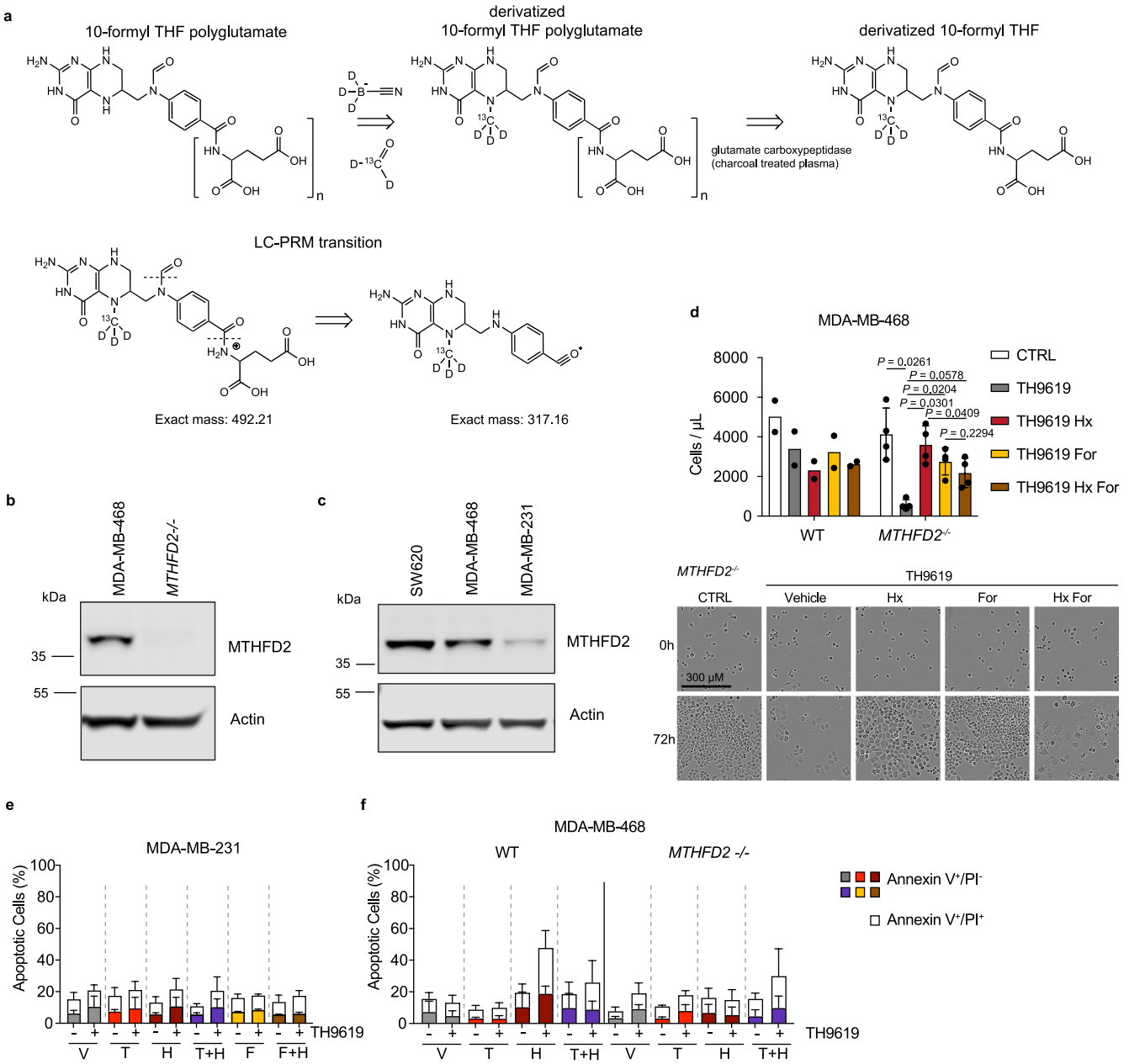

Extended Data Fig. 6 | Breast cancer cells MDA-MB-468 can be sensitized to TH9619. (**a**) Top: Reductive methylation reaction described by Schittmayer *et al.*[42] to stabilize the THF intermediates, followed by the cleavage of the glutamate tails by glutamate carboxypeptidase[43]. Bottom: Suggested mechanism for the tandem mass spectrometry fragmentation of 10-CHO-THF. (**b**, **c**) Protein expression of MTHFD2 was analyzed by Western Blot in MDA-MB-468 WT, MDA-MB-468 *MTHFD2*$^{-/-}$, MDA-MB-231 and SW620 cells to validate MTHFD2 KO in MDA-MB-468 cells and different expression levels in WT cells. β-actin was used as loading control. Images are representative of 3 independent repeats. Signal intensity was quantified and normalized to loading control and global mean and is shown in Fig. 7i. (**d**) Absolute cell count was measured as cell number/uL by flow cytometry in MDA-MB-468 WT and MDA-MB-468 *MTHFD2*$^{-/-}$ in response to 96 h treatment with 1 µM TH9619 and 50 µM hypoxanthine and 1 mM formate (cultured in RPMI-dFBS), means ± SD (n = 2 for WT and n = 4 for *MTHFD2*$^{-/-}$); one-way ANOVA with Tukey's multiple comparisons test was performed for *MTHFD2*$^{-/-}$ cells. Representative images for Fig. 7k of MDA-MB-468 *MTHFD2*$^{-/-}$ cell density and morphology are shown at 0 h and 72 h after treatment with 1 µM TH9619, 50 µM hypoxanthine and 1 mM formate (cultured in RPMI-dFBS). (**e**, **f**) Cell death analysis measured by AnnexinV/PI staining of MDA-MB-231, MDA-MB-468 WT and *MTHFD2*$^{-/-}$ cells in response to 96 h treatment with 1 µM TH9619, 50 µM hypoxanthine (H), 50 µM thymidine (T) and 1 mM formate (F, cultured in RPMI-dFBS), means ± SD (n = 2-6).

https://doi.org/10.1038/s42255-023-00771-5

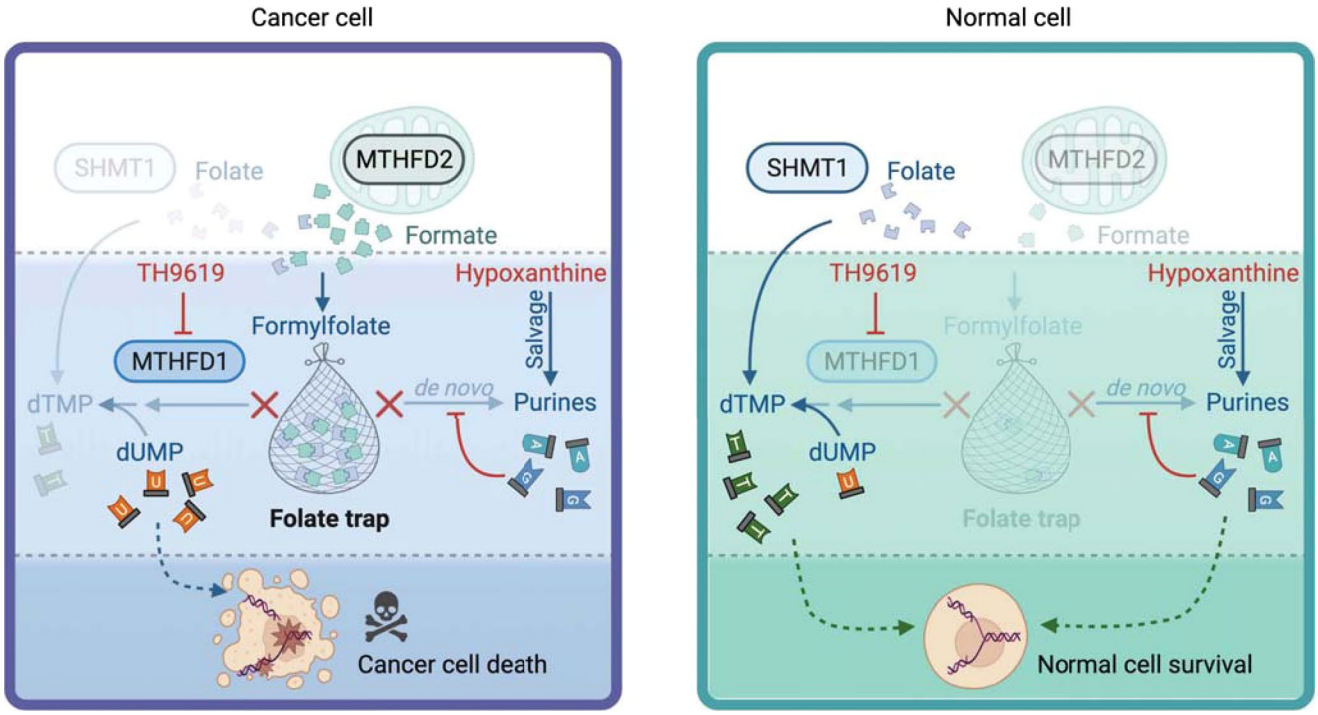

Extended Data Fig. 7 | TH9619 creates a folate trap in MTHFD2-expressing cancer cells, but not normal cells. Schematic shows generation of a cancer-specific folate trap with TH9619 treatment. High MTHFD2 expression, which is common in cancer cells, causes formate overflow from the mitochondria. Human physiological levels of hypoxanthine activate the purine salvage pathway, causing feedback inhibition on *de novo* purine synthesis, and preventing consumption of 10-formyl-tetrahydrofolate (10-CHO-THF). Simultaneous inhibition of MTHFD1 with TH9619 also blocks consumption of 10-formyl-tetrahydrofolate for synthesis of thymidylate. This generates a folate trap and depletes cells of the THF substrate that can no longer be used to synthesize thymidylate via SHMT1. As a consequence, dUMP accumulates, and leads to toxic DNA damage and cancer cell death. Healthy cells do not express high levels of MTHFD2 and hence lack the formate overflow required to fuel the folate trap. Image created with BioRender.com.

nature portfolio

Corresponding author(s): Johannes Meiser

Last updated by author(s): Feb 13, 2023

Reporting Summary

Nature Portfolio wishes to improve the reproducibility of the work that we publish. This form provides structure for consistency and transparency in reporting. For further information on Nature Portfolio policies, see our Editorial Policies and the Editorial Policy Checklist.

Statistics

For all statistical analyses, confirm that the following items are present in the figure legend, table legend, main text, or Methods section.

n/a	Confirmed	
☐	☒	The exact sample size (*n*) for each experimental group/condition, given as a discrete number and unit of measurement
☐	☒	A statement on whether measurements were taken from distinct samples or whether the same sample was measured repeatedly
☐	☒	The statistical test(s) used AND whether they are one- or two-sided *Only common tests should be described solely by name; describe more complex techniques in the Methods section.*
☒	☐	A description of all covariates tested
☐	☒	A description of any assumptions or corrections, such as tests of normality and adjustment for multiple comparisons
☐	☒	A full description of the statistical parameters including central tendency (e.g. means) or other basic estimates (e.g. regression coefficient) AND variation (e.g. standard deviation) or associated estimates of uncertainty (e.g. confidence intervals)
☐	☒	For null hypothesis testing, the test statistic (e.g. *F*, *t*, *r*) with confidence intervals, effect sizes, degrees of freedom and *P* value noted *Give P values as exact values whenever suitable.*
☒	☐	For Bayesian analysis, information on the choice of priors and Markov chain Monte Carlo settings
☒	☐	For hierarchical and complex designs, identification of the appropriate level for tests and full reporting of outcomes
☒	☐	Estimates of effect sizes (e.g. Cohen's *d*, Pearson's *r*), indicating how they were calculated

Our web collection on statistics for biologists contains articles on many of the points above.

Software and code

Policy information about availability of computer code

Data collection	Xcalibur 4.4.16.14 (Thermo Fisher), ImageStudio 5.2 (LI-COR Biosciences), NovoExpress 1.5.0 (Agilent), IncuCyte ZOOM 2021C and 2018A (Essen Bioscience), BD FACSDiva 8.0.1 (BD Bioscience), Hidex Sense Software 1.0 (Hidex Oy), Cytation 5 (Agilent)
Data analysis	TraceFinder 4.1 (Thermo Fisher), ImageStudio 5.2 (LI-COR Biosciences), FlowJo 10.6.2 or 10.7.2 (BD Biosciences), GraphPad Prism Vers9, IncuCyte ZOOM 2021C and 2018A (Essen Bioscience), ImageJ Fiji 2.5.0 (National Institutes of Health, MD, USA), Skyline software (21.2), CellProfiler, CRISPResso2 online tool

For manuscripts utilizing custom algorithms or software that are central to the research but not yet described in published literature, software must be made available to editors and reviewers. We strongly encourage code deposition in a community repository (e.g. GitHub). See the Nature Portfolio guidelines for submitting code & software for further information.

Data

Policy information about availability of data

All manuscripts must include a data availability statement. This statement should provide the following information, where applicable:

- Accession codes, unique identifiers, or web links for publicly available datasets
- A description of any restrictions on data availability
- For clinical datasets or third party data, please ensure that the statement adheres to our policy

All data generated or analyzed during the present study, including source data, can be found in the article, Extended Data or Supplementary Information. Source data are provided with this paper.

Human research participants

Policy information about studies involving human research participants and Sex and Gender in Research.

Reporting on sex and gender	N/A
Population characteristics	N/A
Recruitment	N/A
Ethics oversight	N/A

Note that full information on the approval of the study protocol must also be provided in the manuscript.

Field-specific reporting

Please select the one below that is the best fit for your research. If you are not sure, read the appropriate sections before making your selection.

☒ Life sciences ☐ Behavioural & social sciences ☐ Ecological, evolutionary & environmental sciences

For a reference copy of the document with all sections, see nature.com/documents/nr-reporting-summary-flat.pdf

Life sciences study design

All studies must disclose on these points even when the disclosure is negative.

Sample size	For flow cytometry, between 10,000 and 30,000 single cell events were acquired and quantified per replicate and condition following the guidelines by Cossarizza et al., 2019 (Guidelines for the use of flow cytometry and cell sorting in immunological studies - 2nd edition). Unless otherwise stated, n=3 was chosen as the minimal number of biological replicates per experiment that would allow for adequate analysis to draw meaningful conclusions of the data. We determined this to be sufficient based on the low observed variability between samples from these cell culture in vitro experiments.
Data exclusions	No data were excluded from analysis.
Replication	All experiments in this study were performed at least twice under independent experimental conditions. All attempts at replication have been successful. To ensure reproducibility, same reagent suppliers and catalog numbers were maintained as long as possible at all concerned experimental locations. When new reagents needed to be used, validation and optimization experiments were conducted to ensure comparable results.
Randomization	In vitro experiments were not randomized, but independent experiments were for example performed in different formats and by different investigators as mitigiation measures to cancel out experimental bias. Also, cells were randomly seeded from one cell population and plate lanes were randomly allocated to condtions. All Mass Spec samples were randomized during analysis to avoid bias from e.g. instrument drift.
Blinding	Blinding was not possible for in vitro experiments as treatment conditions were evident from the data. Quantifications were performed using computational pipelines (FlowJo for flow cytometry analysis, Tracefinder and MetaboliteDetector for Mass Spectrometry analysis).

Reporting for specific materials, systems and methods

We require information from authors about some types of materials, experimental systems and methods used in many studies. Here, indicate whether each material, system or method listed is relevant to your study. If you are not sure if a list item applies to your research, read the appropriate section before selecting a response.

Materials & experimental systems

n/a	Involved in the study
☐	☒ Antibodies
☐	☒ Eukaryotic cell lines
☒	☐ Palaeontology and archaeology
☒	☐ Animals and other organisms
☒	☐ Clinical data
☒	☐ Dual use research of concern

Methods

n/a	Involved in the study
☒	☐ ChIP-seq
☐	☒ Flow cytometry
☒	☐ MRI-based neuroimaging

Antibodies

Antibodies used

Anti-β-Actin (8H10D10) (Cell Signaling Technology Cat#3700; RRID:AB_2242334); Anti-MTHFD2 (Abcam Cat#ab56772; RRID:AB_2147537); Anti-MTHFD2 (D8W9U) (Cell Signaling Technology Cat#41377; RRID:AB_2799200); anti-MTHFD1 (Atlas Antibodies Cat#HPA000704; RRID:AB_1079424); Anti-MTHFD1 (Thermo Fisher Scientific Cat#PA5-42825; RRID:AB_2609491); MTHFD1L (Proteintech Cat.#16113-1-AP; RRID:AB_2250974); Anti-SHMT1 (Sigma-Aldrich Cat#HPA023314; RRID:AB_1856830); Anti-SHMT2 (Sigma-Aldrich Cat#HPA020549; RRID:AB_1856834); anti-HSP60 (Abcam Cat#ab46798; RRID:AB_881444); anti-Vinculin (Cell Signaling Technology Cat#4650; RRID:AB_10559207); anti-Lamin A/C (Cell Signaling Technology Cat#2032; RRID:AB_2136278); anti-α-Tubulin (Abcam Cat#ab7291; RRID:AB_2241126); anti-ATP synthase beta (Thermo Fisher Scientific Cat#A21351; RRID:AB_221512); anti-TOM20 (Proteintech Cat#11802-1-AP; RRID:AB_2207530); anti-SOD-1 (G-11) (Santa Cruz Biotechnology Cat#sc-17767; RRID:AB_628301); Alexa Fluor® 488 anti-Histone H3 Phospho (Ser10) Antibody (BioLegend Cat#650803; RRID:AB_10917386); eFluor 506 anti-human Ki-67 Antibody (Thermo Fisher Scientific Cat# 69-5698-82; RRID:AB_11151689); Goat Anti-Mouse IgG (H+L) (IRDye® 680RD) (LI-COR Biosciences Cat#926-68070; RRID:AB_10956588); Donkey Anti-Rabbit IgG (H+L) (IRDye® 800CW) (LI-COR Biosciences Cat#926-32213; RRID:AB_621848); Donkey Anti-Mouse IgG (H+L) (IRDye® 800CW) (LI-COR Biosciences Cat#926-32212; RRID:AB_621847); Peroxidase-AffiniPure Donkey Anti-Rabbit IgG (H+L) (Jackson ImmunoResearch Cat#711-035-152; RRID:AB_10015282); Peroxidase-AffiniPure Donkey Anti-Mouse IgG (H+L) (Jackson ImmunoResearch Cat#715-035-150; RRID:AB_234077).

Validation

All antibodies have been validated for use as stated on the manufacturer's product page:
Anti-β-Actin (8H10D10): KO validated. Suitable for ICC/IF, WB. Reacts with M, R, B, Dg, H, Mk, Hm. HeLa, Jurkat, NIH/3T3, PC-12, Rat2, CHO, MDBK and MDCK (DOx-inducible b-actin) whole cell lysates were used as positive controls.
Anti-MTHFD2 (Abcam): KO validated. Suitable for WB, IHC-P, Flow Cyt. Reacts with H. HEK293T, HepG2 and HeLa whole cell lysates were used as positive controls. In-house validation for IF and WB using siRNA KD and CRISPR KO.
Anti-MTHFD2 (D8W9U): Suitable for WB, IP. Reacts with H. HeLa and 293 whole cell lysates were used as positive control. In-house validation for WB using CRISPR KO.
anti-MTHFD1 (Atlas): Suitable for WB, IHC. Reacts with H, M, R. Validated with siRNA KD in A-431 whole cell lysates. In-house validation for WB using CRISPR KO.
anti-MTHFD1 (ThermoFisher): Suitable for WB, IHC. Reacts with H. Hep-G2 whole cell lysates were used as positive controls. In-house validation for WB using CRISPR KO.
Anti-MTHFD1L: Suitable for WB, IP, IHC, IF. Reacts with H, M. HEK-293, COLO 320, mouse ovary tissue, HeLa, HepG2 lysates were used as positive controls. In-house validation for WB using CRISPR KO and shRNA KD.
Anti-SHMT1: Suitable for WB, IHC. Reacts with H. U2-OS cells, human liver, testis and kidney tissue were used as positive control. In-house validation for WB using CRISPR KO.
Anti-SHMT2: Suitable for WB, IHC. Reacts with H, M, R. RH-30, NIH3T3, NBT-II, A-431 and U251 MG cells were used as positve control. In-house validation for WB using CRISPR KO.
anti-HSP60: Suitable for WB, IHC, IF, Flow Cyt, IP. Reacts with M, R, H, P. T47-D, MCF6, SW480 whole cell lysates were used as positive control.
anti-Vinculin: Suitable for WB. Reacts with H, M, R, Mk, Dg. HeLa, IGROV1, HepG2, RD, COS and MDCK whole cell lysates were used as positive control.
anti-Lamin A/C: Suitable for WB, IHC. Reacts with H, M, R. HeLa, Raw 264.7 and PC12 whole cell lysates were used as positive control. In-frame truncation mutation of lamin-encoding gene LMNA in HeLa cells was used for validation.
anti-α-Tubulin: Suitable for Flow Cyt, IF, IHC, WB. Reacts with M, R, H. HeLa, PC12, SV40LT-SMC, NIH/3T3, Rat liver tissue, Rat heart tissue lysate was used as positive control.
anti-ATP synthase beta: Suitable for WB, IF. Reacts with B, H, M, Mk, R. HepG2, SK-Ov-3, MDA-MB-231 were used as positive controls. Validated with siRNA KD in HepG2 cells.
anti-TOM20: Suitable for WB, IP, IHC, IF, Flow Cyt, ELISA. Reacts with H, M, R, B, C, Hm, Mk, P. HEK-293, HeLa, SH-SY5Y, mouse kidney tissue, rat kidney tissue lysates were used as positive control.
anti-SOD-1 (G-11): Suitable for WB, IP, IF, IHC, ELISA. Reacts with H. Jurkat, DU 145 an HEK293T whole cell lysates were used as positive controls.
Alexa Fluor® 488 anti-Histone H3 Phospho (Ser10): Suitable for Flow Cyt. Reacts with H. Validated in Nocodazole-treated HeLa cells.
eFluor 506 anti-human Ki-67: Suitable for Flow Cyt. Reacts with H, M, R. Validated with anti-mouse CD3e stimulated vs unstimulated mouse splenocytes.

Eukaryotic cell lines

Policy information about cell lines and Sex and Gender in Research

Cell line source(s)

SW620, HCT116, MDA-MB-468, MDA-MB-231 cells (ATCC), PA-TU-8988T cells (DSMZ). SW620 MTHFD2-/- and SHMT1-/- pools were purchased from Synthego. SW620 MTHFD2-/- and SHMT1-/- clones were generated from pools provided by Synthego, after validation of target deletion, early passage clonal cell lines were used in experiments. MDA-MB-468 MTHFD2-/- cells were generated and validated as described previously (Kiweler et al. 2022; 10.1038/s41467-022-30363-y).

	Optimization experiments were performed in 3-4 clones, and then one clone was selected for use in experiments across each location.
Authentication	SW620 and HCT116 cells were authenticated by STR analysis, frozen down and these stocks were used in experiments. PA-TU-8988T cells used in this study were newly purchased from DSMZ and the authenticity was confirmed by STR analysis by the supplier prior purchasing. These cells were cultured and expanded from the original vial obtained from the supplier frozen down and used in experiments.
Mycoplasma contamination	Cell lines were routinely tested for mycoplasma contamination using the MycoAlertTM Mycoplasma Detection Kit (Lonza). All cell lines in this study tested negative for mycoplasma contamination.
Commonly misidentified lines (See ICLAC register)	None of the cell lines used in this study are listed in the ILAC register of commonly misidentified cell lines.

Flow Cytometry

Plots

Confirm that:

☒ The axis labels state the marker and fluorochrome used (e.g. CD4-FITC).

☒ The axis scales are clearly visible. Include numbers along axes only for bottom left plot of group (a 'group' is an analysis of identical markers).

☒ All plots are contour plots with outliers or pseudocolor plots.

☒ A numerical value for number of cells or percentage (with statistics) is provided.

Methodology

Sample preparation	For Cell Cycle Analysis: Adherent cells were collected, washed and resuspended in PBS. Cells were resuspended in fixation/permeabilization buffer and washed in permeabilization buffer (Thermo Fisher Scientific). Cells were stained with Ki-67 eFluor 506 (1:20, BioLegend) and p-Histone H3 AlexaFluor488 (1:50, BioLegend) or isotype controls in permeabilization buffer at 4°C in the dark. Cells were washed twice in permeabilization buffer then resuspended in 100 µl PBS containing 10 ug/ml Hoechst 33342 (Life Technologies) and 100 ug/ml RNaseA5 (Thermo Scientific) and incubated for 15 minutes at room temperature in the dark. Samples were analyzed on a BD LSRII (BD Biosciences) and data analyzed in FlowJo (10.7.2, BD). For Cell Death Analysis: Adherent cells were washed with PBS. PBS fraction was collected and cells were detached with trypsin. Detached cells were collected in medium. All collected fractions were combined and centrifuged. The pellet was washed with PBS and resuspended in 50 µl AnnexinV-FITC staining solution (5% AnnexinV-FITC in AnnexinV binding buffer (10 mM HEPES pH 7.4, 140 mM NaCl, 2.5 mM CaCl2, 0.1% BSA in ddH2O)) and incubated for 15 min on ice in the dark. 450 µl PI-staining solution (1.1 µg/ml PI in AnnexinV binding buffer) was added immediately prior to measurement using NovoCyte Quanteon (Agilent) and NovoExpress software (Agilent, version 1.5.0). Analysis was performed in FlowJo Version 10.6.2 (BD).
Instrument	NovoCyte Quanteon (4025) (Agilent); BD LSR II 4 laser (BD Bioscience)
Software	Data aquisition: BD FACSDiva 8.0.1 (BD Bioscience) or NovoExpress 1.5.0 (Agilent); Data Analysis: FlowJo Software (Vers 10.6.2 or 10.7.2) (BD Biosciences)
Cell population abundance	A minimum of 10,000 events were acquired per sample following debris and doublet exclusion. Positive populations were determined using single-stained negative (unstained or isotype) and positive controls (e.g. heat-treated cell population for cell death analysis).
Gating strategy	FSC/SSC gating to exclude debris using unstained control (debris defined as small FSC vs. SSC). Doublets and cell aggregates were excluded by gating of FSC-A/FSC-H (for cell death analysis) or FSC/TOF (for cell cycle analysis).

☒ Tick this box to confirm that a figure exemplifying the gating strategy is provided in the Supplementary Information.

Purine Inhibition affects Redox State and activates Compensatory Mechanisms in Persistent Cancer Cells

Kim Eiden[1,2], Christina Krötz[1], Elisabeth Letellier[4], Nathalie Legrave[3,] Johannes Meiser[1]

[1]Cancer Metabolism Group, Department of Cancer Research, Luxembourg Institute of Health, Luxembourg, Luxembourg.

[2]Faculty of Science, Technology and Medicine, University of Luxembourg, Belvaux, Luxembourg.

[3]Metabolomics Platform, Department of Cancer Research, Luxembourg Institute of Health, Luxembourg, Luxembourg

[4]Department of Life Sciences and Medicine at the University of Luxembourg, University of Luxembourg, Belvaux, Luxembourg

Contact: Johannes.meiser@lih.lu

Abstract

Enzymes involved in purine nucleotide biosynthesis have emerged as promising drug targets, due to their high expression across various cancer types [1-4]. As the inhibition of enzymes involved in essential metabolic pathways often leads to an activation of adaptation and resistance mechanisms, we aimed to elucidate the metabolic rewiring occurring in purine inhibited cancer cells. In the present study, we show that purine depletion, leads to proliferation arrest but does not induce toxicity in cancer cells. However, the activity of the pentose phosphate pathway (PPP) is entirely shut down in those cells. Consequently, purine deleted cancer cells have to withstand increased levels of reactive oxygen species (ROS). We observe that cancer cells increase glutamine consumption and enhance activity of malic enzyme (ME), potentially compensating for PPP loss. In sum, our study provides deep mechanistic insight into the metabolic changes occurring upon purine depletion and elucidates metabolic vulnerabilities, which could serve as secondary targets leading to a more efficient elimination of tumor cells.

Introduction

Purine biosynthesis is a critical metabolic pathway for rapidly proliferating cells, including cancer cells, as purines such as adenine and guanine represent essential building blocks for DNA and RNA synthesis. Furthermore, they are involved in energy metabolism and serve as signalling molecules. Enzymes catalysing purine biosynthesis are often upregulated in various tumor types and are linked to a poor patient prognosis [2, 3, 5-7].

The generation of purine nucleotides occurs via two main pathways: the *de novo* pathway, constructing purine nucleotides using small molecule precursors (glutamine, glycine, aspartate, CO_2, formate) and the salvage pathway recycling purines such as hypoxanthine, guanine and adenine into nucleotides. Although it is traditionally believed that the *de novo* pathway is the predominant source for purines in cancers cells, recent studies demonstrated that also the salvage pathway contributes to the cellular nucleotide pool, to different extends depending on the tumor's tissue of origin [8].

The high reliance of cancer cells on nucleotide production makes it a metabolic vulnerability and a promising drug target for cancer therapy, which has been widely exploited since the 1950s, with antifolates and thymidylates synthesis (TYMS) inhibitors, being the first chemotherapeutic drugs used in the clinic [9].

However, despite strong preclinical efficacy of purine specific inhibitors, their clinical success remained moderate, especially for solid tumors. Lometrexol, inhibits the enzyme glycinamide ribonucleotide formyltransferase (GART) and has been studied as a potential cancer target. It entered phase I of clinical studies, however, its development was curtailed due to significant toxicities [10]. Also the bifunctional enzyme phosphoribosylaminoimidazole carboxylase and phosphoribosylaminoimidazolesuccinocarboxamide synthetase (PAICS) has emerged as a promising drug target as it is overexpressed in many cancers and depletion of PAICS has been shown to reduce tumor growth in various cancer models [11, 12]. But so far toxic side effects of PAICS inhibitors in *in vivo* models could not be excluded. Nevertheless, new inhibitors against nucleotide biosynthesis keep being developed and purine metabolism remains a promising approach to target tumor growth. Purines play an essential role not only in cancer cells but also in the tumor microenvironment (TME), influencing immune cell function. Interestingly, studies demonstrated that purine levels can positively affect tumor-specific immune regulation, highlighting the potential of purine inhibitors as complementary strategies in cancer immunotherapy [13-16].

Despite the great potential to target purine metabolism, metabolic flexibility may activate compensatory mechanisms thereby limiting treatment efficacy. In the present study we focus on such adaptation mechanisms. We provide mechanistic insights into the metabolic changes

occurring in purine inhibited cancer cells, which in contrast to pyrimidine inhibition undergo proliferation arrest, but do not necessarily die. Instead, purine depleted cancer cells persist in a growth arrested state, undergo epithelial to mesenchymal (EMT) transition and even gain migratory potential, providing key traits leading to the onset of metastasis [17]. Here, we show that metabolic rewiring allows purine inhibited cancers cells to sustain. At the same time these adaptations reveal secondary targets to potentially increase the therapeutic efficacy of anti-purine therapies.

Results

Inhibition of purine biosynthesis induces proliferation arrest but no toxicity in cancer cells

To investigate the metabolic adaptations in purine inhibited cancer cells, we used two different cellular models: cancer cells lacking bifunctional methylenetetrahydrofolate dehydrogenase/cyclohydrolase 2 (MTHFD2) treated with TH9619 and tumor cells treated with specific purine *de novo* synthesis protein inhibitors against PAICS (PAICSi) [12] and against GART (GARTi) [10] (Fig. 1a). In MTHFD2 deficient cells, the transfer of one carbon units into the purine ring could still occur via the reverse cytosolic one carbon metabolism (OCM) flux. To prevent this, MTHFD2$^{-/-}$ cells were treated with 1 µM TH9619, which inhibits the dehydrogenase/cyclohydrolase (DC) function of trifunctional methylenetetrahydrofolate dehydrogenase/cyclohydrolase/formyltetrahydrofolate synthetase 1 (MTHFD1) [18, 19]. TH9619 treatment of MTHFD2-/- cells thereby prevents the endogenous production of 10-CHO-THF, the essential building block for purine de novo synthesis. In both models, intracellular levels of the purine containing nucleotides ATP and GTP were significantly reduced (Fig. 1b,c). Of note, in SW620 WT cells, TH9619 had no effect on purine levels, emphasising that the mitochondrial OCM is sufficient to sustain purine *de novo* biosynthesis (Fig. 1b). The decrease of ATP and GTP pools in MTHFD2$^{-/-}$ cells was completely rescued by providing exogenous purine derivative hypoxanthine (HX) which can restore purine levels through the salvage pathway. Purine depletion and rescue by HX was replicated by targeting purine biosynthesis with GARTi or PAICSi (Fig. 1c). In contrast, treatment with pemetrexed (PEM), an antifolate and inhibitor of thymidylate synthetase (TYMS) [20] and fluorouracil (5FU), also blocking TYMS [21], left purine levels unchanged or even led to a small increase (Fig 1c).

We have shown previously, that treating WT cells with TH9619 leads to thymidylate (dTMP) depletion and induces cancer cell death. Surprisingly, when giving cells HX in addition to TH9619, we observed that the purine derivative exacerbated the toxicity of TH9619 by promoting dTMP depletion in WT cells [19]. The mechanism behind has been identified as the so called “folate trap”, where the lack of free THF prohibits dTMP synthesis, which becomes toxic for proliferating cancer cells as they start incorporating uridine instead of thymidine into newly synthesized DNA, resulting in DNA damage and cell death [19]. In MTHFD2$^{-/-}$ cells, the free THF pool remains stable and TH9619 leads to purine inhibition, which has no effect on cancer cell toxicity (Fig. 1d, Suppl. Fig. 1a). Of note, it is important to emphasise the differential role of HX in both scenarios, whereas the purine derivative acts as a rescue in the purine depleted condition (MTHFD2$^{-/-}$ cells treated with TH9619) the molecule becomes toxic in WT cells treated with TH9619 as it enhances the trapping of free folate (Fig. 1b,d) [19].

Here, we were able to recapitulate those results with specific inhibitors. PEM and 5FU significantly lowered dTMP levels (Fig 1e) and consequently induced early and late apoptosis (Fig. 1f,g). However, inhibition of purine biosynthesis by GARTi and PAICSi only induced growth arrest but did not affect cell death (Fig. 1f, h). Furthermore, while looking at DNA damage markers at protein level, we observed a clear upregulation upon dTMP depletion but not in purine inhibited cells (Suppl. Fig. 1b).

Mechanistically, we observed an inactivation of the mTOR pathway upon purine inhibition (Suppl. Fig. 1c), presumably enabling tumor cells to metabolically adapt and slowing down proliferation. Indeed it has been shown that mTORC1 signalling is sensitive to purine nucleotide levels [22, 23] . This goes in line with activation of AMP-activated protein kinase (AMPK), a key energy sensor and counter regulator to mTOR (Suppl. Fig. 1d), allowing cell survival via reduced energy consumption, in purine depleted cancer cells.

These observations, demonstrate a clear difference between pyrimidine and purine inhibition and their effect on cancer cell viability. Whereas dTMP depletion leads to cancer cell toxicity, purine inhibited cancer cells only undergo proliferation arrest (Fig. 1g) but do not necessarily die. We therefore aimed to understand how purine inhibited cancer cells manage to persist, by looking at potential metabolic adaptations.

Purine depletion inhibits the pentose phosphate pathway

Having observed that targeting purine biosynthesis only induced growth arrest but not cell death we aimed to identify hard-wired metabolic liabilities that could become a vulnerability of cancer cells during purine biosynthesis inhibition. In order to investigate the metabolic changes occurring in purine depleted tumor cells, we performed metabolomics and observed a significant drop in pentose phosphate pathway (PPP) intermediates sedoheptulose-7-phosphate (S7P) and glyceraldehyde-3-phosphates (GA3P) (Fig. 2a). In parallel, phosphoribosyl pyrophosphate (PRPP) levels increased up to 3-fold in MTHFD2$^{-/-}$ cells treated with TH9619 (Fig. 2b). PRPP acts as precursor for the sugar backbone of purine nucleotides, hence PRPP accumulation can be explained because it is no longer consumed when purine biosynthesis is inhibited. In parallel we observed the same metabolic phenotype in cancer cells treated with PAICSi or GARTi (Fig. 2c,d).

Interestingly, it has been reported that high PRPP levels serve as negative feedback to the non-oxidative PPP. Especially the transketolase activity, catalysing the conversion of ribose-5-phosphate (R5P) and xylulose-5-phosphate (X5P) to GA3P and S7P, was strongly inhibited by PRPP in a purified enzyme assay [24]. Here, we provide evidence that this mode of action exists also in intact cells (Fig. 2e). Moreover, we investigated whether not only the non- but also the oxidative part of the PPP is affected upon purine biosynthesis inhibition. To do so, we

conducted a [U-^{13}C]-glucose time course tracing experiment in SW620 cells pre-treated with 5 µM PAICSi for 24 hours (Fig. 2f). Indeed, the levels of G6P, F6P and S7P as well as the ^{13}C-enrichment strongly decreased, suggesting that purine inhibition reduces both the non-oxidative and the oxidative part of the PPP(Fig. 2g).

Next, we tested whether exogenous PRPP supplementation would have the same effect and treated WT SW620 cells with different concentrations of PRPP. In line with our previous observations, exogenous PRPP decreased glucose-6-phosphate (G6P) and fructose-6-phosphate (F6P) levels, however, S7P levels surprisingly increased (Suppl. Fig. 2a). It is important to mention that there are no known transporters for PRPP. Hence, it is unclear which intracellular concentrations of PRPP can be reached. Potentially, the oxidative branch of the PPP becomes already inhibited at lower PRPP concentrations. Additionally, other yet unknown regulatory mechanisms may be involved in a dose-dependent manner. Nevertheless, our results provide strong evidence that targeting purine biosynthesis results in PRPP accumulation that subsequently inhibits the PPP.

Purine inhibited cancer cells increase their reliance on glutamine to fuel the TCA cycle

The PPP is running in parallel to glycolysis, generates pentoses and is a major regulator of the cellular redox balance. Even though this essential pathway isuppressed upon purine inhibition, cancer cells still manage to persist. Therefore, we aimed to elucidate metabolic adaptations and activation of potential compensatory mechanisms, allowing cell survival.

Metabolic flexibility is a well-known feature of tumor cells to overcome challenging metabolic conditions [25, 26]. As a response to purine inhibition, cancer cells manage to persist even though their glucose metabolism is heavily altered. MTHFD2$^{-/-}$ cells treated with TH9619 and cells treated with PAICSi and GARTi therefore switched from glucose towards glutamine as carbon source (Fig. 3a, b). We observed a reduction in glucose uptake and lactate secretion with concomitant significant increase in glutamine consumption, accompanied by higher glutamate release (Fig. 3a,b).

To monitor intracellular flux alterations following these different exchange rates, we performed [U-^{13}C]-glucose tracing (Fig. 3c) and measured TCA cycle intermediates in MTHFD2 deficient SW620 cells treated with TH9619 (Fig. 3d) and cells treated with PAICSi (Supp. Fig. 3a). We observed a strong reduction in glucose derived ^{13}C contribution to the tricarboxylic acid (TCA) cycle intermediates (citrate, alpha-ketoglutarate (aKG), fumarate, succinate and malate). Since we found that purine depleted tumor cells increased their glutamine uptake, we repeated the tracing experiments, using fully labelled ^{13}C glutamine (Fig. 3e). Indeed, the labelled fraction coming from the glutamine tracer was increased in all TCA cycle intermediates in MTHFD2$^{-/-}$ cells treated with TH9619 (Fig. 3f) as well as in cells treated with the PAICS and

GARTi (Suppl. Fig. 3b). In both models, the addition of HX was able to rescue this metabolic phenotype. Interestingly, this switch from glucose to glutamine fuelling the TCA cycle, occurred only in purine, but not pyrimidine inhibited cancer cells (Suppl. Fig. 3b).

These results highlight that purine depleted cancer cells can metabolically adapt to a dysfunction in glucose metabolism by using glutamine as carbon source to maintain TCA cycle activity. This dependency on glutamine could represent a potential metabolic vulnerability of cancer cells treated with purine inhibitors. To functionally validate this glutamine addiction we starved purine inhibited cancer cells for glutamine and measured cell death. Indeed, the absence of glutamine in the cell culture medium, lead to an increased percentage of apoptotic cells in combination with PAICSi (Fig. 3g,h). These observations reveal glutamine availability as a metabolic vulnerability of purine depleted cancer cells.

Next, we wanted to validate these glutamine starvation experiments with a pharmacological approach by combined treatment of PAICSi with telaglenastat or CB-839, a glutaminase 1 inhibitor (GLS1i), blocking the conversion of glutamine to glutamate. Using these small molecules, we only observed a slight increase in apoptotic cells, comparing PAICSi treatment alone with the combination of both (Suppl. Fig. 3c). It remains to be further investigated if the molecules show complete on-target engagement since our tracing data clearly show that the conversion of glutamine to glutamate via GLSi was not entirely blocked, as we still observed labelled TCA cycle intermediates in cells cultured in [U-^{13}C]-glutamine. Also increasing concentrations of GLSi failed to prevent ^{13}C conversion to glutamate (Suppl. Fig. 3d). Furthermore, as telaglenastat inhibits specifically GLS1 and not GLS2, we can not rule out that glutamate is still generated via the second GLS isoform which may be sufficient to keep the TCA cycle functional. Moreover, glutamine at 37°C is highly unstable and can be converted to glutamate independently of the action of GLS, which is another explanation for the lack of efficacy of GLS inhibition. Nevertheless, our starvation data clearly demonstrate a functional link between purine depletion and glutamine dependency.

In summary, we discovered a metabolic adaptation of purine inhibited tumor cells, as a response to PPP inhibition and a dysregulated glucose metabolism. Cells rewire their metabolism by reducing their glucose consumption, therefore increasing glutamine consumption as alternative carbon source. This increased glutamine dependency allows purine depleted cancer cells to maintain TCA cycle activity, but at the same time it represents a context-dependent metabolic vulnerability of tumor cells.

Purine depletion enhances malic enzyme activity

As the PPP is a major regulator of the cellular redox balance through its generation of NADPH, we monitored redox state and reactive oxygen species (ROS) levels in purine depleted cancer

cells. To assess ROS levels we stained PAICSi treated SW620 cells with the fluorescent DCF-DA dye and we detected a significant increase in cytosolic ROS activity (Fig. 4a). While looking at the cellular redox state, we measured a strong reduction in NADH/NAD+ ratio and a trend towards a lower NADPH/NADP+ ratio (Fig. 4b). In sum, these data suggest a redox imbalance caused by the PPP inhibition.

Alternative enzymes that can compensate for lower PPP activity are ME or isocitrate dehydrogenase (IDH), both being linked to TCA cycle activity.Interestingly, while looking at the [U-^{13}C]glutamine labelled TCA cycle intermediates, we noticed a fraction of citrate M+6, meaning that all 6 carbons are ^{13}C atoms (Fig. 4d). To obtain fully labelled citrate, fully labelled pyruvate is required to generate ^{13}C labelled acetyl-CoA that can then enter the TCA cycle. Indeed, fractional M+3 enrichment in pyruvate increased upon PAICS and GART inhibition but not in 5FU and PEM treated SW620 cells (Fig. 4d, Suppl. Fig. 4b). Of note, as we could not detect any labelled phosphoenolpyruvate (PEP) from [U-^{13}C]glutamine, we excluded a potential activity of phosphoenolpyruvate carboxykinase (PEPCK), which catalyses the conversion of oxaloacetate to PEP and could have been an alternative potential source for fully labelled pyruvate (Suppl. Fig. 4a).

Hence, the pyruvate M+3 and the resulting citrate M+6 labelling pattern can only occur through the activity of malic enzyme (ME), converting malate to pyruvate (Fig. 4e). This metabolic remodelling upon purine inhibition occurred in many different cancer cell lines. Here we tested colorectal cancer (SW620, SW480, HCT116), lung cancer (NCI-H460), pancreatic cancer (Panc-1), breast cancer (MDA-MB-468, MDA-MB-231) and glioblastoma (LN-229) cell lines. Albeit not all cell lines showed statistical significance, we observed a generally increased ME activity upon purine inhibition independent of the tumor type (Fig. 4f,g).

The activity of ME is compartmentalized through cytosolic (ME1) and mitochondrial isoforms (ME2 and ME3). In all subcellular compartments, it generates pyruvate from malate, in a $NADP^+$ dependent manner, thereby producing NADPH. Since the PPP is a major cytosolic NADPH generator we hypothesized that mainly ME1 gets activated as a compensatory mechanism. To investigate the impact of ME loss on cytosolic ROS levels we generated stable ME1$^{-/-}$ and ME2$^{-/-}$ SW620 knock-out cell lines, with two different single cell clones for each isoform (Fig. 4h). Loss of ME showed a trend of increased ROS levels during PAICSi treatment. This trend seemed to be more consistent in the two ME1 clones compared to the two ME2 clones (Fig. 4i). Since ROS maintenance is of such importance for cellular survival, potentially additional other NADPH producing enzymes, (i.e. IDH1 or ALDH1L1 or NADK) might become more active to balance a loss of ME. Nevertheless, we still observed a small but significant increase in cancer cell death, comparing purine inhibited ME1$^{-/-}$ cells to the SCR

(Fig. 4j). This supports our hypothesis that NADPH produced by ME1 provides a selective advantage to purine depleted cancer cells suffering from PPP inhibition.

Interestingly, previous studies have reported the presence of an ATP-binding site at the active centre of ME1, leading to an inactivation of the enzyme [27, 28]. Hence, the increase in ME activity upon purine inhibition, could therefore be a consequence of purine depletion.

In sum our findings substantiate, that purine levels control ME1 activity. We demonstrate that low purine levels lead to increased ME1 activity supporting cellular redox balance upon PPP loss.

Purines regulate ME and PEPCK activity reciprocally

Previous studies demonstrated, that cancer cells increase their glutamine usage, when glucose or pyruvate is deprived [29-31]. To keep the TCA cycle running upon glutamine, cancer cells need to shuffle carbons from glutamine to pyruvate to ensure the generation of acetyl-CoA, which we observe in our experimental settings. However, glucose deprivation also limits other important anabolic pathways branching off glycolysis, especially serine de novo synthesis from 3PG. To sustain 3PG pools with glutamine as the dominant carbon source, PEPCK activity is required (Fig. 5a). However, in our experimental setting PEPCK was completely inactive (Suppl. Fig 4a), raising the question how purine depleted cancer cells can adapt to glucose deprived conditions.

To investigate the regulatory role of purine availability on these two enzymes in a glucose limited microenvironment, we cultured cells in galactose and treated them with 5 µM of PAICSi. Upon galactose, cancer cells were still able to grow as it can be metabolized to G6P via the Leloir pathway [32], however this process requires four biochemical reactions and is much slower than glucose catabolism via glycolysis. Hence, in our study replacing glucose by galactose served as a tool to mimic glucose limitation in tumor cells without entirely starving them for hexoses. Importantly, we observed that glutamine uptake is generally higher in the galactose comparted to the glucose condition (Fig. 5b), suggesting a high relevance of glutamine addiction as metabolic vulnerability in glucose depleted environments, such as the tumor core.

Following [U-^{13}C]-glutamine tracing, we confirmed activation of PEPCK via PEP M+3 and serine M+3 (Fig. 5c,d) labelling. Pyruvate M+3 was also strongly increased in galactose. However, this labelling could be generated from the activity of both PEPCK or ME (Fig. 5e). Surprisingly, upon PAICSi treatment the labelling in PEP disappeared almost entirely (Fig. 5d) whereas, the fully labelled pyruvate (Fig. 5e) decreased only by a few percentages, suggesting retained activity of ME. Considering that PEPCK requires GTP as phosphate donor to form to

PEP from oxaloacetate [33], we concluded that purine depletion hampers PEPCK activity in a glucose limited microenvironment (Fig. 5g). Consequently, cancer cells become entirely dependent on ME to generate pyruvate from glutamine. Following this hypothesis, we were wondering if purine levels are maintained in energy limiting conditions such as during galactose exposure.

Indeed,, intracellular ATP and GTP levels remained unchanged under galactose conditions despite energy stress and AMPK activation [34] (Fig. 5f). However, when cells cultured in galactose, were treated with PAICSi we saw the same strong decline in purine levels as under galactose, indicating that purine availability dictates ME and PEPCK activity through allosteric regulation.

In summary, we show a reciprocal regulation of PEPCK and ME during purine depletion favouring catabolic TCA cycle activity over anabolic carbon shunting (Fig. 5i). This distinct adaption demonstrates a regulatory function of purines to impose a cellular persisted state. It illustrates how a change in one of the central metabolites of mammalian metabolism triggers a multi-layered and coordinated adaptation process to survive within challenging conditions such as in cancer tissues or during the metastatic cascade.

Conclusion

Our study highlights the capability of cancer cells to adapt their metabolism in response to purine biosynthesis inhibition. We elucidated a fundamental difference between the impact of targeting dTMP compared to purine synthesis on cancer cell toxicity. Whereas depletion of dTMP leads to genome instability and cancer cell death, purine inhibited cancer cells undergo proliferation arrest but remain in a persistent, growth-arrested state. Following this observation the interest arose to mechanistically understand what makes those purine inhibited cancer cells sustain and find secondary intervention points to more efficiently eliminate them.

Our findings demonstrate that the impact of purine depletion goes beyond the sole ablation of the nucleotide pool, but is also perturbing one of the key glucose oxidizing pathways, the PPP. Consequently, we observed a massive perturbation in glucose metabolism, leading to an increased dependency on glutamine as a carbon source to maintain TCA cycle activity. This glutamine addiction in purine depleted cancer cells represents a metabolic vulnerability as glutamine starvation in combination with purine biosynthesis inhibitor PAICSi led to a significant increase in cancer cell toxicity. Hence, we believe that targeting glutamine metabolism in addition to purine synthesis could represent a promising approach for a combinatory therapy.

Moreover, the PPP represents a major NADPH source, providing reducing power for essential biological processes. Its complete inhibition upon purine inhibition due to a strong accumulation in PRPP levels led to a significant increase in cellular ROS. Consequently, purine inhibited cancer cells need to activate compensatory mechanisms to ensure NADPH production to combat oxidative stress. Our metabolomics data revealed an increased activity of NADPH producing enzyme ME1 upon purine depletion. Hence, we assume that ME1 contributes to some extend (together with other NADPH producing enzymes) to a controlled redox equilibrium upon PPP dysfunction.

Additionally, redox disbalance might not be the only driver of ME activity, knowing that ATP can act as allosteric inhibitor of the enzyme. Hence a drop in ATP would increase its activity, which is the phenotype that we observed in our models. Moreover, AMPK activation could be an additional driver of ME activity, this has already been shown in the context of metastasizing breast cancer cells [35].

To which extend our findings are exploitable therapeutically remains to be elucidated. As ME was shown to play an essential role in cancer stemness, TME acidosis, hypoxic adaptation and EMT, many functional implications remain to be explored. Especially, given that previous studies reported, an enhanced migratory potential and metastasis formation upon purine nucleotide inhibition [17, 36], it would be highly interesting to assess the role of ME in this context. Moreover, the role of ROS during the metastatic cascade is a controversial topic, studies have demonstrated its pro- as well as antimetastatic properties [37-39]. ME as a mediator of the cellular redox balance might confer the ability to maintain intracellular ROS levels within a tolerable range but still high enough to function as a pro-migratory signal. Exploring the role of ME during cancer cell migration and metastasis formation represents a relevant subject for a future study. In sum, the significance of ME activity in purine inhibited cancer cells represents a relevant mechanistic observation, as there might be therapeutic potential in specific cancer types. For instance, in would be interesting to compare the effect of purine inhibitors between tumors with high ME expression to those unable to increase ME activity.

Finally, showing that purines act as regulators of enzymatic activity, by controlling the metabolic fork between ME and PEPCK in a glucose restricted environment, highlights that beyond their canonical role as DNA precursors, energy form and signalling molecule, purines control the activity of key enzymes involved in the central carbon metabolism. Hence, our study provides some fundamental mechanistic understanding on how changes in purine levels can trigger a cascade of downstream metabolic adaptations and is exemplary for the metabolic plasticity and flexibility of cancer cells.

Material and Methods

Reagents/Chemicals	Reference
TH11130 (PAICS inhibitor)	From the Helleday Lab
Lometrexol (GART inhibitor)	Sanbio, Cat. No. 18049-1
TH9619 (MTHFD1/2 inhibitor)	From the Helleday Lab
Hypoxanthine	Fisher Scientific, Cat. No. 122011000
CB-839 (GLS1 inhibitor)	MedKoo Biosciences, Cat. No. 206153
Pemetrexed (Pem)	Bioconnect, Cat. No. S7785
5-fluorouracil (5FU)	Sanbio, Cat. No. F6627

Reagents/Chemicals	Reference
FBS - Dialyzed by ultrafiltration against 0.15 M NaCl	Sigma Adrich, Cat. No. F0392
Matrigel	Corning, Cat. No. 354237
H2O2	Sigma Aldrich, Cat. No. 1086001000
EDTA	Fisher, Cat. No. 17892
RIPA lysis buffer	Thermo, Cat. No. 89901
Annexin V-FITC	Immunotools, Cat. No. 31490013X2
Propidium iodide (PI)	Fisher, Cat. No. 11599296
DCF-DA	Vendor
Annexin binding buffer	Biolegend, Cat. No. 422201
M Bovine Serum Albumin (BSA)	Sigma, Cat. No. A7030-50G
PhosSTOP	Sigma, Cat. No. 4906837001
cOmplete Mini Protease Inhibitor	Sigma, Cat. No. 4693124001
Bradford reagent	
PageRuler Prestained Protein Ladder	Lifetec, Cat. No. 26619
REVERT Total Protein Stain Solution	Westburg, Cat. No. LI 926-11021
NewBlot Nitro Stripping Buffer	Westburg, Cat. No. LI 928-40030
NuPAGE™ LDS Sample Buffer	Lifetech, Cat. No. NP0007
MOPS SDS running buffer	Lifetech, Cat. No. NP0001
SurePAGE™, Bis-Tris, 10x8, 4-12%, 12 wells	GenScript, Cat. No. M00653
SurePAGE™, Bis-Tris, 10x8, 4-12%, 15 wells	GenScript, Cat. No. M00654

Tween20	Sigma Aldrich, cat. No. P9416
DMF: N,N-Dimethylformamide	Fisher, Cat. No. 10295761
DL-Dithiothreitol; DTT	Merck, Cat. No. D9163

Cell Culture :

All cell lines were cultured in Dulbecco's modified Eagle's medium (DMEM) without phenol red supplemented with 2 mM glutamine (Thermo Fisher Scientific), 17 mM glucose, and 10% fetal bovine serum (FBS) at 37 °C and 5% CO2. SW620 wt cells were obtained from the Helleday Lab Karolinska Institutet, the SW620 MTHFD2 CRISPR/Cas9 KO cells were generated and used previously [19]. ME1 and ME2 CRISPR/Cas9 KO SW620 cells were generated using the single guide sequences TTATTACTATCCACGATCGA for ME1 and TGGTGGAAACTACTCTTAAC, targeting exon 2 of ME2. CRISPR plasmids were ordered via VectorBuilder. SW480 (Elisabeth Letellier lab at the University of Luxemburg, originally form ATCC), H460 (Arnaud Blomme lab at the GIGA Stem Cells laboratory at the University of Liège), A549 (Arnaud Blomme lab at the GIGA Stem Cells laboratory at the University of Liège), MDA-MB-468 (Lewis Cantley lab at Weill Cornell Medical College, originally from ATCC), MDA-MB-231 (Alexei Vazquez lab at the Beatson Institute for Cancer Research, originally form ATCC), LN229 (Alexei Vazquez lab at the Beatson Institute for Cancer Research, originally form ATCC), PANC1 (from ATCC), HCT116 (Elisabeth Letellier lab at the University of Luxemburg, originally form ATCC) cell lines. For the galactose treatment, DMEM was supplemented with 17 mM galactose instead of glucose. For all experiments, FBS was replaced by dialysed FBS, which doesn't contain hypoxanthine.

Spheroid Growth:

Cells were seeded at a concentration of 5000 cells/well (NCI-H460) and 10 000 cells/well (SW620) in 200 µL cold DMEM 17mM glucose, 2mM glutamine 10% FBS and 2,5% cold matrigel (Matrigel Basement Membrane, Corning) in ultra-low attachment 96-well plates (San-Bio). The seeding was performed with the plate on ice in order to avoid matrigel polymerisation. Plate was centrifuged at 200g for 2 min at 4 °C, then incubated for 5 days at 37 °C and 5% CO2. After 5 days, the spheres were transferred into fresh medium containing, which can then contain a drug or a tracer for metabolite analysis.

Western blot:

Cells were washed with cold PBS and cell lysis buffer (150 mM NaCl, 1 mM EDTA, 50 mM Tris-HCl, 1% NP-40, with proteases and phosphatases inhibitors (Roche)) was added directly to the well and kept on ice. Lysates were harvested using a cell scraper, transferred into

Eppendorf tubes and kept on ice for 10 min, while being vortexed a few times. Lysis efficiency was maximized by sonication for 10min. Samples were centrifuged at full speed at 4°C for 10 min and supernatant was collected into fresh Eppendorf tubes. Protein concentration was assessed with a Bradford assay. 20-40 µL of protein were loaded on NuPAGE 4–12% Bis-Tris gels (Life Technologies) using 4x NuPage LDS Sample buffer (Thermo Fisher Scientific) supplemented with 10 mM DTT (Sigma Aldrich) and electrophoresis gels were run for 10 min at 90V and then for 1 hour at 120V. After migration, proteins were blotted on a nitrocellulose membrane for 1.5 hours at 70V. To determine the total protein amount, the membrane was stained with REVERT staining solution (LI-COR) and imaged with Odyssey CLx Imaging System (LI-COR). Thereafter, the membrane was washed and incubated in a 5% milk powder in Tris-Buffered Saline +0.1% tween (TBS-T) solution, to prevent unspecific binding of the primary antibody. Incubation with primary antibody was done overnight at 4°C, then the membrane was washed in TBS-T and incubated with the secondary antibody during 1 hour at room temperature, before being imaged on the Odyssey CLx. The ImageStudioLite Software Vers.5.2 (LI-COR) was used for analysis.

Antibodies used in this paper:

Primary Antibody	**Reference**
p70 S6 Kinase	Cell signaling, Cat. No. 9202S
P-p70 S6 Kinase (T389)	Cell signaling, Cat. No. 9205S
Vinculin	Cell Signalling, Cat. No. 13901S
ME1	Santa Cruz, Cat. No. 365891
ME2	Cell signalling, Cat. No. 12399S
ME3	Cell signalling, Cat. No. 18457S
4E-BP1	Cell signalling, Cat. No. 9644T
P-4E-BP1	Cell signalling, Cat. No. 2855T
AMPKα	Cell signalling, Cat. No. 5831S
P-AMPKα (T172)	Cell signalling, Cat. No. 2535S
ATM	Cell signalling, Cat. No. 2873T
p-ATM (Ser1981)	Cell signalling, Cat. No. 13050S
Chk2	Cell signalling, Cat. No. 2662T
p-Chk2 (Thr68)	Cell signalling, Cat. No. 2197S
Actin	Cell signalling, Cat. No. 3700S
Tuberin/TCS2	Cell signalling, Cat. No. 3612S

Secondary Antibody	Reference
Anti rabbit IRDye 800CW (donkey)	Westburg/LICOR, Cat. No. 925-32213
Anti mouse IRDye 800CW (goat)	Westburg/LICOR, Cat. No. 926-32210
Anti rabbit IRDye 680RD (donkey)	Westburg/LICOR, Cat. No. 926-68070
Anti mouse IRDye 680RD (goat)	Westburg/LICOR, Cat. No. 926-68073

Stable isotope tracing:

Stable isotope tracing experiments were performed in DMEM supplemented with 2 mM glutamine, 17 mM glucose, and 10 % dialyzed FBS and [U-^{13}C]-glucose or [U-^{13}C]-glutamine (Cambridge Isotope Laboratories) were used as tracer. 80 000 to 150 000 cells were seeded in 24-well plates (Greiner), 24 hours prior addition of the tracer to allow the cells to attach and adapt. For each experimental condition, three technical replicates were used. In parallel, additional triplicates per condition were seeded for counting, to calculate the packed cell volume (PCV), which was used for normalization. After medium replacement cells were incubated with the tracer during specific time points, steady state conditions were considered after 24 hours. At extraction day, medium of all triplicates was collected to analyse uptake and release rates of metabolites. Three empty 24 wells were filled with medium and incubated for the same time, to assess the basal metabolite composition and determine the exchange rates. Collected medium samples were centrifuged at 300 g for 5 min at 4°C, supernatant was collected and stored at -20°C until metabolite extraction.

Intracellular metabolite extraction:

First, medium was removed from the 24-well plate and cells were washed with 500 µL of cold PBS. Then, 100-200 µL of ice cold extraction solvent (50% methanol, 30% acetonitrile, 20% H_2O containing internal standards (AMP, CPA, CPR, TNAD, TFL) were added and the plate was put on ice under agitation for 5 min. As a blank control, 100-200 µL of extraction solvent were added to an empty well. Extracts were collected into 1.5 mL Eppendorf tubes on ice and centrifuged at full speed at 4°C for 10 min. Supernatant was collected on ice into fresh 1.5 mL Eppendorf tubes as backup and 50 to 100 µL were transferred to glass inserts in brown LC-MS vials and stored at -80°C until measurement. A PBQC sample war prepared combining 5 µL of each sample.

Metabolite extraction from medium:

From the medium samples, 10 µL was added to 990 µL of ice cold extraction solvent and vortexed for 20 s. Tubes were centrifuged at full speed at 4°C for 5 min and supernatant was transferred into LC-MS vial with inserts, which were stored at -80°C until measurement.

Metabolite extraction from spheroids:

10 spheres per condition were collected in a 15 mL falcon tube on ice and were centrifuged at 600g for 3 min at 4°C. Supernatant was removed and spheres were washed in 5 mL cold PBS and centrifuged again at 600g for 3 min at 4°C. After removal of the supernatant, spheres were resuspended in 900 µL cold PBS and transferred to a 2 mL Eppendorf tube and centrifuged at 4°C 600g for 3 min. When aspirating we made sure that as much matigel/PBS is removed as possible. For the extraction, 900 µL of cold MeOH was added then 300 µL H_2O and 300 µL $CHCl_3$. Tubes containing the spheres were vortexed, sonicated 3 times with 5 min breaks in between at 4°C. Tubes were spinned at 4°C, 12 000 g for 10 min, supernatant was transferred into a 2 mL Eppenforf tube and dried in a speed-vac at 4°C. The pellet was let air dry for protein quantification, for later normalisation to protein content. The dry metabolic extracts were resuspended in 50 µL chloroform, then 300 µL methanol:water (1:1 v/v) were added. Samples were vortexed and spinned in a microcentrifuge for 5min at 12 000g at 4°C. At this point the extracts can be separated into 3 phases, the upper, aqzueous phase, containing the polar metabolites, the lower, apolar phase containing lipidic metabolites and the interphase with protein and cells debris. 80 µL op the polar phase were transferred to brown LC-MS vials and can be stored at -80°C until being measured.

LC-MS measurements,

The LC-MS measurements were performed using a Vanquish Flex LC coupled to a Q Exactive Plus Orbitrap mass spectrometer. Chromatographic separation was performed using a SeQuant ZIC-pHILIC 5 µm polymer 150 × 2.1 mm column (Merck AG.) equipped with a SeQuant ZIC-pHILIC Guard 20 × 2.1 mm pre-column, which was maintained at 45°C. The mobile phases consisted of 20 mmol/L ammonium carbonate in water, pH 9.2 and supplemented with 5 µM of medronic acid (Eluent A) and acetonitrile (Eluent B). The flow rate was set to 0.2 mL/min. The gradient program was set to 0.2 mL/min flow rate and loading starts from 80% in 2min, followed by linear gradient ranging from 80 % B to 20 % B in 15 min; at 18 min starts the regeneration step with 80 % B; from 20 min until 24,5 min column is re-equilibrated with 80 % B at flow rate of 0.4 mL/min. 5 µL of sample was injected into the machine. Mass spectrometry acquisition was performed using a polarity switch between positive and negative electrospray ionization modes. The parameters applied were: sheath gas flow rate, 30; aux gas flow rate, 10; sweep gas flow rate, 0; spray voltage, 4 kV (+)/3.5 kV (−); capillary temperature, 350 °C; S-lense RF level, 50; aux gas heater temperature, 100°C. The mass analyser operated in full-scan mode with a resolving power of 70 000 at 200 m/z, covering a scan range of 75–1000 m/z with an automatic gain control set to 10^6, and a maximum injection time of 250 ms. Data from IC-MS and LC-MS measurements were acquired

using the Thermo Xcalibur software (Version 4.3.73.11) and analyzed with TraceFinder (Version 4.1). Relative quantification of the metabolites was obtained from the calculation of the area under the curve. Natural isotope correction and subsequent analysis was performed with the Autoplotter software [40]

IC-MS measurements:

The extraction procedure is equal to LC-MS, samples are kept in Eppendorf tubes instead of glass vials and the polar extracts were dried overnight under vacuum. Pellets were reconstituted in 25 µL H_2O (Milli-Q Advantage A10) of with 20 µL were injected into the IC-MS system. A Dionex ICS-6000+ ion chromatograph was coupled to a QExactive high resolution mass spectrometer (Thermo Fisher Scientific). The electrospray ionization (ESI) was set at 2 500 kV, with gas temperature of 420°C. For MS1 data acquisition, the m/z scan range was set from 80-750 with a resolution of 17500 at 200 m/z. The maximum injection time was 100 milliseconds and the data was acquired with two micro-scans.

Cell proliferation:

5000-8000 cells were seeded in 100 µL in triplicates in a 96-well plate (Greiner or Corning) and treated 24 hours later. To determine cells proliferation, cell confluence was measured at treatment day, which marks time 0. For each time point, proliferation rate was determined using the equation: cell confluence at time x/ cell confluence at time 0.

ROS DCF-DA measurements with FACS:

For ROS staining, 250 000-350 000 cells were seeded in a 6-well plate, 24 hours later the cells were treated for the specific time points. Cells were washed with 1 mL PBS, then trypsinized, inactivated with medium containing FBS and passed into Eppendorf tubes. Tubes were centrifuged at 350 g at room temperature for 5min, then washed with PBS and centrifuged once more at the same speed. The staining solution contained 10 µL of DCF-DA (Vendor) in simple DMEM without any supplementation. Pellets were resuspended in 200 µL of the staining solution and incubated for 30 min at 37°C. Afterwards, cells were centrifuged at 350g at 4°C for 5 min, washed with cold PBS and centrifuged again. After removing the supernatant 100-300 µL of ice cold FACS buffer (1X PBS, 10% FBS, 2 mM EDTA) was added, samples were maintained on ice in the dark before being measured. DCF-DA signal was recorded in the FITC channel (B530/30) on the Quanteon. The analysis was done using the FlowJo software (v.10.7.2, BD), for statistics the MFI (mean fluorescence intensity) was retrieved and the fold change was calculated to the stained untreated control. For visualization, histogram of the singlets in the FITC channel were displayed.

AnnexinV-FITC/PI measurements with FACS:

AnnexinV-FITC/PI double staining was used to determine cell death induction. On the first day, cells were seeded into a 6-well plate plus two untreated control samples. Medium was replaced and the respective treatments were added on day 2. After 72 hours, supernatant of all samples was collected into a 15 mL Falcon tube and washed with PBS, which was collected too. Cells were trypsinized and deactivated with DMEM containing FBS and the empty cell was washed once with PBS to make sure all cells have been harvested. Tubes were centrifuged at 300 g for 5 min at room temperature, supernatant was discarded and cell pellet was resuspended in PBS and transferred into FACS tubes. The control tubes are split in two, serving as unstrained and double stained control. From the second control tube, half of the sample is heated at 60°C for 5min and when cooled down, mixed with the other half. This tube serves as sample for the single (AnnexinV-FITC or PI) and double stained (AnnexinV-FITC + PI) controls as half on the population is dead. Tubes were centrifuged at 300 g for 5 min at 4°C, supernatant was discarded and 50 µL of the AnnexinV-FITC/ABB staining mix (2.5 µL of AnnexinV-FITC + 47.5 µL of 1× ABB). Samples were incubates on ice in the dark for 15 min. 450 µL of the PI/ABB (main stock (1mg/ml) diluted 1:20 in PBS, then 10 µl in 440 µl ABB for final concentration 1 µl /mL) was added right before measurement. Measurement wasdone on the Cytoflex, the AnnexinV-FITC signal was detected in the FITC-A channel the PI emission was detected in the PC5.5-A channel.

Statistics:

In the present study, n was defined as one independent biological replicate of an experiment, the technical mean within one biological experiment was considered as one n. Unpaired t-test with Welch's correction was applied for comparison between two groups. For comparison of multiple groups one-way ANOVA with Dunnett's multiple comparison or Holm-Sidàk multiple comparison test, with a single pooled variance. Data were plotted and statistically analysed using GraphPad Prism (version 10.3.1)

References

1. Hung, M.H., et al., *Purine anabolism creates therapeutic vulnerability in hepatocellular carcinoma through m 6 A-mediated epitranscriptomic regulation.* Hepatology, 2023. **78**(5): p. 1462-1477.
2. Chakravarthi, B.V., et al., *Expression and Role of PAICS, a De Novo Purine Biosynthetic Gene in Prostate Cancer.* Prostate, 2017. **77**(1): p. 10-21.
3. Chakravarthi, B., et al., *A Role for De Novo Purine Metabolic Enzyme PAICS in Bladder Cancer Progression.* Neoplasia, 2018. **20**(9): p. 894-904.
4. Huo, A. and X. Xiong, *PAICS as a potential target for cancer therapy linking purine biosynthesis to cancer progression.* Life Sci, 2023. **331**: p. 122070.
5. Agarwal, S., et al., *PAICS, a De Novo Purine Biosynthetic Enzyme, Is Overexpressed in Pancreatic Cancer and Is Involved in Its Progression.* Transl Oncol, 2020. **13**(7): p. 100776.
6. Hany, D., V. Vafeiadou, and D. Picard, *CRISPR-Cas9 screen reveals a role of purine synthesis for estrogen receptor α activity and tamoxifen resistance of breast cancer cells.* Sci Adv, 2023. **9**(19): p. eadd3685.
7. Kim, S., et al., *Elucidating prognostic significance of purine metabolism in colorectal cancer through integrating data from transcriptomic, immunohistochemical, and single-cell RNA sequencing analysis.* Mol Oncol, 2025.
8. Tran, D.H., et al., *De novo and salvage purine synthesis pathways across tissues and tumors.* Cell, 2024. **187**(14): p. 3602-3618.e20.
9. Farber, S., *Some observations on the effect of folic acid antagonists on acute leukemia and other forms of incurable cancer.* Blood, 1949. **4**(2): p. 160-7.
10. Laohavinij, S., et al., *A phase I clinical study of the antipurine antifolate lometrexol (DDATHF) given with oral folic acid.* Invest New Drugs, 1996. **14**(3): p. 325-35.
11. Meng, M., et al., *Knockdown of PAICS inhibits malignant proliferation of human breast cancer cell lines.* Biol Res, 2018. **51**(1): p. 24.
12. Škerlová, J., et al., *Crystal structures of human PAICS reveal substrate and product binding of an emerging cancer target.* J Biol Chem, 2020. **295**(33): p. 11656-11668.
13. Kumar, V., *Adenosine as an endogenous immunoregulator in cancer pathogenesis: where to go?* Purinergic Signal, 2013. **9**(2): p. 145-65.
14. Muller-Haegele, S., L. Muller, and T.L. Whiteside, *Immunoregulatory activity of adenosine and its role in human cancer progression.* Expert Rev Clin Immunol, 2014. **10**(7): p. 897-914.
15. Antonioli, L., et al., *Immunity, inflammation and cancer: a leading role for adenosine.* Nat Rev Cancer, 2013. **13**(12): p. 842-57.
16. Keshet, R., et al., *Targeting purine synthesis in ASS1-expressing tumors enhances the response to immune checkpoint inhibitors.* Nat Cancer, 2020. **1**(9): p. 894-908.
17. Soflaee, M.H., et al., *Purine nucleotide depletion prompts cell migration by stimulating the serine synthesis pathway.* Nat Commun, 2022. **13**(1): p. 2698.
18. Bonagas, N., et al., *Pharmacological targeting of MTHFD2 suppresses acute myeloid leukemia by inducing thymidine depletion and replication stress.* Nat Cancer, 2022. **3**(2): p. 156-172.
19. Green, A.C., et al., *Formate overflow drives toxic folate trapping in MTHFD1 inhibited cancer cells.* Nat Metab, 2023. **5**(4): p. 642-659.
20. Joerger, M., et al., *The role of pemetrexed in advanced non small-cell lung cancer: special focus on pharmacology and mechanism of action.* Curr Drug Targets, 2010. **11**(1): p. 37-47.
21. Peters, G.J., et al., *Thymidylate synthase inhibition after administration of fluorouracil with or without leucovorin in colon cancer patients: implications for treatment with fluorouracil.* J Clin Oncol, 1994. **12**(10): p. 2035-42.
22. Emmanuel, N., et al., *Purine Nucleotide Availability Regulates mTORC1 Activity through the Rheb GTPase.* Cell Rep, 2017. **19**(13): p. 2665-2680.
23. Hoxhaj, G., et al., *The mTORC1 Signaling Network Senses Changes in Cellular Purine Nucleotide Levels.* Cell Rep, 2017. **21**(5): p. 1331-1346.

24. Hosomi, S., et al., *Inhibitory effect of 5-phosphoribosyl 1-pyrophosphate and ADP on the nonoxidative pentose phosphate pathway activity.* Biochem Med Metab Biol, 1989. **42**(1): p. 52-9.
25. Faubert, B., A. Solmonson, and R.J. DeBerardinis, *Metabolic reprogramming and cancer progression.* Science, 2020. **368**(6487).
26. Fendt, S.M., C. Frezza, and A. Erez, *Targeting Metabolic Plasticity and Flexibility Dynamics for Cancer Therapy.* Cancer Discov, 2020. **10**(12): p. 1797-1807.
27. Yang, Z., C.W. Lanks, and L. Tong, *Molecular mechanism for the regulation of human mitochondrial NAD(P)+-dependent malic enzyme by ATP and fumarate.* Structure, 2002. **10**(7): p. 951-60.
28. Hung, H.C., et al., *Functional roles of ATP-binding residues in the catalytic site of human mitochondrial NAD(P)+-dependent malic enzyme.* Biochemistry, 2005. **44**(38): p. 12737-45.
29. Le, A., et al., *Glucose-independent glutamine metabolism via TCA cycling for proliferation and survival in B cells.* Cell Metab, 2012. **15**(1): p. 110-21.
30. Yang, C., et al., *Glutamine oxidation maintains the TCA cycle and cell survival during impaired mitochondrial pyruvate transport.* Mol Cell, 2014. **56**(3): p. 414-424.
31. Benzarti, M., et al., *PKM2 diverts glycolytic flux in dependence on mitochondrial one-carbon cycle.* Cell Rep, 2024. **43**(3): p. 113868.
32. Frey, P.A., *The Leloir pathway: a mechanistic imperative for three enzymes to change the stereochemical configuration of a single carbon in galactose.* Faseb j, 1996. **10**(4): p. 461-70.
33. Yang, J., S.C. Kalhan, and R.W. Hanson, *What is the metabolic role of phosphoenolpyruvate carboxykinase?* J Biol Chem, 2009. **284**(40): p. 27025-9.
34. Meiser, J., et al., *Serine one-carbon catabolism with formate overflow.* Sci Adv, 2016. **2**(10): p. e1601273.
35. Ramakrishnan, G., et al., *Deletion of AMP-activated protein kinase impairs metastasis and is rescued by ROS scavenging or ectopic CD36 expression.* Cell Rep, 2025. **44**(1): p. 115183.
36. Kiweler, N., et al., *Mitochondria preserve an autarkic one-carbon cycle to confer growth-independent cancer cell migration and metastasis.* Nat Commun, 2022. **13**(1): p. 2699.
37. Piskounova, E., et al., *Oxidative stress inhibits distant metastasis by human melanoma cells.* Nature, 2015. **527**(7577): p. 186-91.
38. Labuschagne, C.F., et al., *Cell Clustering Promotes a Metabolic Switch that Supports Metastatic Colonization.* Cell Metab, 2019. **30**(4): p. 720-734.e5.
39. Le Gal, K., et al., *Antioxidants can increase melanoma metastasis in mice.* Sci Transl Med, 2015. **7**(308): p. 308re8.
40. Pietzke, M. and A. Vazquez, *Metabolite AutoPlotter - an application to process and visualise metabolite data in the web browser.* Cancer Metab, 2020. **8**: p. 15.

Abbreviations

PAICS	phosphoribosylaminoimidazole carboxylase and phosphoribosylaminoimidazolesuccinocarboxamide synthetase
GART	Glycinamide ribonucleotide synthetase/glycinamide ribonucleotide transformylase/aminoimidazole ribonucleotide synthetase
MTHFD2	Bifunctional methylenetetrahydrofolate dehydrogenase/cyclohydrolase 2
MTHFD1	Trifunctional methylenetetrahydrofolate dehydrogenase/cyclohydrolase/formyltetrahydrofolate synthetase 1
OCM	One carbon metabolism
AMP	Adenosine monophosphate
GMP	Guanosine monophosphate
ATP	Adenosine triphosphate
GTP	Guanosine triphosphate
S7P	Sedoheptulose-7-phosphate
GA3P	Glyceraldehyde-3-phosphate
PRPP	Phosphoribosyl pyrophosphate
G6P	Glucose-6-phosphate
F6P	Fructose-6-phosphate
PPP	Pentose phosphate pathway
NAD+	Nicotinamide adenine dinucleotide (oxidized form)
NADH	Nicotinamide adenine dinucleotide hydrogen (reduced form)
NADP+	Nicotinamide adenine dinucleotide phosphate (oxidized form)
NADPH	Nicotinamide adenine dinucleotide phosphate hydrogen (reduced form)
MIDs	Mass isotopomer distribution
TCA	Tricarboxylic acid
aKG	Alpha keltoglutarate
ME	Malic Enzyme

PEPCK	Phosphoenolpyruvate carboxykinase
PEP	Phosphoenolpyruvate
mTOR	Mammalian Target of Rapamycin
mTORC1	Mammalian target of rapamycin complex 1
AMPK	AMP-activated protein kinase
TSC2	Tuberous sclerosis complex 2
4E-BP1	Eukaryotic translation initiation factor 4E-binding protein 1
70S6	Ribosomal protein S6
GLS	Glutaminase
5FU	Fluorouracil
PEM	Pemetrexed
MTX	Methotrexate
dTMP	Thymidylate

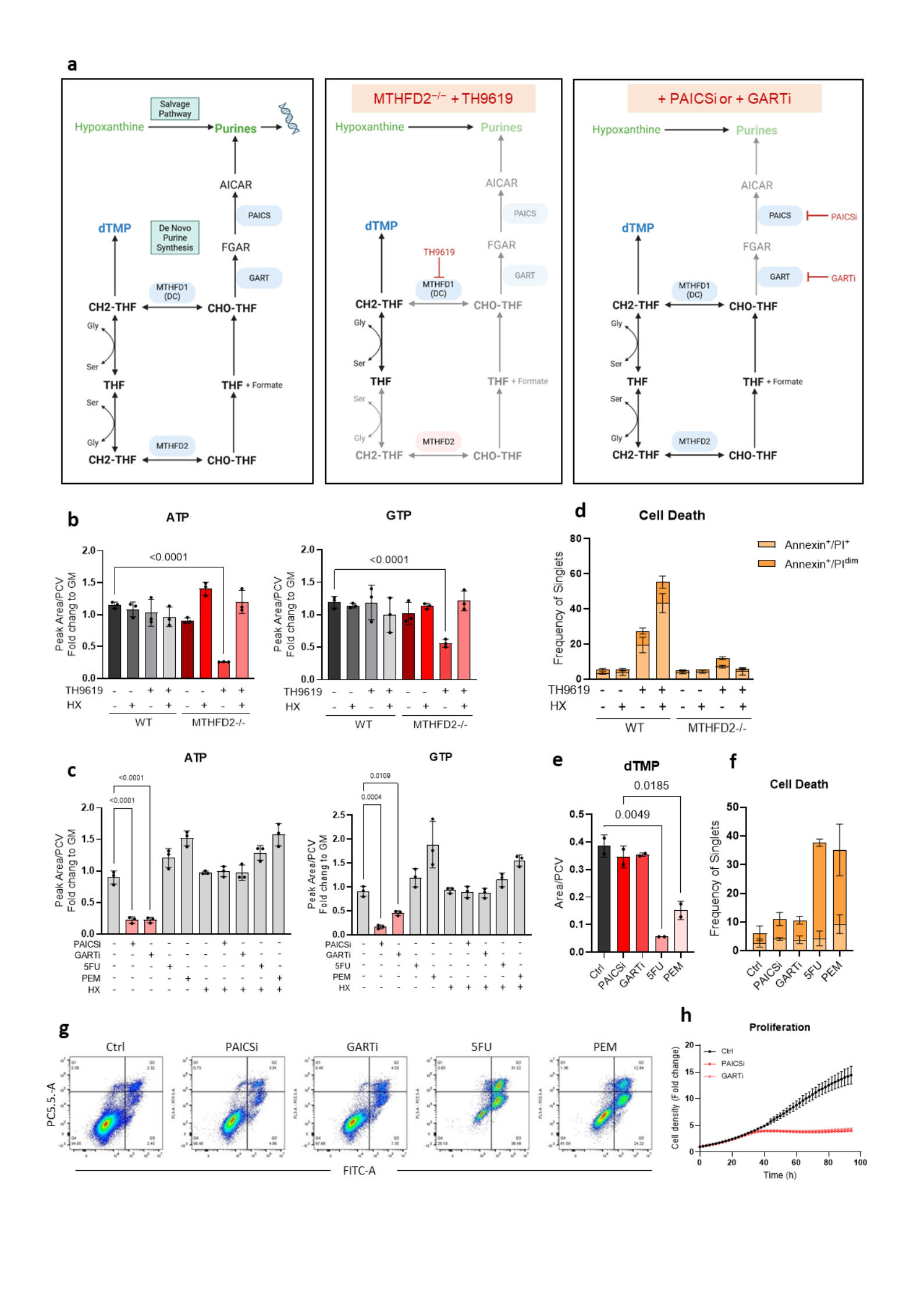
a
Salvage Pathway
Hypoxanthine
Purines
AICAR
PAICS
dTMP
De Novo Purine Synthesis
FGAR
GART
MTHFD1 (DC)
CH2-THF
CHO-THF
Gly
Ser
THF
THF + Formate
MTHFD2
MTHFD2−/− + TH9619
TH9619
+ PAICSi or + GARTi
PAICSi
GARTi
b
ATP
GTP
Peak Area/PCV Fold chang to GM
<0.0001
TH9619
HX
WT
MTHFD2-/-
d
Cell Death
Frequency of Singlets
Annexin+/PI+
Annexin+/PIdim
c
ATP
GTP
<0.0001
0.0109
0.0004
PAICSi
GARTi
5FU
PEM
HX
e
dTMP
0.0185
0.0049
Area/PCV
Ctrl
f
Cell Death
g
Ctrl
PAICSi
GARTi
5FU
PEM
PC5.5.-A
FITC-A
h
Proliferation
Cell density (Fold change)
Time (h)

Figure 1: Purine inhibition induces proliferation arrest but not cancer cell toxicity

(a) Purine biosynthesis via the de novo or the purine salvage pathway. Models for purine inhibition: MTHFD2$^{-/-}$ + TH9619 or targeting PAICS or GART.

(b) Intracellular ATP and GTP levels normalized to PCV and the global mean (GM) of all conditions in SW620 WT and MTHFD2$^{-/-}$ cells treated with 1 µM TH9619 and/or 50 µM HX for 24h.

(c) ATP and GTP levels normalized to PCV and GM in SW620 cells treated with 5 µM PAICSi, 2 µM GARTi, 2 µM 5FU, 2 µM PEM and/or 50 µM HX for 24h.

(d) Cell death analysis by annexinV-FITC and PI staining of SW620 WT and MTHFD2$^{-/-}$ cells after 72 h treatment with 1 µM TH9619 and/or 50 µM HX (*n=3).*

(e) dTMP peak areas normalized to PCV in NCI-H460 cells treated with 5 µM PAICSi, 2 µM GARTi, 2 µM 5FU, 2 µM PEM and/or 50 µM HX for 24h.

(f) Cell death analysis by annexinV/PI staining of NCI-H460 cells treated with 5 µM PAICSi, 2 µM GARTi, 2 µM 5FU or 2 µM PEM for 72 h (*n=3).*

(g) Exemplary gating for annexinV-FITC and PI measurement using NCI-H460 cells treated with 5 µM PAICSi, 2 µM GARTi, 2 µM 5FU, 2 µM PEM and/or 50 µM HX for 72h. Detection of annexinV-FITC in the FITC-A channel and PI in the PC5.5-A channel using the Cytoflex.

(h) Proliferation of SW620 cells upon treatment with 5 µM PAICSi or 2 µM GARTi. Mean ± SEM of independent experiments (*n*=2).

Each dot represents one biological replicate, which is the mean of technical triplicates. Statistical analysis was done using one-way ANOVA with Holm-Sidàk multiple comparison test, with a single pooled variance, with representation of the mean ± s.d., unless stated otherwise. *P* values indicate comparisons to the untreated control.

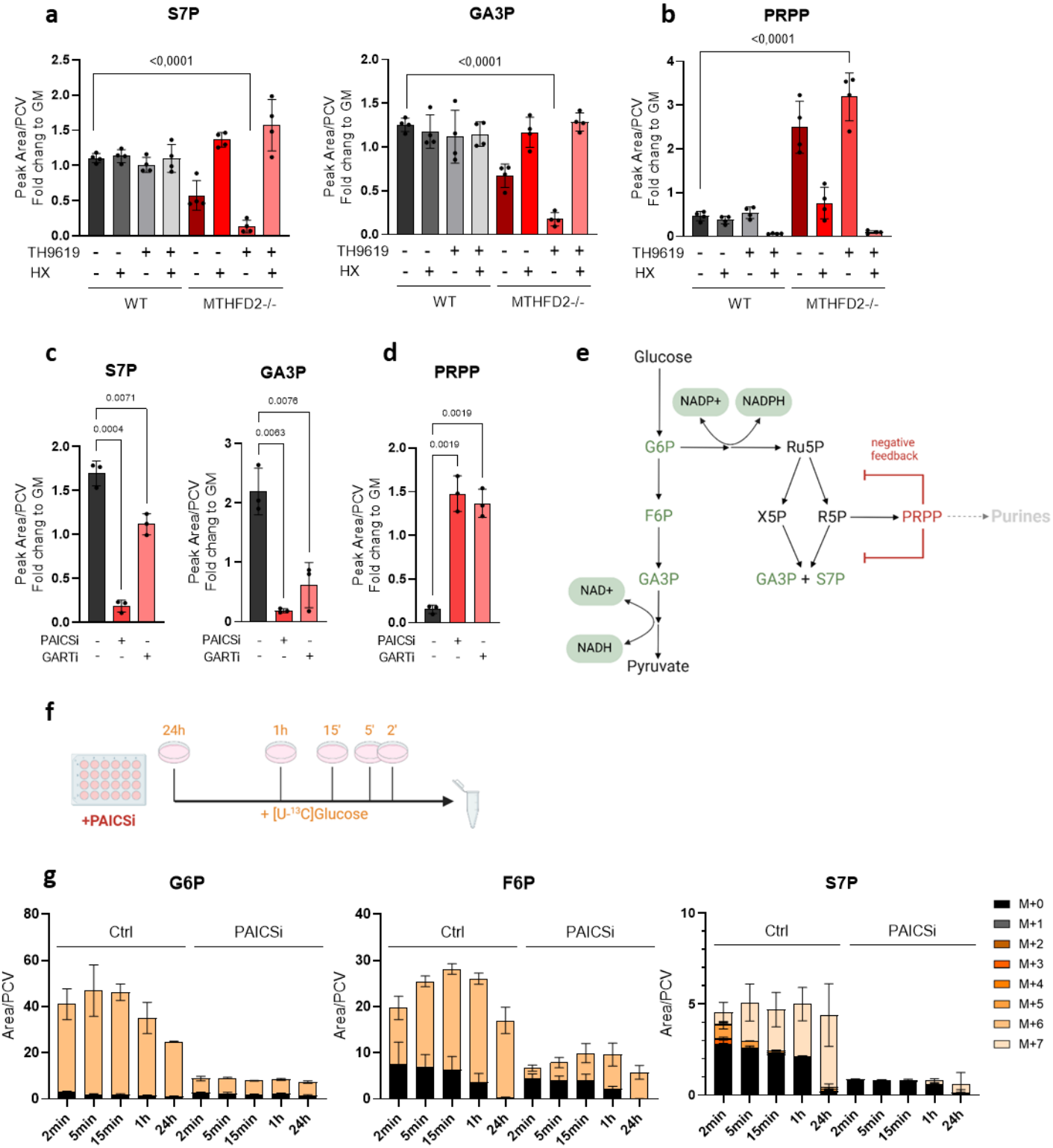
a
S7P
GA3P
b
PRPP
<0,0001
Peak Area/PCV
Fold chang to GM
TH9619
HX
WT
MTHFD2-/-
c
S7P
GA3P
d
PRPP
0.0071
0.0004
0.0076
0.0063
0.0019
0.0019
PAICSi
GARTi
e
Glucose
NADP+
NADPH
G6P
Ru5P
negative feedback
F6P
X5P
R5P
PRPP
Purines
GA3P
GA3P + S7P
NAD+
NADH
Pyruvate
f
24h
1h
15'
5'
2'
+PAICSi
+ [U-13C]Glucose
g
G6P
F6P
S7P
Ctrl
PAICSi
Area/PCV
2min
5min
15min
1h
24h
M+0
M+1
M+2
M+3
M+4
M+5
M+6
M+7

Figure 2: Purine depletion leads to PRPP accumulation and pentose phosphate pathway inhibition

(a) Intracellular S7P, GA3P levels in SW620 WT and MTHFD2-/- cells normalized to PCV after treatment with 1 µM TH9619 and/or 50 µM HX for 24h.

(b) PRPP levels in SW620 WT and MTHFD2-/- cells upon treatment with 1 µM TH9619 and/or 50 µM HX for 24h.

(b) S7P, GA3P and PRPP levels in SW620 cells upon 24h treatment with 5 µM PAICSi or 2 µM GARTi.

(d) PRPP levels in SW620 cells upon 24h treatment with 5 µM PAICSi or 2 µM GARTi.

(e) Simplified scheme of the pentose phosphate pathway (PPP), coupled to purine *de novo* biosynthesis via PRPP.

(f) Schematic representation of the time course [U-^{13}C]-glucose tracing in SW620 cells.

(g) Labeled intracellular levels of G6P, F6P and S7P normalized to PCV from [U-^{13}C]-glucose. SW620 cells pretreated with 5 µM PAICSi for 24h, tracer was added prior extraction at the indicated timepoints ($n = 3$).

Each dot represents one biological replicate, which is the mean of technical triplicates. Statistical analysis was done using one-way ANOVA with Holm-Sidàk multiple comparison test, with a single pooled variance, with representation of the mean ± s.d., unless stated otherwise. *P* values indicate comparisons to the untreated control.

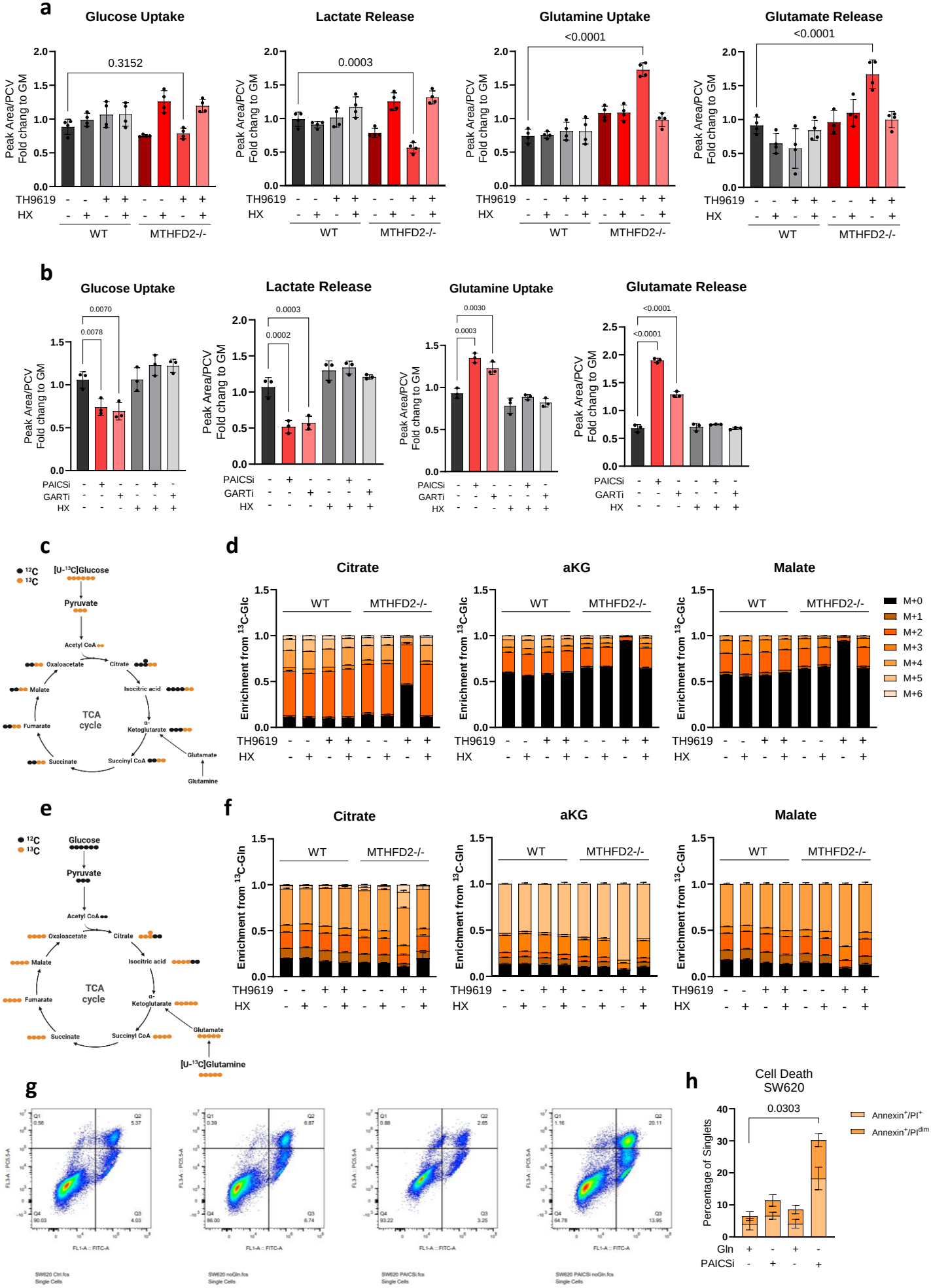
a
Glucose Uptake
Lactate Release
Glutamine Uptake
Glutamate Release
Peak Area/PCV
Fold chang to GM
0.3152
0.0003
<0.0001
<0.0001
TH9619
HX
WT
MTHFD2-/-
b
Glucose Uptake
Lactate Release
Glutamine Uptake
Glutamate Release
0.0070
0.0078
0.0003
0.0002
0.0030
0.0003
<0.0001
<0.0001
PAICSi
GARTi
HX
c
[U-13C]Glucose
Pyruvate
Acetyl CoA
Oxaloacetate
Citrate
Isocitric acid
α-Ketoglutarate
Succinyl CoA
Succinate
Fumarate
Malate
TCA cycle
Glutamate
Glutamine
d
Citrate
aKG
Malate
Enrichment from 13C-Glc
WT
MTHFD2-/-
TH9619
HX
M+0
M+1
M+2
M+3
M+4
M+5
M+6
e
Glucose
[U-13C]Glutamine
f
Enrichment from 13C-Gln
g
h
Cell Death
SW620
0.0303
Percentage of Singlets
Annexin+/PI+
Annexin+/PIdim
Gln
PAICSi

Figure 3: Purine inhibited cancer cells develop a dependency on glutamine

(a) Medium measurements of SW620 WT and MTHFD2$^{-/-}$ cells, treated with 1 µM TH9619 and/or 50 µM HX for 24h. Lactate and glutamate release rates represented as peak area, fresh subtracted and normalized to PCV and GM. For glucose and glutamine uptake, the positive values are represented.

(b) Release rates of lactate and glutamate and uptake of glucose and glutamine in SW620 cells treated with 5 µM PAICSi, 2 µM GARTi and/or 50 µM HX. Represented as peak area, fresh subtracted and normalized to PCV and GM.

(c) Schematic representation of the [U-^{13}C]-glucose tracer entering the TCA cycle.

(d) [U-^{13}C]-glucose derived mass isotopomer distribution (MIDs) of citrate, aKG and malate in SW620 WT and MTHFD2$^{-/-}$ cells upon treatment with 1 µM TH9619 and/or 50 µM HX for 24h (*n=3)*.

(e) [U-^{13}C]-glutamine labelling of TCA cycle intermediates.

(f) MIDs from [U-^{13}C]-glutamine of citrate, aKG and malate in SW620 WT and MTHFD2$^{-/-}$ cells treated with 1 µM TH9619 and/or 50 µM HX for 24h (*n=3)*.

(g) Exemplary gating for annexinV-FITC/PI staining of SW620 WT cells treated with 5 µM PAICSi upon glutamine starvation for 72h.

(h) Cell death analysis by annexinV/PI staining of SW620 cells treated with 5 µM PAICSi with or without glutamine supplementation for 72h (*n=3).*

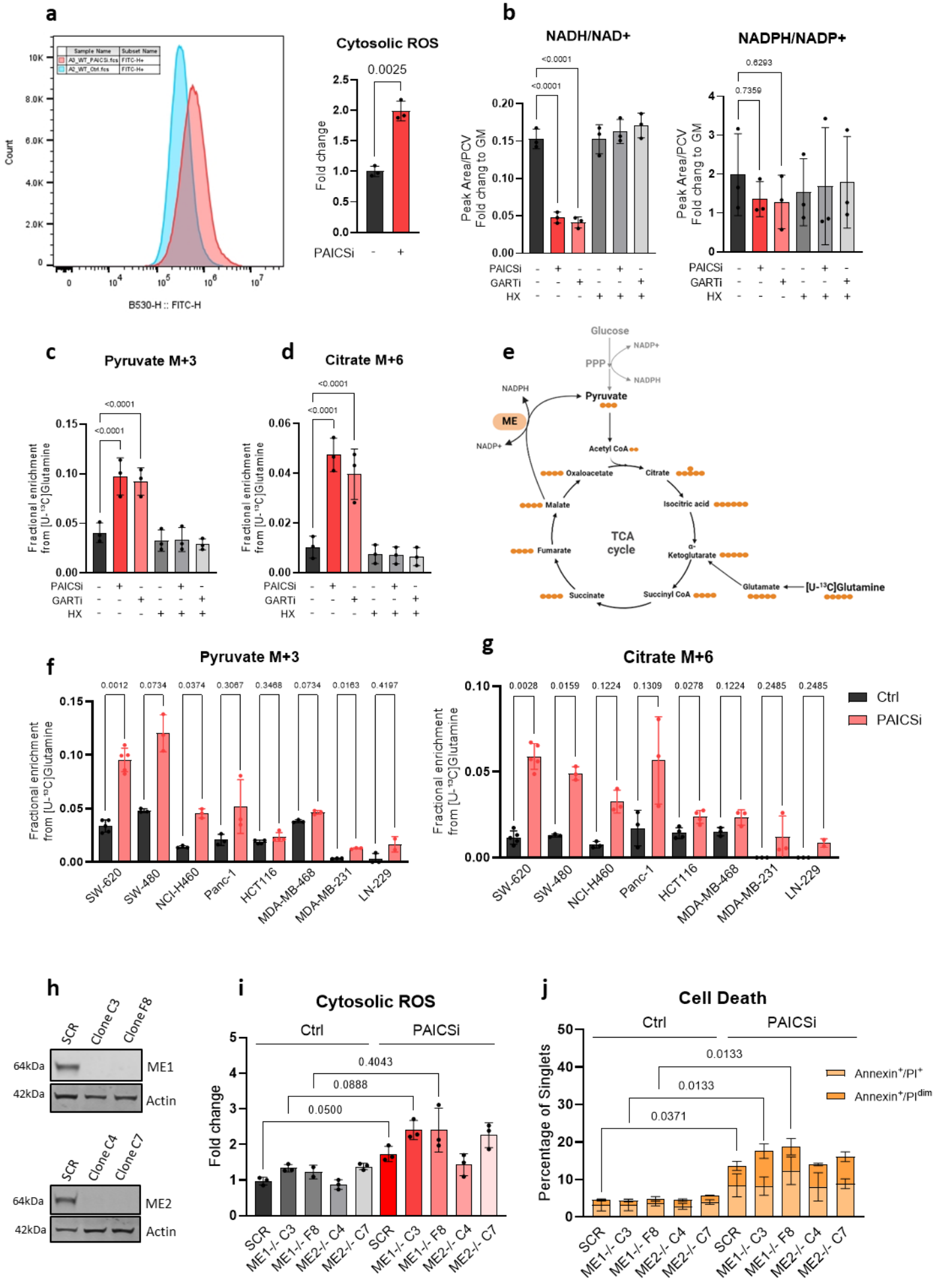
a
Sample Name
Subset Name
A3_WT_PAICSi.fcs
FITC-H+
A2_WT_Ctrl.fcs
FITC-H+
Count
B530-H :: FITC-H
Cytosolic ROS
0.0025
Fold change
PAICSi
b
NADH/NAD+
<0.0001
<0.0001
Peak Area/PCV
Fold chang to GM
NADPH/NADP+
0.6293
0.7359
PAICSi
GARTi
HX
c
Pyruvate M+3
<0.0001
<0.0001
Fractional enrichment from [U-13C]Glutamine
d
Citrate M+6
<0.0001
<0.0001
e
Glucose
PPP
NADP+
NADPH
Pyruvate
ME
Acetyl CoA
Oxaloacetate
Citrate
Malate
Isocitric acid
TCA cycle
Fumarate
α-Ketoglutarate
Succinate
Succinyl CoA
Glutamate
[U-13C]Glutamine
f
Pyruvate M+3
0.0012
0.0734
0.0374
0.3067
0.3468
0.0734
0.0163
0.4197
SW-620
SW-480
NCI-H460
Panc-1
HCT116
MDA-MB-468
MDA-MB-231
LN-229
g
Citrate M+6
0.0028
0.0159
0.1224
0.1309
0.0278
0.1224
0.2485
0.2485
Ctrl
PAICSi
h
SCR
Clone C3
Clone F8
64kDa
42kDa
ME1
Actin
Clone C4
Clone C7
ME2
i
Cytosolic ROS
Ctrl
PAICSi
0.4043
0.0888
0.0500
Fold change
SCR
ME1-/- C3
ME1-/- F8
ME2-/- C4
ME2-/- C7
j
Cell Death
0.0133
0.0133
0.0371
Annexin+/PI+
Annexin+/PIdim
Percentage of Singlets

Figure 4: Purine inhibited cells rely on ME1 to maintain Redox balance

(a) Cytosolic ROS measurement using DCF-DA dye in SW620 cells treated with 5 μM PAICSi for 24h. Mean ± s.d, unpaired, two-tailed t-test with Welch's correction.

(b) NADH/NAD+ and NADPH/NADP+ ratio in SW620 cells treated with 5 μM PAICSi, 2 μM GARTi and/or 50 μM HX for 24h.

(c) Fractional enrichment in pyruvate M+3 upon [U-13C]-glutamine supplementation after 24h in SW620 cells.

(d) Citrate M+6 from [U-13C]-glutamine after 24h in SW620 cells.

(e) Schematic representation of [U-13C]-glutamine tracing and labelling of TCA cycle intermediates upon malic enzyme (ME) activity.

(f) Pyruvate M+3 fractional enrichment from [U-13C]-glutamine after 24h in SW620 (n=5), SW480 (n=3), NCI-H460 (n=3), Panc-1 (n=3), HCT116 (n=4), MDA-MB-468 (n=3), MDA-MB-231 (n=3), LN-229 (n=3) cells.

(g) Citrate M+6 fractional enrichment from [U-13C]-glutamine after 24h in different cancer cell lines.

(h) ME1 and ME2 protein expression in SW620 cells.

(i) Cytosolic ROS measurements in SW620 WT, SCR, $ME1^{-/-}$ and $ME2^{-/-}$ cells, treated with PAICSi for 24h. Mean ± s.d., one-way ANOVA with Dunnett's multiple comparison test.

(j) Cell death of SW620 WT, SCR, $ME1^{-/-}$ and $ME2^{-/-}$ cells, treated with 5 μM PAICSi for 72h, using annexinV-PI. Mean ± s.d., one-way ANOVA with Dunnett's multiple comparison test (*n=5*)

Each dot represents one biological replicate, which is the mean of technical triplicates. Statistical analysis was done using one-way ANOVA with Holm-Sidàk multiple comparison test, with a single pooled variance, with representation of the mean ± s.d., unless stated otherwise. *P* values indicate comparisons to the untreated control.

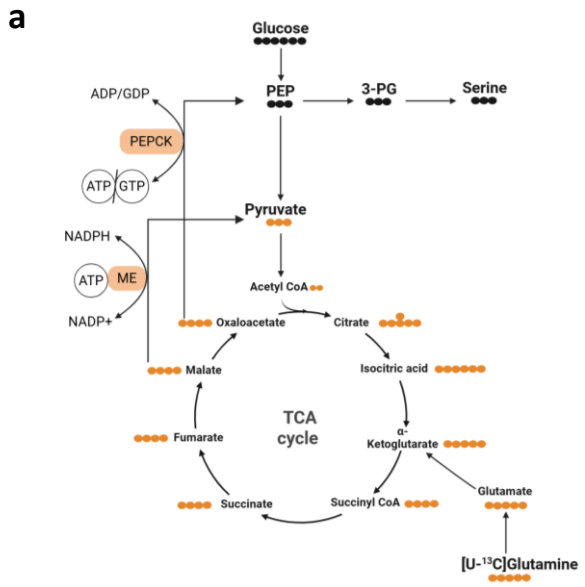

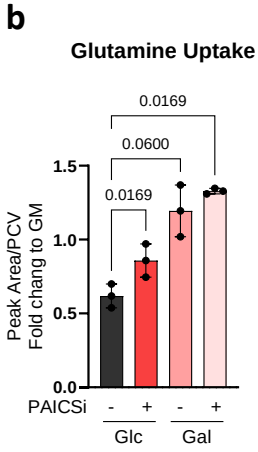

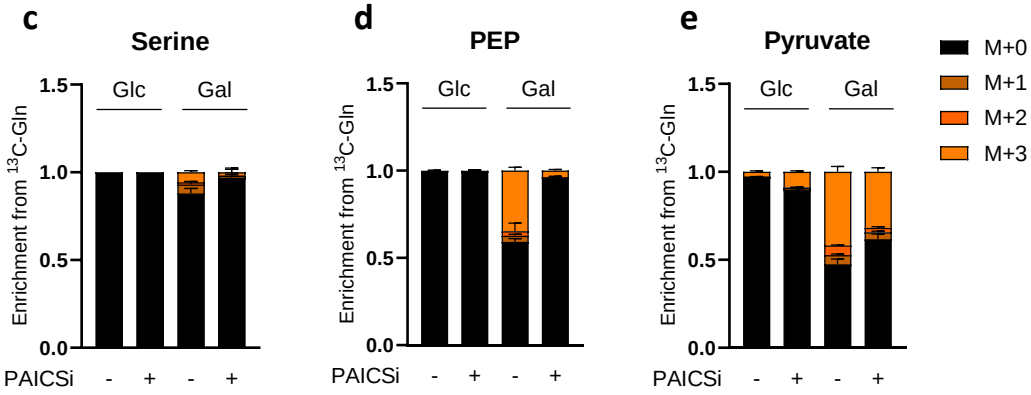

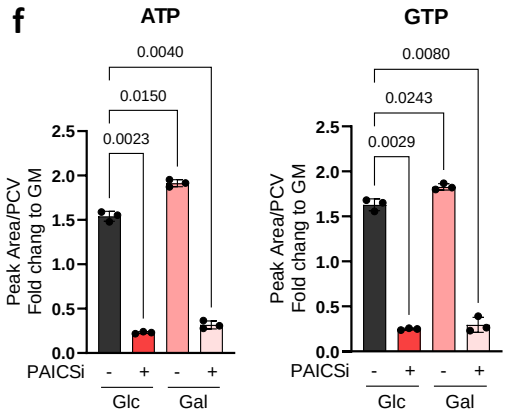

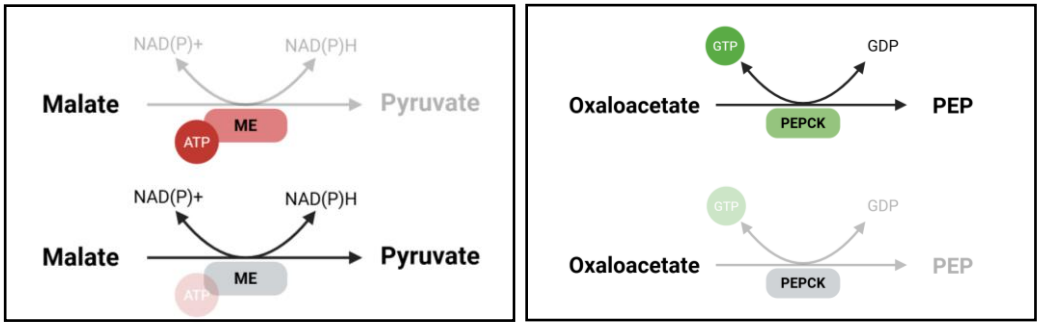

ATP inhibiting ME

GTP activating PEPCK

Figure 5: Purines levels regulate ME and PEPCK activity

(a) Graphical illustration of [U-13C]-glutamine tracing and labelling of upon ME activity.

(b) Glutamine consumption of SW620 cells after 24h incubation with either glucose or galactose medium, treated with 5 μM PAICSi. Peak areas normalized to PCV and GM.

(c) MIDs of serine in SW620 cells treated with 5 μM PAICSi in glucose or galactose for 24h (n=3).

(d) MIDs of PEP from [U-13C]-glutamine after 24h incubation with either glucose or galactose medium, treated with 5 μM PAICSi in SW620 cells (n=3).

(e) Pyruvate MIDs after 24h incubation with [U-13C]-glutamine in SW620 cells, treated with 5 μM PAICSi (n=3).

(f) Intracellular ATP and GTP levels upon 5 μM PAICSi treatment for 24h in SW620 cells incubated in glucose or galactose medium. Peak areas normalized to PCV and GM.

(g) Graphical representation of ME and PEPCK activity, regulated by ATP and GTP.

Each dot represents one biological replicate, which is the mean of technical triplicates. Statistical analysis was done using one-way ANOVA with Holm-Sidàk multiple comparison test, with a single pooled variance, with representation of the mean ± s.d., unless stated otherwise. *P* values indicate comparisons to the untreated control.

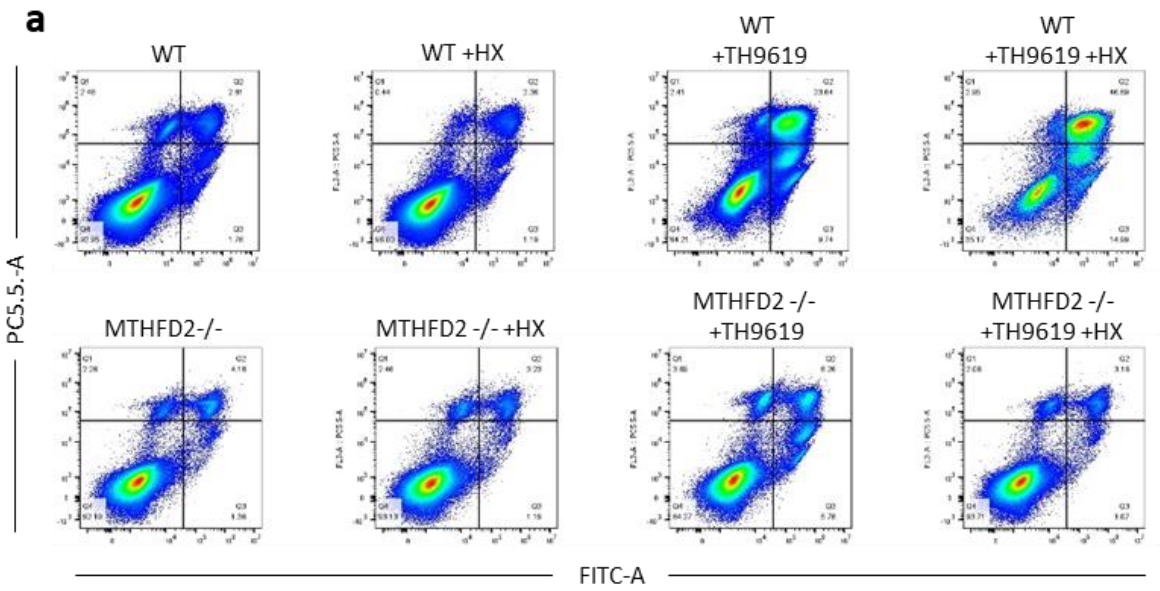
a
WT
WT +HX
WT +TH9619
WT +TH9619 +HX
MTHFD2-/-
MTHFD2 -/- +HX
MTHFD2 -/- +TH9619
MTHFD2 -/- +TH9619 +HX
PC5.5.-A
FITC-A

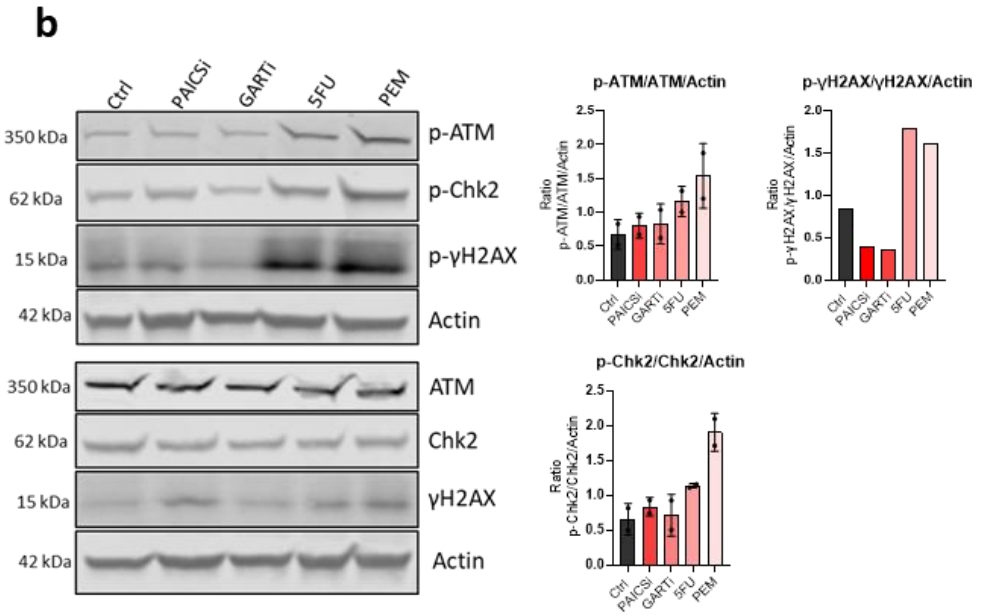
b
Ctrl
PAICSi
GARTi
5FU
PEM
350 kDa
p-ATM
62 kDa
p-Chk2
15 kDa
p-γH2AX
42 kDa
Actin
350 kDa
ATM
62 kDa
Chk2
15 kDa
γH2AX
42 kDa
Actin
p-ATM/ATM/Actin
Ratio p-ATM/ATM/Actin
p-γH2AX/γH2AX/Actin
Ratio p-γH2AX/γH2AX/Actin
p-Chk2/Chk2/Actin
Ratio p-Chk2/Chk2/Actin

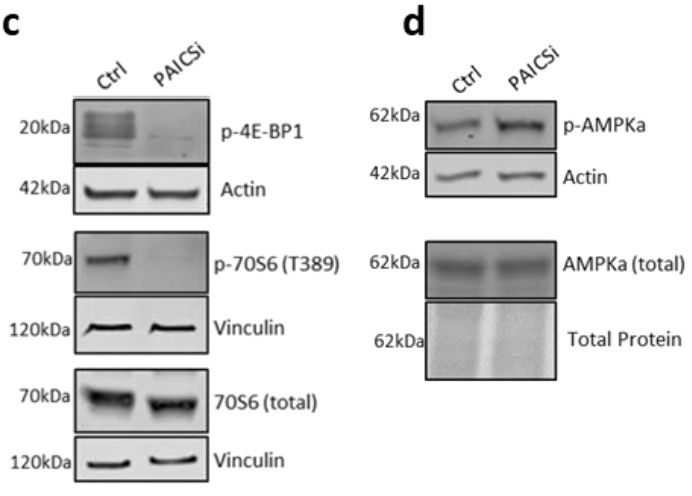
c
Ctrl
PAICSi
20kDa
p-4E-BP1
42kDa
Actin
70kDa
p-70S6 (T389)
120kDa
Vinculin
70kDa
70S6 (total)
120kDa
Vinculin
d
Ctrl
PAICSi
62kDa
p-AMPKa
42kDa
Actin
62kDa
AMPKa (total)
62kDa
Total Protein

Supplementary Figure 1: DNA damage markers. mTOR and AMPK signal upon purine depletion

(a) Exemplary gating for annexinV-FITC/PI staining of SW620 WT and MTHFD2$^{-/-}$ cells treated with 1 µM TH9619 and/or 50 µM HX for 72h.

(b) (p-)ATM, (p-)Chk2 and (p-)γH2AX protein expression and quantification of DNA damage markers in SW620 cells treated with 5 µM PAICSi, 2 µM GARTi, 2 µM 2FU, 2 µM PEM for 24h.

(c) Protein quantification of mTOR related genes, (p-)4E-BP1 and (p-)70S6) in SW620 cells upon 5 µM PAICSi tratement for 24h.

(d) AMPKa and p-AMPKa protein expression in SW620 cells treated with 5 µM PAICSi treatment for 24h.

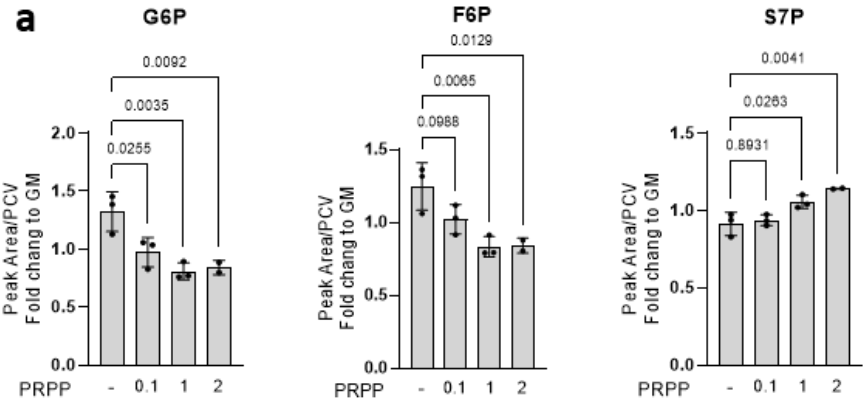
a
G6P
F6P
S7P
0.0092
0.0035
0.0255
0.0129
0.0065
0.0988
0.0041
0.0263
0.8931
Peak Area/PCV
Fold chang to GM
PRPP
-
0.1
1
2

Supplementary Figure 2: Effect of exogenous PRPP supplementation

(a) Intracellular G6P, F6P and S7P levels, peak area normalized to PCV and GM in SW620 cell treated with 0.1, 1 and 2 mM of PRPP. Mean ± s.d., one-way ANOVA with Dunnett's multiple comparison test.

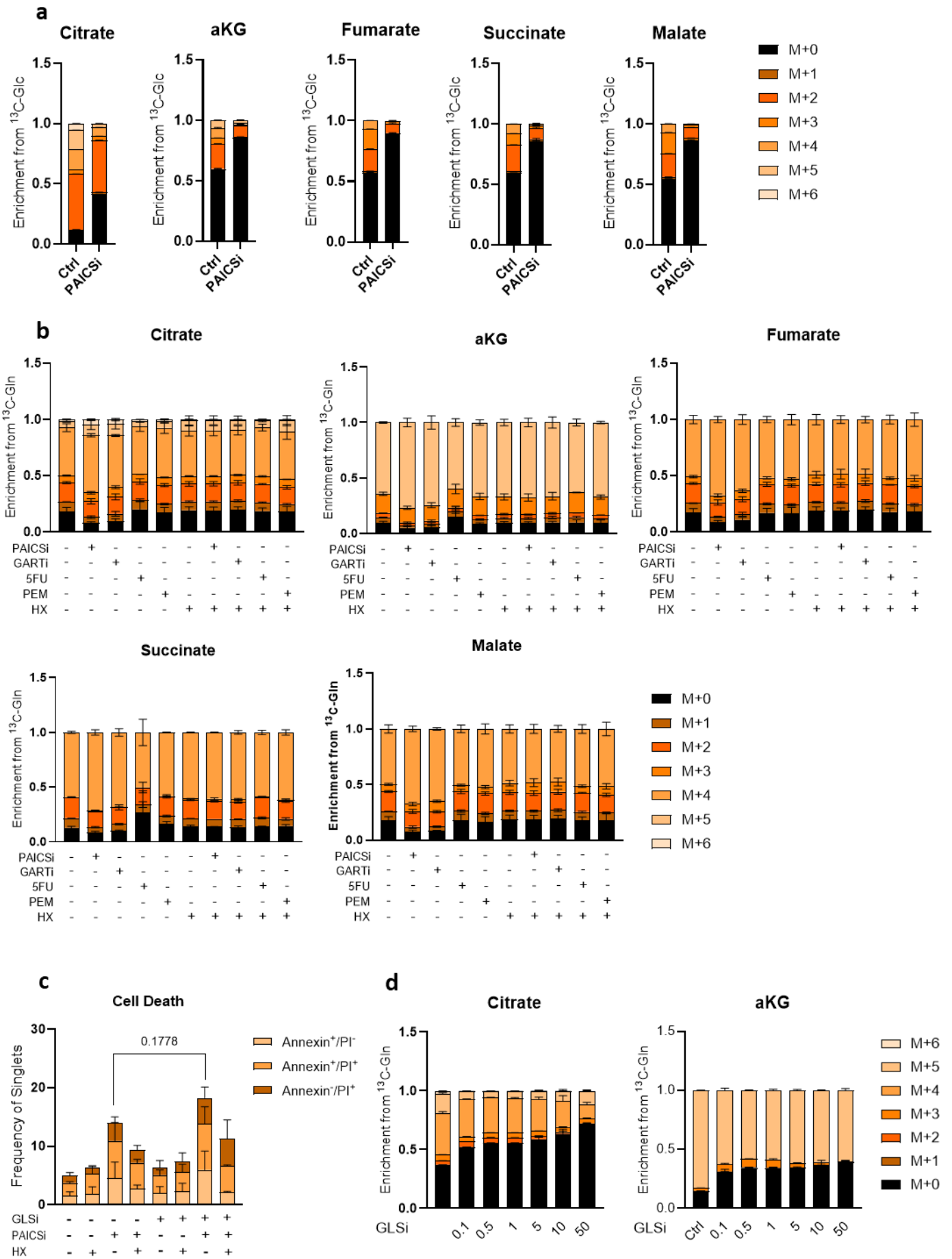
a
Citrate
aKG
Fumarate
Succinate
Malate
Enrichment from 13C-Glc
Ctrl
PAICSi
M+0
M+1
M+2
M+3
M+4
M+5
M+6
b
Citrate
aKG
Fumarate
Succinate
Malate
Enrichment from 13C-Gln
PAICSi
GARTi
5FU
PEM
HX
c
Cell Death
Frequency of Singlets
0.1778
Annexin+/PI-
Annexin+/PI+
Annexin-/PI+
GLSi
PAICSi
HX
d
Citrate
aKG
Enrichment from 13C-Gln
GLSi
Ctrl
0.1
0.5
1
5
10
50

Supplementary Figure 3: Purine inhibited cancer cell switch to glutamine instead of glucose as preferred carbon source for TCA cycle

(a) MIDs of citrate, aKG, fumarate, succinate and malate cultured in medium containing [U-13C]-glucose and treated with 5 μM PAICSi for 24h (*n=3*).

(b) TCA cycle intermediates MIDs upon treatment with with 5 μM PAICSi, 2 μM GARTi, 2 μM 5FU, 2 μM PEM and/or 50 μM HX for 24h in medium containing [U-13C]-glutamine (*n=3*).

(c) Cell death, using annexinV/PI, of SW620 cells treated with 5 μM PAICSi and/or 0,5 μM GLSi and/or 50 μM HX during 72h. Mean ± s.d., one-way ANOVA with Šídák's multiple comparisons test (*n=3*).

(d) MIDs of citrate and aKG cultured in medium containing [U-13C]-glutamine and treated with 0.1-50 μM GLS inhibitor for 24h (*n=3*).

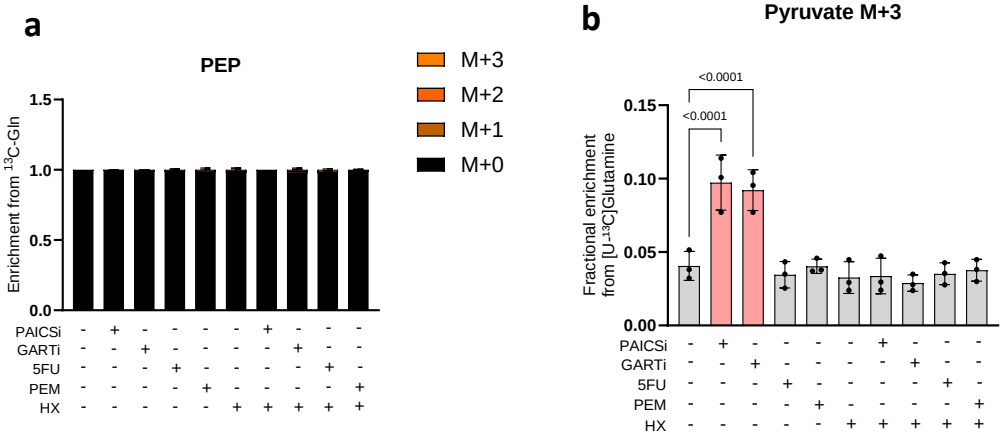
a
PEP
M+3
M+2
M+1
M+0
Enrichment from 13C-Gln
1.5
1.0
0.5
0.0
PAICSi - + - - - - + - - -
GARTi - - + - - - - + - -
5FU - - - + - - - - + -
PEM - - - - + - - - - +
HX - - - - - + + + + +
b
Pyruvate M+3
Fractional enrichment from [U-13C]Glutamine
<0.0001
<0.0001
0.15
0.10
0.05
0.00
PAICSi - + - - - - + - - -
GARTi - - + - - - - + - -
5FU - - - + - - - - + -
PEM - - - - + - - - - +
HX - - - - - + + + + +

Supplementary Figure 4

(a) PEP MIDs after 24h incubation with [U-13C]-glutamine medium and treatment with 5 μM PAICSi, 2 μM GARTi, 2 μM 5FU, 2 μM PEM and/or 50 μM HX (*n=3*).

(b) Fractional enrichment in pyruvate M+3 upon [U-13C]-glutamine supplementation after 24h in SW620 cells treated with 5 μM PAICSi, 2 μM GARTi, 2 μM 5FU, 2 μM PEM and/or 50 μM HX (n=3).

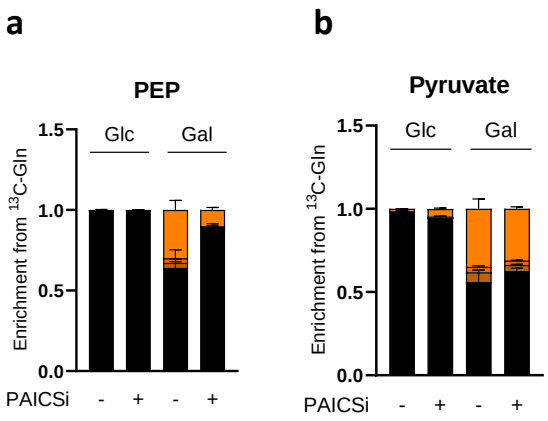
a
PEP
Glc
Gal
1.5
1.0
0.5
0.0
Enrichment from 13C-Gln
PAICSi - + - +
b
Pyruvate
Glc
Gal
1.5
1.0
0.5
0.0
Enrichment from 13C-Gln
PAICSi - + - +

Supplementary Figure 5

(d) MIDs of PEP from [U-13C]-glutamine after 24h incubation with either glucose or galactose medium, treated with 5 μM PAICSi in NCI-H460 cells (n=3).

(e) Pyruvate MIDs after 24h incubation with [U-13C]-glutamine in NCI-H460 cells, treated with 5 μM PAICSi (n=3).

nature COMMUNICATIONS

ARTICLE

https://doi.org/10.1038/s41467-022-30363-y OPEN

Mitochondria preserve an autarkic one-carbon cycle to confer growth-independent cancer cell migration and metastasis

Nicole Kiweler[1], Catherine Delbrouck[1,2], Vitaly I. Pozdeev[3], Laura Neises[1], Leticia Soriano-Baguet[2,4,5], Kim Eiden[1,2], Feng Xian[6], Mohaned Benzarti[1,2], Lara Haase[1,2,7], Eric Koncina[3], Maryse Schmoetten[3], Christian Jaeger[7], Muhammad Zaeem Noman[8], Alexei Vazquez[9], Bassam Janji[8], Gunnar Dittmar[2,6], Dirk Brenner[4,5,10], Elisabeth Letellier[3] & Johannes Meiser[1]✉

Metastasis is the most common cause of death in cancer patients. Canonical drugs target mainly the proliferative capacity of cancer cells, which leaves slow-proliferating, persistent cancer cells unaffected. Metabolic determinants that contribute to growth-independent functions are still poorly understood. Here we show that antifolate treatment results in an uncoupled and autarkic mitochondrial one-carbon (1C) metabolism during cytosolic 1C metabolism impairment. Interestingly, antifolate dependent growth-arrest does not correlate with decreased migration capacity. Therefore, using methotrexate as a tool compound allows us to disentangle proliferation and migration to profile the metabolic phenotype of migrating cells. We observe that increased serine de novo synthesis (SSP) supports mitochondrial serine catabolism and inhibition of SSP using the competitive PHGDH-inhibitor BI-4916 reduces cancer cell migration. Furthermore, we show that sole inhibition of mitochondrial serine catabolism does not affect primary breast tumor growth but strongly inhibits pulmonary metastasis. We conclude that mitochondrial 1C metabolism, despite being dispensable for proliferative capacities, confers an advantage to cancer cells by supporting their motility potential.

[1] Cancer Metabolism Group, Department of Cancer Research, Luxembourg Institute of Health, Luxembourg, Luxembourg. [2] Faculty of Science, Technology and Medicine, University of Luxembourg, 2 avenue de Université, Esch-sur-Alzette, Luxembourg. [3] Faculty of Science, Technology and Medicine, Department of Life Sciences and Medicine, Molecular Disease Mechanisms Group, University of Luxembourg, Esch-sur-Alzette, Luxembourg. [4] Experimental & Molecular Immunology, Department of Infection and Immunity, Luxembourg Institute of Health, 29 Rue Henri Koch, Esch-sur-Alzette, Luxembourg. [5] Immunology & Genetics, Luxembourg Centre for Systems Biomedicine, University of Luxembourg, 7 Avenue des Hauts Fourneaux, Esch-sur-Alzette, Luxembourg. [6] Proteomics of cellular signaling, Department of Infection and Immunity, Luxembourg Institute of Health,1a Rue Thomas Edison, Strassen, Luxembourg. [7] Luxembourg Centre for Systems Biomedicine, University of Luxembourg, Esch-sur-Alzette, Luxembourg. [8] Tumor Immunotherapy and Microenvironment (TIME) Group, Department of Cancer Research, Luxembourg Institute of Health, Luxembourg, Luxembourg. [9] Institute of Cancer Sciences, University of Glasgow, Glasgow, UK. [10] Odense Research Center for Anaphylaxis (ORCA), Department of Dermatology and Allergy Center, Odense University Hospital, University of Southern Denmark, Odense, Denmark. ✉email: johannes.meiser@lih.lu

The survival rates of patients harboring primary tumors steadily increase due to targeted treatment schemes. However, in case of tumor relapse and metastatic disease, effective therapies are mostly lacking with the consequence that secondary tumors account for the majority of cancer deaths[1]. Classical chemotherapeutic approaches to counteract cancer growth aim to target biomass production by interfering with the synthesis of proteins, lipids, and nucleotides and thereby directly interfere with central pathways of cancer cell metabolism[2,3]. Prospectively, therapeutic approaches targeting metabolic pathways that also support the invasive and migratory properties of cancer cells would help to prevent metastatic progression of the initial disease. However, profound knowledge of specific metabolic dependencies that support growth-independent processes during the metastatic cascade, are only starting to be understood[4].

Nucleotide synthesis is an essential requirement for cancer cell proliferation. Consequently, antifolates such as Methotrexate (MTX) and related compounds have been proven as successful chemotherapeutics for several decades. Although differences between the various antifolates exist, a shared mode of action is the inhibition of one-carbon (1C) metabolism which provides essential building blocks for thymidylate and purine synthesis. Additionally, 1C metabolism has implications in supporting methylation reactions, glutathione, heme, sphingolipid and protein synthesis[5]. 1C metabolism describes a metabolic cycle that is spread across mitochondrion and cytoplasm and it is mainly fueled by the non-essential amino acid serine. De-novo serine synthesis is catalyzed by the rate limiting enzyme phosphoglycerate dehydrogenase (PHGDH) which is amplified in different tumors[6–8]. Hence, targeting serine synthesis, serine catabolism or serine availability by starvation or inhibition of PHDGH has been proven successful to inhibit cancer progression[9–17]. To support the various anabolic programs, cytosolic 1C metabolism is of particular importance, while mitochondrial 1C metabolism is dispensable due to the reversibility of the cytosolic 1C metabolism[16]. In fact, depending on intracellular folate levels, cytosolic 1C metabolism can be the dominant route to provide one-carbon units for nucleotide synthesis[17]. In that light, reasons for conserved mitochondrial 1C metabolism are still not fully understood. Previous evidence suggests implications of mitochondrial 1C metabolism for mitochondrial translation[18,19]. One additional explanation resides in the observation that mitochondrial derived formate lowers the pool of free cytosolic folates by increasing the 10-CHO-THF pool thereby protecting it from degradation. Upon MTX, degradation is facilitated as folates accumulate in the oxidized DHF form, impeding the 10-CHO-THF synthetase activity of MTHFD1[20]. However, if mitochondrial folate-dependent 1C metabolism and formate production remains functional under conditions of cytosolic 1C metabolism impairment and whether mitochondrial 1C metabolism itself confers additional functions that contribute to tumorigenesis remains unknown.

We have previously shown that a reduction of biomass demand can result in increased formate release from cancer cells to their surrounding microenvironment[21] and that the rate of serine catabolism to formate is significantly increased in adenomas of the small intestine and breast tumors compared to normal tissue[22]. Importantly, enhanced formate release rates and increased extracellular formate concentrations have been shown to increase the invasiveness of glioblastoma cells in vitro[22].

Apart from our previous findings on formate overflow and its potential implications for cancer cell invasion[21,22], other reports substantiate a role of serine metabolism in the context of metastasis[7,14,23–25]. However, such studies were so far focused on the relevance of serine de novo synthesis via PHGDH or extracellular serine availability for metastatic outgrowth (proliferative aspect) in the secondary tissue[7,14,23–25]. In contrast, whether mitochondrial serine catabolism also has a growth-independent role in promoting cancer cell motility that potentially increases the rate of cancer cell escape from the primary tumor has not been addressed so far. Being able to identify and target metabolic programs that promote the early steps of the metastatic cascade would help to contain the tumor, a clinical phenotype with more favorable therapeutic outcome compared to advanced metastatic stages.

In the present study, we observed that antifolates, albeit being strongly cytostatic, did not decrease the cell's motility potential. Using MTX as a tool compound to selectively inhibit cytosolic 1C metabolism, we show that mitochondrial 1C metabolism runs as an autarkic, compartmentalized pathway that is important to drive cancer cell motility. In contrast, the cytosolic part of 1C metabolism, which is essential for nucleotide synthesis during proliferation, is dispensable for the cellular motility potential. Hence, we provide mechanistic evidence that one selective advantage of mitochondrial 1C metabolism is to support cell motility. We corroborate this hypothesis in an orthotopic breast cancer model. Here, we demonstrate that ablating mitochondrial 1C metabolism effectively blocks mitochondrial serine catabolism but does not affect primary tumor growth. Yet, it strongly inhibits pulmonary metastasis formation.

Results

Inhibition of anabolic synthesis routes differentially impacts the motility potential of cancer cells. To assess the relative importance of different anabolic pathways for cancer cell migration, we employed a panel of metabolic perturbations targeting glycolysis, mitochondrial electron transport chain (ETC) as well as lipid, protein, and nucleotide synthesis (Fig. 1a). As expected, the chosen metabolic interventions inhibited proliferation and affected cell cycle progression of MDA-MB-468 breast cancer cells with no to mild toxic effects after 48 h treatment (Fig. 1b–c, S1A). Inhibition of glycolysis, ETC, lipid, and protein synthesis significantly reduced migration of MDA-MB-468 cells (Fig. 1d). Surprisingly and in contrast to all other growth-inhibiting conditions, inhibition of nucleotide synthesis with various drugs did not diminish migration of MDA-MB-468 cells (Fig. 1e). Calculation of the area under curve (AUC) allowed us to quantitatively compare wound closure over time (Fig. 1d, e) and confirmed that wound closure was significantly reduced upon treatment with rotenone (Rot), galactose (Gal), simvastatin (SIM) and sirolimus (rapamycin, SIR). However, treatment with the antifolates methotrexate (MTX) and pemetrexed (PEM), as well as with hydroxyurea (HU) and clofarabine (CLO) did not affect or did even significantly increase wound closure in scratch assays in comparison to fully proliferative, untreated control cells. While cell migration correlates with reduced cell growth for all other metabolic perturbations, nucleotide synthesis inhibition does not reduce cell migration in correlation to growth inhibition (Fig. 1f, g). Sustained migration in response to nucleotide synthesis inhibition was verified in LN229 glioblastoma and 4T1 breast cancer cells (Fig. S1B–D). Of note, using dialyzed or normal FBS did not change the result (Fig. S1E). This observation was also confirmed in trans-well migration assays using Boyden chambers (Fig. 1h, S1F, G). Furthermore, using ECM-collagen coating in trans-well assay, we found that nucleotide synthesis inhibition also had no impact on the invasive capacity of MDA-MB-468 cells (Fig. 1h), LN229 and 4T1 cells (Fig. S1F, G). To validate if MTX resistance results in a pro-migratory effect, we generated MTX-resistant MDA-MB-468 cells by long-term cultivation in 50 nM MTX for 2 months. The resulting MTX-resistant MDA-MB-468 cells proliferate in the presence of increasing

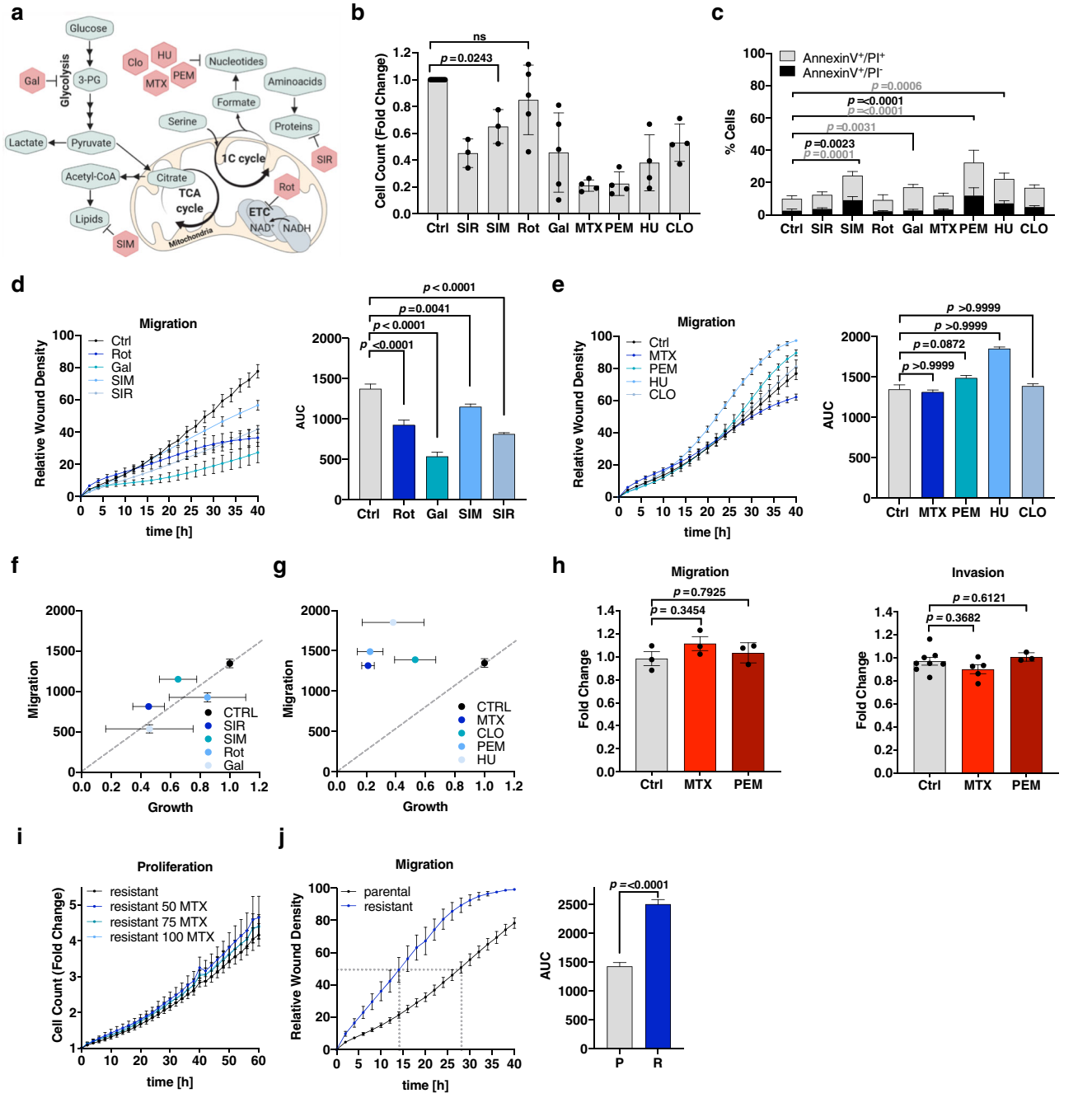

Fig. 1 Inhibition of major anabolic synthesis routes differentially impacts the motility potential of cancer cells. a Synthesis routes of metabolic building blocks (lipids, nucleotides, and proteins) and pharmacologic intervention points of the selected drug panel. **b** MDA-MB-468 cells were counted after 48 h treatment with 100 nM Sirolimus (SIR) ($n = 3$), 1 µM Simvastatin (SIM) ($n = 3$), 50 nM Rotenone (Rot) ($n = 5$), galactose (Gal) ($n = 5$) supplementation, 50 nM Methotrexate (MTX) ($n = 4$), 1 µM Pemetrexed (PEM) ($n = 4$), 0.5 mM hydroxyurea (HU) ($n = 4$), and 100 nM Clofarabine (CLO) ($n = 4$). Mean ± SD; ordinary one-way ANOVA with Dunnett's multiple comparisons test. Unlabeled comparisons to Ctrl are all significant with $p < 0.0001$. **c** MDA-MB-468 cells were treated as in (**b**). Cell death was assessed by flow cytometry and AnnexinV-FITC/PI-staining; mean ± SD of independent experiments ($n = 8$ (Ctrl), $n = 4$ (SIR, SIM, PEM, CLO), $n = 3$ (Rot, Gal, MTX, HU)). Two-way ANOVA with Dunnett's multiple comparisons test. **d**, **e** Migration of MDA-MB-468 cells upon (**d**) 50 nM Rot ($n = 5$), Gal ($n = 5$), 1 µM SIM ($n = 3$), and 100 nM SIR ($n = 4$) or (**e**) 50 nM MTX ($n = 7$), 1 µM PEM ($n = 3$), 0.5 mM HU ($n = 4$), and 100 nM CLO (n = 4) and respective area under curve (AUC); mean ± SEM of independent experiments; Brown-Forsythe and Welch one-way ANOVA with Dunnett's multiple comparisons test. **f**, **g** Correlation of cell migration (AUC over 40 h, mean ± SEM, ($n =$ as in (**d**, **e**)) and proliferation (fold cell growth after 48 h, mean ± SD ($n =$ as in (**b**)). MDA-MB-468 cells were treated as in (**b**) and (**d**, **e**). **h** Migration and invasion of MDA-MB-468 cells treated for 24 h with 50 nM MTX using non-coated (migration) or ECM-Collagen-coated (invasion) Boyden chambers. Mean ± SEM (Migration: $n = 3$, Invasion: $n = 7$ (Ctrl), 5 (MTX, 3 (Pem)); Brown-Forsythe and Welch one-way ANOVA with Dunnett's multiple comparisons test. **i** Proliferation of MTX-resistant MDA-MB-468 cells upon the indicated concentrations of MTX [nM]; mean ± SEM of independent experiments ($n = 4$). **j** Migration of parental and MTX-resistant MDA-MB-468 cells and respective AUC; mean ± SEM of independent experiments (parental $n = 15$, resistant $n = 6$); unpaired, two-tailed *t*-test with Welch's correction. Time point of 50% wound closure is indicated. Source data are provided as a Source Data file.

concentrations of MTX (Fig. 1i) and display enhanced migratory capacity compared to the parental MDA-MB-468 cell line (Fig. 1j).

In conclusion, the perturbation of any major anabolic route results in growth repression. However, the impact on cell migration highly depends on the targeted metabolic pathway, with nucleotide synthesis being an ineffective target to abrogate cell motility. Furthermore, prolonged nucleotide synthesis inhibition in drug-resistant cells acts as a selection pressure for more motile cancer subpopulations.

Sustained motility upon MTX is supported by a ROS-driven EMT phenotype. As MTX induced the strongest growth repression without increasing cell death (Fig. 1b, c), we used it as a tool compound to disentangle proliferation from migration to investigate the metabolic processes that support cancer cell migration. After testing multiple concentrations (Fig. S2A), we chose a concentration of 50 nM MTX for subsequent experiments. 50 nM MTX is significantly growth- and cell cycle-arresting in MDA-MB-468 cells (Fig. 1b, S1A) and has also been shown to be within the therapeutic window[26–29]. As this concentration of 50 nM is significantly lower compared to earlier in vitro studies[20,30–33], we first set out to validate known drug effects of MTX in our system. We observed that 48 h MTX treatment of MDA-MB-468 cells resulted in altered cellular morphology with individual cells visibly increasing in cell size and exhibiting an outstretched cell shape with protruding edges (Fig. 2a). MTX-resistant MDA-MB-468 cells showed comparable morphologic alterations (Fig. S2B). While the observed cell cycle and proliferation arrest upon MTX treatment was rapidly reversible (Fig. S2C, D) upon MTX removal, [U-^{13}C]serine tracing and metabolic flux analysis confirmed that 50 nM MTX did strongly inhibit nucleotide synthesis (Fig. 2b). Of note, nucleotide synthesis was partially restored in MTX-resistant MDA-MB-468 cells (Fig. S2E). Stable isotope labeling by amino acids in cell culture (SILAC) and quantitative proteomics analysis further confirmed the efficacy of the selected MTX dose as mechanistic targets of MTX such as dihydrofolate reductase (DHFR), thymidylate synthase (TYMS), and thymidine kinase (TK1) were upregulated by treatment as expected (Fig. S2F). DHFR expression was also increased in MTX resistant cells, while FolRa expression was slightly decreased (Fig. S2G). Moreover, superoxide dismutase (SOD) was one of the most significantly upregulated proteins in response to treatment (Fig. S2F), which corresponds to prior reports that depict MTX as a potent inducer of oxidative stress[30,34,35]. We validated these prior findings with our low dose of MTX by measuring a moderate but significant increase of mitochondrial and cytosolic reactive oxidant species (ROS) upon acute MTX treatment and in the MTX resistant cells (Fig. S2H, I, J). In line with increased ROS levels we observed NRF2 stabilization, however, this did not result in activation of the BACH1 axis, as reported earlier for metastatic lung cancer[36,37] (Fig. S2K, I). Increased ROS levels upon MTX correspond to earlier reports that highlight the potential of oxidative stress as a driver of cancer cell transformation via epithelial-mesenchymal transition (EMT)[38–44]. EMT is also a known general mechanism to escape chemotherapy induced effects.

In line with previous reports, we found that *ZEB1* and *ZEB2* expression as well as *VIM* expression was upregulated in a time-dependent manner in response to acute MTX treatment and in the MTX-resistant cell line (Fig. 2c, d, S2F, M, N). MTX-treatment also induced the expression of the collagenase *MMP9* (Fig. S2O), an enzyme which is involved in the degradation of the extracellular matrix during cancer cell invasion[45]. Treatment of cells with the antioxidant N-acetylcysteine (NAC) reduced ROS levels in MTX-treated MDA-MB-468 cells (Fig. S2P) and resulted in a significant reduction of MTX-induced cell migration (Fig. 2e) and EMT phenotype induction (Fig. 2f). These findings confirm that the chosen low dose of MTX is sufficient to promote EMT in a ROS dependent manner, supporting earlier reports suggesting EMT onset in context of pulmonary fibrosis using high doses of MTX[46,47]. Such moderate increase in cellular ROS levels after MTX might contribute to a pro-migratory stimulus that subsequently results in the observed sustained migration.

MTX-treated cells sustain high metabolic rates and enhance de novo serine synthesis. In addition to the here reported MTX-specific effects on ROS and EMT, we wanted to take advantage of the MTX effect (sustained migration) to identify growth-independent metabolic liabilities that support cell migration.

To that end, we profiled central carbon metabolism using [U-^{13}C]glutamine and [U-^{13}C]glucose tracing to monitor glycolytic activity and glutamine- or glucose-derived carbon oxidation through the TCA cycle (Fig. 3a, d). Absolute consumption and release (CORE) rates of glutamine and glutamate were sustained in response to MTX treatment (Fig. 3b), while the relative TCA-cycle flux of [U-^{13}C]glutamine was significantly increased in response to MTX (Fig. 3c). Absolute quantification of CORE rates of glucose and lactate also revealed sustained high glycolytic rates upon MTX treatment (Fig. 3e). This came as a surprise, as lactate release rates were previously shown to correlate with cell growth rates[48]. In MDA-MB-468 cells, the maintained glycolytic rate and the associated lactate release at constant high levels (Fig. 3e) indicate a constant generation of glycolysis-derived ATP even in the presence of reduced energetic demand for anabolic reactions in growth-arresting MTX conditions. Consequently, [U-^{13}C] glucose distribution within the TCA-cycle was sustained by MTX treatment in MDA-MB-468 cells (Fig. 3f) as well as in 4T1 and LN229 cells (Fig. S3A, B). It has previously been shown that MTX inhibits oxygen consumption rates (OCR) in HCT116 cells[18]. We could replicate this finding and observed a ~30 % reduction of OCR in HCT116 cells upon MTX (Fig, S3C), while OCR in MDA-MB-468, LN229, and 4T1 cells was sustained (Fig. 3g). This indicates cell line specific effects of MTX on OCR. Furthermore, MTX treatment significantly increased the relative flux of glucose to serine despite decreased anabolic demands for nucleotide synthesis (Fig. 3h, S3D). Protein levels of PHGDH, PSPH, and PSAT1 that catalyze the serine de novo synthesis pathway from glucose were unaltered in response to MTX treatment in multiple cell lines (Fig. S3E–H). In agreement with Diehl et al[49]. who showed that changes in NAD^+/NADH ratio can increase PHGDH activity and in consequence serine de novo synthesis rates, we observed an increased NAD^+/NADH ratio upon MTX (Fig. 3i). As MTX is well characterized as an inhibitor of DHFR and thus 1C metabolism, it came to our surprise that MTX treatment did also increase the abundance of extracellular formate M + 1 isotopologues derived from [U-^{13}C]glucose through serine and the mitochondrial 1C metabolism (Fig. 3j, S3I).

In summary, the metabolic profiling demonstrates that, despite decreased metabolic demand for biomass production, MTX-treated cells sustain high metabolic rates that are comparable to fully proliferating cells. Additionally, and in contrast to general assumptions, cytosolic DHFR inhibition results in increased rates of serine synthesis and downstream mitochondrial formate excretion suggesting an uncoupling of mitochondrial 1C metabolism from cytosolic 1C metabolism.

Mitochondria protect 1C metabolism-dependent serine catabolism upon cytosolic 1C pathway inhibition. Our finding of

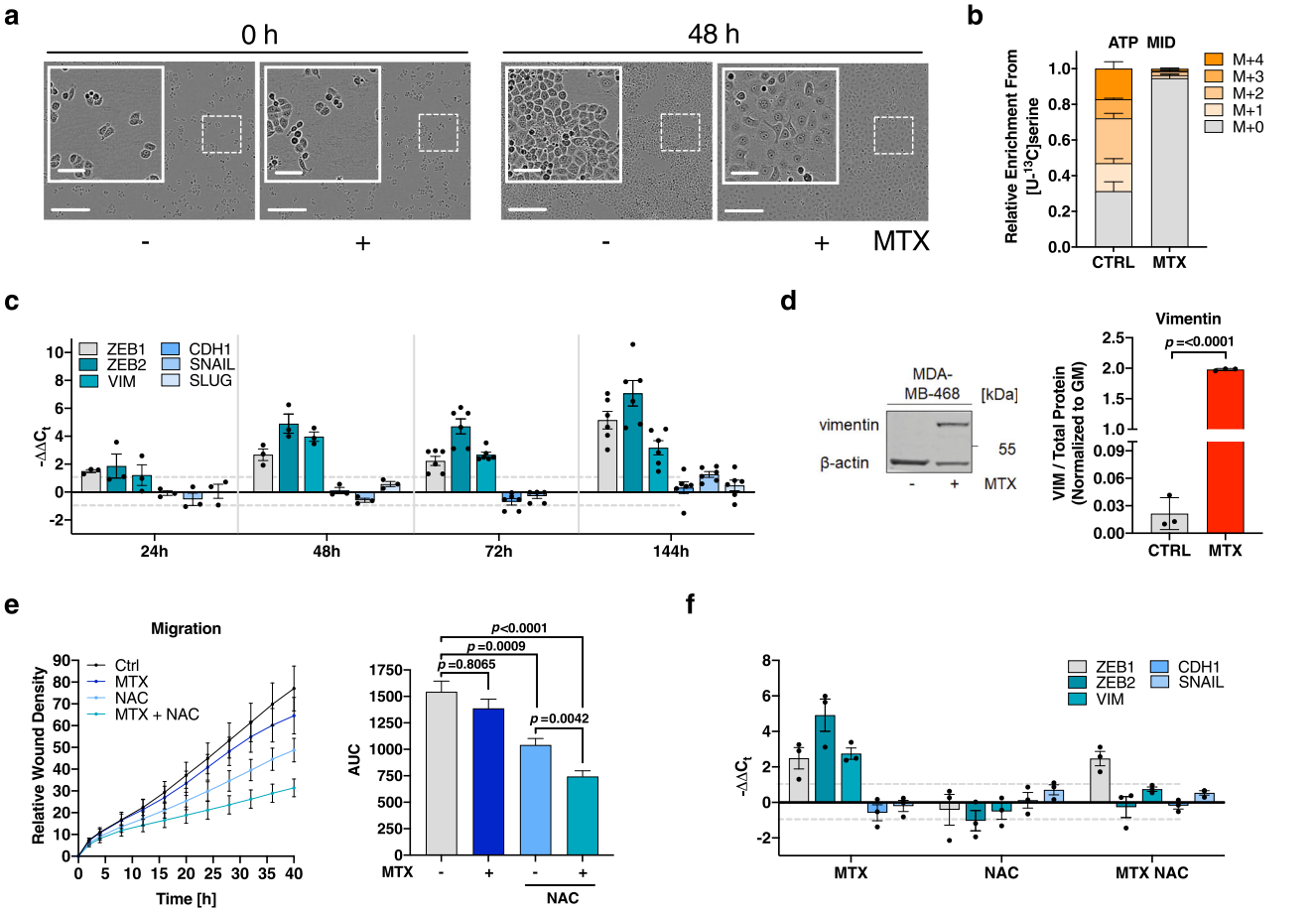

Fig. 2 Enhanced motility under MTX is supported by a ROS-driven EMT phenotype. a Morphology of MDA-MB-468 cells after 48 h 50 nM MTX. Bright-field images are representative of 3 independent experiments. Scale bars correspond to 60 and 300 µm. **b** Mass isotopomere distribution (MID) of intracellular ATP upon [U-^{13}C]serine tracer in response to 24 h 50 nM MTX in MDA-MB-468 cells. Mean ± SEM of 5 independent experiments each measured in triplicate wells. **c** mRNA expression from the indicated target genes in MDA-MB-468 cells upon 50 nM MTX at the indicated time points measured by real-time RT-qPCR. Mean ± SEM ($n = 3$ (24 h, 48 h), 6 (72 h, 144 h)). No data measured for SLUG expression at 72 h. **d** Protein levels of vimentin in MDA-MB-468 cells after 240 h 50 nM MTX; β-actin as loading control. Quantification of vimentin signal relative to total protein stain. Mean ± SD ($n = 3$); unpaired, two-tailed *t*-test with Welch's correction. **e** Migratory potential of MDA-MB-468 cells in response to 10 mM N-acetylcysteine (NAC) and 50 nM MTX as quantification of relative wound density in IncuCyte and respective AUC. Graph shows mean ± SEM of independent experiments ($n = 3$); Brown-Forsythe and Welch ANOVA test with Games-Howell's multiple comparisons test. **f** mRNA expression from the indicated target genes in MDA-MB-468 cells upon 10 mM NAC and 50 nM MTX at 72 h measured by real-time RT-qPCR. Mean ± SEM ($n = 3$). Source data are provided as a Source Data file.

increased [U-^{13}C]glucose-derived M + 1 formate excretion under MTX (Fig. 3j, S3I), allows the hypothesis that mitochondrial 1C metabolism can function in an autarkic manner when cytosolic 1C metabolism is inactivated (Fig. 4a). To corroborate this hypothesis, we employed [U-^{13}C]serine tracing to monitor serine flux through 1C metabolism. We observed that cytosolic block of 1C metabolism via MTX did not reduce the exchange rates of serine, glycine and formate in MDA-MB-468 or LN229 cells (Fig. 4b, C, S4A, C). In contrast, the formate release rate was significantly increased and the increased fraction of labeled formate proved that most of the released formate is derived from [U-^{13}C]serine and not from other carbon sources that could alternatively generate formate in presence of MTX. Of note, sustained serine consumption and formate overflow via 1C metabolism upon DHFR inhibition could also be confirmed in Plasmax medium[50], which is a culture medium closer to human physiology (Fig. S4D). Since cell dry mass composition is constituted by around 60% of proteins[51], growth arresting conditions generally result in decreased consumption rates of proteinogenic amino acids. In fact, a general trend for decreased consumption of essential amino acids was observed (Fig. S4b). Hence, sustained serine consumption rates upon growth arrest suggest that spared serine that is otherwise used for anabolic processes such as nucleotide synthesis, is used for alternative metabolic pathways that support cell motility and survival.

Mechanistically, 1C metabolism follows a cycle in which serine can be resynthesized in the cytoplasm and mitochondrion from glycine via serine hydroxymethyltransferase 1 and 2 (SHMT1, SHMT2) (Fig. 4a). As the SHMT reaction is highly reversible, the serine labeling pattern from [U-^{13}C]serine is composed of a mix of M + 1, M + 2 and M + 3 isotopologues, which represents the different recombination events with labeled and unlabeled glycine and formate[16,21,52]. Consequently, M + 1 and M + 2 serine isotopologues are expected to be absent upon complete 1C metabolism inhibition. Intriguingly, cytosolic DHFR inhibition with MTX neither completely abrogated serine M + 1 and M + 2 isotopologues upon [U-^{13}C]serine nor did it significantly affect the serine to glycine level ratio in MDA-MB-468 or LN229 cells (Fig. 4d, e, S4E, F), further supporting our hypothesis of a persistent mitochondrial 1C metabolism upon DHFR inhibition.

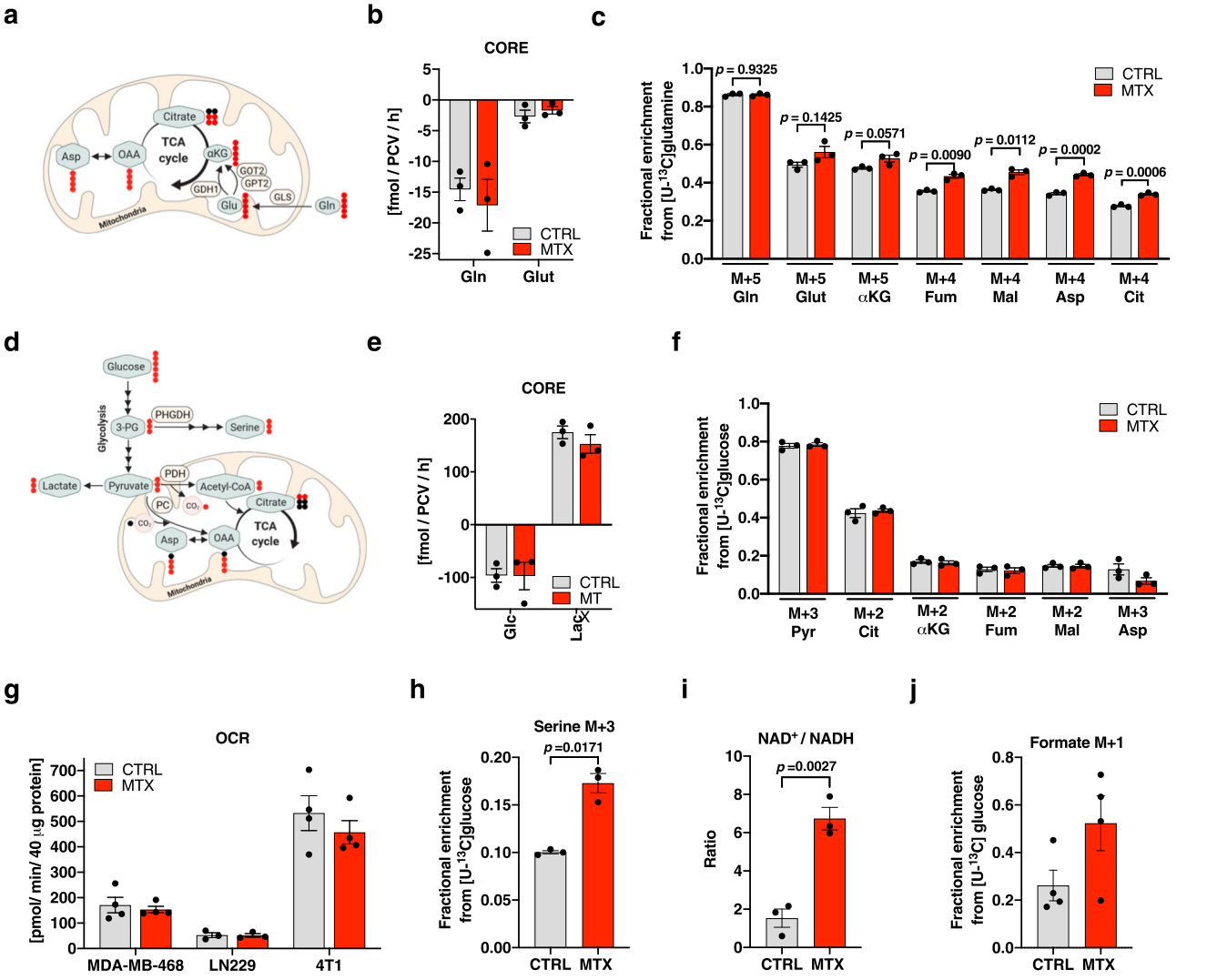

Fig. 3 MTX-treated cells sustain high metabolic rates and enhance de novo serine synthesis. a Interdependence of glycolysis and tricarboxylic acid (TCA) cycle and metabolic ^{13}C label pattern from [U-^{13}C]glutamine. **b** Absolute consumption and release (CORE) rates of glutamine (Gln) and glutamate (Glut) in the culture medium of MDA-MB-468 cells after 24 h 50 nM MTX. Dots represent the mean of an individual experiments composed of triplicate wells; mean ± SEM ($n = 3$). **c** Enrichment of selected isotopologues of Gln, Glut, α-ketoglutarate (αKG), fumarate (Fum), malate (Mal), aspartate (Asp), and citrate (Cit) upon [U-^{13}C]glutamine tracer in response to 24 h 50 nM MTX in MDA-MB-468 cells. Dots represent the mean of an independent experiments in triplicate wells; mean ± SEM; unpaired, two-tailed *t*-test with Welch's correction ($n = 3$). **d** Interdependence of glycolysis and TCA cycle and metabolic ^{13}C label pattern from [U-^{13}C]glucose. **e** Absolute CORE rates of lactate and glucose in the culture medium of MDA-MB-468 cells after 24 h 50 nM MTX. Dots represent the mean of an individual experiments composed of triplicate wells; mean ± SEM ($n = 3$). **f** Enrichment of selcted isotopologues of pyruvate (Pyr), Cit, αKG, Fum, Mal, and Asp upon [U-^{13}C]glucose tracer in response to 24 h 50 nM MTX in MDA-MB-468 cells. Dots represent the mean of an individual experiments composed of triplicate wells; mean ± SEM; unpaired *t*-test with Welch's correction ($n = 3$). **g** Basal cellular respiration upon 24 h 50 nM MTX in MDA-MB-468, LN229, and 4T1 cells as quantification of mitochondrial oxygen consumption rate (OCR). Dots represent the mean of an individual experiments composed of six technical replicates; mean ± SEM ($n = 3$ (LN229), 4 (MDA-MB-468, 4T1)). **h** Enrichment of M + 3 isotopologue of serine upon [U-^{13}C]glucose upon 24 h 50 nM MTX in MDA-MB-468 cells. Dots represent the mean of an independent experiments in triplicate wells; mean ± SEM; unpaired, two-tailed *t*-test with Welch's correction ($n = 3$). **i** Ratio of absolute intracellular NAD^+ to NADH in MDA-MB-468 cells upon 24 h 50 nM MTX. Dots represents the mean of an individual experiments composed of triplicate wells; mean ± SEM; unpaired *t*-test with Welch's correction ($n = 3$). **j** M + 1 isotopologue of extracellular formate in MDA-MB-468 cells from [U-^{13}C]glucose upon 24 h 50 nM MTX. Dots indicate the mean of an independent experiments measured in triplicate wells; mean ± SEM ($n = 4$). Source data are provided as a Source Data file.

To mechanistically disentangle cytosolic from mitochondrial 1C metabolism, we analyzed a panel of CRISPR knockouts in HAP1 cells in which either the cytosolic (SHMT1), the mitochondrial (MFT, SHMT2), or both compartments (FPGS, MFT + SHMT1) of 1C metabolism were abrogated[53]. Here, cytosolic *SHMT1* KO did not eliminate intermediary M + 1 and M + 2 serine isotopologues from [U-^{13}C]serine comparable to MTX treatment, whereas mitochondrial or combined cytosolic and mitochondrial inhibition of 1C metabolism upon *MFT* KO, *SHMT2* KO, *FPGS* KO and *MFT* + *SHMT1* KO resulted in a complete loss of M + 1 and M + 2 serine isotopologues (Fig. 4f). In mutants harboring a full inhibition of 1C metabolism or mitochondrial 1C metabolism alone, we additionally observed an increase in the ratio of serine to glycine levels, whereas MTX treatment and *SHMT1* KO did not substantially increase serine to glycine ratio (Fig. 4g).

Of note the protein abundance of mitochondrial serine catabolism enzymes was not increased upon MTX. MTHFD2

abundance even decreased upon MTX, however, this did apparently not affect the rate of serine catabolism (Fig. S4G, H).

To test if knock-out of mitochondrial serine catabolism stops formate overflow, we monitored formate release flux upon MTX in HAP1 cells deficient for SHMT1 or SHMT2. As expected, loss of SHMT2 completely abolished formate overflow, while SHMT1 KO increased formate overflow (Fig. 4h). This experiment was then validated in MDA-MB-468 cells harboring *MTHFD1L* KO[20]

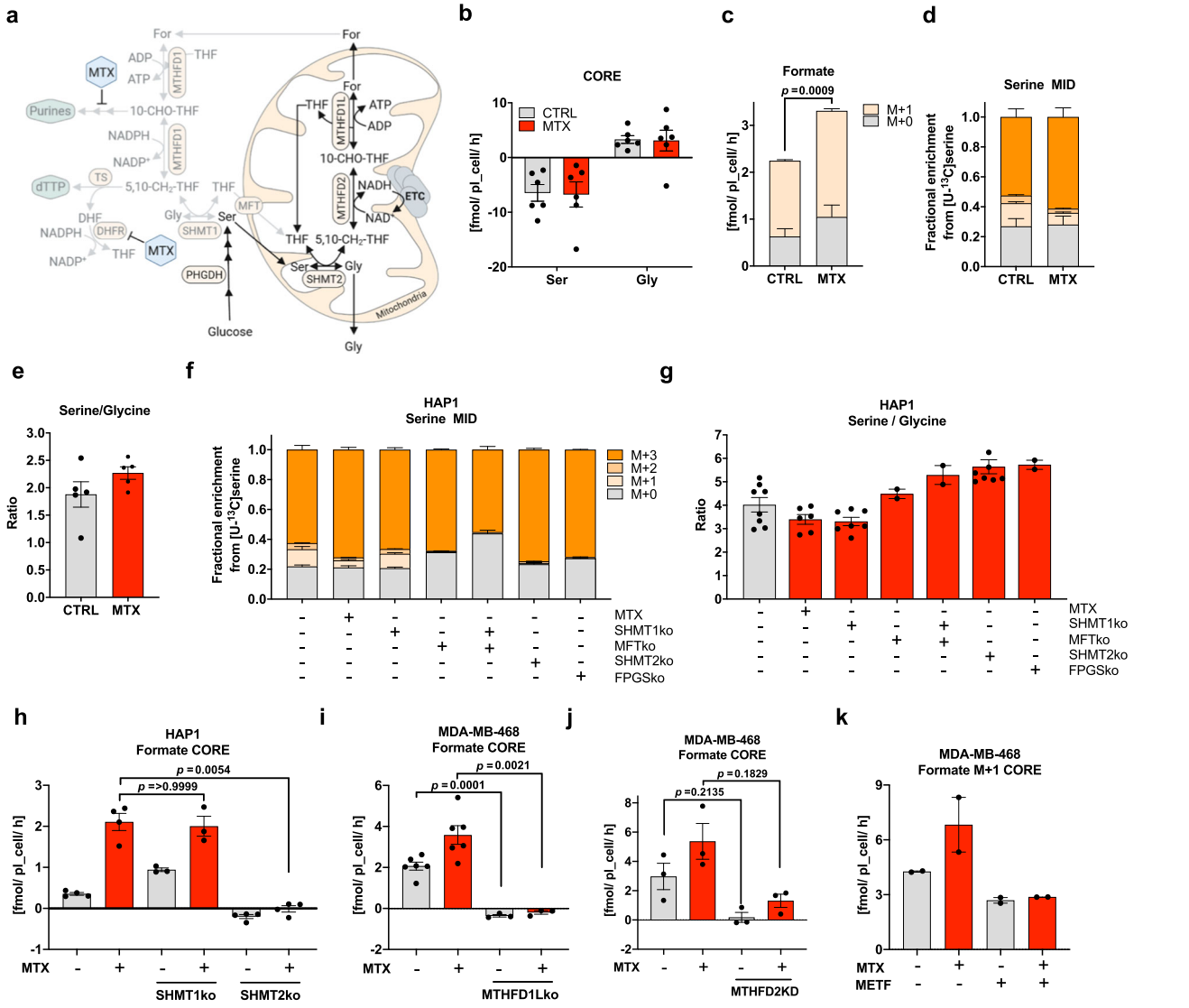

Fig. 4 Mitochondria protect 1C metabolism-dependent serine catabolism upon cytosolic 1C pathway inhibition. a Cytosolic and mitochondrial 1C metabolism and the pharmacologic intervention points of MTX. **b** Absolute consumption and release (CORE) rates of serine (Ser) and glycine (Gly) from MDA-MB-468 cells upon 24 h 50 nM MTX. Dots represent the mean of an individual experiment each measured in triplicate wells; mean ± SEM ($n = 6$). **c** Formate release rate upon [U-^{13}C]serine in MDA-MB-468 cells after 24 h 50 nM MTX; mean ± SEM of three independent experiments each measured in triplicate wells; unpaired *t*-test with Welch's correction for M + 1 isotopologue ($n = 3$). **d** MID of intracellular serine upon [U-^{13}C]serine in MDA-MB-468 cells upon 24 h 50 nM MTX; mean ± SEM of four independent experiments each measured in triplicate wells. **e** Ratio of absolute intracellular serine and glycine after 24 h 50 nM MTX in MDA-MB-468 cells. Dots represent the mean of an independent experiment in triplicate wells; mean ± SEM ($n = 5$). **f** MID of intracellular serine upon [U-^{13}C]serine in SHMT1, MFT, SHMT2, and FPGS-depleted HAP1 cells; mean ± SEM of independent experiments each measured in triplicate wells ($n = 8$ for CTRL, SHMT1ko, and SHMT2ko; $n = 5$ for MTX; $n = 2$ for FPGSko, MFTko and MFT/SHMT1ko). **g** Ratio of absolute intracellular serine and glycine levels in SHMT1, MFT, SHMT2, and FPGS depleted HAP1 cells. Dots represent the mean of an independent experiment in triplicate wells; mean ± SEM ($n = 8$ for CTRL and SHMT2ko, $n = 7$ for SHMT1ko, $n = 6$ for MTX, $n = 2$ for FPGSko, MFTko and MFT/SHMT1ko). **h** Absolute CORE rates of formate from WT and SHMT1- or SHMT2-depleted HAP1 cells upon 24 h 50 nM MTX. Each dot indicates the mean of an individual experiment measured in triplicate wells; Brown-Forsythe and Welch ANOVA test with Dunnetts multiple comparisons test. Mean ± SEM ($n = 4$ for CTRL, MTX, SHMT2ko, SHMT2ko MTX; $n = 3$ for SHMT1ko and SHMT1ko MTX) **i** Absolute CORE rates of formate from WT and MTHFD1L-depleted MDA-MB-468 cells upon 24 h 50 nM MTX. Mean ± SEM ($n = 6$ for CTRL and MTX; $n = 3$ for MTHFD1Lko + /- MTX) of an individual experiment measured in triplicate wells; Brown-Forsythe and Welch ANOVA test with Dunnetts multiple comparisons test. **j** Absolute CORE rates of formate from SCR and MTHFD2 KD MDA-MB-468 cells upon 24 h 50 nM MTX. Dots represent mean of an individual experiment measured in triplicate wells; mean ± SEM; ($n = 3$) Brown-Forsythe and Welch ANOVA test with Dunnetts multiple comparisons test. **k** Absolute CORE rates of formate from MDA-MB-468 cells upon 24 h treatment with 2.5 mM Metformin and 50 nM MTX. Dots represent mean of an individual experiment measured in triplicate wells; mean ± SEM ($n = 2$). Source data are provided as a Source Data file.

or shRNA mediated *MTHFD2* knock-down and *MTHFD2* KO (Fig. 4i, j, S4I-M). All genetic interventions resulted in a strong suppression of formate overflow during MTX treatment, further suggesting that increased formate overflow upon MTX depends on mitochondrial serine catabolism via the folate pathway (Fig. 4i, j, S4J, M).

As an alternative approach to genetic silencing we used Metformin to target complex 1 of the electron transport chain (ETC). We have previously shown that mitochondrial formate production depends on active ETC[21,22]. Here, we demonstrate that targeting of complex 1 with Metformin strongly suppresses mitochondrial formate production both at baseline and in presence of MTX, further supporting our finding that formate production in presence of MTX depends on mitochondrial 1C metabolism (Fig. 4k). To proof that Metformin indeed inhibits respiration under the applied conditions, we performed Seahorse experiments to measure the expected drop in oxygen consumption rate (Fig. S4N). We also monitored a reduction in proliferation (Fig. S4O) and we performed [U-^{13}C]glutamine tracing to monitor the expected strong increase in reductive carboxylation (Fig. S4P, Q), a well-known phenomenon upon ETC inhibition[54,55].

In summary, these results show that mitochondria provide a protected cellular environment that permits autarkic folate-mediated serine catabolism independent of the cytosolic folate metabolism.

Limiting serine availability decreases formate overflow and cancer cell migration. As we observed increased glucose derived serine synthesis and subsequent downstream catabolism of serine via mitochondrial 1C metabolism, we investigated if interfering with serine synthesis is effective to reduce sustained cell migration upon pharmacologic inhibition of cytosolic 1C metabolism. First, to identify an effective inhibitor of serine de novo synthesis, we tested multiple available allosteric and one competitive inhibitor of PHGDH. Indicated by the strong abrogation of labeled serine, we observed that the competitive inhibitor BI-4916 (BI)[12] had superior efficacy compared to the allosteric inhibitors WQ-2101 (WQ)[11], NCT-502 (NCT)[9], and CBR-5884 (CBR)[15] (Fig. 5a). Released M + 1 formate from [U-^{13}C]glucose was also effectively inhibited after BI treatment alone or in combination with MTX (Fig. 5b). Additionally, routine screening for metabolic side effects revealed that treatment with the allosteric inhibitors WQ, NCT, and CBR did result in a significant reduction of mitochondrial OCR (Fig. 5c), which was not observed with the competitive inhibitor BI (Fig. 5c). WQ and NCT also negatively affected TCA cycle activity as characterized by a reduction of M + 2 isotopologue abundance of TCA cycle associated metabolites (Fig. 5d). In contrast to the other inhibitors, BI had no adverse effect on TCA cycle activity and proliferation rate and thus emerged as the preferred PHGDH inhibitor in all subsequent experiments (Fig. 5d, S5A–D). Combined treatment with the specific PHGDH inhibitor BI significantly reduced MTX-mediated cell migration (Fig. 5e). This inhibitory effect was further enhanced upon combined PHGDH inhibition and serine and glycine (S/G) starvation (Fig. 5f). While S/G starvation alone resulted only in moderate inhibitory effects on migration of MTX-treated cells, combined treatment with PHGDH inhibition fully blunted cell migration (Fig. 5f). Similar results were observed in 4T1 cells (Fig. S5F). As all MTX conditions resulted in full growth arrest (Fig. S5E), this finding indicates a role for mitochondrial 1C metabolism in cell motility that is independent of serine's anabolic function to support biosynthetic processes.

While neither BI treatment alone nor S/G starvation alone were sufficient to prevent the induction of the observed EMT-phenotype, combined inhibition and starvation did minimize *ZEB1*, *ZEB2*, and *VIM* upregulation upon DHFR inhibition (Fig. 5g). This indicates that serine represents an underlying requirement for EMT onset upon DHFR inhibition. Importantly, S/G starvation did not further increase cell death after combined MTX and BI treatment (Fig. 5h). Of note, we also found that BI treatment was effective to reduce the migratory capacity of MTX-resistant, pro-migratory MDA-MB-468 cells (Fig. 5i). In summary, using MTX as a tool compound to study cell migration in absence of proliferation revealed that serine is essential to sustain full cancer cell migratory capacity (Fig. 5j).

Mitochondrial 1C metabolism supports cell motility and depends on mitochondrial THF availability. As withdrawal of serine can affect different aspects of cell physiology, we aimed to investigate more specifically the role of mitochondrial 1C metabolism in promoting cell migration. Analogue to the interventions presented in Fig. 4i–k, we used Metformin to target the ETC and genetic interventions to target *MTHFD2* or *MTHFD1L* both in MDA-MB-468 and 4T1 cells.

Metformin treatment of MTX exposed (growth arrested) cells reduced the migration of MDA-MB-468 cells (Fig. 6A), suggesting that one function of the ETC is to support cell migration.

Next, we investigated the role of mitochondrial serine catabolism in context of migration directly, by monitoring the migration of MTX treated *MTHFD2* or *MTHFD1L* silenced MDA-MB-468 and 4T1 cells. Of note, neither *MTHFD2* nor *MTHFD1L* silencing reduced cell proliferation or sensitivity to the growth-arresting effects of MTX (Fig. S6A–D). Also, cell death rates upon MTX were not affected by *MTHFD2* or *MTHFD1L* silencing (Fig. S6E–H). Scratch assay analysis showed that *MTHFD2* silencing markedly reduced MTX-mediated cell motility both in MDA-MB-468 and 4T1 cells (Fig. 6b, c). As shRNA used to silence human and murine *MTHFD2* were different, we do not expect shRNA specific off-target effects. Nevertheless, we confirmed the shMTHFD2 KD results in MDA-MB-468 cells with *MTHFD2* knock-out cells (Fig. S6I).

Mthfd1l silencing of MTX treated 4T1 cells also resulted in decreased migration (Fig. 6d). Somewhat surprisingly, loss of *MTHFD1L* in MDA-MB-468 cells had no negative effect on the migration of MTX treated cells (Fig. 6e). By following different hypotheses and various experiments, we realized that there is a striking difference in ALDH1L2 expression in 4T1 versus MDA-MB-468 cells, while MTHFD1L expression was comparable between these two cell lines (Fig. 6f, g).

This observation reminded us that in MDA-MB-468 cells, ALDH1L2 can act as an alternative outlet to oxidize formyl-THF to CO_2 thereby regenerating mitochondrial THF (in contrast to 4T1). That said, in MTHFD1L deficient cells, the ALDH1L2 status can be decisive whether THF can be regenerated or if THF will be trapped as 10-CHO-THF in the mitochondrion. Loss of free THF will potentially inhibit the autarkic mitochondrial cycle that can otherwise act in presence of MTX (Fig. 6h). In support of this hypothesis, we also measured increased formate release flux in 4T1 cells compared to MDA-MB468 (Fig. S6J), suggesting that in 4T1 cells less 10-CHO-THF is oxidized via Aldh1l2 and instead catabolized through Mthfd1l.

To test this hypothesis, we targeted *ALDH1L2* in MTHFD1L KO cells and monitored migration. We found that combinatorial depletion of *MTHFD1L* and *ALDH1L2* in MDA-MB-468 cells resulted at least in a reduction of migration upon MTX compared to single depletion of *MTHFD1L* alone. This was observed both for shRNA as well as for siRNA mediated knockdown of *ALDH1L2* (Fig. 6i, S6K).

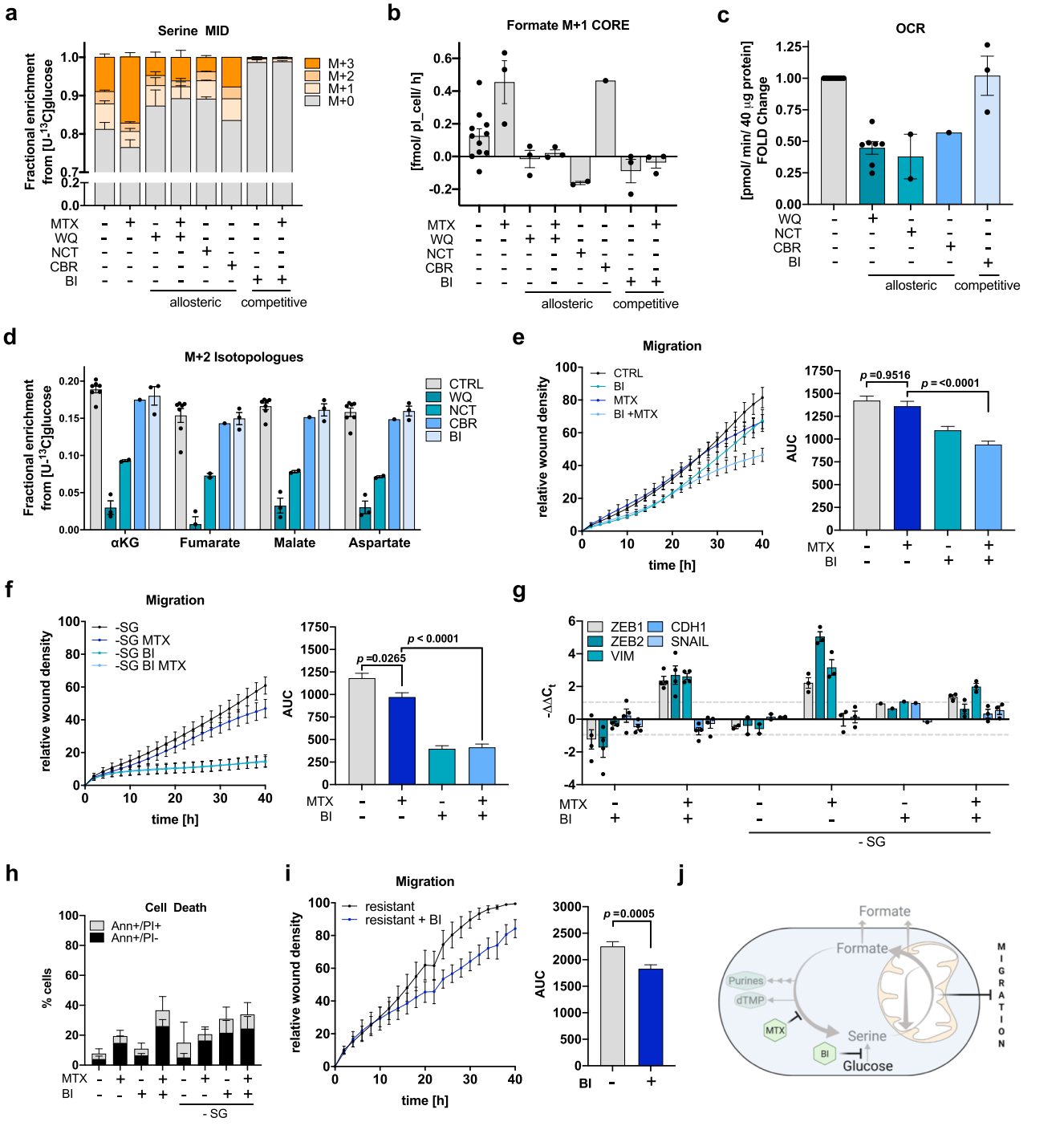

In conclusion, these results reveal a growth-independent role of mitochondrial 1C metabolism for cancer cell motility. Interestingly, the pool of free THF might be relevant for the functionality of the autarkic mitochondrial 1C cycle and ALDH1L2 can serve as an alternative outlet to regenerate THF when MTHFD1L is missing (summarized in Fig. 6J).

Genetic targeting of mitochondrial 1C metabolism reduces metastasis formation in vivo. According to our model, we predict that sole inhibition of mitochondrial 1C metabolism might be sufficient and effective to reduce cancer cell escape from the primary tumor and subsequent metastasis formation. To test this hypothesis, we employed the 4T1 cells with *Mthfd1l* KD to study the metastatic cascade in orthotopic tumors in vivo.

To evaluate first if Mthfd1l KD cells are more prone to oxidative stress, which could impact metastatic dissemination in vivo[56], we measured ROS levels in MTHFD1L silenced MDA-MB-468 and 4T1 cells at baseline and after MTX treatment. At baseline, ROS levels between MTHDF1L silenced and control cells were unchanged. MTX treatment induced ROS levels to comparable extends and 500 µM of H_2O_2 treatment did induce cell death rate comparable to Ctrl cells (Fig. S7A–C). In summary, these experiments do not indicate that loss of MTHFD1L results in increased cellular ROS levels or increased susceptibility to oxidative insults.

We then injected 4T1 cells with or without silenced *Mthfd1l* into the mammary fat pad of immunocompetent BALB/c mice to form orthotopic tumors (Fig. 7a). Primary tumor growth was

Fig. 5 Limiting serine availability decreases formate overflow and cancer cell migration. a MID of intracellular serine in MDA-MB-468 cells upon [U-^{13}C]glucose and 24 h 10 μM WQ-2101, 10 μM NCT-502, 30 μM CBR-5884, 15 μM BI-4916, and 50 nM MTX; mean ± SEM ($n = 10$ for CTRL; $n = 3$ for WQ, MTX, WQ MTX, BI, BI MTX; $n = 2$ for NCT; $n = 1$ for CBR) of independent experiments each measured in triplicate wells. **b** Formate M + 1 isotopologue exchange rate in MDA-MB-468 cells using [U-^{13}C]glucose and treatment as in (**a**). Dots indicate independent experiments measured in triplicate wells; mean ± SEM ($n = 10$ for CTRL; $n = 3$ for WQ, MTX, WQ MTX, BI, BI MTX; $n = 2$ for NCT; $n = 1$ for CBR). **c** Basal cellular respiration upon 24 h 10 μM WQ-2101, 10 μM NCT-502, 30 μM CBR-5884, and 15 μM BI-4916 in MDA-MB-468 cells as fold mitochondrial OCR compared to control. Dots represent individual experiments composed of six technical replicates; mean ± SEM ($n = 10$ for CTRL, $n = 7$ for WQ, $n = 3$ for BI, $n = 2$ for NCT, $n = 1$ for CBR). **d** M + 2 isotopologues of selected TCA-metabolites in MDA-MB-468 cells upon [U-^{13}C]glucose and treatment as in (**b**). Dots indicate independent experiments measured in triplicate wells; mean ± SEM ($n = 7$ for CTRL, $n = 3$ for WQ, BI, $n = 2$ for NCT, $n = 1$ for CBR). **e** Migration of MDA-MB-468 cells upon 50 nM MTX, 15 μM BI-4916 and **f** serine- and glycine starvation and respective AUC; mean ± SEM of independent experiments ($n = 5$ for (**e**), $n = 4$ for (**f**)); Brown-Forsythe and Welch one-way ANOVA with Dunnett's multiple comparisons test. **g** mRNA expression from indicated genes in MDA-MB-468 cells upon 72 h 50 nM MTX, 15 μM BI-4916, and serine- and glycine starvation measured by real-time RT-qPCR. Mean ± SEM ($n = 4$ for BI, BI + MTX, $n = 3$ for MTX-SG, MTX-SG + BI, $n = 2$ for -SG, $n = 1$ for BI-SG). **h** Cell death induction in MDA-MB-468 cells upon 48 h 50 nM MTX, 15 μM BI-4916 and serine- and glycine starvation was assessed by flow cytometry and AnnexinV-FITC/PI-staining; mean ± SD of independent experiments ($n = 3$). Two-way ANOVA with Dunnett's multiple comparisons test. **i** Migration of MTX-resistant MDA-MB-468 cells upon 50 nM MTX and 15 μM BI-4916 and respective AUC; mean ± SEM of independent experiments ($n = 4$); Brown-Forsythe and Welch one-way ANOVA with Dunnett's multiple comparisons test. **j** Cytosolic and mitochondrial compartments of 1C metabolism and the pharmacologic intervention points of MTX and inhibitors of PHGDH. Source data are provided as a Source Data file.

monitored over 6 weeks. In concordance with the in vitro data, primary tumor growth was not affected and tumor weight at endpoint was not different compared to Ctrl conditions (Fig. 7b, c). Knock-down of Mthfd1l in the primary tumors was confirmed by Western Blot (Fig. 7d, S7D–F). In line with our hypothesis, the number of macroscopic lung metastases was significantly reduced in mice that were carrying tumors deficient in Mthfd1l (Fig. 7e). While all mice that were injected with Mthfd1l-expressing 4T1 cells exhibited lung metastases, over 50% of mice injected with *Mthfd1l* KD cells did not show macroscopic metastatic lesions. Of note, expression of EMT related genes in the primary tumor was unchanged between the two groups (Fig. S7G). H&E staining of lungs and quantification of the metastatic area per lung confirmed reduced metastasis in Mthfd1l deficient tumors (Fig. 7f, g).

These in vivo findings further strengthen the key relevance of mitochondrial 1C metabolism as a cornerstone to support cancer cell migration independent of primary tumor growth and cancer cell proliferation rates.

Discussion

In this study, we uncover a growth-independent function of mitochondrial serine catabolism to drive cancer cell motility. Importantly, by using MTX as a tool compound to study migration independent of proliferation, we observed that upon inhibition of cytosolic 1C metabolism, mitochondria sustain an autarkic 1C metabolism that is sufficient to sustain full migratory capacity.

Such compartmentalization of 1C metabolism during MTX treatment is feasible because release of the 1C unit from THF in the mitochondrial MTHFD1L reaction is, in contrast to cytosolic thymidylate synthetase reaction, not oxidizing THF to DHF. Therefore, the mitochondrial THF pool is sustained to allow SHMT2-dependent mitochondrial serine catabolism, while cytosolic 1C metabolism enzymes are inhibited due to accumulating DHF species. Our finding that ALDH1L2 can serve as an alternative source for THF regeneration in MTHFD1L deficient cells, supports the notion that mitochondria can maintain an independent THF pool that is required for an autarkic mitochondrial 1C metabolism as long as there is THF available that can accept the hydroxymethyl group in the first (SHMT2 dependent) step of serine catabolism.

An autarkic mitochondrial 1C metabolism is further supported by a chemical modification of folate species that alters their transport activities across the mitochondrial membrane. For maximal biologic activity, folate species need to be polyglutamated by folylpolyglutamate synthase (FPGS) and the resulting polyglutamate species were shown to be only poorly transported across the mitochondrial membrane[57,58]. Consequently, polyglutamated folate species can be chemically trapped within the mitochondria to sustain the mitochondrial 1C cycle. Especially, upon growth arrest when cells can retain their mitochondrial content and don't need to amplify their content as it is required during proliferation. Additionally, there is evidence that transport activity of the mitochondrial folate transporter is limited to reduced folates[59]. This indicates a limited transport of MTX and folic acid itself across the mitochondrial membrane. Taken together, such compartmentalization of 1C metabolism and autarkic function of mitochondrial 1C metabolism emerges as a selective advantage in cells upon perturbation of cytosolic 1C metabolism and indicates a function of the mitochondrial 1C metabolism pathway to support cell motility.

While our data demonstrate that mitochondrial serine catabolism is needed to allow full migratory capacity, the specific biochemical output conferring this function still needs to be determined in more detail. Mitochondrial serine catabolism can generate NADH, NADPH, ATP, glycine, CO_2, methylene- and formyl-THF and formate. The plasticity of this pathway allows tailoring the catabolism towards current cellular needs[38]. Therefore, it can be possible that serine is differentially catabolized along the metastatic cascade in a context dependent manner. We have previously shown that exogenous formate promotes cancer cell invasion[22] and various cellular stress situations such as energy stress[21] or MTX treatment (this study) can increase the rate of formate overflow which results in increased extracellular formate concentrations. It is therefore tempting to speculate that increasing formate concentrations in the tumor microenvironment promote a more invasive phenotype of stressed cancer cells. In more general terms, it could be possible that mitochondrial serine catabolism can selectively promote cell motility in response to extrinsic or intrinsic stress stimuli such as growth inhibition or nutrient deprivation. On the other hand, MDA-MB-468 MTHFD1L KO cells are also formate overflow negative but do not show reduced migration. As ROS levels are neither increased in MDA-MB-468 nor in 4T1 MTHFD1L deficient cells, we do not think that the observed migration effects in this study are ROS dependent. Given previous work[22] and the current study, there might also be differences when comparing migration with invasion.

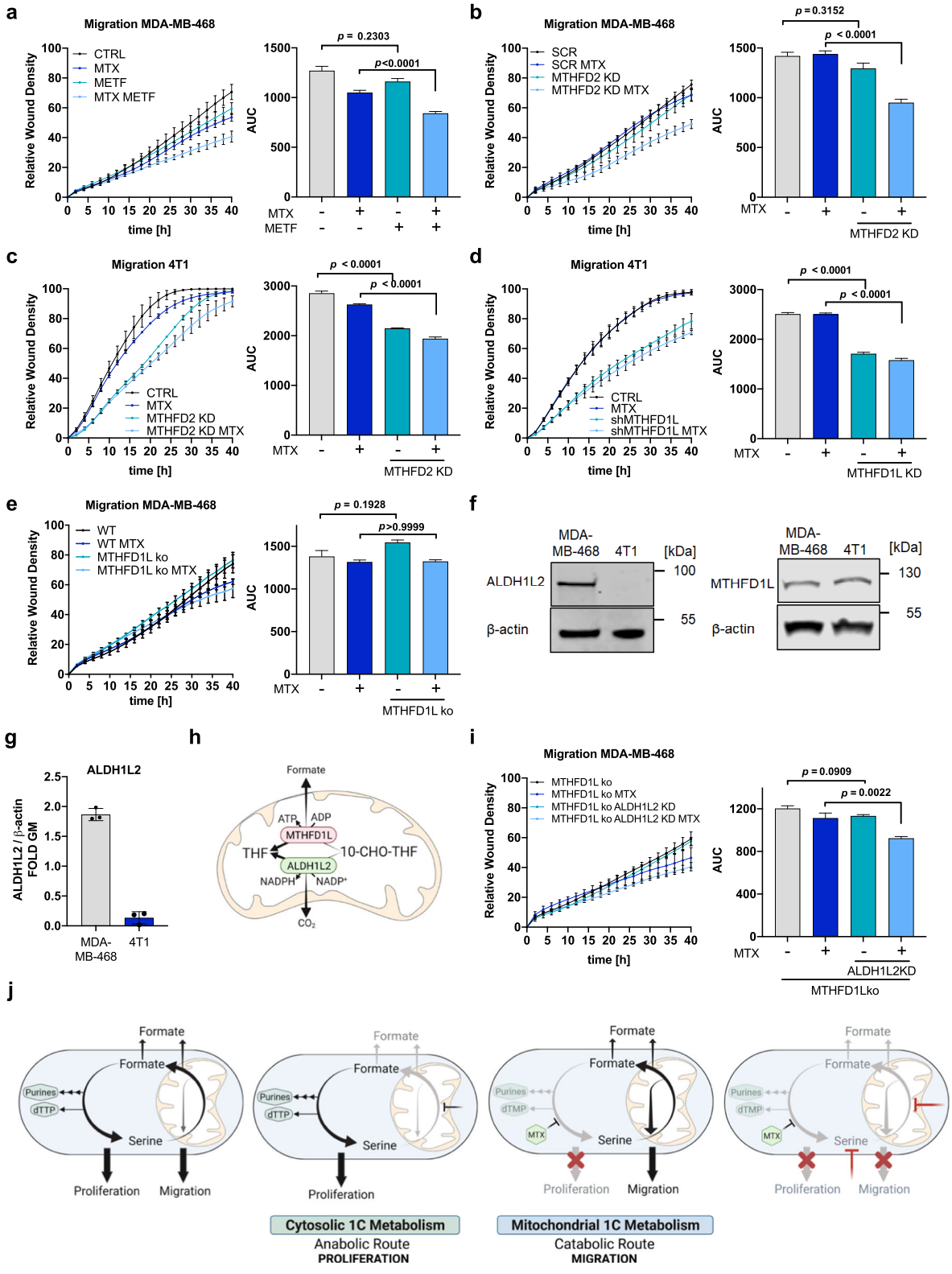

Ongoing work in our lab will help clarifying these questions in the future. To do so, it will be of particular importance to further disentangle effects arising from exogenous formate from effects depending on endogenous serine catabolism. Independent of these yet unknown details, we remain with the conclusion that mitochondrial serine catabolism contributes to cancer cell migration and metastasis independent of its known anabolic functions.

Finally, we would like to note that although we mainly use MTX as a tool compound to separate proliferative from migratory processes and to inhibit cytosolic 1C metabolism, our results have also some implications in regard to MTX as an anchor drug in chronic treatment of autoimmune diseases. Intracellular erythrocyte and mean plasma concentration of MTX were reported to be in a comparable, even slightly higher, nM range to our chosen drug concentration[60,61]. Finally, we also

Fig. 6 Mitochondrial 1C metabolism supports cell motility and depends on mitochondrial THF availability. a Migration of MDA-MB-468 cells upon 2.5 mM Metformin and 50 nM MTX and respective AUC; mean ± SEM of independent experiments ($n = 3$); Brown-Forsythe and Welch one-way ANOVA with Dunnett's multiple comparisons test. **b** Migration of MDA-MB-468 cells upon MTHFD2 knockdown and 50 nM MTX and respective AUC; mean ± SEM of independent experiments ($n = 4$); Brown-Forsythe and Welch one-way ANOVA with Dunnett's multiple comparisons test. **c** Migration of 4T1 cells upon Mthfd2 knockdown and 75 nM MTX and respective AUC; mean ± SEM of independent experiments ($n = 3$); Brown-Forsythe and Welch one-way ANOVA with Dunnett's multiple comparisons test. **d** Migration of 4T1 cells upon Mthfd1l knockdown and 75 nM MTX and respective AUC; mean ± SEM of independent experiments ($n = 3$); Brown-Forsythe and Welch one-way ANOVA with Dunnett's multiple comparisons test. **e** Migration of MDA-MB-468 cells upon MTHFD1L knockout and 50 nM MTX and respective AUC; mean ± SEM of independent experiments ($n = 3$); Brown-Forsythe and Welch one-way ANOVA with Dunnett's multiple comparisons test. **f** ALDH1L2 and MTHFD1L protein expression in MDA-MB-468 and 4T1 cells. **g** Signal intensity of ALDH1L2 on Western Blot was quantified relative to β-actin as loading control. Mean ± SEM ($n = 3$); unpaired *t*-test with Welch's correction. **h** MTHFD1L- and ALDH1L2-dependent reactions in mitochondrial 1C metabolism. **i** Migration of MDA-MB-468 cells upon MTHFD1L knockout, ALDH1L2 knockdown and 50 nM MTX and respective AUC; mean ± SEM of independent experiments ($n = 3$); Brown-Forsythe and Welch one-way ANOVA with Dunnett's multiple comparisons test. **j** Model summarizing the autarkic activity of mitochondrial and cytosolic 1C metabolism and their respective relevance for cell migration and cell proliferation. Source data are provided as a Source Data file.

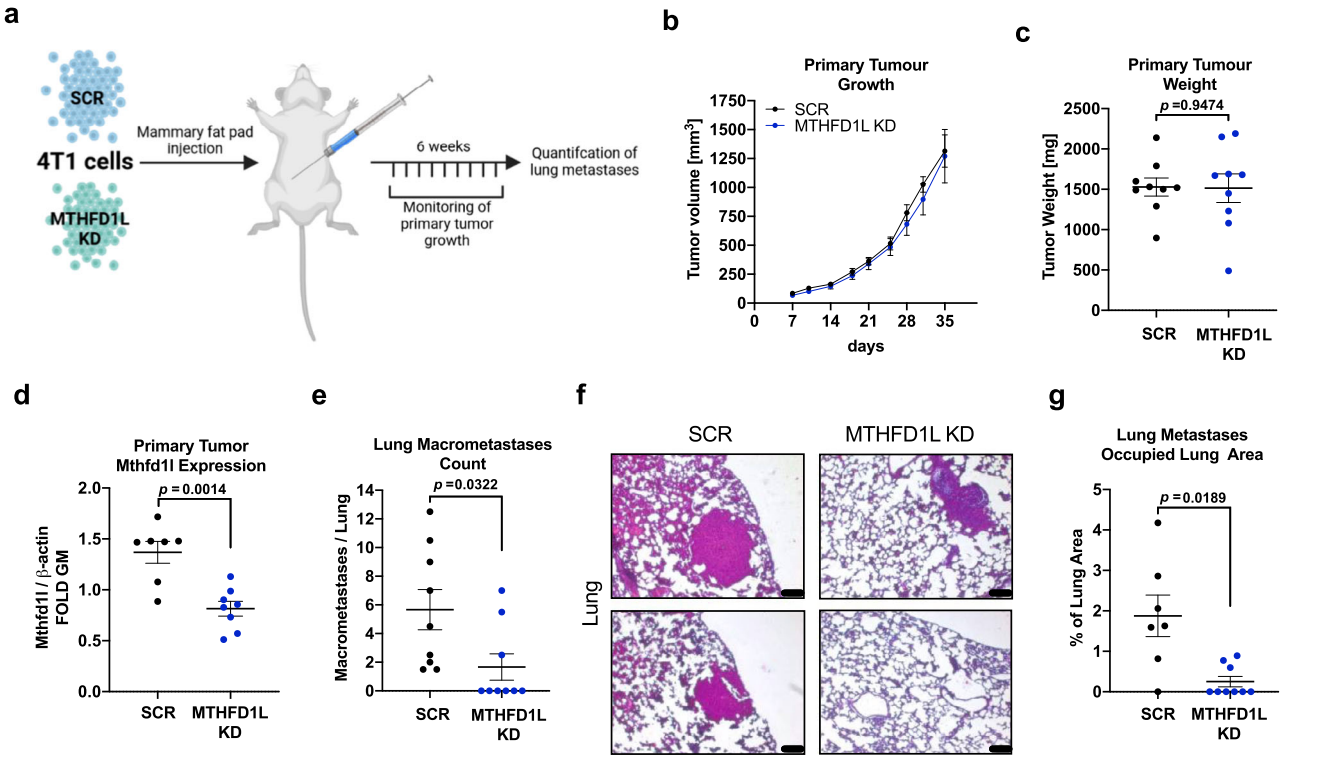

Fig. 7 Genetic targeting of mitochondrial 1C metabolism reduces metastasis formation in vivo. a 4T1 breast cancer cells transfected with non-targeting control (SCR, $n = 9$) and 4T1 cells with KD of *Mthfd1l* ($n = 9$) were injected into the mammary fat pads of immunocompetent female Balb/c mice. Primary tumor growth was monitored and lung metastasis formation was evaluated at end-point. **b** Primary tumor size was measured and mean tumor volume for each group was calculated; mean ± SEM ($n = 8$ (Scr) and 9 (Mthfd1l KD)). **c** Primary tumor weight was measured at the end-point. Dots indicate individual animals; mean ± SEM ($n = 9$); unpaired, two-tailed *t*-test with Welch's correction. **d** Primary tumor tissue was analyzed for Mthfd1l protein expression by Western Blot and quantified relative to β-actin as loading control. Dots indicate individual animals; mean ± SEM ($n = 7$ (Scr) and 8 (Mthfd1l KD)); unpaired, two-tailed *t*-test with Welch's correction. Protein lysates from tumors with significantly low Mthfd1l and β-actin expression relative to total protein were judged to be not pure tumor lysate and discarded from analysis (see Figure S7D–F for details). **e** Macroscopic lung metastases were counted and are depicted as number of metastases per lung. Dots indicate individual animals; mean ± SEM ($n = 9$); unpaired, two-tailed t-test with Welch's correction. **f** Lung tissue was embedded in paraffin and stained with H&E. 2 representative images per group are presented to show microscopic lung metastasis; scale bar corresponds to 100 µm. **g** Metastatic area per lung was quantified and is expressed as % area of lung tissue. Dots indicate individual animals; mean ± SEM ($n = 7$ (Scr) and 9 (Mthf1l KD)); unpaired, two-tailed *t*-test with Welch's correction. Source data are provided as a Source Data file.

would like to refer to a parallel and independent (back-to-back) publication that provides additional evidence that purine depletion promotes serine de novo synthesis and cell migration[62]. Interestingly, in this parallel work, the authors provide data that MTX also promotes the metastatic potential of melanoma cells in vivo. Hence, our findings on mitochondrial 1C metabolism might justify future investigations in cancer patients and patients that undergo chronic MTX therapy for an arthritic comorbidity.

Methods

Chemicals. Methotrexate, rotenone, PKUMDL-WQ-2101, galactose, hydroxyurea, NAC, metformin and fluorouracil were purchased from Sigma Aldrich. Clofarabine, pemetrexed disodium hydrate, sirolimus were purchased from Bio Connect. Simvastatin was purchased from Sanbio. CBR-5884 and BI-4916 were purchased from MedChemExpress. NCT-502 was purchased from ApeXBio.

Cell culture. All cell lines (except HAP1 cells) were cultured in Dulbecco's modified Eagle's medium (DMEM) without phenol red, glucose, and glutamine (Thermo Fisher Scientific) and supplemented with 2 mM glutamine, 17 mM

glucose, and 10% fetal bovine serum (FBS) at 37 °C and 5% CO_2. HAP1 cells were cultured in IMDM medium supplemented with 10% FBS. For galactose treatment, supplemented glucose was replaced by 17 mM galactose at the beginning of the experiment. For serine/glycine starvation experiments cells were kept in MEM (Thermo Fisher Scientific) supplemented with or without 400 µM glycine and serine, 2 mM glutamine, 17 mM glucose and 10% dialyzed FBS.

MDA-MB-468 and MTHFD1L CRISPR/Cas9 KO cells were obtained from Lewis Cantley lab, Weill Cornell Medical College, USA[20]. MDA-MB-468 were authenticated by STR profiling in our lab in 2021 (originally from ATCC); LN229 cells obtained from Alexei Vazquez lab Beatson Institute for Cancer Research (authenticated by STR profiling in our lab in 2021) (originally from ATCC); 4T1 cells from Luxembourg Institute of Health, Clement Thomas lab (authenticated by Clement lab in 2018) (originally from ATCC). HCT-116 cells from University of Luxembourg, Elisabeth Letellier lab (originally from ATCC), HEK293T: NorLux Lab, Luxembourg Institute of Health (originally from ATCC). HAP1 cells were obtained from Patel's laboratory[53] (originally from Horizon Discovery). MTX-resistant MDA-MB-468 cells were generated through prolonged culturing of MDA-MB-468 cells with 50 nM MTX for 2 months until cells started to regrowth under MTX. All cell lines were routinely tested for mycoplasma contamination.

Metabolic characterization. For metabolic characterization of cell lines, previously established protocols for absolute quantification of exchange fluxes and intracellular fluxes of one-carbon metabolism were applied[21].

Stable isotope tracing and metabolite extraction. Stable isotope tracing experiments with [U-^{13}C]-glucose tracer or [U-^{13}C]-glutamine tracer (Cambridge Isotope Laboratories, CLM-1396) were performed in DMEM supplemented with 2 mM glutamine, 17 mM glucose, and 10 % FBS. Stable isotope tracing experiments with [U-^{13}C]-serine tracer (Cambridge Isotope Laboratories) were performed in MEM (Thermo Fisher Scientific) supplemented with 400 µM glycine, 2 mM glutamine, 17 mM glucose, 400 µM serine tracer, and 10% FBS. To allow for adaptation, cells were cultivated in MEM for at least one passage prior to [U-^{13}C]-serine tracer experiments. 150,000 to 200,000 cells were seeded in 12-well plates in triplicates for each experimental condition. Identical triplicate wells were seeded to allow for cell count and cell volume determination (to calculate the packed cell volume (PCV)) at the start and end of each tracing experiment. The day after seeding, growth medium was replaced by tracer medium and cells were cultured for 24 h. In parallel, 3 wells per condition were counted to assess starting PCV. After 24 h, triplicate wells were counted to assess PCV at the end of the experiment and one set of triplicates was used for subsequent metabolite extraction. Medium of these triplicates were collected and analyzed for exchange rates. To determine the basal medium composition for the subsequent calculation of exchange rates, identical medium was incubated in triplicates in empty 12 wells throughout the experiment and analyzed in parallel to the medium samples. Collected medium samples were centrifuged at 300 g for 5 min. Supernatant was collected and stored at −20°C until extraction of metabolites. Formate extraction, derivatization, and quantification as well as metabolite extraction for LC-MS analysis was performed as described in[21]. For metabolite extraction for GC-MS analysis after [U-^{13}C]-glucose tracing and [U-^{13}C]-glutamine tracing, cells were washed with cold 0.9% NaCl solution. 400 µl ice-cold MeOH/H_2O_{MQ} [(ratio, 1:1) containing the internal standards pentanedioc-d6 acid and [U-^{13}C]-ribitol at a final concentration of 1 µg/ml and Tridecanoid-d25 acid at a final concentration of 5 µg/ml] was added to each well. Plates were incubated for 5 min at 4°C on a rocking shaker. Supernatant was collected, mixed with 200 µl $CHCl_3$, and centrifuged for 5 min at 13,000 g at 4°C. Upper polar phase was collected and stored at −20°C for subsequent MS analysis of polar metabolites.

GC-MS measurements

Analysis of formate release rates. Formate derivatization in the culture medium was performed using MCF derivatization as described in[21]. GC-MS analysis was performed using an Agilent 7890 A GC coupled to an Agilent 5975 C inert XL Mass Selective Detector (Agilent Technologies). A sample volume of 1 µl was injected into a Split/Splitless inlet, operating in split mode (20:1) at 270 °C. The gas chromatograph was equipped with a 30 m (I.D. 250 µm, film 0.25 µm) DB-5MS capillary column (Agilent J&W GC Column, 122-5532 G). Helium was used as carrier gas with a constant flow rate of 1.4 ml/min. GC oven temperature was held at 80 °C for 1 min and increased to 130 °C at 10 °C/min followed by a post run time of 4 min at 280 °C. Total run time was 15 min. Transfer line temperature was set to 280 °C. Mass selective detector (MSD) was operating under electron ionization at 70 eV. MS source was held at 230 °C and the quadrupole at 150 °C. For precise quantification, measurements were performed in selected ion monitoring mode. Target ions (*m/z*) and dwell times are shown in Table S1. GC-MS chromatograms were processed using Agilent MassHunter Quantitative Analysis for GC-MS, Version B.08.00. Final determination of release rates was performed as described in[21].

Determination of mass isotopomere distribution (MID) of Intracellular TCA Cycle Metabolites following Stable Isotope Tracing. First, polar metabolites were derivatized for 90 min at 55 °C with 20 µl of methoxyamine (c = 20 mg/ml) in pyridine under continuous shaking and subsequently for 60 min at 55 °C with additional 20 µl of MTBSTFA w/ 1% TBDMCS. GC-MS analysis was performed using an Agilent 7890B GC coupled to an Agilent 5977 A Mass Selective Detector (Agilent Technologies). A sample volume of 1 µl was injected into a Split/Splitless inlet, operating in splitless mode at 270 °C. Gas chromatograph was equipped with a 30 m (I.D. 250 µm, film 0.25 µm) ZB-35MS capillary column with 5 m guard column (Phenomenex). Helium was used as carrier gas with a constant flow rate of 1.2 ml/min. GC oven temperature was held at 100°C for 2 min and increased to 300°C at 10°C/min and held for 4 min. Total run time was 26 min. Transfer line temperature was set to 280°C. Mass selective detector (MSD) was operating under electron ionization at 70 eV. MS source was held at 230°C and the quadrupole at 150 °C. For precise quantification of the MID, measurements were performed in selected ion monitoring mode. Target ions (*m/z*) and dwell times are shown in Table S2.

The MetaboliteDetector software package (Version 3.220180913) was used for mass spectrometric data post processing, quantification, MID calculations, correction of natural isotope abundance, and determinations of fractional carbon contributions[63].

Analysis of medium exchange rates. Polar metabolites of the culture medium were derivatized for 90 min at 45°C with 20 µl of methoxyamine (c = 20 mg/ml) in pyridine under continuous shaking and subsequently for 30 min at 45 °C with 20 µl of MSTFA. GC-MS analysis was performed using an Agilent 7890B GC coupled to an Agilent 5977 A Mass Selective Detector (Agilent Technologies). A sample volume of 1 µl was injected into a Split/Splitless inlet, operating in split mode (10:1) at 270°C. Gas chromatograph was equipped with a 30 m (I.D. 250 µm, film 0.25 µm) ZB-35MS capillary column with 5 m guard column (Phenomenex). Helium was used as carrier gas with a constant flow rate of 1.2 ml/min. GC oven temperature program: 90°C for 1 min, 9°C/min to 270°C, 25°C/min to 320°C and held for 7 min. Total run time was 30 min. Transfer line temperature was set to 280°C. MSD was operated under electron ionization at 70 eV. MS source was held at 230°C and the quadrupole at 150°C. Full scan mass spectra were acquired between m/z 70 and 700.

The MetaboliteDetector software package (Version 3.220180913) was used for quantification. Briefly, peak areas of all isotopologues of defined quantification ions were summed up and divided by the peak area of the internal standard for normalization. In addition, a calibration curve was prepared to calculate absolute concentrations. Absolute uptake and release rates were calculated as described in[21]

LC-MS measurements. Untargeted LC-MS analysis was carried out as previously described in[21].

Nucleotide and NAD/NADH analysis. The following analytical conditions are based on a protocol from[21]. Metabolite analyses were performed using a Thermo Vanquish Flex Quaternary LC coupled to a Thermo Q Exactive HF mass spectrometer. Chromatography was carried out with a SeQuant ZIC-pHILIC 5 µm polymer (150 × 2.1 mm) column connected to the corresponding SeQuant ZIC-pHILIC Guard (20 × 2.1 mm) pre-column. Column temperature was maintained at 45 °C. The flow rate was set to 0.2 mL/min and the mobile phases consisted of 20 mmol/L ammonium carbonate in water, pH 9.2 (Eluent A) and Acetonitrile (Eluent B). The gradient was: 0 min, 80% B; 2 min, 80% B; 17 min, 20% B; 18 min 20% B; 19 min 80 % B; 20 min 80% B (0.4 mL/min); 24 min 80% B (0.4 mL/min); 24.5 min 80% B. The injection volume was 5 µL. All MS experiments were performed using electrospray ionization with polarity switching enabled (+ESI/-ESI). The source parameters were applied as follows: sheath gas flow rate, 25; aux gas flow rate, 15; sweep gas flow rate, 0; spray voltage, 4.5 kV (+) / 3.5 kV (–); capillary temperature, 325°C; S-lense RF level, 50; aux gas heater temperature, 50°C. The Orbitrap mass analyzer was operated at a resolving power of 30,000 in full-scan mode (scan range: *m/z* 75…1000; automatic gain control target: 1e6; maximum injection time: 250 ms). Data were acquired with Thermo Xcalibur software (Version 4.3.73.11) and analyzed with TraceFinder (Version 4.1). Subsequent data analysis for normalization and natural isotope subtraction were performed using in house scripts as in[21].

Western blot. Total cell lysates from cells cultured in vitro were prepared by 30 min incubation of cell pellets on ice in cell lysis buffer (150 mM NaCl, 1 mM EDTA, 50 mM Tris-HCl, 1% NP-40). Protein lysates from tumor tissue were obtained by lysing 10 mg tumor tissue pieces in 150 µl cell lysis buffer. Homogenization of tumor tissue lysates was achieved with TissueLyser II (Quiagen) using 5 mm metal beads. Lysis efficiency was maximized by sonification. Lysis solution was centrifuged at 13,000 g for 15 min at 4°C and supernatant was collected and stored at −80°C. Protein concentration was determined by Bradford assay. 15 – 30 µg of total protein were loaded on NuPAGE 4–12% Bis-Tris gels (Life Technologies) or RunBlue 4–12% Bis-Tris gels (Westburg) using 4x NuPage LDS Sample buffer (Thermo Fisher Scientific) supplemented with 10 mM DTT (Sigma Aldrich) and blotted on nitrocellulose membrane according to standard protocols. Membranes were stained with REVERT staining solution (LI-COR) and analyzed for total protein abundance. Subsequently, membranes were blocked with Odyssey TBS blocking buffer (LI-COR) or 5% milk-powder in TBST and incubated with the

indicated primary antibodies over night at 4°C. Incubation with secondary antibody occurred for 2 h at RT. Detection was performed with the Odyssey CLx Infrared Imaging System (LI-COR). ImageStudioLite Software Vers.5.2 (LI-COR) was used for image analysis. All uncropped and unprocessed scans are available in the source data file. Antibodies used for Western blot analysis in this study:

MTHFD1L (16113-1-AP, LOT: 00024322, RRID: AB_2250974) from Proteintech; Vimentin (3390, clone 5G3F10, LOT:2, RRID: AB_2216128), β-actin (3700, clone 8H10D10, LOT: 18, RRID: AB_2242334), NRF2 XP(R) (12721, clone D179C, LOT: 8, RRID: AB_2715528) and MTHFD2 (41377, D8W9U, LOT: 1, RRID: AB_2799200) from Cell Signaling Technology (CST); PHGDH (HPA021241, LOT: B115626, RRID: AB_1855299), PSAT1 (HPA042924, LOT: R40839, RRID: AB_2678223), PSPH (HPA020376, LOT: B115600, RRID: AB_1855867), SHMT1 (HPA023314, LOT: A78402, RRID: AB_1856830), and SHMT2 (HPA020549, LOT: A96534, RRID: AB_1856834) from Sigma Aldrich; LaminB (ab16048, LOT: GR32836742, RRID: AB_443298) from Abcam; IRDye 680RD Goat Anti-Mouse IgG (H + L) (926-68070, LOT: C90910-21, RRID: RRID AB_10956588) and IRDye 800CW Donkey Anti-Rabbit IgG (H + L) (926-32213, LOT: 926-32213, RRID: RRID AB_621848) from LI-COR (used in a 1:10,000 dilution). All antibodies were used in a 1:1,000 dilution unless stated otherwise.

Poly-L-Lysine coating. Poly-L-lysine (P1274) was purchased from Sigma-Aldrich and reconstituted at 500 µg/ml in H_2O_{MQ}. Wells were coated with PLL prior to Seahorse measurement and Scratch assay. To this end, PLL solution was diluted 1:20 in H_2O_{MQ} and added to the plates at least 1 h prior to seeding. Following incubation with PLL at 37°C and prior to cell seeding, plates were washed twice with H_2O_{MQ} and allowed to air-dry.

Seahorse measurements. The day prior to measurement, 40,000 cells were seeded on poly-L-lysine coated plates and treated the subsequent day as indicated. XF96 Extracellular Flux Analyzer (Seahorse Bioscience) was used to measure basal OCR following manufacturer's instructions using WAVE software. OCR was normalized to the protein concentration or cell number in the wells following the protocol described in[64] using Bradford assay.

Flow cytometric analysis of cell cycle distribution and cell death. 200,000 cells were seeded in 2 ml DMEM and treated the subsequent day as indicated. After incubation, medium was collected and cells were washed with PBS. PBS fraction was collected and cells were detached with trypsin. Detached cells were collected in DMEM. The combined, collected solutions were centrifuged and pellet was washed with PBS.

Cell cycle distribution. Centrifugation yielded a pellet that was resuspended in 100 µl PBS and fixed with ice-cold 80% EtOH. Fixed cells were stored at −20°C for at least 1 h and maximum 5 days prior to measurement. Cells were centrifuged, pellet was incubated for 1 h in 200 µl RNAse A in PBS (30 µg/ml) at RT. Immediately prior to measurement, 98 µl propidium iodide (PI) in PBS (50 µg/ml) was added. Flow cytometric analysis was performed using BD FACSCanto and BD FACSDiva software (version 8.0.1). Analysis was performed in FlowJo Version 10.6.2.

Cell death analysis. Pellet following centrifugation was resuspended in 50 µl AnnexinV-FITC staining solution (5% AnnexinV-FITC in AnnexinV binding buffer (10 mM HEPES pH 7.4, 140 mM NaCl, 2.5 mM $CaCl_2$, 0.1% BSA in $_{dd}H_2O$)) and incubated for 15 min on ice in the dark. 450 µl PI-staining solution (1.1 µg/ml PI in AnnexinV binding buffer) was added immediately prior to measurement using BD FACSCanto and BD FACSDiva software (version 8.0.1) (for wild-type cells) or NovoCyte Quanteon and software NovoExpress (version 1.5.0) (for GFP-positive transfected cells). Analysis was performed in FlowJo Version 10.6.2.

Flow cytometric analysis of ROS levels. 250,000 MDA-MB-468 cells were seeded in 2 ml medium and treated the subsequent day as indicated. Following incubation, cells were detached with trypsin, centrifuged at 350 *g* for 5 min and washed with warm DMEM. Cells were stained in 100 µl DMEM supplemented with 1:2,000 DAPI and 1:500 DCFDA for 30 min at 37°C. Following incubation, samples were centrifuged at 350 *g* for 5 min and washed with PBS. Following centrifugation at 350 *g* for 5 min, cells were resuspended in 100 µl PBS and measured using the BD LSRFortessa™ system and BD FACSDiva software (version 8.0.1). Data analysis was performed using FlowJo software Version 10.6.2.

Cell proliferation. Cell proliferation was determined using the IncuCyte® Live-Cell Analysis system (Essen Bioscience). Cell proliferation was either determined as measurement of cell density (confluence) or by quantification of red nuclei using the IncuCyte® NucLight Rapid Red Reagent (Essen Bioscience). Staining was performed according to manufacturer's instructions. Alternatively, viable cell number was determined by trypan blue staining and automatic counting using a Countess™ Cell Counting Chamber Slide (Thermo Fisher).

Migration assay (wound closure). Cell migration was determined using the IncuCyte® Scratch Wound Assay system for 96 well plates (Essen Bioscience). 96 well image lock plates (Essen Bioscience) were PLL coated prior to seeding of 40,000 cells per well. Wound application was performed 24 h post seeding using the 96-pin IncuCyte WoundMaker tool (Essen Bioscience) and indicated treatments were applied simultaneously. Measurement was performed in technical replicates ($n = 4–8$) and repeated as independent, biological experiments as stated for the respective experiment in figure legends.

Invasion and migration assay (transwell assay). Invasion and migration was analyzed by Boyden chamber assay as described in Meiser et al., 2018[22]. Transwells were coated with ECM-Collagen for invasion assays and left un-coated for migration assay. Treatment and migration/invasion was carried out for 18 h to 24 h.

RNA extraction, cDNA synthesis, and qPCR analysis. Total RNA was extracted from cell culture dishes following manufacturer instructions of RNeasy Mini Kit (Qiagen, 74104) or NucleoSpin RNA Kit (Machery&Nagel, 740955). For RNA extracts from tumor tissue, 10 mg tissue were homogenized in 350 µL RNA using 5 mm metal beads in TissueLyser II (Quiagen). RNA was transcribed to cDNA with High-capacity cDNA Reverse Transcription Kit (ThermoFisher, 4368814). qPCR was performed from 20 ng cDNA per sample using Fast SYBR™ Green Master Mix (ThermoFisher, 4385612). All samples were analyzed in technical duplicates or triplicates. qPCR using Fast SYBR Green was conducted at 95°C for 20 s, 40 cycles of 95°C for 1 s and 60°C for 20 s using the QuantStudio 5 Real-Time PCR System (Applied Biosciences, ThermoFisher Scientific). Specificity was verified by melt curve analysis. Relative quantification of each mRNA was done by QuantStudio Design&Analysis v1.5.1 software (Applied Biosciences, ThermoFisher Scientific) and comparative Ct method. All expression data was normalized to two housekeeping genes (*GAPDH* and *CycloA*). All primers used in this study are listed in Table S3.

shRNA-mediated gene silencing. Knockdown with shRNA was performed in MDA-MB-468 and 4T1 cells using lentiviral particles expressing two different shRNAs targeting the gene of interest and one non-silencing control vector (pGIPZ-shSCR: TTACTCTCGCCCAAGCGAG (Code: RHS4346). For silencing of the *MTHFD2* gene in MDA-MB-468 cells, pGIPZ shMTHFD2-2: ATTG-CATTTCTATTGGCCT (V2LHS_90968) purchased from Horizon Discovery was used. For silencing of the *ALDH1L2* gene in MDA-MB-468 cells, pGIPZ shALDH1L2: ACTGCTTTATCAACATCCG (Code: V3LHS_385780) purchased from Horizon Discovery was used. For silencing of the *Mthfd1l* gene in 4T1 cells, pGIPZ shMTHFD1L-2: TAGATTTCAATTTCATCTG (Code: V2LHS_96542) purchased from Horizon Discovery was used. For silencing Mthfd2 gene in 4T1 cells, pGIPZ shMthfd2-2: ATGACAACGGCTTCATTTC (Code: V2LMM_23800) purchased from Horizon Discovery was used. Plasmids used for generation of lentivirus were amplified from glycerol stocks, isolated (Machery&Nagel plasmid isolation kit), and used for transfection of HEK293T cells. Lentivirus was produced for 24 h in HEK293T cells co-transfected with the viral core packaging construct pCMVR8.74, the VSV-G envelope protein vector pMD2.G and the respective pGIPZ-shRNA-target plasmid using lipofectamine 3000 (Invitrogen #L3000008). Filtered virus supernatant was used to transduce MDA-MB-468 and 4T1 cells in DMEM supplemented with 2% FBS. After 24 h incubation at 37 °C, virus was removed and cells were cultured in DMEM supplemented with 10 % FBS for 48 h. 96 h post transduction, cells were cultured in selection media containing 2 µg/mL of puromycin (Sigma #P8833) for five passages to obtain stably transduced GFP-positive cells.

Generation of KO cells. Gene knock-out (KO) using the CRISPR-Cas9 system was performed in MDA-MB-468 using a vector expressing hCas9 and the respective guideRNA to target the gene of interest. For silencing of the *MTHFD2* gene in MDA-MB-468 cells, two different gRNA sequences (gRNA#918: CGCCAAC-CAGGATCACACTC (Vector ID: VB190718-1104ncn); gRNA1.Ex: GCTCGCGGCAGTTCGGTAAGA (Vector ID: VB190719-1026vzh) purchased from VectorBuilder were used. A control vector was used scramble_gRNA (GTGTAGTTCGACCATTCGTG (Vector ID: VB190718-1103vja) together with both constructs. To generate a *MTHFD2*-KO cell line, 300.000 cells were seeded the day prior to transfection into a 6 well plate in DMEM supplemented with 10% FBS. 24 h later, the culture medium was replaced with 2 mL of DMEM-F12 (LONZA #12-719 F) supplemented with 10 % FBS, Glucose (17 mM final concentration), Glutamine (2 mM final concentration), and 1 mM Sodium Formate and the cells were transfected using Opti-MEM, Lipofectamine, P3000 and 2 µg of plasmid DNA. Post incubation for 24 h, the transfection mix was removed and cells were replaced with fresh DMEM-F12. 72 h post transfection, cells were sorted into single cells by FACS based on their GFP fluorescence. Single cells were grown in DMEM-F12 supplemented with 1% Pen-Strep (Sigma, # P4333) until the formation of single colonies. These were further expanded and characterised by means of Western Blot.

siRNA-mediated gene silencing. 500.000 MDA-MB-468 cells were transfected with 40 pmol siRNA upon seeding in 6 well-plates using Lipofectamine 3000 (ThermoFisher) according to the manufacturer's instructions. Non-silencing control siRNA (siRNA ON-TARGETplus Human non-targeting (1810-10-05) siRNA SMARTpool) and siRNA directed against human *ALDH1L2* mRNA (siRNA ON-TARGETplus Human ALDH1L2 (160428; 26918-01-0005) siRNA SMARTpool) were purchased from Dharmacon.

Animal model. Animal experiments were performed according to all applicable laws and regulations, after receiving approval by the institution's Animal Experimentation Ethics Committee at UL (AEEC) and the veterinarian service of the Ministry of Agriculture, Viniculture & Rural Development (TumorMetab LUPA 2020/01). They ensure that care and use of animals for research purposes was conducted according to the EU Directive 2010/63/EU, as well as the Grand-Ducal Regulation of January 11, 2013 on the protection of animals used for scientific purposes. These included the justification of the use of animals, their welfare and the incorporation of the principles of the 3 R's (Replacement, Reduction and Refinement). A biostatistician reviewed all animal protocols. Mice were housed in a specific pathogen free (SPF) facility at a relative humidity of 40–70%, at 22 °C, and in 12 h dark/light cycles. Syngeneic 4T1 mammary carcinoma cells were orthotopically implanted into the left mammary fat pads (1 injection/mouse) of immune competent female Balb/c mice (8-10 month old) according to established protocols[65]. Briefly, each injection contained 2000 cells in a mixture of 25 µL PBS and 25 µL matrigel. 9 mice per group were injected with either 4T1 SCR or 4T1 *Mthfd1l* KD cells. Primary tumor growth was monitored between day 7 and day 35 of the experiment. Weight was monitored and no weight loss was observed. Experiment was terminated after 6 weeks and lung and liver were prepared for examination of metastatic outgrowth. No metastases were found in the liver. Macroscopic lung metastases were blindly counted under a microscope and microscopic lung metastases were visualized by H&E staining.

H&E staining. H&E staining was performed on 10 µm sections of paraffin embedded lung tissue. Staining was performed according to established protocols. Briefly, selected sections were dehydrated with MeOH and stained with Gill 2 hematoxylin. Sections were neutralized with successive washes of tap water, hard water (10 g $MgSO_4$ and 0.7 g $NaHCO_3$ per L), and distilled water. Subsequently, sections were stained with Eosin-solution and dehydrated through successive washes with 80%, 95%, 100% EtOH and Xylol prior to mounting. Images for quantification were acquired using BioTek Cytation 5 Cell Imaging Multimode Reader. Area of lung and metastasis were measured in ImageJ. Representative images for publication were acquired using Olympus IX83 microscope. Collapsed lungs were excluded from quantitative analysis.

Proteomics. SILAC (Stable Isotope Labeling with Amino acids in Cell culture) strategy was used for proteomic analysis. In general, MDA-MB-468 cells were cultivated in DMEM-F12 SILAC medium supplemented either with Lys^0 and Arg^0 (light channel) or Lys^8 and Arg^{10} (heavy channel). After 6 passages, labeling efficiency of heavy channel was confirmed using LC-MS/MS. Cells in light channel were treated with 50 nM MTX for 24 h and 72 h, while heavy channel was used as control. Cell pellets of biological duplicates were collected. Proteins were extracted in lysis buffer (50 mM ammonium bicarbonate, 6 M Urea, 2 M Thio-urea, pH 8) following a 30 min incubation at 4°C in the presence of protease inhibitors (cOmplete™ EDTA-free Protease Inhibitor Cocktail, Roche). Following centrifugation at 16,000 *g* for 10 min, supernatants were taken for protein quantification. Samples from light channel (50 µg protein) were mixed with control heavy channel (50 µg protein) for protein reduction (5 mM DTT, 1 h incubation at 37°C) and alkylation (10 mM IAA, 45 min in dark at room temperature). Protein digestion was performed with Lys-C (FUJIFILM Wako, 125-05061) at 1:30 ratio (enzyme/protein substances) for 4 h at 37 °C, then samples were diluted 4 times with 50 mM ammonium bicarbonate and digested overnight with 1 µg of trypsin at 37°C. Digestion was terminated through addition of formic acid (1% final concentration). Digested peptides were cleaned up with reverse phase Sep-Pak C18 1 cc Vac Cartridge (Waters, WAT054955) and eluted with 1 mL 50% ACN. Eluted peptides were dried by Speedvac (Thermo Fisher Scientific) and re-suspended in 0.1% formic acid. Peptide concentration was measured with Nanodrop. Peptides were measured by LC-MS/MS on Q-Exactive HF mass spectrometer (Thermo Fisher) connected to a Dionex Ultimate 3000 (Thermo Fisher). 500 ng of peptides were loaded onto a trap column (Acclaim PepMap 75 µm x 2 cm, C18, 3 µm) and separated on a 25 cm Acclaim pepmap RSLC column (75 µm x 25 cm, C18, 2 µm) using a 150 min gradient (2% to 90% acetonitrile) with a flow rate of 0.3 µL/min. MS data were acquired in data-dependent mode. Survey scans of peptide precursors from 375 to 1500 m/z were performed at 70,000 resolution with a 3×10^6 ion count target and the top 12 abundant peaks from survey scan were selected for fragmentation. Tandem MS was performed by isolation at 1.4 m/z with the quadrupole, HCD fragmentation with a normalized collision energy of 28. The MS2 ion count target was set to 1×10^5 and the max injection time was 45 ms. Only precursors with a charge state of 2–7 were sampled for MS2. The dynamic exclusion duration was set to 20 s with a 10 ppm mass tolerance around the selected precursor and its isotopes. Each sample was analyzed twice as technical replicates. All raw data was analyzed with MaxQuant (version 1.6.7.0) and searched with Andromeda against the Homo sapiens database from Uniprot. The minimal peptide length was set to 7 amino acids and the maximum of 3 missed cleavages were allowed. The search included variable modifications of methionine oxidation and N-terminal acetylation, deamidation (N and Q) and fixed modification of carbamidomethyl cysteine. The "Match between run" was checked within 1 min retention time window. Mass tolerance for peptide precursor and fragments were set as 10 ppm and 20 ppm, respectively. The FDR was set to 0.01 for peptide and protein identifications. SILAC based protein quantification (MaxQuant built-in) was used for quantitative evaluation of identified proteins. ProTIGY (https://github.com/broadinstitute/protigy), an R based tool, was used for differential analysis of MaxQuant output.

Statistics. Unpaired *t*-test with Welch's correction was applied for pairwise comparison (two-sided) using GraphPad Software Vers.8. For comparison of multiple groups ordinary Brown Forsythe & Welch one-way or two-way ANOVA with Dunnett's multiple comparison or Games-Howell's multiple comparisons test was performed using GraphPad Software Vers.8. Resulting *p*-values for comparisons of interest are given as numerical values within the respective graphs. For normalization, data points of one experiment were either normalized to the untreated control or divided by the global mean of the individual experiment. We define one *n* as one independent biological experiment (in some cases further consisting of several wells, e.g. triplicate wells for all stable isotope tracing experiments). The technical mean of one biological experiment was considered as one *n*. The mean values of several independent, biological experiments (as indicated in figure legends) were plotted and used for statistical analysis as indicated.

Reporting summary. Further information on research design is available in the Nature Research Reporting Summary linked to this article.

Data availability

Source data are provided with this paper. Proteomics data is available at the proteomics identification database (PRIDE) under the id: PXD027175 (INSERT URL here, once available). The remaining metabolomics data from targeted analysis are available within the article and the supplementary information files (source data file). Source data are provided with this paper.

Received: 24 January 2022; Accepted: 22 April 2022;
Published online: 16 May 2022

References

1. Siegel, R. L., Miller, K. D. & Jemal, A. Cancer statistics, 2019. *CA Cancer J. Clin.* **69**, 7–34 (2019).
2. Luengo, A., Gui, D. Y. & Vander, M. G. Heiden, targeting metabolism for cancer therapy. *Cell Chem. Biol.* **24**, 1161–1180 (2017).
3. Counihan, J. L., Grossman, E. A. & Nomura, D. K. Cancer metabolism: current understanding and therapies. *Chem. Rev.* **118**, 6893–6923 (2018).
4. Bergers, G. and S. M. Fendt, The metabolism of cancer cells during metastasis. *Nat. Rev. Cancer* **21**(3),162–180 (2021).
5. Locasale, J. W. Serine, glycine and one-carbon units: cancer metabolism in full circle. *Nat. Rev. Cancer* **13**, 572–583 (2013).
6. Locasale, J. W. et al. Phosphoglycerate dehydrogenase diverts glycolytic flux and contributes to oncogenesis. *Nat. Genet* **43**, 869–874 (2011).
7. Pollari, S. et al. Enhanced serine production by bone metastatic breast cancer cells stimulates osteoclastogenesis. *Breast Cancer Res Treat.* **125**, 421–430 (2011).
8. Possemato, R. et al. Functional genomics reveal that the serine synthesis pathway is essential in breast cancer. *Nature* **476**, 346–350 (2011).
9. Pacold, M. E. et al. A PHGDH inhibitor reveals coordination of serine synthesis and one-carbon unit fate. *Nat. Chem. Biol.* **12**, 452–458 (2016).
10. Tajan, M. et al. Serine synthesis pathway inhibition cooperates with dietary serine and glycine limitation for cancer therapy. *Nat. Commun.* **12**, 366 (2021).
11. Wang, Q. et al. Rational design of selective allosteric inhibitors of PHGDH and serine synthesis with anti-tumor activity. *Cell Chem. Biol.* **24**, 55–65 (2017).
12. Weinstabl, H. et al. Intracellular trapping of the selective phosphoglycerate dehydrogenase (PHGDH) inhibitor bi-4924 disrupts serine biosynthesis. *J. Med Chem.* **62**, 7976–7997 (2019).
13. Maddocks, O. D. K. et al. Modulating the therapeutic response of tumours to dietary serine and glycine starvation. *Nature* **544**, 372–376 (2017).
14. Ngo, B. et al. Limited environmental serine and glycine confer brain metastasis sensitivity to PHGDH inhibition. *Cancer Disco.* **10**, 1352–1373 (2020).

15. Mullarky, E. et al. Identification of a small molecule inhibitor of 3-phosphoglycerate dehydrogenase to target serine biosynthesis in cancers. *Proc. Natl Acad. Sci. USA* **113**, 1778–1783 (2016).
16. Ducker, G. S. et al. Reversal of cytosolic one-carbon flux compensates for loss of the mitochondrial folate pathway. *Cell Metab.* **24**, 640–641 (2016).
17. Lee, W. D. et al. Tumor reliance on cytosolic versus mitochondrial one-carbon flux depends on folate availability. *Cell Metab.* **33**, 190–198.e6 (2021).
18. Morscher, R. J. et al. Mitochondrial translation requires folate-dependent tRNA methylation. *Nature* **554**, 128–132 (2018).
19. Minton, D. R. et al. Serine catabolism by SHMT2 is required for proper mitochondrial translation initiation and maintenance of formylmethionyl-tRNAs. *Mol. Cell* **69**(4), 610–621.e5 (2018).
20. Zheng, Y. et al. Mitochondrial one-carbon pathway supports cytosolic folate integrity in cancer cells. *Cell* **175**(6), 1546–1560.e17 (2018).
21. Meiser, J. et al. Serine one-carbon catabolism with formate overflow. *Sci. Adv.* **2**(10), e1601273 (2016).
22. Meiser, J. et al. Increased formate overflow is a hallmark of oxidative cancer. *Nat. Commun.* **9**(1), 1368 (2018).
23. Rossi, M., et al., Heterogeneity in PHGDH protein expression potentiates cancer cell dissemination and metastasis. https://doi.org/10.1101/2021.01.24.427949 (2021).
24. Samanta, D. et al. PHGDH expression is required for mitochondrial redox homeostasis, breast cancer stem cell maintenance, and lung metastasis. *Cancer Res* **76**, 4430–4442 (2016).
25. Rinaldi, G. et al. In vivo evidence for serine biosynthesis-defined sensitivity of lung metastasis, but not of primary breast tumors, to mTORC1 inhibition. *Mol. Cell* **81**, 386–397.e7 (2021).
26. Stoller, R. G. et al. Use of plasma pharmacokinetics to predict and prevent methotrexate toxicity. *N. Engl. J. Med* **297**, 630–634 (1977).
27. Chabner, B. A. & Young, R. C. Threshold methotrexate concentration for in vivo inhibition of DNA synthesis in normal and tumorous target tissues. *J. Clin. Invest* **52**, 1804–1811 (1973).
28. Huang, S. et al. Study on relationships of tumor status and gene polymorphism with blood concentration of MTX and toxicities in 63 pediatric mature B cell lymphoma in chinese population. *Technol. Cancer Res Treat.* **20**, 1533033821995288 (2021).
29. Kawakatsu, S. et al. Population pharmacokinetic analysis of high-dose methotrexate in pediatric and adult oncology patients. *Cancer Chemother. Pharm.* **84**, 1339–1348 (2019).
30. Phillips, D. C., Woollard, K. J. & Griffiths, H. R. *T*he anti-inflammatory actions of methotrexate are critically dependent upon the production of reactive oxygen species. *Br. J. Pharm.* **138**, 501–511 (2003).
31. Soula, M. et al. Metabolic determinants of cancer cell sensitivity to canonical ferroptosis inducers. *Nat. Chem. Biol.* **16**, 1351–1360 (2020).
32. Wu, S. et al. Activation of RSK2 upregulates SOX8 to promote methotrexate resistance in gestational trophoblastic neoplasia. Lab Invest. 2021.
33. AlBasher, G. et al. Methotrexate-induced apoptosis in human ovarian adenocarcinoma SKOV-3 cells via ROS-mediated bax/bcl-2-cyt-c release cascading. *Onco Targets Ther.* **12**, 21–30 (2019).
34. Garcia-Sanchez, A., Miranda-Diaz, A. G. & Cardona-Munoz, E. G. The role of oxidative stress in physiopathology and pharmacological treatment with pro- and antioxidant properties in chronic diseases. *Oxid. Med Cell Longev.* **2020**, 2082145 (2020).
35. Babiak, R. M. et al. Methotrexate: pentose cycle and oxidative stress. *Cell Biochem Funct.* **16**, 283–293 (1998).
36. Lignitto, L. et al. Nrf2 activation promotes lung cancer metastasis by inhibiting the degradation of Bach1. *Cell* **178**, 316–329 e18 (2019).
37. Wiel, C. et al. BACH1 stabilization by antioxidants stimulates lung cancer metastasis. *Cell* **178**, 330–345 e22 (2019).
38. Benzarti, M. et al. Metabolic potential of cancer cells in context of the metastatic cascade. *Cells* **9**, 2035 (2020)
39. Nguyen, H. L. et al. Oxidative stress and prostate cancer progression are elicited by membrane-type 1 matrix metalloproteinase. *Mol. Cancer Res* **9**, 1305–1318 (2011).
40. Rhyu, D. Y. et al. Role of reactive oxygen species in TGF-beta1-induced mitogen-activated protein kinase activation and epithelial-mesenchymal transition in renal tubular epithelial cells. *J. Am. Soc. Nephrol.* **16**, 667–675 (2005).
41. Chen, D. et al. MiR-373 drives the epithelial-to-mesenchymal transition and metastasis via the miR-373-TXNIP-HIF1alpha-TWIST signaling axis in breast cancer. *Oncotarget* **6**, 32701–32712 (2015).
42. Reczek, C. R. & Chandel, N. S. ROS-dependent signal transduction. *Curr. Opin. Cell Biol.* **33**, 8–13 (2015).
43. Hunter, M. V. et al. Oxidative stress orchestrates cell polarity to promote embryonic wound healing. *Dev. Cell* **47**, 377–387 e4 (2018).
44. Porporato, P. E. et al. A mitochondrial switch promotes tumor metastasis. *Cell Rep.* **8**, 754–766 (2014).
45. Piperigkou, Z. et al. Key matrix remodeling enzymes: functions and targeting in cancer. *Cancers (Basel)*, **13**(6):1441 (2021)
46. Kawami, M. et al. Methotrexate-induced epithelial-mesenchymal transition in the alveolar epithelial cell line A549. *Lung* **194**, 923–930 (2016).
47. Ohbayashi, M. et al. Involvement of epithelial-mesenchymal transition in methotrexate-induced pulmonary fibrosis. *J. Toxicol. Sci.* **39**, 319–330 (2014).
48. Vazquez, A. et al. Catabolic efficiency of aerobic glycolysis: The Warburg effect revisited. *BMC Syst. Biol.* **4**, 58 (2010).
49. Diehl, F. F. et al. Cellular redox state constrains serine synthesis and nucleotide production to impact cell proliferation. *Nat. Metab.* **1**, 861–867 (2019).
50. Vande Voorde, J. et al. Improving the metabolic fidelity of cancer models with a physiological cell culture medium. *Sci. Adv.* **5**, eaau7314 (2019).
51. Palm, W. & Thompson, C. B. Nutrient acquisition strategies of mammalian cells. *Nature* **546**, 234–242 (2017).
52. Tibbetts, A. S. & Appling, D. R. Compartmentalization of Mammalian folate-mediated one-carbon metabolism. *Annu Rev. Nutr.* **30**, 57–81 (2010).
53. Burgos-Barragan, G. et al. Mammals divert endogenous genotoxic formaldehyde into one-carbon metabolism. *Nature* **548**, 549–554 (2017).
54. Mullen, A. R. et al. Reductive carboxylation supports growth in tumour cells with defective mitochondria. *Nature* **481**, 385–U171 (2012).
55. Metallo, C. M. et al. *Reductive glutamine metabolism by IDH1 mediates lipogenesis under hypoxia*. *Nature* **481**(7381), 380–384 (2011).
56. Piskounova, E. et al. Oxidative stress inhibits distant metastasis by human melanoma cells. *Nature* **527**, 186–191 (2015).
57. Lawrence, S. A. et al. Mammalian mitochondrial and cytosolic folylpolyglutamate synthetase maintain the subcellular compartmentalization of folates. *J. Biol. Chem.* **289**, 29386–29396 (2014).
58. Lowe, K. E. et al. Regulation of folate and one-carbon metabolism in mammalian cells. II. Effect of folylpoly-gamma-glutamate synthetase substrate specificity and level on folate metabolism and folylpoly-gamma-glutamate specificity of metabolic cycles of one-carbon metabolism. *J. Biol. Chem.* **268**, 21665–21673 (1993).
59. Horne, D. W., Holloway, R. S. & Said, H. M. Uptake of 5-formyltetrahydrofolate in isolated rat liver mitochondria is carrier-mediated. *J. Nutr.* **122**, 2204–2209 (1992).
60. den Boer, E. et al. Determinants of erythrocyte methotrexate polyglutamate levels in rheumatoid arthritis. *J. Rheumatol.* **41**, 2167–2178 (2014).
61. Zhu, T. et al. Investigation of potential drug-drug interactions between peficitinib (ASP015K) and methotrexate in patients with rheumatoid arthritis. *Clin. Drug Investig.* **40**, 827–838 (2020).
62. Soflaee, M. H. et al. Purine nucleotide depletion prompts cell migration by stimulating the serine synthesis pathway. *Nat. Commun.* https://doi.org/10.1038/s41467-022-30362-z (2022).
63. Hiller, K. et al. MetaboliteDetector: comprehensive analysis tool for targeted and nontargeted GC/MS based metabolome analysis. *Anal. Chem.* **81**, 3429–3439 (2009).
64. Dranka, B. P. et al. Assessing bioenergetic function in response to oxidative stress by metabolic profiling. *Free Radic. Biol. Med* **51**, 1621–1635 (2011).
65. Kocaturk, B. & Versteeg, H. H. Orthotopic injection of breast cancer cells into the mammary fat pad of mice to study tumor growth. *J. Vis. Exp.* 8(96), 51967 (2015).

Acknowledgements

We thank Fabien Rodriguez (Letellier lab) for technical support during the tissue analysis of the in vivo experiment. We are grateful to Lewis Cantley (Weill Cornell Medical College) for providing MDA-MB-468 cells with MTHFD1L KO[20] and to Patel's laboratory (Cambridge, UK) for providing various HAP1 KO cells[53] We thank Clément Thomas (LIH, Luxembourg) for providing 4T1 cells and Saverio Tardito (Cancer Research UK Beatson Institute, Glasgow, UK) for providing Plasmax medium.

We would like to thank: the LCSB Metabolomics Platform, especially Xiangyi Dong and Floriane Vanhalle, for providing technical and analytical support; the National Cytometry Platform (Quantitative Biology Unit, LIH) and especially Thomas Cerutti for support with flow cytometric analyses; Magretta Adiamah for her diligent proofreading of the manuscript; all our collaboration partners for fruitful discussions and constructive feedback. All graphical figures were produced with BioRender.com (Agreement Number *OJ23O9J9QD*).

J.M. is supported by the FNR-ATTRACT program (A18/BM/11809970), J.M. and L.H. are supported by the FNR-PRIDE NEXTIMMUNE (PRIDE/11012546) and J.M. and K.E. by the FNR-PRIDE i2Tron (PRIDE19/14254520) program. N.K. is supported by the LIH Career Launchpad program (Legs Baertz) and by a DFG fellowship (KI 2508/1-1). D.B. is supported by the FNR-ATTRACT program (A14/BM/7632103), the FNR-CORE program (C18/BM/12691266 and C21/BM/15796788) and the i2Tron (PRIDE19/14254520) grant. D.B. and L.S.B. are funded by the FNR-PRIDE (PRIDE/11012546/NEXTIMMUNE) scheme. E.L. is supported by the FNR-CORE program (C16/BM/11282028 and C20/BM/14591557), by a Proof of Concept FNR grant (PoC/18/12554295), a PRIDE17/11823097 and by i2Tron (PRIDE19/14254520). G.D. and F.X. are supported by FNR-

CORE (C17/BM/11642138). B.J. and M.Z.N. are supported by Luxembourg National Research Fund (C18/BM/12670304/COMBATIC) and FNRS Televie grant (7.4579.20).

Author contributions

Conceptualization, J.M., N.K.; Methodology, J.M., N.K., C.J., M.Z.N., B.J., E.L., D.B., G.D., V.I.P.; Software, A.V., F.X.; Validation, N.K., J.M., L.N., C.D., K.E., L.H.; Formal Analysis, N.K., C.D., L.N., M.B., L.S.B., F.X., V.I.P., M.S., C.J., K.E., E.K., L.H.; Investigation, N.K., C.D., L.N., M.B., L.S.B., F.X., V.I.P., M.S., E.L., K.E., L.H.; Resources, C.J., A.V., J.M., E.L.; Data Curation, N.K., J.M., F.X., A.V.; Writing – Original Draft, N.K., J.M.; Writing – Review & Editing, All Authors; Visualization, N.K., J.M., L.S.B., F.X., V.I.P.; Supervision, J.M., D.B., A.V., E.L., G.D.; Project Administration, J.M., Funding Acquisition, J.M., D.B., E.L., A.V., G.D.

Competing interests

The authors declare no competing interests.

Additional information

Supplementary information The online version contains supplementary material available at https://doi.org/10.1038/s41467-022-30363-y.

Correspondence and requests for materials should be addressed to Johannes Meiser.

Peer review information *Nature Communications* thanks the anonymous reviewer(s) for their contribution to the peer review of this work.

Reprints and permission information is available at http://www.nature.com/reprints

Publisher's note Springer Nature remains neutral with regard to jurisdictional claims in published maps and institutional affiliations.

Open Access This article is licensed under a Creative Commons Attribution 4.0 International License, which permits use, sharing, adaptation, distribution and reproduction in any medium or format, as long as you give appropriate credit to the original author(s) and the source, provide a link to the Creative Commons license, and indicate if changes were made. The images or other third party material in this article are included in the article's Creative Commons license, unless indicated otherwise in a credit line to the material. If material is not included in the article's Creative Commons license and your intended use is not permitted by statutory regulation or exceeds the permitted use, you will need to obtain permission directly from the copyright holder. To view a copy of this license, visit http://creativecommons.org/licenses/by/4.0/.

© The Author(s) 2022

SUPPLEMENTARY INFORMATION Kiweler et al.

Mitochondria preserve an autarkic one-carbon cycle to confer growth-independent cancer cell migration and metastasis

Nicole Kiweler[1], Catherine Delbrouck[1,2], Vitaly I. Pozdeev[3], Laura Neises[1], Leticia Soriano-Baguet[2,4,5], Kim Eiden[1,2], Feng Xian[6], Mohaned Benzarti[1,2], Lara Haase[1,2,7], Eric Koncina[3], Maryse Schmoetten[3], Christian Jaeger[7], Muhammad Zaeem Noman[8], Alexei Vazquez[9], Bassam Janji[8], Gunnar Dittmar[2,6], Dirk Brenner[4,5,10], Elisabeth Letellier[3], Johannes Meiser[1]*

[1] Cancer Metabolism Group, Department of Cancer Research, Luxembourg Institute of Health, Luxembourg, Luxembourg;

[2] Faculty of Science, Technology and Medicine, University of Luxembourg, 2 avenue de Université, Esch-sur-Alzette, Luxembourg;

[3] Faculty of Science, Technology and Medicine, Department of Life Sciences and Medicine, Molecular Disease Mechanisms Group, University of Luxembourg, Esch-sur-Alzette, Luxembourg;

[4] Experimental & Molecular Immunology, Department of Infection and Immunity, Luxembourg Institute of Health, 29 Rue Henri Koch, Esch-sur-Alzette, Luxembourg

[5] Immunology & Genetics, Luxembourg Centre for Systems Biomedicine, University of Luxembourg, 7 Avenue des Hauts Fourneaux, Esch-sur-Alzette, Luxembourg

[6] Proteomics of cellular signaling, Department of Infection and Immunity, Luxembourg Institute of Health,1a Rue Thomas Edison, Strassen, Luxembourg

[7] Luxembourg Centre for Systems Biomedicine, University of Luxembourg, Esch-sur-Alzette, Luxembourg;

[8] Tumor Immunotherapy and Microenvironment (TIME) Group, Department of Cancer Research, Luxembourg Institute of Health, Luxembourg, Luxembourg

[9] Institute of Cancer Sciences, University of Glasgow, Glasgow, United Kingdom

[10] Odense Research Center for Anaphylaxis (ORCA), Department of Dermatology and Allergy Center, Odense University Hospital, University of Southern Denmark, Odense, Denmark;

*Correspondence:

Email: johannes.meiser@lih.lu

Twitter: @JohannesMeiser

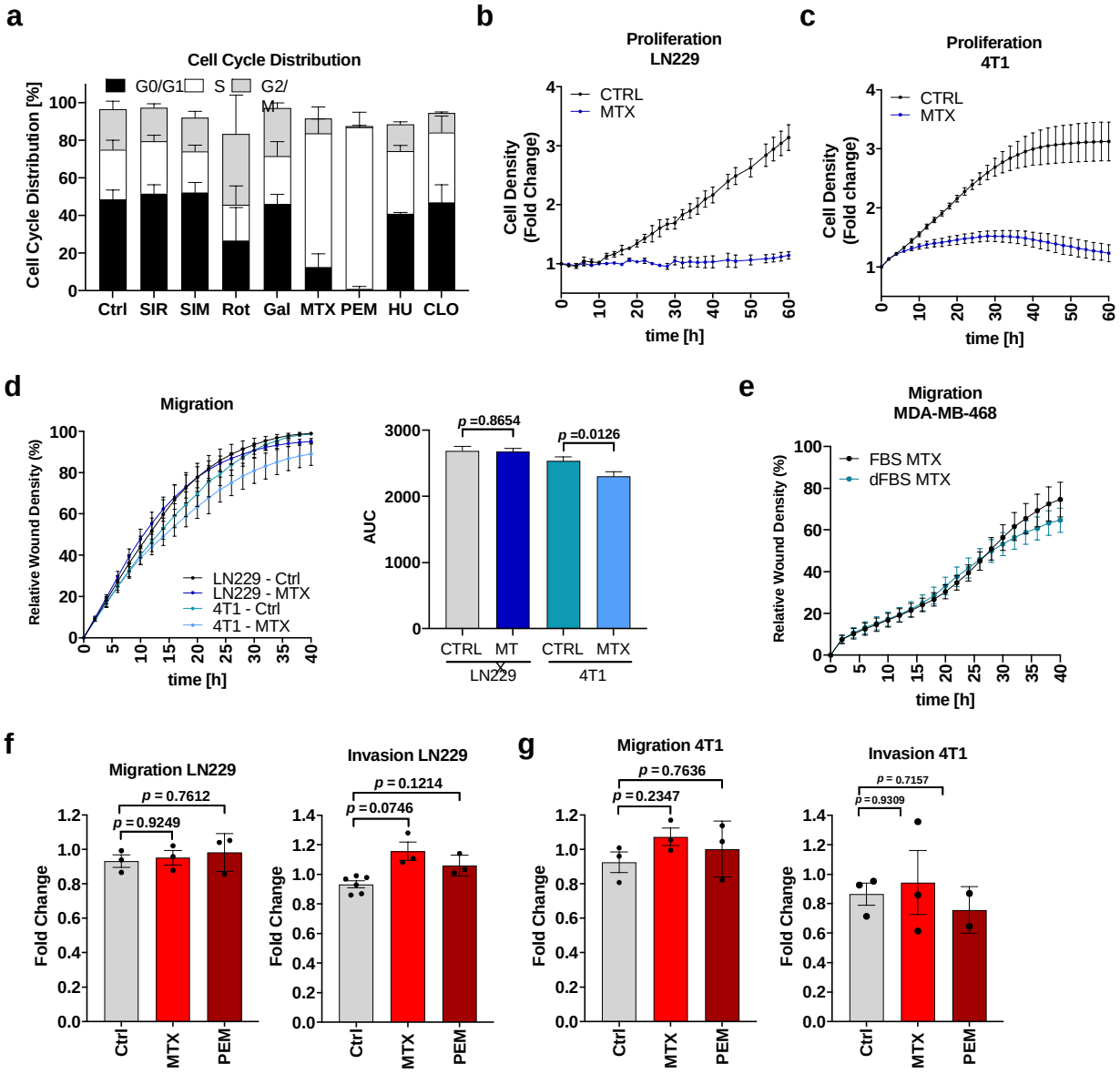

Supplementary Figure 1: (A) MDA-MB-468 cells were treated for 48 h with 100 nM Sirolimus (SIR), 1 µM Simvastatin (SIM), 50 nM Rotenone (Rot), galactose (Gal) supplementation, 50 nM Methotrexate (MTX), 1 µM Pemetrexed (PEM), 0.5 mM hydroxyurea (HU), and 100 nM Clofarabine (CLO). Cells were analyzed for cell cycle distribution by flow cytometry of PI-stained cells; mean ± SD of independent experiments (n = 11 for CTRL; n = 4 for SIR, MTX, PEM; n = 3 for SIM, Rot, Gal, HU, CLO). (B) Proliferation of LN229 cells in response to 50 nM MTX; mean ± SEM of independent experiments (n = 3). (C) Proliferation of 4T1 cells in response to 75 nM MTX; mean ± SEM of independent experiments (n = 4). (D) Migration of LN229 and 4T1 cells in response to 50 (LN229) or 75 (4T1) nM MTX and respective AUC; mean ± SEM of independent experiments (n = 5); unpaired, two-tailed t-test with Welch's correction. (E) Migration of MDA-MB-468 cells after 24 h treatment with 50 nM MTX in medium supplemented with normal or dialyzed FBS; graph shows mean ± SEM of four independent experiments. (F), (G) Migration and invasion of LN229 (F) and 4T1 (G) cells after 24h treatment with 50 nM (F), 75 nM (G) MTX was assessed using ECM-Collagen-coated or non-coated Boyden chambers. Each dot represents an independent experiment; mean ± SEM (n = 3); Brown-Forsythe and Welch one-way ANOVA with Dunnett's multiple comparisons test. Source data are provided as a Source Data file.

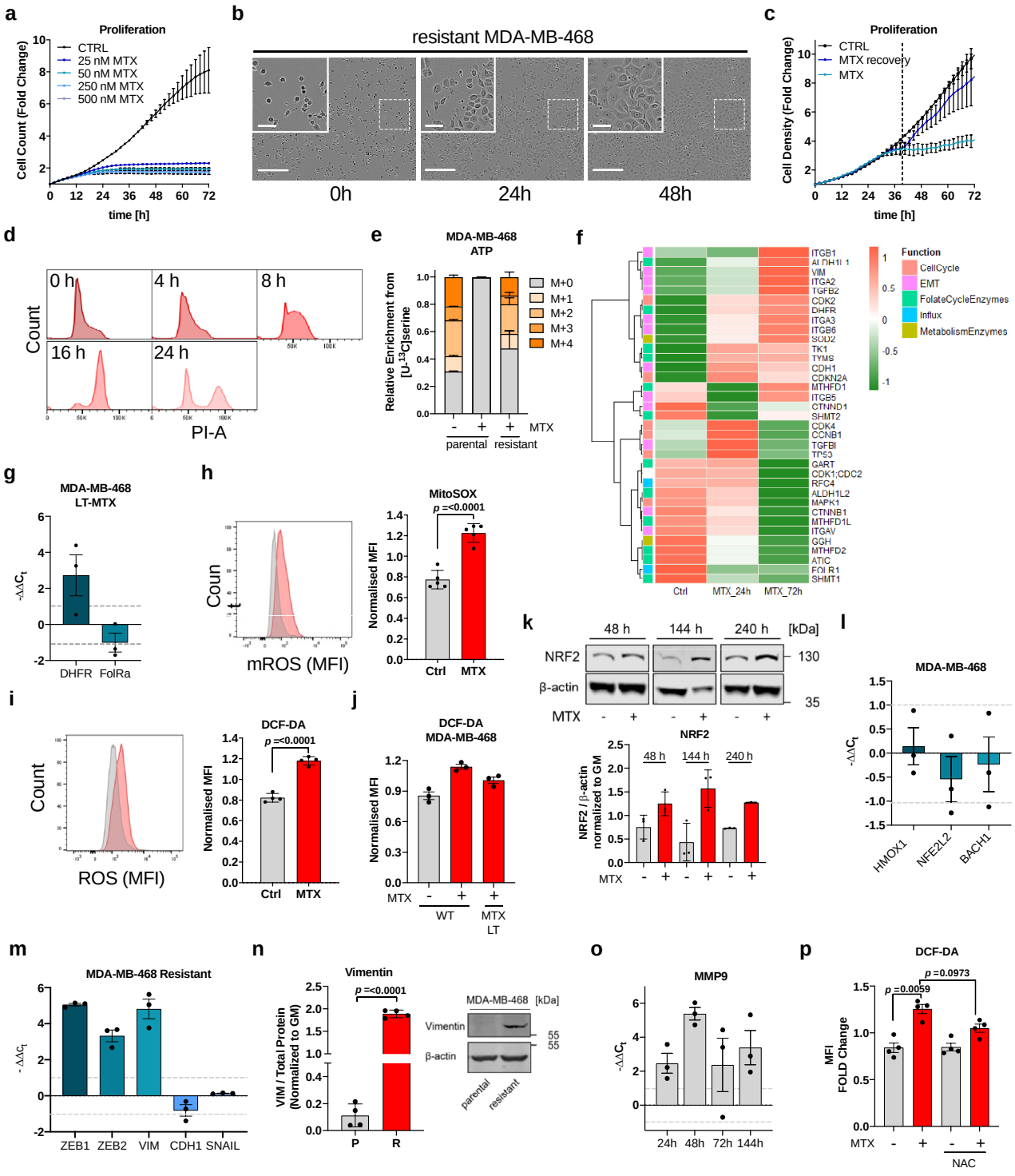

Supplementary Figure 2: (A) Proliferation of NucLight Rapid Red stained MDA-MB-468 cells upon the indicated concentrations of MTX; mean ± SEM of independent experiments (n = 3). **(B)** Morphology of proliferating MTX-resistant MDA-MB-468 cells. Bright-field images are representative of independent experiments. Scale bars correspond to 60 and 300 µm. **(C)** Growth of MDA-MB-468 cells in response to 50 nM MTX and growth recovery upon removal of MTX after 38 h assessed as fold change of cell density; mean ± SEM of independent experiments (n = 3). **(D)** Recovery of cell cycle profile at the indicated time points after MTX removal as in (C). Histograms are representative of three independent experiments. **(E)** MID of intracellular ATP upon [U-^{13}C]serine tracer in response to 24 h 50 nM MTX in parental MDA-MB-468 cells and MTX-resistant MDA-MB-468 cells. Graph shows mean ± SEM of two independent experiments each measured in triplicate wells. **(F)** Heatmap of selected protein expressions from SILAC quantitative proteomics measurement with different MTX

treatment durations. The log2 fold changes of each protein were standardized by row. Molecular function of proteins are indicated with colors. **(G)** mRNA expression from the indicated genes was quantified by real-time RT-qPCR in resistant long-term (LT) MTX treated MDA-MB-468 cells relative to MDA-MB-468 WT cells. Each dot represents one independent experiment; mean ± SD (n = 3). (**H**) Mitochondrial ROS levels in response to 24 h 50 nM MTX measured by flow cytometric quantification of MitoSOX mean fluorescence intensity. Each dot represents an independent experiment; mean ± SD (n = 5); unpaired, two-tailed t-test with Welch's correction. **(I)** Intracellular ROS levels in response to 24 h 50 nM MTX measured by flow cytometric quantification of DCF-DA mean fluorescence intensity. Each dot represents an independent experiment; mean ± SD (n = 4); unpaired, two-tailed t-test with Welch's correction. **(J)** Intracellular ROS levels in response to 24 h MTX treatment in MDA-MB-468 WT cells and in LT MTX treated MTX_resistant MDA-MB-468 cells measured by flow cytometric quantification of DCF-DA mean fluorescence intensity. Each dot represents one independent experiment; mean ± SD (n = 3). (**K**) NRF2 expression in MDA-MB-468 cells after treatment with 50 nM MTX for the indicated time was quantified by Western Blot. Normalized signal intensity was quantified relative to β-actin signal. Each dot represents an independent experiment; mean ± SD (n = 3). (**L**) mRNA expression from the indicated target genes in MDA-MB-468 cells was measured after 144 h 50 nM MTX and quantified relative to untreated cells using real-time RT-qPCR. Each dot represents one independent experiment; mean ± SD (n = 3). (**M**) mRNA expression from the indicated target genes in MTX-resistant MDA-MB-468 cells relative to parental MDA-MB-468 cells as measured using real-time RT-qPCR. Each dot represents an independent experiment; mean ± SEM (n = 3). **(N)** Expression of vimentin in parental and MTX-resistant MDA-MB-468 cells; β-actin serves as loading control. Quantification of vimentin signal intensity relative to total protein stain. Each dot represents an independent experiment; mean ± SD (n = 4); unpaired, two-tailed t-test with Welch's correction. (**O**) mRNA expression of MMP9 was quantified in MDA-MB-468 cells after 50 nM MTX at the indicated time points using real-time RT-qPCR. Each dot represents an independent experiment; mean ± SEM (n = 3). **(P)** Intracellular ROS levels in MDA-MB-468 cells in response to 24 h 50 nM MTX and 10 mM NAC as measured by flow cytometric quantification of DCF-DA mean fluorescence intensity. Each dot represents an independent experiment. Graph shows mean ± SD (n = 4); Brown-Forsythe and Welch ANOVA test with Games-Howell's multiple comparisons test. Source data are provided as a Source Data file.

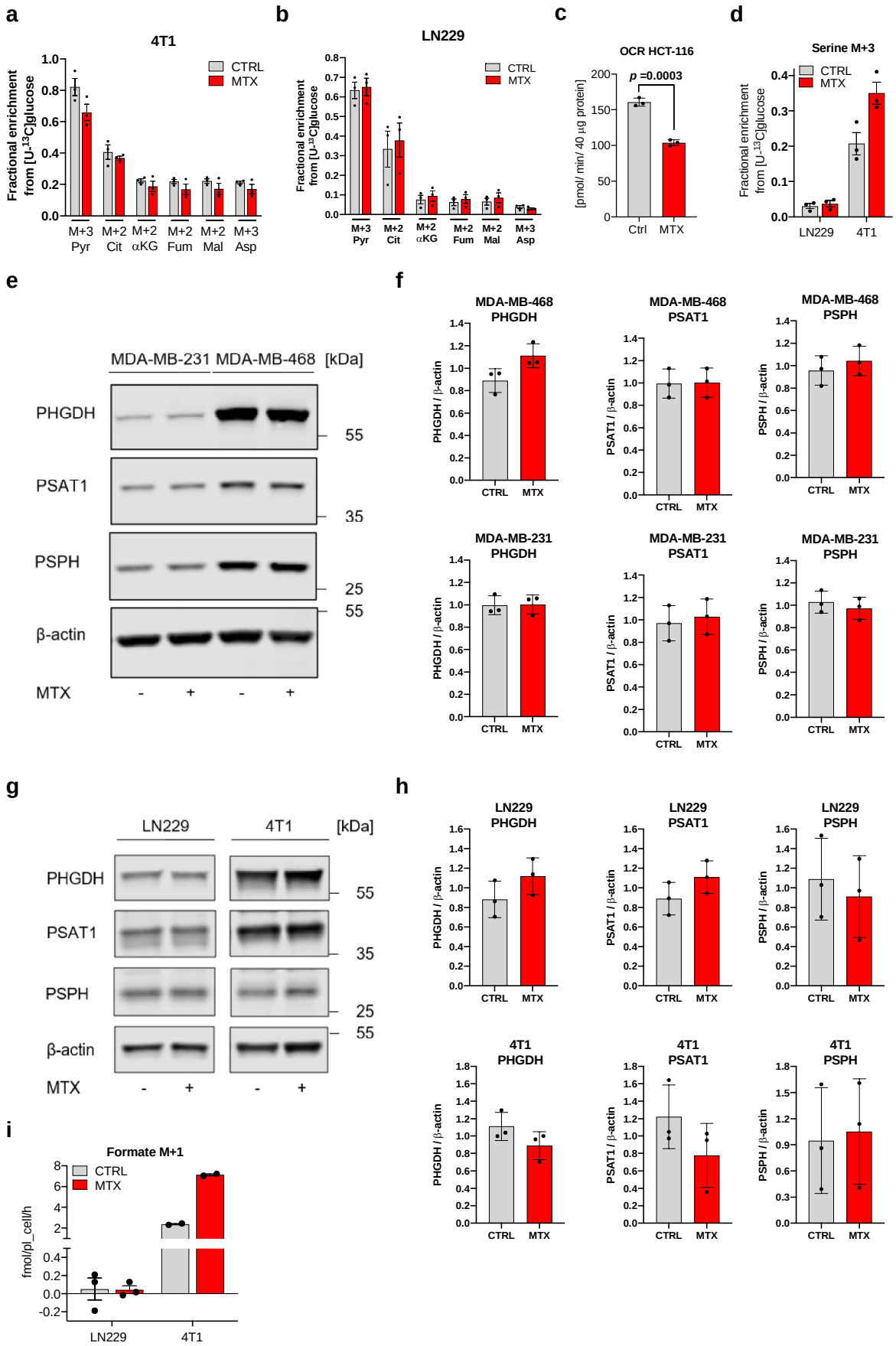

Supplementary Figure 3: (A), (B) Relative isotopologue abundance following [U-^{13}C]glucose tracing in 4T1 (A) and LN229 (B) cells in response to 24 h 75 nM MTX (A) and 50 nM MTX (B). Each dot represents an individual experiment composed

of triplicate wells; mean ± SEM (n = 3). **(C)** Basal cellular respiration in response to 24 h 50 nM MTX treatment was determined in HCT-116 cells as quantification of mitochondrial OCR. Each dot represents an individual experiment composed of six technical replicates; mean ± SEM (n = 3); unpaired, two-tailed t-test with Welch's correction. **(D)** M+3 isotopologue abundance of serine upon [U-^{13}C]glucose tracing in response to 24 h 50 nM MTX in LN229 and 24 h 75 nM MTX in 4T1 cells. Each dot represents an independent experiment in triplicate wells; mean ± SEM (n = 3). **(E)** Expression of PHGDH, PSAT1, and PSPH in MDA-MB231 and MDA-MB-468 cells upon 24 h 50 nM MTX treatment; β-actin serves as loading control. **(F)** Treatment as in (E). Quantification of PHGDH, PSAT1, and PSPH Western blot signal intensity relative to β-actin normalized to global mean in MDA-MB231 and MDA-MB-468 cells. Each dot represents an independent experiment; mean ± SD (n = 3). **(G)** Expression of PHGDH, PSAT1, and PSPH in LN229 and 4T1 cells upon 24 h 50 nM MTX (LN229) and 75 nM MTX (4T1) treatment; β-actin serves as loading control. **(H)** Treatment as in (G). Quantification of PHGDH, PSAT1, and PSPH Western blot signal intensity relative to β-actin and normalized to global mean in LN229 and 4T1 cells. Each dot represents an independent experiment; mean ± SD (n = 3). **(I)** M+1 formate release rate in LN229 and 4T1 cells after 24 h [U-^{13}C]glucose tracing and treatment with 50 nM (LN229) and 75 nM (4T1) MTX. Each dot indicates an independent experiment measured in triplicate wells; mean ± SEM (n = 3 (LN229), n = 2 (4T1)). Source data are provided as a Source Data file.

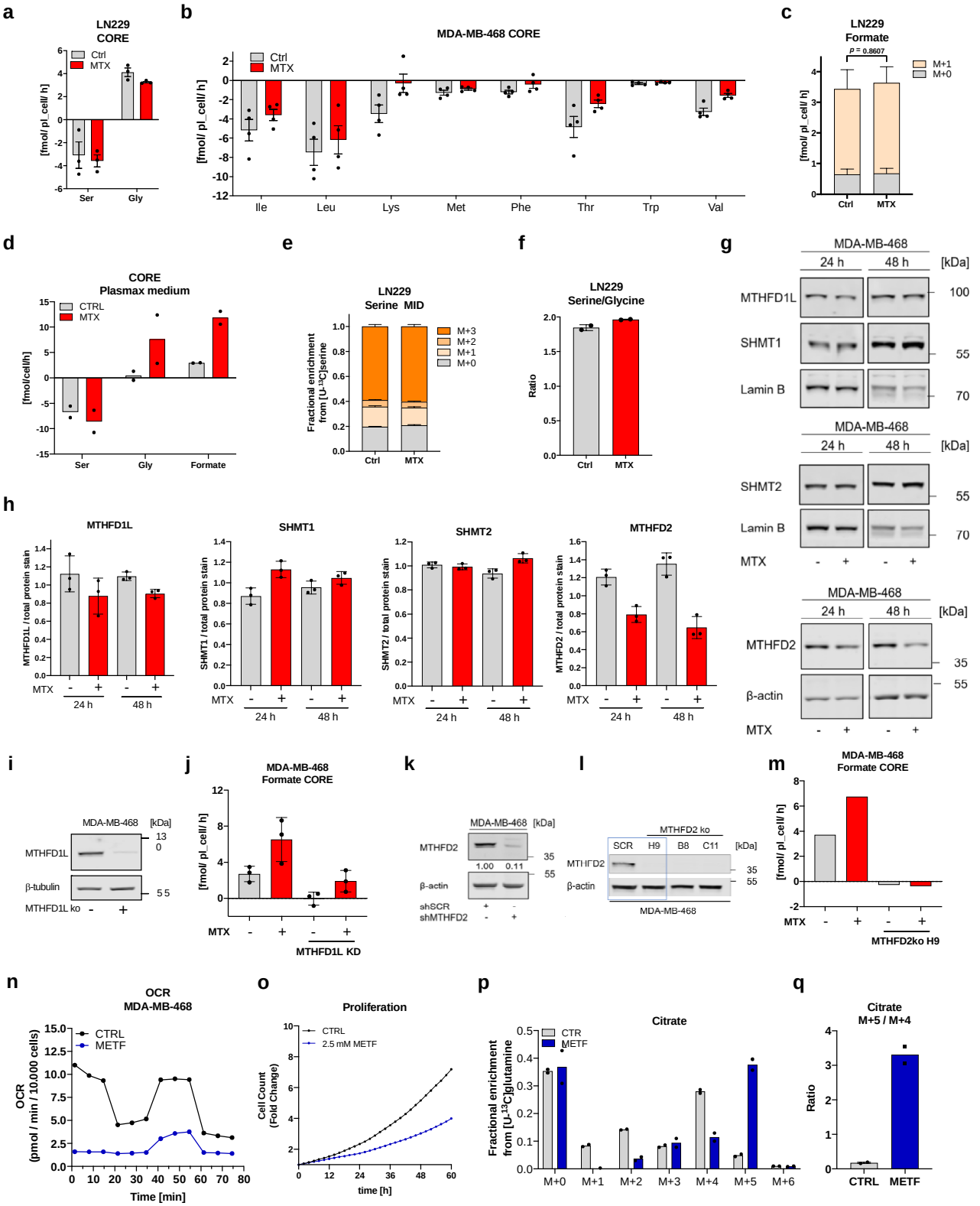

Supplementary Figure 4: (A) Absolute CORE rates of serine and glycine of LN229 cells in response to 24 h 50 nM MTX. Each dot represents the mean of an individual experiment each measured in triplicate wells; mean ± SEM. **(B)** Absolute CORE rates of essential amino acids as indicated in response to 24 h 50 nM MTX. Each dot represents an independent experiment in triplicate wells; mean ± SEM (n = 3). **(C)** Formate release rates of M+0 and M+1 formate isotopologues upon [U-^{13}C]serine tracing in LN229 cells in response to 24 h 50 nM MTX. Graph shows mean ± SEM of three independent experiments each measured in triplicate wells; unpaired, two-tailed t-test with Welch's correction. **(D)** Absolute CORE rates of serine, glycine, and formate in MDA-MB-468 cells in response to 24 h 50 nM MTX in Plasmax medium. Mean of two independent experiments in triplicate wells. **(E)** MID of intracellular serine upon [U-^{13}C]serine tracing in LN229 cells in response to 24 h 50 nM MTX; mean ± SEM of two independent experiments each measured in triplicate wells. **(F)** Ratio

of intracellular serine and glycine levels in response to 24 h 50 nM MTX in LN229 cells. Mean ± SEM of independent experiments in triplicate wells (n = 2). **(G)** Expression of MTHFD1L, SHMT1, SHMT2, and MTHFD2 in MDA-MB-468 cells 24 h and 48 h 50 nM MTX; β-actin serves as loading control. **(H)** Treatment as in (G). Quantification of MTHFD1L, SHMT1, SHMT2, and MTHFD2 Western blot signal intensity relative to total protein stain normalized to GM in MDA-MB-468 cells. Each dot represents an independent experiment; mean ± SD (n = 3). **(I)** Residual MTHFD1L protein expression in MDA-MB-468 MTHFD1L CRISPR KO cells was determined on Western Blot. β-tubulin serves as loading control. **(J)** Absolute CORE rates of formate from mock or shMTHFD1L-transfected MDA-MB-468 cells upon 24 h 50 nM MTX. Dots represent technical replicates of a representative experiment; mean ± SD (n = 3). **(K)** Residual MTHFD2 protein expression in mock or shMTHFD2-transfected MDA-MB-468 cells was determined on Western Blot. β-actin serves as loading control. **(L)** Residual MTHFD2 protein expression in three MDA-MB-468 MTHFD2 CRISPR KO clones was determined on Western Blot. β-actin serves as loading control. **(M)** Absolute CORE rates of formate from MDA-MB-468 cells upon depletion of MTHFD2 (CRISPR clone H9) and 24 h 50 nM MTX. Plot shows the median of one experiment done in triplicate wells. **(N)** Oxygen consumption rate (OCR) in MDA-MB-468 cells after 24h treatment with 2.5 mM Metformin. Graph shows mean of six technical replicates. **(O)** Proliferation of MDA-MB-468 cells in response to treatment with 2.5 mM Metformin. Graph shows mean of two independent experiments. **(P)** Citrate MID from [U-^{13}C]glutamine tracing in MDA-MB-468 cells after 24 h treatment with 2.5 mM Metformin. Graph shows mean of two independent experiments. Dots indicate the mean of each independent experiment performed in triplicate wells. **(Q)** Ratio of M+5/M+4 istotopologues of citrate after 24 h treatment with 2.5 mM Metformin and tracing with [U-^{13}C]glutamine tracing. Graph shows mean of two independent experiments. Dots indicate the mean of each independent experiment performed in triplicate wells. Source data are provided as a Source Data file.

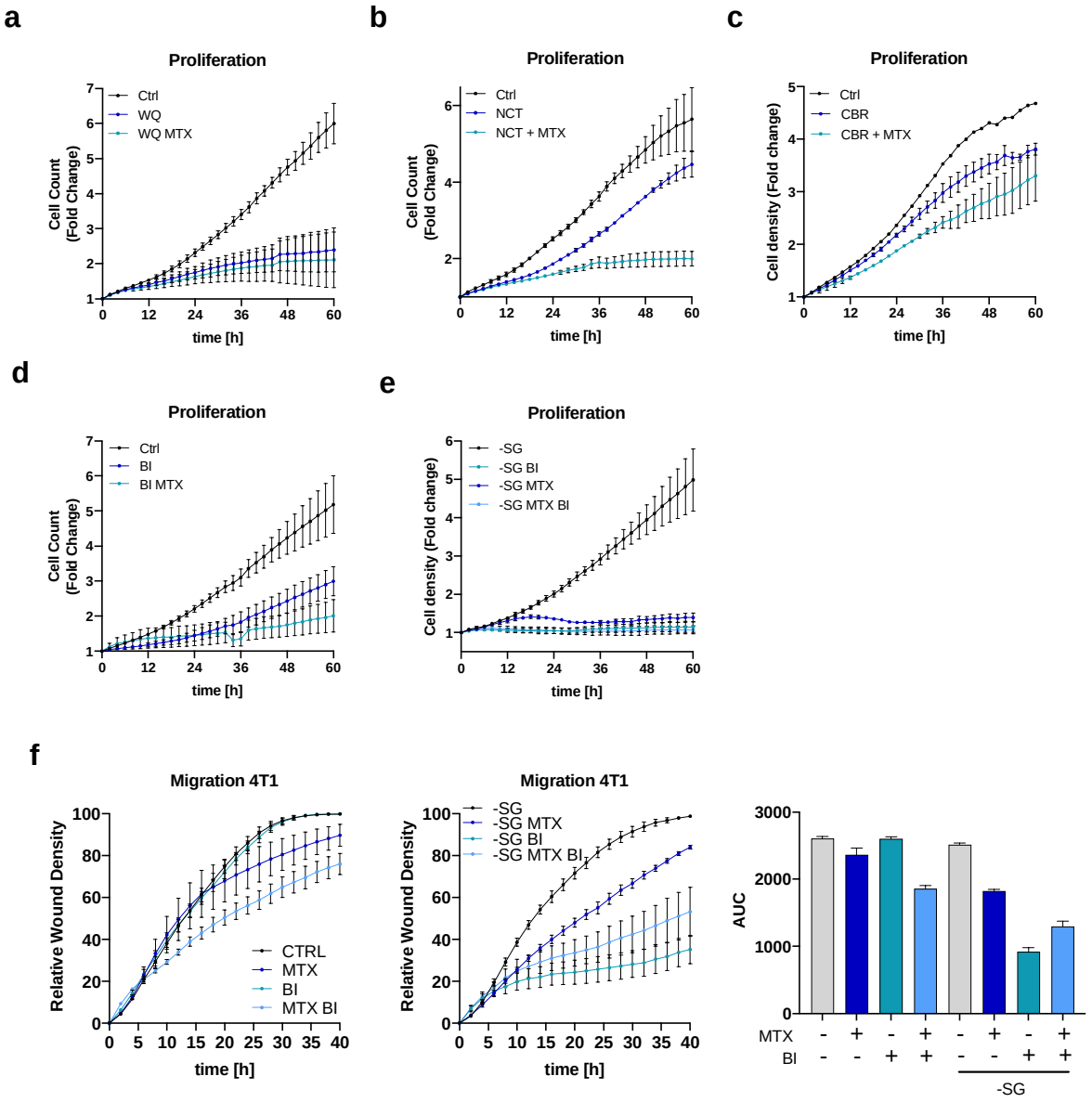

Supplementary Figure 5: (A) Proliferation of NucLight Rapid Red stained MDA-MB-468 cells upon treatment with 10 µM WQ-2101 and 50 nM MTX as indicated; mean ± SEM of independent experiments (n = 6). **(B)** Proliferation of NucLight Rapid Red stained MDA-MB-468 cells upon treatment with 10 µM NCT-502 and 50 nM MTX as indicated; mean ± SEM of independent experiments (n = 4). **(C)** Proliferation of MDA-MB-468 cells measured as fold cell density upon treatment with 30 µM CBR-5884 and 50 nM MTX as indicated; mean ± SEM of independent experiments (n = 1 (CTRL), n = 2 (CBR, CBR+MTX)). **(D)** Proliferation of NucLight Rapid Red stained MDA-MB-468 cells upon treatment with 15 µM BI-4916 and 50 nM MTX as indicated; mean ± SEM of independent experiments (n = 7). **(E)** Proliferation of serine- and glycine-starved MDA-MB-468 cells measured as fold cell density upon treatment with 15 µM BI-4916 and 50 nM MTX as indicated; mean ± SEM of independent experiments (n = 3). (**F**) Migration of 4T1 cells upon treatment with 75 nM MTX and 15 µM BI in the presence or absence of serine and glycine in culture medium and respective AUC over 40 h. Graph shows mean ± SD of one representative experiment performed in technical replicates (n = 3 for all –SG conditions, n = 4 for all others). Source data are provided as a Source Data file.

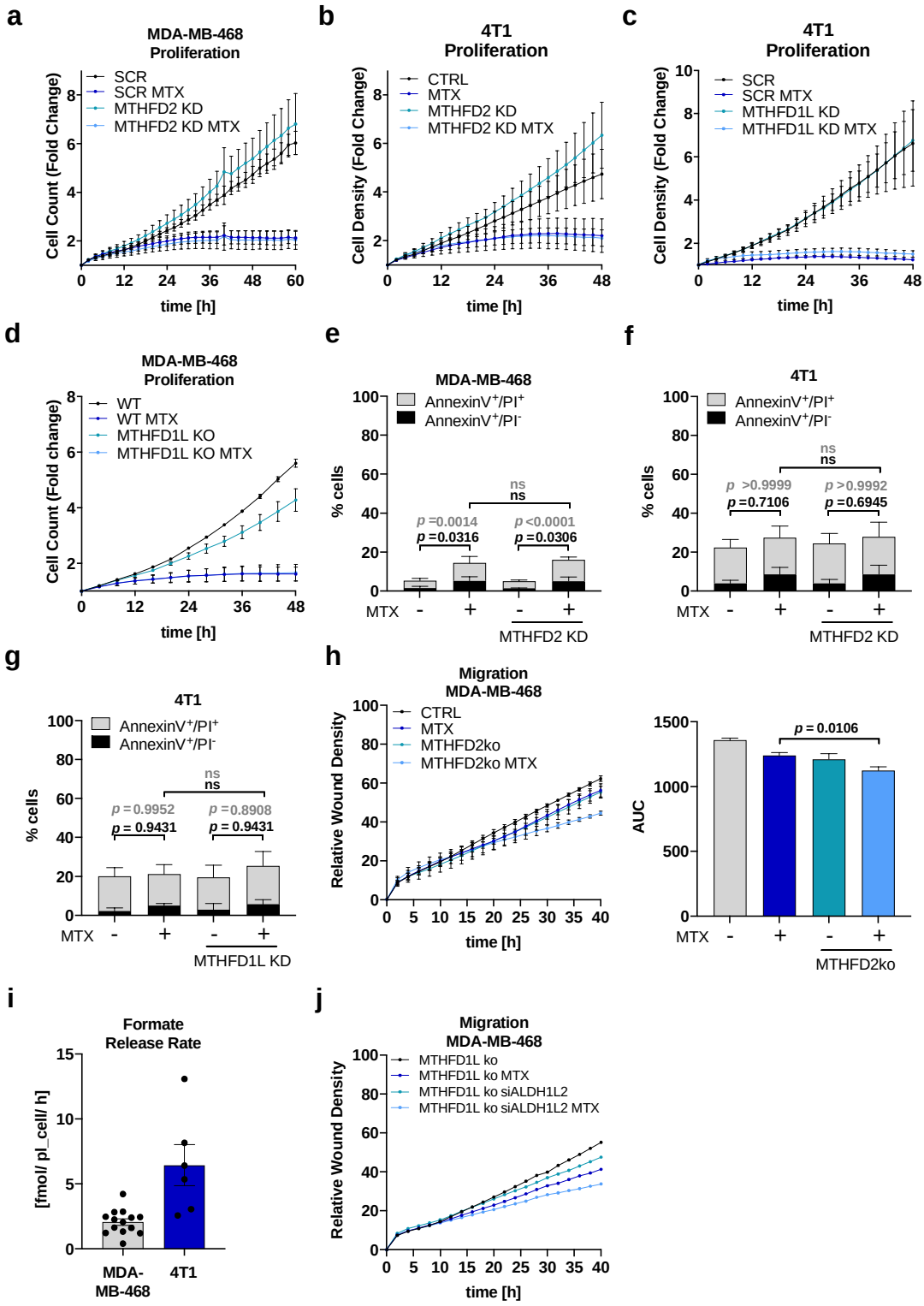

Supplementary Figure 6: (A-D) Proliferation of MDA-MB-468 (A,D) and 4T1 (B,C) cells upon MTHFD1L and MTHFD2 depletion as indicated after treatment with 50 nM MTX (A,D) or 75 nM MTX (B,C). Graph shows mean ± SEM of independent experiments (n = 6 (A); 3 (B); 1 (SCR MTX), 3 (SCR, MTHFD1LKD MTX) or 4 (MTHFD1LKD) (C); 4 (D)). (**E-G**) MDA-MB-468 (E) and 4T1 (F,G) cells depleted for MTHFD2 or MTHFD1L were treated with 50 nM (E) or 75 nM (F, G) MTX for 48h. Cell death was assessed by flow cytometry and AnnexinV-FITC/PI-staining; mean ± SD of independent experiments (n = 4). 2-way ANOVA with Dunnett's multiple comparisons test. **(H)** Migration of MDA-MB-468 cells (clone H9) in response to MTHFD2 knockout and 50 nM MTX treatment. Graph shows mean ± SEM (n = 3); Brown-Forsythe and Welch one-way ANOVA with Dunnett's multiple comparisons test. **(I)** Absolute formate release from MDA-MB-468 and 4T1

cells. Graph shows mean ±SEM of independent experiments, each performed in triplicate wells (n = 14 (MDA-MB-468), n = 6 (4T1)). **(J)** Migration of MDA-MB-468 MTHFD1L knockout cells in response to siRNA-mediated knockdown of ALDH1L2 and 50 nM MTX treatment. Graph shows mean of technical replicates (n = 7 (MTHFD1Lko, MTHFD1lko MTX) – 8 (MTHFD1Lko siALDH1L2, MTHFD1Lko siALDH1L2 MTX) wells). Source data are provided as a Source Data file.

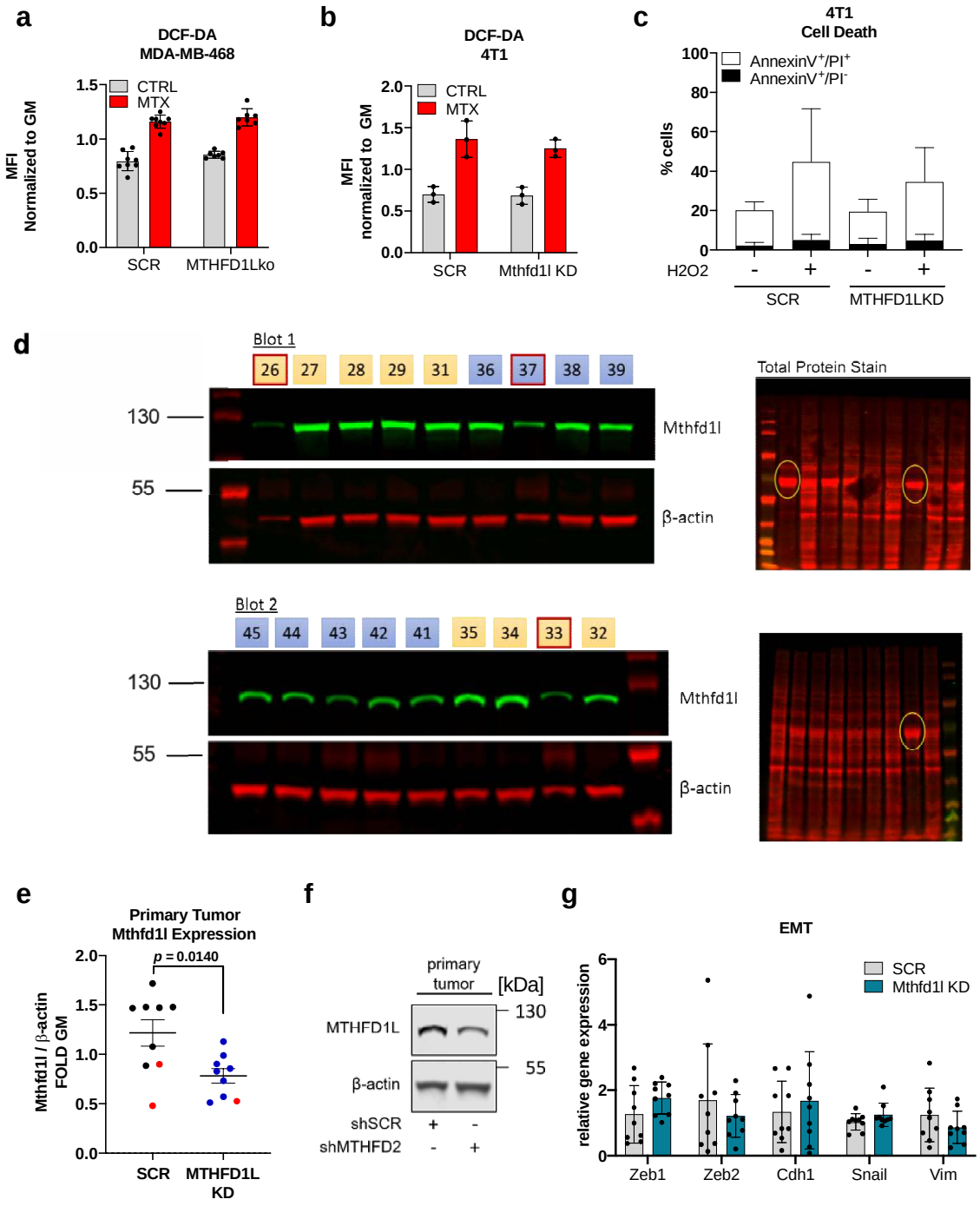

Supplementary Figure 7: (A, B) Intracellular ROS levels in MDA-MB-468 and 4T1 cells in response to 24 h 50 nM MTX (A) or 75 nM MTX (B) measured by flow cytometric quantification of DCF-DA mean fluorescence intensity. Each dot represents one independent experiment; mean ± SD (n = 7 (MTHFD1Lko) – 8 (SC) (A) or n = 3 (B)). **(C)** 4T1 cells depleted or not for Mthfd1l were treated with 500 µM H_2O_2 for 24 h. Cell death was assessed by flow cytometry and AnnexinV-FITC/PI-staining; mean ± SD of independent experiments (n = 4). **(D)** Western blot images of protein lysates from primary tumor tissue. Indicated replicates (red frame around box) were excluded from analysis in Figure 7D, due to the here presented finding that total protein in these samples was mainly composed of a single protein (see Total Stain). This indicates unreliability of the sample. (E) Mthfd1l expression in primary tumor tissue obtained by orthotopic implantation of 4T1 SCR and Mthfd1lKD breast cancer cells. Red dots indicate data points that were excluded as explained in (D); mean ± SD (n = 9) unpaired, two-tailed t-test with Welch's correction.(**F)** Representative Western Blot image of Mthfd1l protein expression in primary tumor tissue in mice after orthotopic implantation of 4T1 scramble or Mthfd1l shRNA transfected breast cancer cells. β-actin serves as loading control. (**G**) mRNA expression from indicated target genes in primary tumor

tissue in mice after orthotopic implantation of 4T1 scramble or Mthfd1l shRNA transfected breast cancer cells measured by real-time RT qPCR. Each dot indicates one individual animal; mean ± SD (n = 9). Source data are provided as a Source Data file.

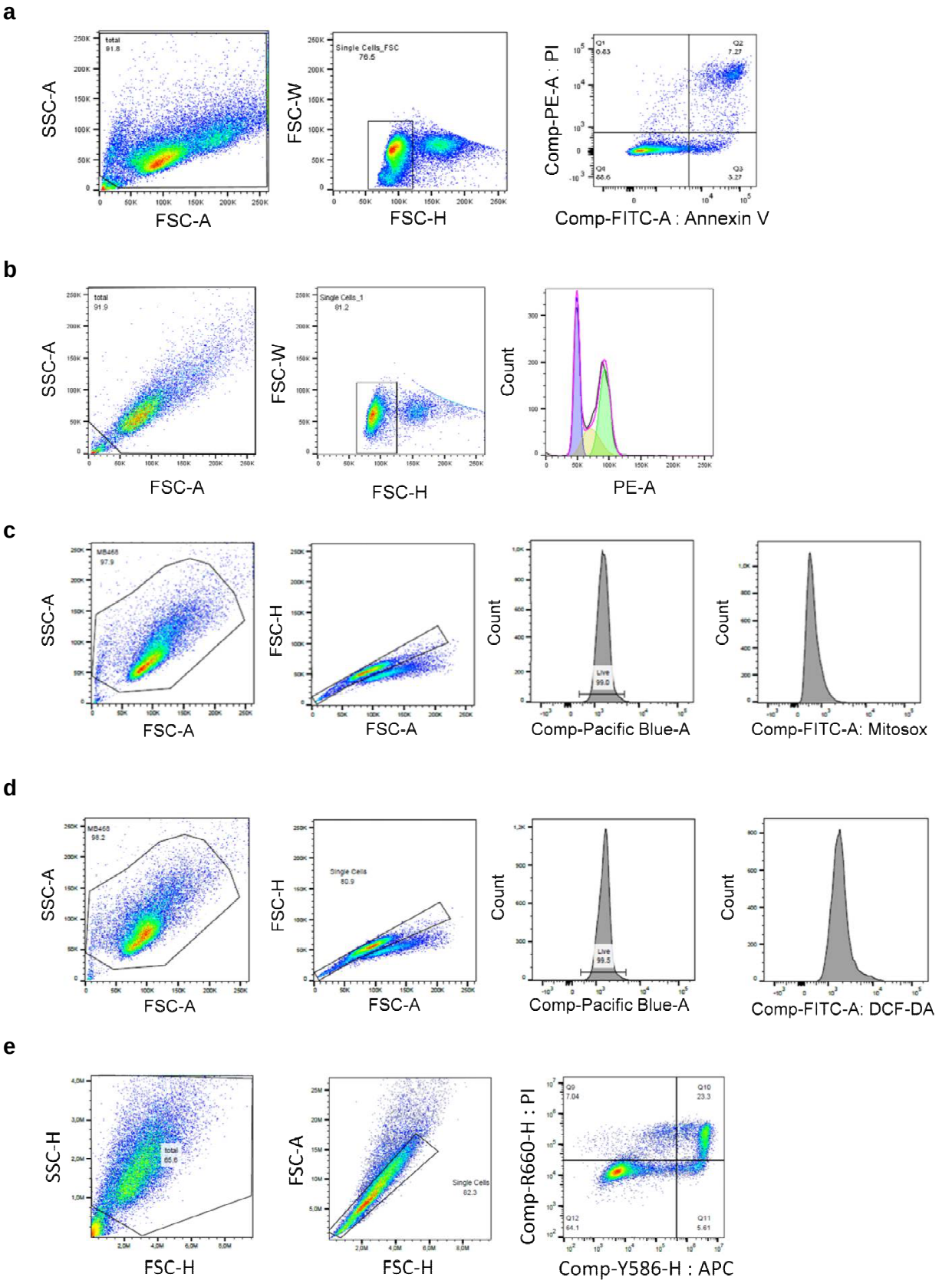

Supplementary Figure 8: (A) Exemplary gating for Annexin-PI measurement using Annexin-V-FITC and PI. **(B)** Exemplary gating for cell cycle analysis using automatic cell cycle analysis tool in FlowJo. **(C)** Exemplary gating for

mitochondrial ROS measurement using Mitosox dye. **(D)** Exemplary gating for cytosolic ROS measurement using DCF-DA dye. (**E**) Exemplary gating for Annexin-PI measurement using Annexin-V-APC and PI in GFP-positive cells.

Supplementary Table 1. Dwell times as well as quantification ions (m/z) for formate compounds.

Derivative (Metabolite)	Quant-Ion (m/z)	Dwell Time (ms)
Benzyl formate (Formic acid) – M_0	136.1	40
Benzyl formate (Formic acid) – M_1	137.1	40
IS Benzyl formate (Formic acid 13C, D) – M_0	138.1	40
IS Benzyl formate (Formic acid 13C, D) – M_1	139.1	40
IS Benzyl formate (Formic acid 13C, D) – M_2	140.1	40

Supplementary Table 2. Dwell times as well as quantification ions (m/z) for the measured compounds.

Derivative (m/z of selected fragment)	Quant-Ions (m/z)	Dwell Time (ms)	Sum Formula (Fragment)	MID size
Pyruvic Acid 1MeOX 1TBDMS (174)	174.0 – 180.1	15	C6H12O3NSi	4
Lactic Acid 2TBDMS (261)	261.1 – 267.1	15	C11H25O3Si2	4
Alanine 2TBDMS (260)	260.1 – 266.1	15	C11H26NO2Si2	4
Glycine 2TBDMS (246)	246.1 – 252.1	15	C10H24NO2Si2	3
Succinic Acid 2TBDMS (289)	289.1 – 296.1	15	C12H25O4Si2	5
Fumaric Acid 2TBDMS (287)	287.1 – 294.1	15	C12H23O4Si2	5
(Internal Standard) Pentanedioic-D6 Acid	235.2, 309.2, 351.3	30		
Serine 3TBDMS (390)	390.2 – 396.2	15	C17H40NO3Si3	4
a-Ketoglutaric Acid 1MeOX 2TBDMS (346)	346.2 – 354.2	10	C14H28NO5Si2	6
Malic Acid 2TBDMS (419)	419.2 – 426.2	15	C18H39O5Si3	5
Aspartic Acid 3TBDMS (418)	418.2 – 425.2	15	C18H40NO4Si3	5
Glutamic Acid 3TBDMS (432)	432.3 – 440.3	10	C19H42NO4Si3	6
Glutamine 3TBDMS (431)	431.3 – 439.3	10	C19H43N2O3Si3	6
Citric Acid 4TBDMS (591)	591.3 – 600.3	10	C26H55O7Si4	7
3-Phosphoglyceric Acid 4TBDMS (585)	585.4 – 592.4	15	C27H63O7PSi4	4

Supplementary Table 3: Realtime RT-qPCR primers used in this study for selcted human and murine genes of interest.

Gene Name	Species	Sequence Fwd (5' – 3')	Sequence Rev (5' – 3')
CDH1	human	AGTGCCAACTGGACCATTCA	TCTTTGACCACCGCTCTCCT
CycloA	human	CAGACAAGGTCCCAAAGACA	CCATTATGGCGTGTGAAGTC
GAPDH	human	CATGAGAAGTATGACAACAGCCT	AGTCCTTCCACGATACCAAAGT
MMP9	human	CGCGCTGGGCTTAGATCATT	GGTTCAGGGCGAGGACCATA
SLUG	human	CTACAGCGAACTGGACACACA	TGGAATGGAGCAGCGGTAGT
SNAIL	human	CGAAAGGCCTTCAACTGCAAA	TGACATCTGAGTGGGTCTGGA
VIM	human	CCTTGAACGCAAAGTGGAATC	GACATGCTGTTCCTGAATCTGAG
ZEB1	human	AAGAACTGCTGGGAGGATGACA	CCTCTTCAGGTGCCTCAGGAAAA
ZEB2	human	GCAAGAGGCGCAAACAAGC	GGGTTGGCAATACCGTCATCC
HMOX1	human	CTGCTCAACATCCAGCTCTTTG	ATCTTGCACTTTGTTGCTGGC
NFE2L2	human	AACTACTCCCAGGTTGCCCA	CAAGTGACTGAAACGTAGCCG
BACH1	human	GCCTCGCACAATATGGTTGAT	TGACATCGCACAGCACATCT
DHFR	human	AATCGGCTCAAAACCGCTTG	TCTGAATTCATTCCTGAGCGG
FolRa	human	TGGAACTGGACTTCAGGGTT	CACTCCCTCGGCTGTAGTTG
Zeb1	mouse	GGGAAATAGCACAGACAGTTGTT	TCACCTCTCCACAATGACGC
Zeb2	mouse	GTCGCTGTGTTTGGTTGCTAGA	CGTTGTCATAGTTCACCACGTT
Cdh1	mouse	TCATCAAATGGGGAAGCGGT	TTCATCACGGAGGTTCCTGG
Snail	mouse	GCTGCTTCGAGCCATAGAACTAAA	TTGAGGGAGGTAGGGAAGTGG
Vim	mouse	AGACCAGAGATGGACAGGTGA	CTGGTACTGCACTGTTGCAC
Gapdh	mouse	CATCACTGCCACCCAGAAGACTG	ATGCCAGTGAGCTTCCCGTTCAG
Sdha	mouse	CTTCGCTGGTGTGGATGTCA	GTGGGAATCCCACCCATGT

STAR Protocols

CellPress
OPEN ACCESS

Protocol

Protocol using *ex vivo* mouse brain slice culture mimicking *in vivo* conditions to study tumor growth and cell motility of glioblastoma cells

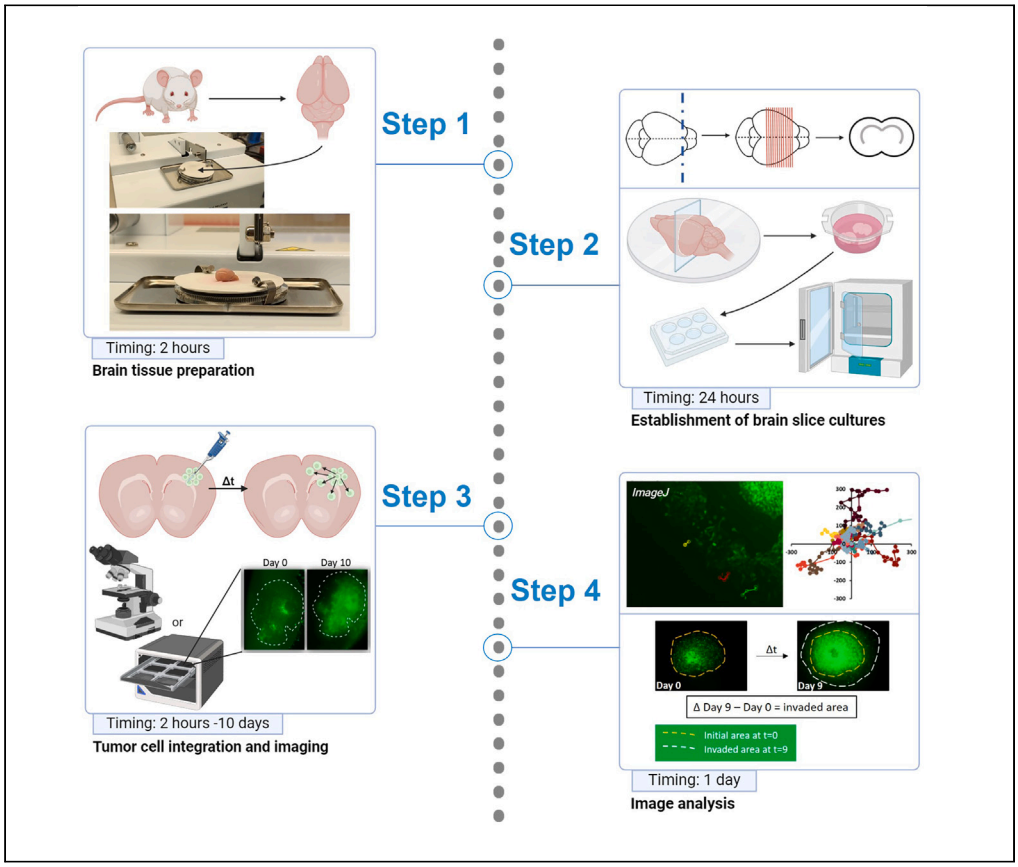

Herein, we present an *ex vivo* approach to study glioblastoma (GBM) cell motility in viable mouse brain slice cultures, closely mimicking *in vivo* features. We detail the preparation and culturing of mouse brain slices followed by tumor cell injection, allowing for the analysis of different aspects of the cellular migration and invasion process. Our assay facilitates testing diverse perturbations including genetic modifications and treatments in a physiological context. Thus, the protocol provides a compromise between *in vitro* assays and *in vivo* models.

Publisher's note: Undertaking any experimental protocol requires adherence to local institutional guidelines for laboratory safety and ethics.

Laura Neises, Catherine Delbrouck, Anne Schuster, ..., Simone P. Niclou, Anna Golebiewska, Johannes Meiser

anna.golebiewska@lih.lu (A.G.)
johannes.meiser@lih.lu (J.M.)

Highlights

Mouse brain slice cultures allow for functional tumor assays *ex vivo*

Tumor cells can be injected into the brain tissue and integrate therein

Motility of integrated tumor cells can be studied in highly physiological brain environment

Functional assessment of cell motility combined with genetic perturbations or treatments

Neises et al., STAR Protocols 5, 103401
December 20, 2024 © 2024 The Author(s). Published by Elsevier Inc.
https://doi.org/10.1016/j.xpro.2024.103401

STAR Protocols

CellPress
OPEN ACCESS

Protocol

Protocol using *ex vivo* mouse brain slice culture mimicking *in vivo* conditions to study tumor growth and cell motility of glioblastoma cells

Laura Neises,[1,5] Catherine Delbrouck,[1,2] Anne Schuster,[3] Mahsa Rezaipour,[2,3] Kim Eiden,[1,2] Anais Oudin,[3] Carina Fabian,[3] Simone P. Niclou,[2,3] Anna Golebiewska,[3,4,*] and Johannes Meiser[1,4,6,*]

[1]Cancer Metabolism Group, Department of Cancer Research, Luxembourg Institute of Health, L-1210 Luxembourg, Luxembourg

[2]Department of Life Sciences and Medicine, Faculty of Science, Technology and Medicine (FSTM), University of Luxembourg, L-4367 Belvaux, Luxembourg

[3]NORLUX Neuro-Oncology Laboratory, Department of Cancer Research, Luxembourg Institute of Health, L-1210 Luxembourg, Luxembourg

[4]These authors contributed equally

[5]Technical contact

[6]Lead contact

*Correspondence: anna.golebiewska@lih.lu (A.G.), johannes.meiser@lih.lu (J.M.)
https://doi.org/10.1016/j.xpro.2024.103401

SUMMARY

Herein, we present an *ex vivo* approach to study glioblastoma (GBM) cell motility in viable mouse brain slice cultures, closely mimicking *in vivo* features. We detail the preparation and culturing of mouse brain slices followed by tumor cell injection, allowing for the analysis of different aspects of the cellular migration and invasion process. Our assay facilitates testing diverse perturbations including genetic modifications and treatments in a physiological context. Thus, the protocol provides a compromise between *in vitro* assays and *in vivo* models.

For complete details on the use and execution of this protocol, please refer to Delbrouck et al.[1] and Schuster et al.[2]

BEFORE YOU BEGIN

The protocol describes the experimental steps to study tumor growth and motility of fluorescently labeled tumor cells in mouse brain tissue. We have optimized the protocol with use of patient-derived GBM cultures. Our initial work was based on LN-229 GBM cells that were genetically modified with either a knockdown of *MTHFD1L* (LN-229 sh*MTHFD1L*[1]) and their specific non-targeting control (LN-229 sh*SCR*[1]) and the respective parental line LN-229 wild type (wt). Genetic engineering was designed to integrate stable expression of Green Fluorescent Protein (GFP) to monitor gene knockdown status and cell tracing. In another study, we applied a similar strategy to GBM stem-like cultures, where tumor cells were stably labeled with GFP (control, sh*SCR*, sh*ZFAND3* and *ZFAND3*-overexpressing conditions[1,2]). The protocol requires access to fresh viable mouse brain tissue. To visualize integration and perturbation of tumor cells inside the brain structures over time, fluorescent labeling is necessary. The fluorescence-based labeling may be achieved via stable transfection as well as fluorescent labeling pre-injection.[3] The experimental protocol can be performed for up to seven to ten days. If available, a live cell imaging system, such as the IncuCyte Live Cell Analysis Instrument, may be of advantage for quantification and analysis.

Institutional permissions

In our work we have applied patient-derived adherent GBM cell lines and stem-like cultures, with stable expression of GFP.[1,2] All models were derived from patient tissue following informed consent of

This is an open access article under the CC BY license (http://creativecommons.org/licenses/by/4.0/).

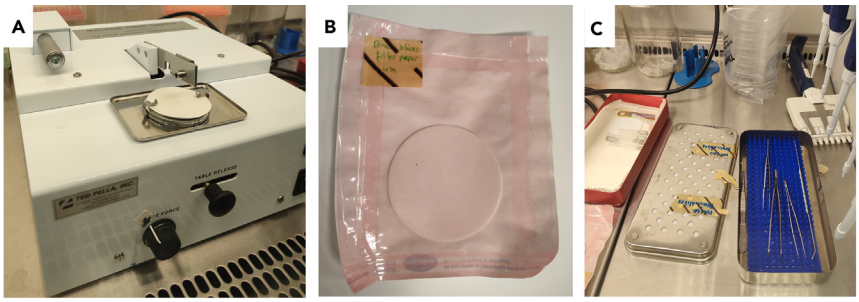

Figure 1. Overview of crucial material needed for preparation of brain tissue slices
This includes (A) McIlwain Tissue chopper, (B) sterilized circular Whatman paper and (C) box of sterilized tweezers and spatulas.

the patients. Animals were housed in a specific pathogen free (SPF) animal facility, under controlled environment (temperature, humidity and light) with free access to water and food *ad libitum*. Mice euthanasia processes strictly followed the European Directive 2010/63/EU. The euthanasia for organ sampling are done by competent persons and in an authorized user/breeder establishment.

Preparation of cells, culture medium and other material

On the day prior the start of the experiment

Timing: 60 min

1. Defrost tumor cells of interest in due time to obtain sufficient numbers of viable cells for injection 24 h after isolation of the mouse brains.

   Note: Ensure that the cells can recover from the defrosting for one to two days and then be cultured for at least two passages before using them for injection into the mouse brain slices.

   Note: At this stage, tumor cells should ideally be mycoplasma-free and >90% viable.

   ⚠ CRITICAL: Ensure that the cells you want to inject into the mouse brain slices durably express a fluorescent marker or plan an additional staining prior the injection (see limitations).

2. Order animals or mouse brain tissue from the animal facility following institutional procedures.

   Note: Fresh mouse brains are required for the protocol. We regularly apply brains extracted from male and female mice aged between 12–20 weeks. We would like to highlight that we used mice of a huge range of age for our technique since we wanted to use surplus or even unused animals. Consequently, we did not produce mice specifically for the purpose of the protocol. Since we regularly perform xenografting of human tumor cells in immunodeficient NOD. Cg-Prkdc^{scid} Il2rg^{tm1Wjl}/SzJ (NSG) and nude male and female mice aged between 8–16 weeks, we applied the same strains to the *ex vivo* brain slice cultures.

   Note: To retain similar conditions as in *in vivo* experiments, we recommend to use immunodeficient mouse stains for injecting human tumor cells. However, since T cells are rare in healthy brain parenchyma, we do not expect host versus graft effects *ex vivo* in immunocompetent mouse strains. Parenchymal microglia and non-parenchymal border-associated macrophages, which represent innate immune cells in the healthy brain, do not cause host versus graft disease.

Note: Mice should be euthanized by competent personnel following the national and EU regulation and according to institutional permissions, cervical dislocation (if needed with CO_2 overdose) can be applied. For cervical dislocation, restrain the mouse on grid, place two fingers behind the base of the skull to firmly block the head and pull back strongly on the tail to induce a rapid separation between skull and the high cervical vertebrae.

⚠ CRITICAL: To ensure an efficient cutting process resulting in high quality tissue slices, we advise to process a maximum of four mouse brains at the same time. The prolonged storage of the brains extracted from the skull adversely impacts the tissue cutting procedure and subsequently quality of the brain slices.

3. Prepare for the setup of a tissue chopper, ideally the McIlwain Tissue chopper (Figure 1A), and compare the machine with the instrument manual to confirm that all essential machine parts are available. To ensure usage of a clean and sterile cutting blade, place at least two blades in a small bucket filled with 70% of Ethanol (EtOH) and store at +4°C.
4. Prepare all required solutions and culture media under sterile conditions. Once prepared, store the solutions at +4°C in a closed standard sterile bottle.

Note: Standard cell culture medium, DMEM has been used for our experiments described in this protocol. This medium can be replaced by other standard cell culture media, depending on the cell type being used. See in the materials and equipment for exact formulation of the cutting solution and the brain slice medium.

5. Cut the Whatman filter paper in circles of an average diameter of 60 mm, covering the size of the cutting disk.

Note: Use a fresh lid from a 60 × 15 mm^2 petri dish as a template. Plan at least one filter paper per mouse brain. Prepare some filter papers in excess.

6. Sterilize the circular Whatman filter papers, two pairs of metallic tweezers (Figure 1B) and a flat spatula (Figure 1C).

Note: Sterilize material using dry sterilization in an autoclave at 121°C at 205 kPa for 30–60 min or equivalent.

7. For enhanced shelf-life, aliquot the extracellular matrix (ECM) (Sigma-Aldrich, Cat. no. E1270) stock solution into 10–20 µL aliquots under sterile conditions and store at −20°C. Avoid freeze-thaw cycles.

⚠ CRITICAL: Defrosting of ECM stock solution at +4°C may require several hours depending on the total volume. Aliquoting procedure requires +4°C.

KEY RESOURCES TABLE

REAGENT or RESOURCE	SOURCE	IDENTIFIER
Chemicals, peptides, and recombinant proteins		
ECM Gel from Engelbreth-Holm-Swarm murine sarcoma	Sigma-Aldrich	E1270
BIT-100	Provitro	2043100
Heparin	STEMCELL Technologies	07980
L-glutamine	Thermo Fisher Scientific	25030081
Glucose	Merck	G8769

(*Continued on next page*)

Continued		
REAGENT or RESOURCE	SOURCE	IDENTIFIER
GlutaMAX	Thermo Fisher Scientific	35050061
DMEM/F12	Thermo Fisher Scientific	11320033
DMEM	Thermo Fisher Scientific	A14430
Pen/Strep	Westburg	LO DE17-602E
HEPES	Thermo Fisher Scientific	15630080
70% EtOH	VWR	85825.360
Hibernate A-medium	Thermo Fisher Scientific	A1247501
Experimental models: Cell lines		
Human: LN229	ATCC	CRL-2611
Experimental models: Organisms/strains		
Mouse: NOD.Cg-Prkdc ^{SCID} Il2rg ^{tm1Wjl} /Sz, 8–20 weeks, male and female	J Charles River, France	RRID:IMSR_JAX:005557
Software and algorithms		
ImageJ	Version 1.52 a	https://imagej.net/ij/index.html
Live-Cell Imaging & Analysis Software	Sartorius	https://www.sartorius.com/en/products/live-cell-imaging-analysis/live-cell-analysis-software
Other		
Consumables		
razor blades (blade size 13 mm)	DM	966935
Whatman filter paper	Merck	WHA1001055
Transwell chambers with the pore size of 1 μm	Greiner Bio-One	657610
Glue stick	Pritt	199986
Machines		
Tissue chopper	McIlwain	https://www.manualslib.com/manual/1298233/Mcilwain-Tissue-Chopper.html
IncuCyte S3 Live-Cell Analysis System	Sartorius	4647

MATERIALS AND EQUIPMENT

Brain slice medium		
Reagent	Final concentration	Amount
Hibernate A	100%	395 mL
BIT-100	20%	100 mL
Pen/Strep	100 U/mL	5 mL
Total	**N/A**	**500 mL**

- Store in a closed standard sterile bottle at +4°C for max. 1 month.

Modified brain slice medium		
Reagent	Final concentration	Amount
Hibernate A	50%	194.3 mL
DMEM-F12	50%	194.3 mL
BIT-100	20%	100 mL
L-glutamine	2 mM	5 mL
Pen/Strep	100 U/mL	5 mL
Heparin	1 U/mL	1.39 mL
Total	**N/A**	**500 mL**

- Store in a closed standard sterile bottle at +4°C for max. 1 month.

Cutting solution		
Reagent	Final concentration	Amount
DMEM	50%	478.3 mL
GlutaMAX	0.1%	0.5 mL
Glucose	17.4 mM	3.7 mL
HEPES	25 mM	12.5 mL
Pen/Strep	100 U/mL	5 mL
Total	N/A	500 mL

- Store in a closed standard sterile bottle at +4°C for max. 1 month.

STEP-BY-STEP METHOD DETAILS

Brain tissue slice preparation

On the day prior to the cell injection into the brain slice

Timing: 1.5 h

Timing: 60 min (for step 1)

Timing: 5 min (for step 2)

Timing: 25 min (for step 3)

This major step divided into three parts describes the precise setup of the tissue chopper, the isolation of the brain from the mouse and the cutting of the freshly isolated mouse brain into tissue slices.

1. Setup of the tissue chopper.

   Note: To maintain sterile conditions, all required material needs to be placed in a biosafety cabinet class II (BSCII).

   Note: The following steps describing the instrumental setup of the tissue chopper need to be done once before starting with the tissue cutting process.

   a. Place the tissue chopper (McIlwain, Figure 3A), two cooling boxes filled with ice, the pre-cooled cutting solution (placed in a box of ice), a petri dish (diameter of 100 mm^2), the tweezers, the spatula as well as the glue stick (Pritt, Cat. no. 199986) in the BSCII.
   b. Pre-warm brain slice medium directly in the bottle to 37°C.

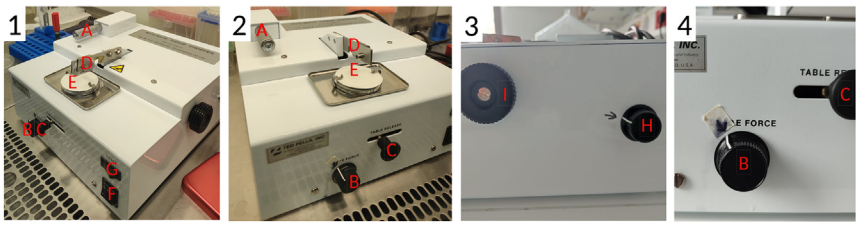

Figure 2. Essential instrument parts of the McIlwain tissue chopper shown placed in the BSCII

Essential parts of the machine are shown as: (A) slice thickness adjustment micrometer, (B) blade force control knob, (C) table release knob, (D) blade holder, (E) cutting disk with filter paper placed on top, (F) On/Off switch, (G) reset switch, (H) speed control knob, (I) manual operating knob. (3) Close-up view on precise orientation of speed control knob (item H). (4) Close-up view on precise orientation of blade force control knob (item B).

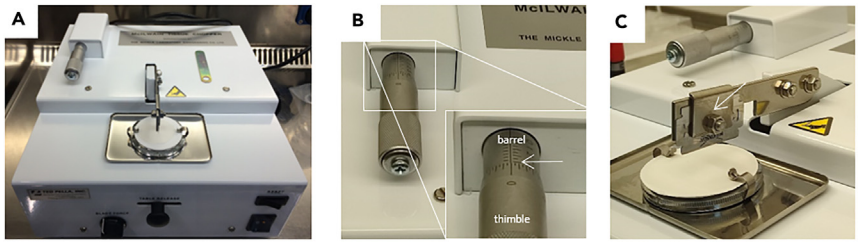

Figure 3. Detailed view on McIlwain tissue chopper

(A) Overview of machine with more precise view on (B) slice thickness adjustment micrometer composed of barrel and thimble to be set to "4" (white arrow) corresponding to a cutting distance of 400 μm and (C) cutting blade fixed to the blade holder (white arrow).

c. Properly clean the surface of the tissue chopper by wiping off the instrument with 70% of Ethanol.
d. Ensure correct installation of the tissue chopper. Apply the following settings:
   i. Set up the control knobs for speed (Figure 2, part 1 and 3, item H) and blade force (Figure 2, part 2 and 4, item B) to a user-defined level. The optimal cutting speed and blade force were empirically tested and determined as follows under CRITICAL.

⚠ CRITICAL: The optimal cutting speed is required to eliminate the risk of the brain slices attaching to the razor blade (speed too low) or to each other (speed too high). The blade force should be sufficientlystrong to cut the filter paper underneath the mouse brain. In case of partial paper cut, increase the blade force. For more visual insight on the cutting procedure, watch Methods videos S1, S2, S3, and S4.

Note: In our experience, the tissue slice thickness (i.e. the cutting distance) of 400 μm is the most optimal for high brain tissue viability during seven to ten days in culture. Slice thickness can be adjusted to the experimental needs and live/dead assays may be useful to assess the ideal slice thickness.

Note: Live/dead discrimination can be applied in the viable tissue with the viable cell membrane impermeable dyes such as DAPI (4′,6-diamidino-2-phenylindole) or PI (propidium

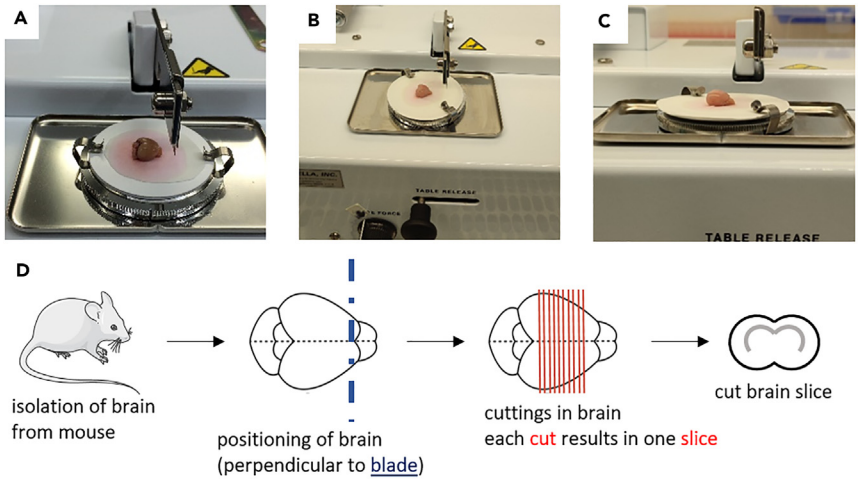

Figure 4. Mouse brain placed on the cutting disk under the blade

(A) Close view from top, (B) zoom out view from top and (C) view from the side.
(D) Schematic overview of mouse brain cutting process, essential parts are highlighted in colors.

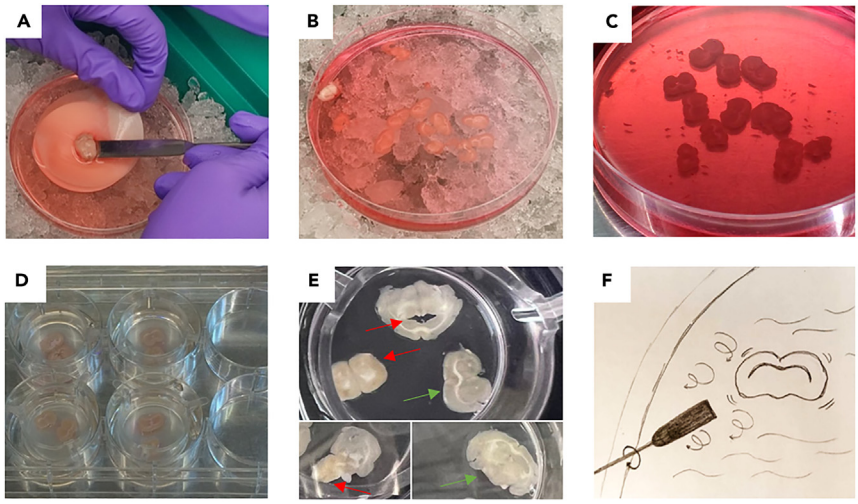

Figure 5. Recovery of the cut brain and separation of the mouse brain slices

(A) Transfer of the cut brain into the cutting solution in the Petri dish.

(B) Separated mouse brain slices in cutting solution stored on ice and (C) Zoom in.

(D) View on the brain slices in the transwell chambers from the side.

(E) Close up view on freshly cut brain slices: Upper image part shows two slices (indicated by a red arrow) that were excluded from further experimentation due to two layers of brain slice attaching together (bottom left) and disrupted tissue (up); the intact slice indicated by the green arrow had been used for cell injection. Lower part left shows a slice where half of the tissue remains folded and thus the slice was excluded from further experimentation. Lower part right shows an intact slice.

(F) Sketch illustrating the creating of soft turbulences in the ice-cold cutting solution using the spatula to facilitate lifting and thus transfer of such onto the transwell chamber membrane.

iodide). Optionally, brain slices can be embedded in paraffin and use for IHC-based visualization of tissue quality.

ii. Turn the thimble of the slice thickness adjustment micrometer (Figure 2, item A) clockwise until its outer rim reaches the marking line "4" on the barrel, as shown by the white arrow in Figure 3B.

iii. Adjust the marking on the thimble to "0" to be in line with the lining on the barrel.

Note: The following steps describing the preparation of some accessory instrumental material need to be repeated for every fresh mouse brain that will be cut.

e. Prepare a sterile 6-well tissue culture plate, at least six transwell chambers with the pore size of 1 μm (or alternatively 3 μm pore size) and pipettes in the range of 1000 μL–10 μL ready-to-use.

f. Use the pair of tweezers to transfer a sterile round-cut Whatman filter paper on top of the tissue chopper.

i. Carefully apply a thin layer of glue on one side of the paper, covering the entire surface.

Note: Avoid unnecessary touching of the filter paper with your gloves to maintain sterility of the filter paper.

ii. Attach it with the adhesive surface directly on the cutting disk (Figure 3C), so that the filter paper adheres to the cutting disk.

Note: The filter paper serves as a cushioned support on the cutting disk for the mouse brain to be placed for the cutting. Glue is needed to adhere the filter paper to the cutting disk.

⚠ CRITICAL: Apply the glue indicated in the material section. Other adhesive material may interfere with the culturing of the brain slices.

g. Carefully place the cutting disk on top of the cutting table on the tissue chopper by tightly closing the two clips.
h. By using the pair of tweezers, take out the blade of the 70% EtOH container and gently dry it on a piece of paper towel.
i. Meanwhile, unscrew the blade holder and carefully insert the blade (Figure 3C).
j. Fix the blade horizontally in line with the blade holder and then tightly screw the holder.

2. Isolation of the brain from the mouse.

Note: Work fast but precise for the following steps. Always ensure proper cooling of the tissue and careful handling of such.

Note: If you decide to perfuse the brain, prepare everything needed to do so at this stage of the experiment. Continue after with the next step of the protocol.

a. Fill 5 mL of cold cutting solution in a 15 mL Falcon tube and place on ice. Isolate the brain from the mouse as described in the following steps.
b. After death confirmation of the animal, decapitate the mouse head at the base of the skull.
c. Cut the scalp from midline until the middle of the eyes.
d. Turn over the scalp to expose properly the skull and firmly fix the brain with the scalp.
e. Insert the delicate bone trimmer in the occipital condyle, stay in ventral part as much as possible and cut on right and left part to make extra space, to easily remove the occipital bone and intraparietal bone. At this stage, the brain stem and the cerebellum are exposed.
f. Insert the bone trimmer on each side along of the parietal bone and cut. Insert the trimmer along of the midline (pay attention to not insert it into the brain).
g. Cut with the premaxilla and nasal bone perpendicularly. Remove carefully the parietal and frontal bones of each side.
h. Extract the brain with a spoon, pay attention to the meninges and the chiasma optic.
i. Carefully transfer the brain into the 15 mL Falcon tube. Use one Falcon tube per brain.

3. Cutting of the mouse brain.

⚠ CRITICAL: Proceed with the cutting of the brain as soon as possible. To ensure a smooth cutting of the freshly isolated brains, do not store them longer than four hours before cutting and ensure continuous storage at +4°C. Otherwise, difficulties during the cutting process may occur, including adhesion of the tissue to the blade or even sticking of the tissue slices to each other.

Note: The longer the brains are kept unprocessed, the greater is the quality loss of the cut brain slices. Brains that were isolated more than four hours prior to starting the cutting process may no longer be usable to cut the tissue into slices.

a. Place the dissected mouse brain in the Falcon tube stored on ice under the BSCII.
b. Place the petri dish on ice and fill it with 10 mL of the ice-cold cutting solution.
c. Transfer the mouse brain into this petri dish.
d. Immediately after, use the tweezers and carefully transfer the brain onto the filter paper on top of the cutting disk, with the olfactory bulb directly under the blade (Figures 4A–4C).

⚠ CRITICAL: Do not over-dry the brain; ensure tissue moistening by adding two-three drops of ice-cold cutting solution on top of the brain. Too much cutting solution may lead to wet brain tissue adhering to the blade during cutting. Once you placed the brain on the filter paper, do not move it anymore.

Note: Adjust the position of the cutting disk by horizontally moving the table release lever (Figure 2, item C). The positioning of the blade can be adjusted using the blade holder and its screw (Figure 3C).

e. Ensure that the blade is in perpendicular position to the brain (Figure 4D), you can still adjust the position by turning the cutting table.

Note: For the scope of this protocol, we only cut the brain in coronal orientation. This cutting orientation comes with the advantage of easy handling of the brain to bring it in the correct position for the cutting process. Moreover, for downstream analysis of tissue from *in vivo* experiments, we cut the respective tissue in the same fashion. We thus did not test cutting of the brain in axial or sagittal orientation.

⚠ CRITICAL: Proceed to cutting fast, since the increasing temperature of the mouse brain tissue will strongly affect the cutting efficiency.

f. Once tissue position is correctly adjusted, flip the On/Off switch to "On" and start cutting the brain into 400 μm thin slices. Visually supervise the cutting process and hold it if necessary by flipping the reset switch (Figure 2, item G).

Note: See Methods videos S1, S2, and S3 for an efficient cutting process, see Methods video S4 for a compromised cutting procedure leading to inadequate slice quality after half of the brain was cut (Methods videos S1, S2, S3, and S4).

⚠ CRITICAL: If brain slices start attaching to the blade, immediately stop the cutting process to release the slice from the blade. This is very crucial as otherwise, the attached tissue slice will negatively affect the quality of your further cutting, see Troubleshooting 1.

Note: Generally speaking, one can state that the longer the brain stays on top of the cutting disk, so the longer the cutting process lasts, the more the temperature increases in the tissue. Cold tissue is very rigid and can be cut without great difficulty. The warmer the tissue becomes, the sticker it gets. Thus, it can also be challenging to restart the cutting after having paused the process (Troubleshooting 2).

g. Cut the brain entirely to reach approximately ten brain slices.

Note: Only brain slices with visible corpus callosum (white matter) can be used for injection of the cells (Figure 5E). This tissue structure has been defined in terms of technical reasons to meet the same criteria as those set for our *in vivo* experiments. Likewise, one thereby ensures that all brain tissue slices used for cell injection retain the same morphological structures and can thus be compared to each other.

Note: We recommend to use ten brain slices as technical replicates per experimental condition for cell injection in step 11. The slices do not necessarily have to come from the same mouse. In our experiments, we processed several mouse brains subsequently and afterwards mixed the conditions over the different mice.

⚠ CRITICAL: Anticipate approximately 10–30% loss of brain slices during the procedure, and thus prepare excess tissue slices for the injection of the tumor cells. You may lose some tissue slices during the cutting procedure due to unequal cutting, where after some slices may end up with disrupted tissue parts (see Figure 5E, indicated with red arrows). The percentage of loss strongly depends on the quality (the time they stay uncut

after isolation from the animal) of the mouse brains and the experience in handling tissue during the cutting process.

h. Unlock the clips on the cutting disk to loosen the filter paper and the cutting disk.
i. Carefully transfer the cutting disk together with the cut brain on the filter paper or the brain solely into the petri dish filled with cutting solution (Figure 5A).
j. Carefully disassemble the cut filter paper stripes. It will allow to gently separate the single brain slices (Figures 5B and 5C). See Troubleshooting 3 for other means to disassemble the cut brain into single tissue slices.

Note: Alternatively, using tweezers, carefully grab the pack of brains slices – they still tightly stick together at this point- and transfer the brain into the cutting solution. Be aware of the increasing risk of damaging the tissue once touching it with the tweezers.

⚠ CRITICAL: Avoid damaging the thin tissue slices. Select the slices that still maintain all essential brain structures needed for the respective type of experiment, in our case we selected only those slices with the corpus callosum clearly visible (Figure 5E). Ensure that the tissue slice is still intact as a whole.

k. Place transwell chambers into the wells of a 6-well tissue culture plate by hanging them each inside one single well.

Note: In our hands, maximum two brain slices can be placed per chamber for optimal follow-up experimental procedures.

l. Using the flat spatula, carefully lift one brain slice after the other and transfer them to the transwell chambers. To place brain slices correctly in the transwell, tilt the spatula to one side, allowing the brain to slowly slip onto the membrane of the transwell chamber. If possible, place both brain slices in the same direction, for ease of orientation in subsequent steps, especially during the cell injection.

Note: Creating soft turbulences in the cutting solution with the spatula (Figure 5F) may help lifting the brain slice onto the spatula.

⚠ CRITICAL: Verify that the brain slice is placed entirely flat on the membrane; any folding of the slice will impede further experiments (Figure 5E). Avoid to no longer touch the slice with the spatula since once the slice is being put on the membrane without any liquid present, it is very fragile. Rather try to unfold it by softly flushing it with some brain slice medium.

Note: The two slices placed in the same chamber should not touch each other (Figures 5D and 5E).

m. Using a pipette, gently remove the cutting solution, which may have accumulated on top of the transwell membrane during the transfer of the brain slices.
n. Transfer 1000 µL of the pre-warmed brain slice medium into the well of the 6 well plate, right below the transwell chamber.

Note: As the chamber is hanging quite deeply in the well, the brain slices will be in direct contact with the brain slice medium. They will not be fully submerged into the medium, as the air liquid interface- which is the standard technique for culture of brain slices- is still maintained. The bottom of the transwell chamber membrane is in contact with the culture medium, allowing nutrients and gases to diffuse upwards. The upper surface of the brain slices is exposed to the air, facilitating better oxygenation.

o. In order to prevent evaporation of the medium, fill the space between the wells with 10 mL of sterile H_2O.
p. Close the plate with its lid and incubate for 18–24 h at 37°C, 5% CO_2 in a humidified classical incubator.

Note: If you continue the cutting process with another brain, use a fresh sterile blade and a fresh piece of sterile filter paper.

Preparation of ECM-tumor cell suspension

Timing: 50 min

This major step accomplishes the preparation of the ECM-cell suspension for injection of the respective tumor cells into the mouse brain slice. We recommend to prepare sufficient cells needed for ten brain slices as technical replicates per experimental condition, with the aim of injecting exactly 1 μL of cell suspension, containing around 2×10^4–5×10^4 cells, per brain slice.

4. Place a box of sterile pipette tips (1–10 μL) at +4°C. Defrost ECM aliquot(s) at +4°C prior the experiment.

Note: Per injection, you will need 1 μL of liquid ECM. Use cold pipette tips for injection of the cells into the brain slices (in step 11) to ensure that the ECM remains liquid prior integration into the tissue. The ECM remains in a liquid state at −20°C, and solidifies as soon as temperature reaches temperatures greater than +4°C.

5. Passage the cells following the dissociation protocol applied regularly per specific tumor cell culture. Count tumor cells to assess their concentration and viability. Aim at cell viability greater than 90%.

Note: The standard protocol is designed for injection of single cells. 3D structures such as spheroids and organoids can also be injected. Feasibility may depend on the size of the 3D cultures and should be tested empirically. Specific testing of Hamilton syringes, plastic tips or glass pipetted is advised.[4] ECM can be avoided, though an additional caution is necessary to retain tumor cells inside the brain slice structure.

⚠ CRITICAL: It is crucial to inject the same number of viable cells per condition that will be compared (Troubleshooting 4).

⚠ CRITICAL: 2×10^4–5×10^4 cells are recommended per injection into one tissue slice. The exact cell number needs to be established for each cell culture depending on the inherent proliferative and invasive properties of the cells, i.e. highly invasive or highly proliferative cells may require fewer cells.

Note: In our case, we empirically determined to inject 5×10^4 cells per brain slice for LN-229 cells. Injection of too few cells into the brain slice may result in tumor cells not properly growing into the tissue due to missing cell-cell contacts. A very high cell number (> 5×10^5 cells) may be difficult to resuspend in 1 μL and injection of such a dense cell suspension can result in improper implantation.

6. Prepare one cell suspension for all technical replicates. Take into account dead volumes during pipetting and prepare excess of single cell solution. e.g., for 20 injections, transfer 1.1×10^6 LN-299 cells in a sterile 1.5 mL Eppendorf tube (for 5×10^4 cells per brain slice).

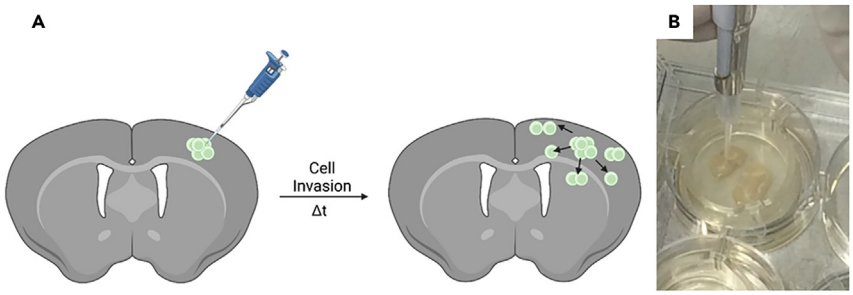

Figure 6. Injection of cells into the mouse brain tissue slice

(A) Schematic of injection of fluorescently labeled cells into the mouse brain slice (left) and monitoring of cell invasion into the brain tissue over time (right). Figure created with BioRender.com.

(B) Picture taken during injection of cells into a mouse brain slice placed in a transwell chamber.

7. Centrifuge the tubes containing single cells for 3 min at 300 × *g* at 22°C. Discard the supernatant as completely as possible. Ideally, aspirate the remaining supernatant using a 10–200 μL pipette.

⚠ CRITICAL: All material applied in the follow-up steps should be pre-cooled, ECM should be defrosted at +4°C. Work fast but precise in the next steps and ensure proper cooling of the ECM.

Note: Verify whether the pure ECM is well homogenized, resuspend on ice without creating air bubbles.

8. Resuspend the prepared cell pellet in pure ice-cold ECM to reach 1 μL per desired cell number per one brain slice. e.g., for planned 20 injections, carefully resuspend the cell pellet in 20 μL of ECM on ice. Keep the mixture on ice until the injection.

Injection of cells into the mouse brain slice

Timing: 20 min per injection

In this step, you will inject the tumor cells of interest in the mouse brain slice using the beforehand prepared solution of cells mixed with liquid ECM.

9. Take out the 6-well cell culture plate harboring the transwell chambers with the mouse brain slices from the incubator and place it on a dark surface.

Note: For better visualization of the brain slice structures by eye, we utilized a black mouse pad wiped with 70% EtOH and tissue paper on the surface and placed it underneath the tissue culture plate.

Note: Intactness of the tissue is crucial for successful implantation of the cells. As described by Eisemann et al.,[4] do neither dehydrate nor excessively immerse the tissue on brain slice media during punching the tissue with the pipette tips (step 11). In our hands, incubating the freshly cut brain slices in 1000 μL of brain slice medium (step n) for 24 h worked well for subsequent injection of the cells.

Note: However, if necrosis or any other degeneration of the tissue can be observed after 24 h of incubation, the respective mouse brain slice cannot be used for subsequent cell injection. We advise to exclude this slice from the experiment.

10. Using a 1–10 μL pipette (and the pre-cooled pipette tips, see step 4), aspirate 1 μL of the ECM-cell mixture. Ensure that the ECM-cell mixture is well homogenized before finally taking of the 1 μL volume needed for cell injection.
11. With the cone of the pipette tip, punch a small hole in the brain tissue, in the cortex, above the corpus callosum (Figures 6A and 6B) and inject the 1 μL while slowly releasing the pipette tip from the mouse brain tissue.

⚠ CRITICAL: Ensure that the pipette tip is inserted to a depth that reaches the target area without penetrating too deeply. During the injection you will feel slight resistance, indicating that the pipette tip reached inside the tissue. If you do not feel this resistance, it means you are injecting at the tissue surface, which may result in many single cells being left on top of the tissue.

Note: If the pipette tip punctures through the brain slice, it can cause excessive damage and affect the accuracy of the injection. Monitor the resistance felt during insertion. A sudden loss of resistance may indicate that the pipette tip has punctured through the tissue.

Note: Try to punch a hole as small as possible into the tissue, to be just about to smoothly inject the cells into the tissue without damaging the tissue. Tissue slices with bigger punching holes can still be used to downstream analysis, as long as the tissue does not start to degenerate from this step onwards.

Note: It is essential to release the pipette tip from the mouse tissue while injecting the cell suspension, to ensure that the cells remain in the tissue.

Note: Due to pre-existing procedures for potential subsequent *in vivo* experiments, we limited the injection of cells to the cortex and did not expand it to other parts of the brain. Importantly, you need to keep in mind that behavior of invasion may differ in between parts of the brain where you inject the cells due to different microenvironments inside the mouse brain.

12. Immediately after having injected the ECM-cell mixture into a single brain slice, verify whether the cells were injected into the mouse brain tissue by using a fluorescent microscope.

Note: If encountering difficulties to directly inject the cells into the tissue, see Troubleshooting 5 to instantly respond to an imprecise cell injection.

13. Once all injections are finalized, cover the 6-well plate with the lid and incubate the plate with all brain slices for 4 h at 37°C, 5% CO_2 in a humidified incubator.

Monitoring and treatment of cells integrating into the mouse brain tissue

Timing: Up to 10 days

In this step of the protocol, integration and motility of injected tumor cells inside the mouse brain tissue will be monitored by fluorescence microscopy. Desired treatment(s) will be applied and mouse brain tissue slices will be maintained for up to ten days. A schematic overview shown in Figure 7B summarizes the up to this point executed steps.

14. After 4 h of incubation, verify the brain slices again at a fluorescent microscope. These images will represent the state of the brain slices before adding any treatment to their media (t = 0).

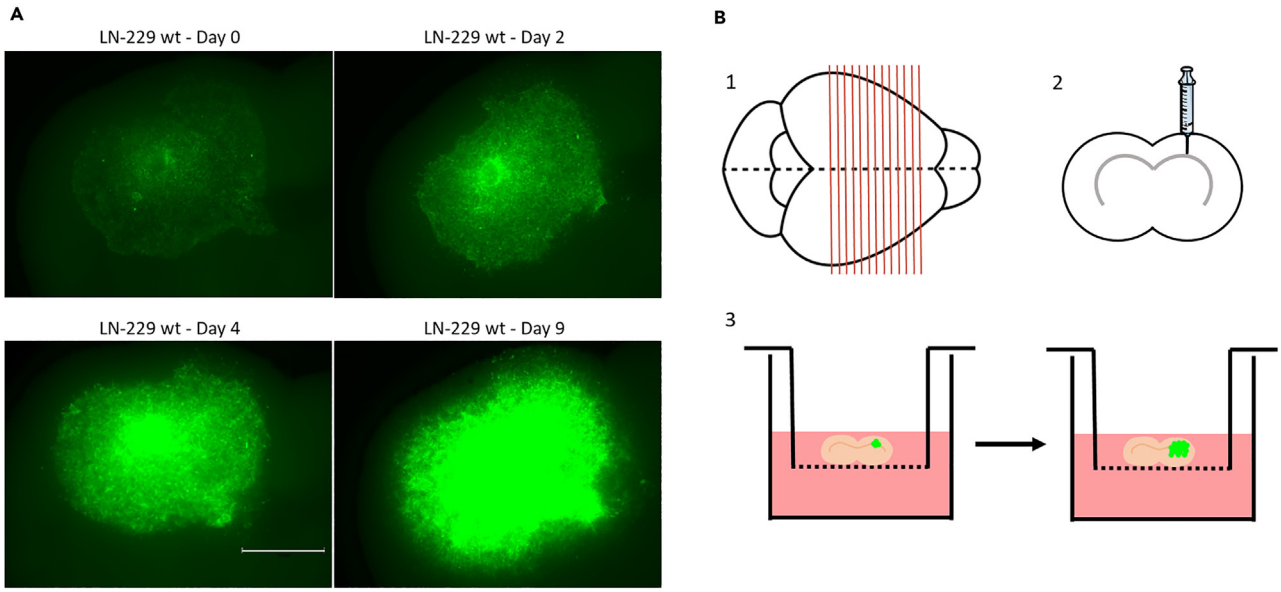

Figure 7. GFP positive cells integrated in brain slice

(A) Representative images of brain slice after injection of GFP-positive GBM LN-229 wt cells during 9 days of culture. Increased GFP signal over time and GFP-positive area indicate continuous proliferation and invasion of tumor cells. Signal at Day 7 and Day 9 is already at the saturation level (scale bar: 1550 μm). Images were taken with an upright epifluorescent microscope.

(B) Schematic overview of *ex vivo* mouse brain slice culture starting from 1; the process of cutting a brain into slices, 2; the injection of cells into the brain slice and 3; the invasion and thus colonization of injected cells into the mouse brain slice placed in a transwell chamber. Figure created with BioRender.com.

Note: Capture one image per brain slice. Image the slice in the respective fluorescence channel, as well as in the bright-field mode. Choose one magnification, set the focus accordingly and record these settings for further imaging.

⚠ CRITICAL: If you observe an increased background fluorescence in the brain slices, presumably originating from remaining blood, perfusion of the brain to remove circulating blood in the blood vessels prior to the mouse sacrifice is recommended, see Troubleshooting 6.

15. Administer desired treatment.

Note: Chemical treatments can be directly applied in the culture medium or directly into the tumor.

   a. Pre-warm the required volume of brain slice medium, supplement it with the desired treatment.
   b. Fill the wells of the culture plate harboring the brain slices with 1 mL of the provided medium.

16. Determine empirically the start of your treatment, considering the growth and invasion characteristics of your tumor cell lines.

Note: Depending on the type of study, you may consider administering the treatment of choice at later time points. In our study, we administered the treatment to the brain slice medium four hours after the cell injection since we aimed to study the effect of the treatment on early stages of invasion.

17. 48 h post injection, remove the culture medium from below the brain slices by soft aspiration.
18. Directly fill the wells of the culture plate harboring the brain slices with 1 mL of fresh pre-warmed brain slice medium, including the required treatment(s) if needed.

19. Verify the brain slices under the fluorescent microscope and confirm the presence and invasion status of tumor cells. Record fluorescence and brightfield applying the same settings as on t = 0 (Figure 7A and Methods video S7). Record the respective time point, the number or label of the brain slice and the scale.
20. Repeat step 17–19 every 48 h to reassure that the injected cells are viable and your treatment(s) still potent. In case of a reduction in tumor cell number or viability, see Troubleshooting 7.
21. Continue the experiment for maximum of seven to ten days at 37°C. Determination of the experiment's endpoint should be empirically tested taking into account the invasive capacity of the injected cells and the administered treatment and/or conditions.

Note: Out of the ten brain slices we used to inject tumor cells per experimental condition, generally we were able to finally analyze eight slices. On average 20% of the brain slices had to be excluded from the final analysis, which was mainly due to problems during cell injection into the brain slice.

⚠ CRITICAL: More detailed explained, the release of cells from the pipette tip during injection ending up below or on top of the tissue and starting to grow on the outer cell layer of the tissue slice instead of inside the brain tissue will exclude the slices from any further analysis. Tissue slices wherein the tissue became necrotic during the experiment need to be excluded from such as well.

22. At the endpoint of the experiment, in the respective case Day 10 of the brain slice incubation, image the brain slices in the bright-field and green fluorescent channel (488 nm) taking pictures every 2 h, ideally for the time course of 24 h.

Note: These images of the brain slices taken every two hours will be required to analyze the velocity of the cells in step 32. Your image set will then consist of 12 pictures per brain slice.

Note: We imaged the brain slices for later analysis using the IncuCyte microscope. However, we believe that the repeated imaging every two hours is also possible with another microscope. Using the IncuCyte live imaging system comes along with the advantage of CO_2 (5%) and temperature (37°C) being controlled throughout the experiment. In this case, one can leave the brain slices in the machine during imaging.

Note: If using another microscope, one may have to transport the well plate containing the brain slices in between the standard incubator and the microscope. Thus it may be difficult and laborious in finding back the area (and the focus) of interest to always track the same cell. Acquisition was done using the 4x objective.

Optional: If possible, live cell imaging should be planned during the experimental procedure to evaluate single cell velocity. We performed live imaging for 24 h at the end point of the experiment (Day 10 of the brain slice incubation). Settings included imaging in the bright-field and the green channel (488 nm), using the 4x objective with pictures taken every two hours.

Note: Saturation of the fluorescent signal of the colonized area should be avoided by adjusting the appropriate incubation time of the brain slices after cell injection. The incubation of such might be stopped shortly before reaching any saturation in the fluorescent signal.

Note: Nonetheless, for later analysis of the colonized area, the intensity of the fluorescent signal will not be taken into account. In our case, rather the entire green fluorescent area was measured, independently of any saturation. Saturation of the fluorescent signal at the endpoint may rather be taken as a mean to assess and confirm the length in days for the incubation of the brain slices.

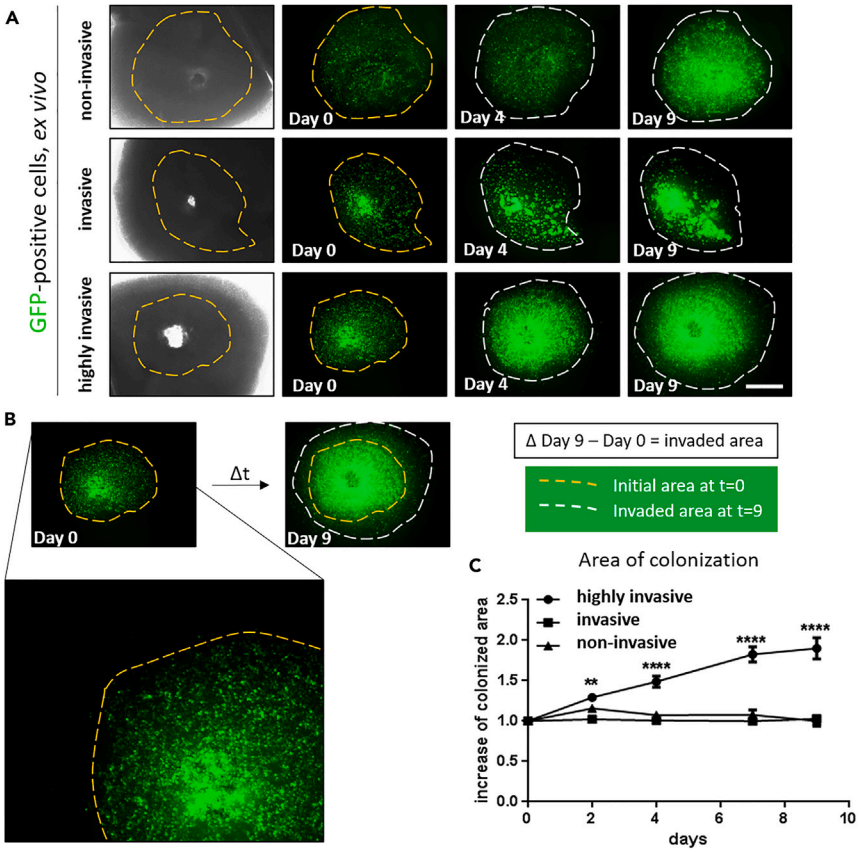

Figure 8. Representative pictures of GBM cells in *ex vivo* brain slices with their area of colonization

(A) The area of colonization of fluorescently labeled GBM cells is shown over time (9 days after injection): Three different cell lines were analyzed and classified into non-invasive, invasive and highly invasive cells based on the measured area of colonization (scale bar 1000 μm).

(B) The area of colonization (outlined with dotted white lines in the representative images) was determined using ImageJ and is represented in the graph. Images in A and B were taken with an upright epifluorescent microscope.

(C) Quantification of increase of colonized area of GBM stem-like cells in *ex vivo* brain slice cultures 9 days after tumor implantation (n = 10), displayed as average ± SEM. Modified from Schuster et al., Nat. Com, 2018.[2]

Quantification and statistical analysis

Here we present two possible strategies to quantify tumor growth as well as migration and invasion characteristics of tumor cells inside mouse brain tissue. The first analysis aims at the measurement of the entire area of tumor cell colonization taking into account all cells that were injected into the mouse brain (Methods video S7). The second quantification focuses on tracking single cells and thus comprises the measurement of individual cell velocity (Methods videos S8, S9, S10, and S11). In our case, ImageJ software was used for image processing.

Area of colonization

To assess the general area of colonization by tumor cells, measure the area of tumor growth over time. A comprehensive exemplary result of such analysis for invasion of GBM cells is shown in Figures 8A–8C. Consider a potential impact of tumor cell proliferation over time. By acquiring images of the brain slices every 48 h and measuring the colonized area in ImageJ, it has to be kept in mind that not only invading cells are analyzed, but also proliferating cells, see Troubleshooting 8.

23. Transfer the images taken of the brain slices for all time points (these should include t = 0, t = 48 h, t = 96 h,…, t = endpoint) to one folder.

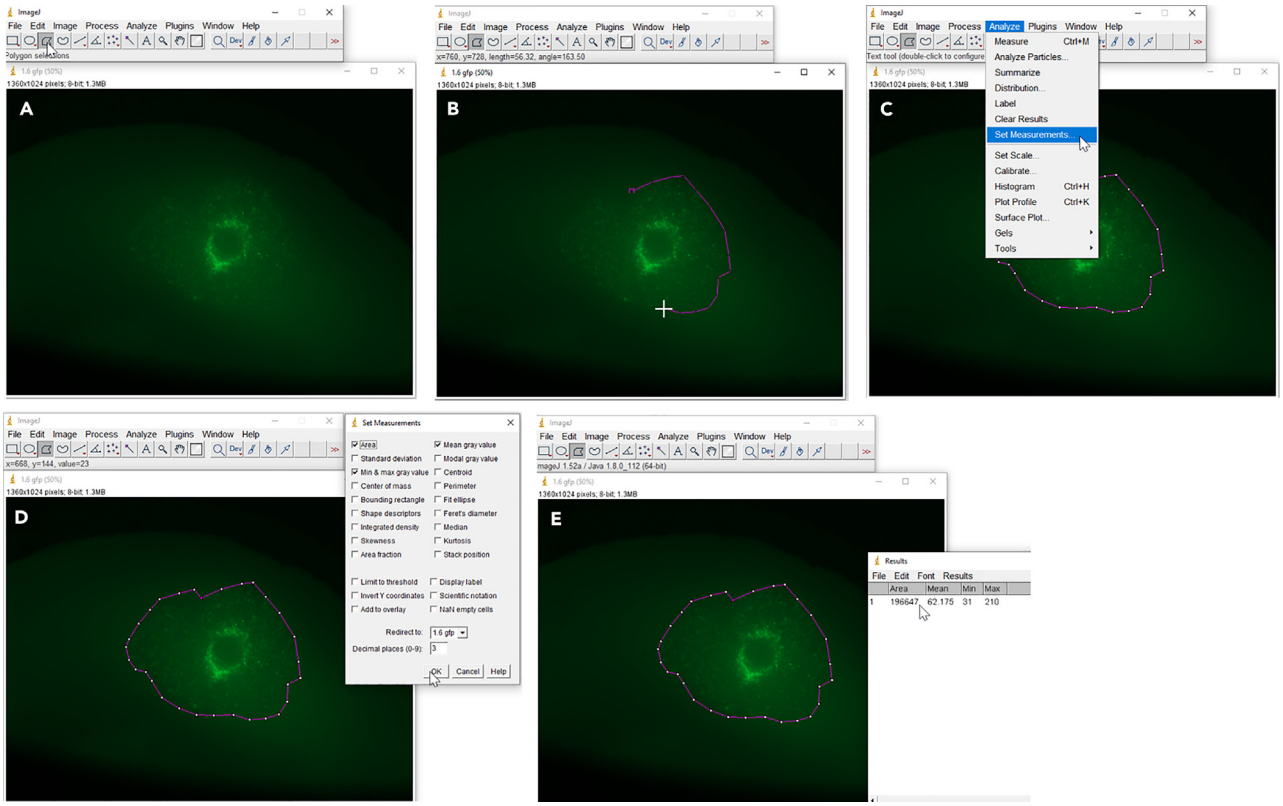

Figure 9. Steps of ImageJ analysis of exemplary brain slice microscopy images to measure the area of cell invasion

(A) Selection of polygon tool to manually start edging the colonized area (B).

(C and D) Two options are displayed to execute the measurement of the encircled area.

(E) Results window shows the quantification of the measured area.

24. Open the image of t = 0 in the ImageJ software and select the polygon tool (Figure 9A).
25. Edge the colonized area, which is the region where the fluorescent cells accumulated within the tissue slice (Figure 9B).
26. Once completed, press CTRL+M to measure the encircled area (Figure 9C).

Note: Alternatively, you can also navigate to "analyze", then "set measurements" and thus select "area", redirect it to the image to be analyzed and confirm by selecting "ok" (Figure 9D).

27. Proceed with the later time point images one after the other. To do so, open the image of the next time point, and again edge manually the colonized area.
28. Once all images have been analyzed with the polygon encircled area, copy the quantification of the measured area being displayed in the results window (Figure 9E) and paste the values in an Excel file.
29. Normalize all values to time point 0 (t = 0) as ratio, by calculating the fold change between t = 0 and any subsequent measurement.
30. Once you analyzed all images, select CTRL+W to close the windows in ImageJ.
31. You can depict the data as a barplot (Figure 10B) and by representative pictures of the edged colonized area (Figure 10A).

Tumor cell velocity

Assessing the velocity of a single cell enables detailed investigation of the process of migration and invasion summarized as the motility at the single cell level without a possible bias linked to the proliferation of the cell(s). Tumor cell velocity can be assessed with ImageJ, analyzing at least 15 randomly selected single cells per condition and ten technical replicates per cell line (LN-229 sh*SCR*,

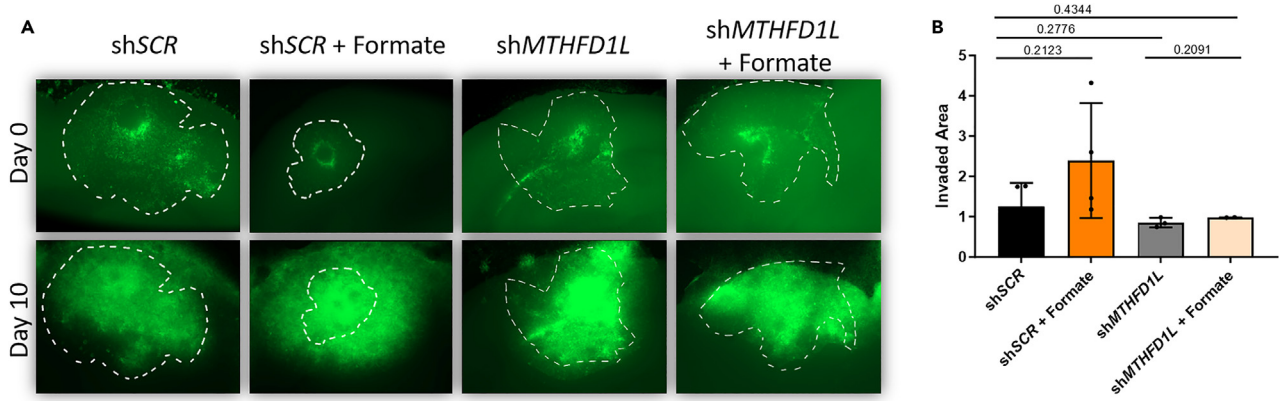

Figure 10. Brain slices imaged after injection of LN-229 sh*SCR* and LN-229 sh*MTHFD1L*[1] cells and respective treatment with 500 μM of sodium formate (Day 0) and following 10 days of incubation (Day 10)

(A) The area of green fluorescent labeled cells was encircled (with white dotted lines) for every condition at Day 0 and the same border was overlaid for the images taken at Day 10. This enables to easily visualize the area of colonized cells throughout the incubation from Day 0 to Day 10. Images were taken with an upright epifluorescent microscope.

(B) Representation of the area of colonized cells over time (numeric analysis). Dots represent biological replicates of independent experiments ± SEM.

LN-229 sh*MTHFD1L*[1]). For random selection of the single cells, consider them not touching the border region of the brain slice, their level of fluorescence being sufficient for subsequent microscopy analysis and the selected cells remaining in the field of view during the course of the analysis. Take images accordingly and save these in an ImageJ compatible format (8-bit).

32. Export the respective image set from the IncuCyte software, as explained in the specific instrument manual (https://www.sartorius.com/en/products/live-cell-imaging-analysis/live-cell-analysis-software).

Note: Based on the IncuCyte scan pattern set to two hours, our image set consisted of 12 pictures per brain slice.

33. To determine the velocity of the cells, the ImageJ software plugin MTrackJ, an ImageJ Plugin for Motion Tracking and Analysis, is required and can be freely downloaded from https://imagescience.org/meijering/software/mtrackj/.
34. Download the plugin "MTrackJ" and install it using the command Ctrl+Shift+M in ImageJ.
35. Once completed, open the IncuCyte software and select relevant images.
36. Start with one experimental condition and select the first brain slice.
37. Once completed, select "image set" and introduce an ID for the images to be exported.
38. Export the images in a .tiff file and subsequently open them in the ImageJ software.
39. Select "analyze", then "set scale" and another window will pop up.
40. Set the parameters for "the distance in pixels" to "1", the "known distance" to "3.5" and the "unit of length" to "μm" (Figure 11A). Concluding, 1 pixel corresponds to a distance of 3.5 μm, a scale that will be applied to any future measurements in this type of analysis.

Note: Theses dimension parameters (in pixels) depend on the IncuCyte instrument version (or on the respective instruments if other microscopes are used for this type of analysis). In every situation, you will have to perform a setting up calibration in ImageJ first, that converts the initial pixel measurement into meaningful measuring units.

41. Tick the box "global" and confirm the settings by selecting "ok" (Figure 11A).
42. Navigate to "images", scroll to "stacks" and select "images to stack" (Figure 11B). In another window, you can name your stack.

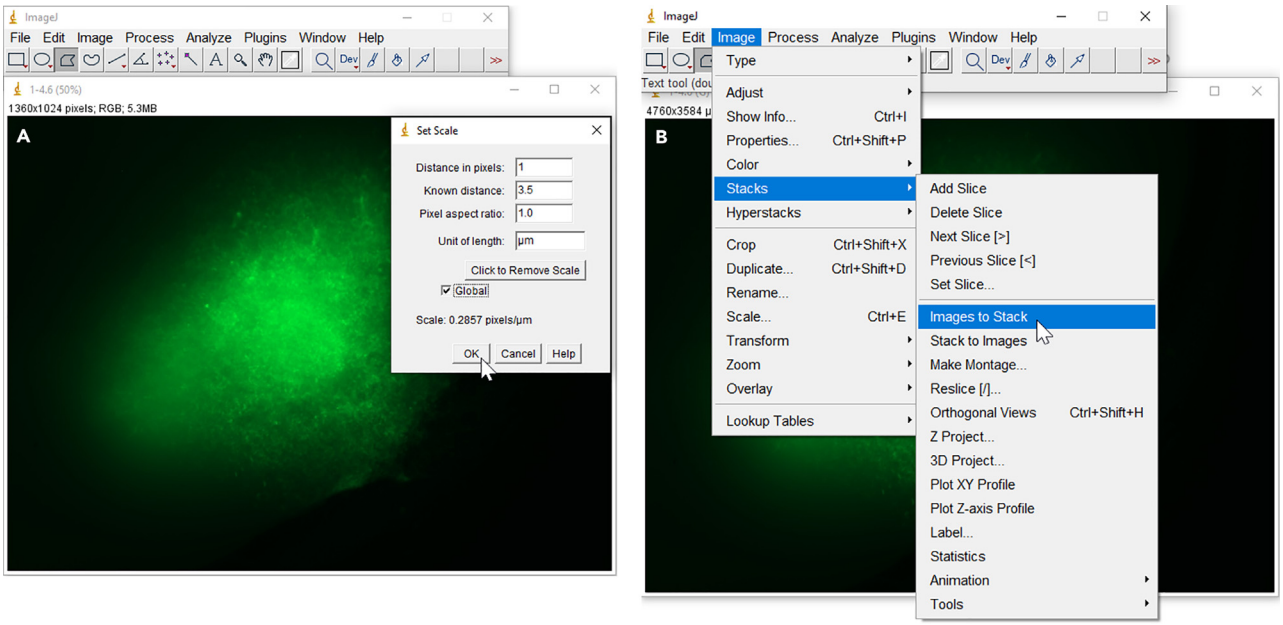

Figure 11. First steps including parameter settings for analysis of cell velocity in ImageJ
ImageJ settings for (A)"Set scale" and (B)"Images to Stack".

Note: Other live-cell imaging setups may be used as well to perform the described analysis. A major requirement is the recording of an identical part of the brain slice during 24 h, so that you are able to monitor the same cells for every time point that you are going to analyze.

43. To measure the distance the cells moved over time, open the image stack and navigate to "Plugins" and therein select "MTrackJ".
44. Select "Add" and thus the button will light up in red meaning it is active to actually select cells (Figure 12A).
45. After having clicked centrally on a randomly selected cell, the image for the following time point will automatically appear where you then need to click on the same cell selected on the first image.
46. Repeat step 45 for all images from the stack (Figure 12A).
47. Once finalized, confirm your selection by clicking "Add" again and the button will change color from red to inactive black (Figure 12B).
48. Repeat step 44–47 for as many cells as you want to analyze.

Note: In our case, we analyzed 15 cells per brain slice (Methods videos S5 and S6).

Note: Ensure to always start with the first image of the stack for the analysis of the single cell velocity in order to start at the earliest time point of the cell's movement tracking.

49. After selecting all cells, select "Measure" and two further windows will open, MTrackJ: "Tracks" and MTrackJ: "Points" (Figure 12C).

Note: The "Tracks" window displays an overview of all individual cells that were selected for analysis. The other window, "Points", provides an overview of the respective selected cell (TID) in all images (PID) of the stack. Hereof, the values determined in µm for "x", "y" and "len" (final length) are needed for further analysis (Figures 12C and 12D).

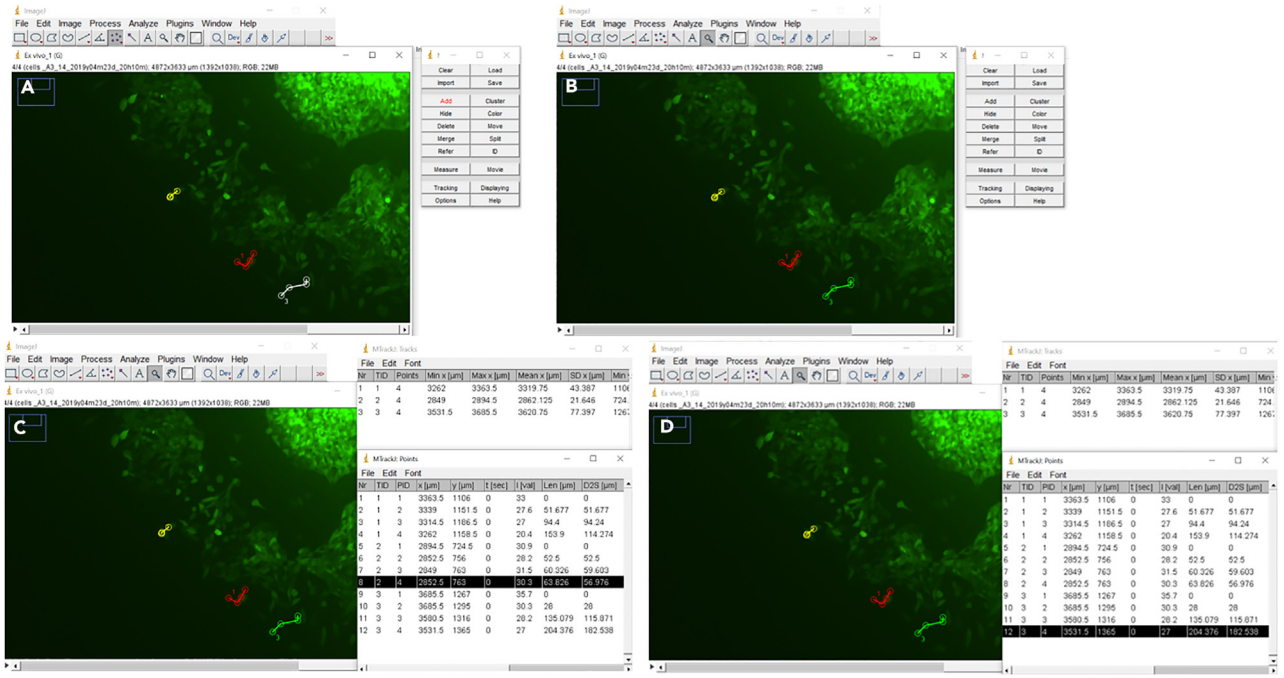

Figure 12. Overview of MTrackJ step by step analysis in ImageJ

(A and B) Tracking of single cells in image stack. Moving distance measured for (C) cell n°2 highlighted in yellow and (D) cell n° 3 highlighted in green.

Note: In order to graphically represent the **displacement of the cells in a bar plot**, values in column "Len [μm]" are needed. These values describe the distance one cell moved over time.

50. Copy the "Len [μm]" value at the end point of your live cell imaging (in our case it was 24 h, see step 22) into an excel file. These values summarize the cell's velocity.
51. Repeat step 50 for every single cell that you have selected in this brain slice.
52. In excel, calculate the average (the arithmetic mean) of the values for the length measured for each cell at time point 24 h.
53. In the same excel file, open another sheet and repeat step 35–52 for every imaged brain slice within that single experimental condition.
54. Open another sheet in the same excel file, copy paste all recently gained arithmetic mean values for the average length of 15 cells per brain slice and calculate their arithmetic mean (Figure 13B). Repeat this step for all brain slices in all tested experimental conditions (Figure 13D).

⚠ CRITICAL: If you plan to show the displacement of the cells in a scatter plot, do not close the MTrackJ: "Points" window. You will need to copy paste certain values from this window in step 58.

55. In addition to the arithmetic mean, also calculate the standard error by dividing the standard deviation of all values by the square root of the number of samples.
56. Finally, you can depict the mean moved distance (displacement of the cells) within one experimental condition, e.g., LN-299 sh*MTHFD1L*[1] (Figure 13A, right bar plot, green bar).
57. Repeat steps 35–56 to compare the displacement of the cells in all experimental conditions.

Note: In order to graphically represent the **displacement of the cells in a scatter plot**, values in column "x[μm]" and "y[μm]" are needed. These values describe the location of the individual cell in the respective image.

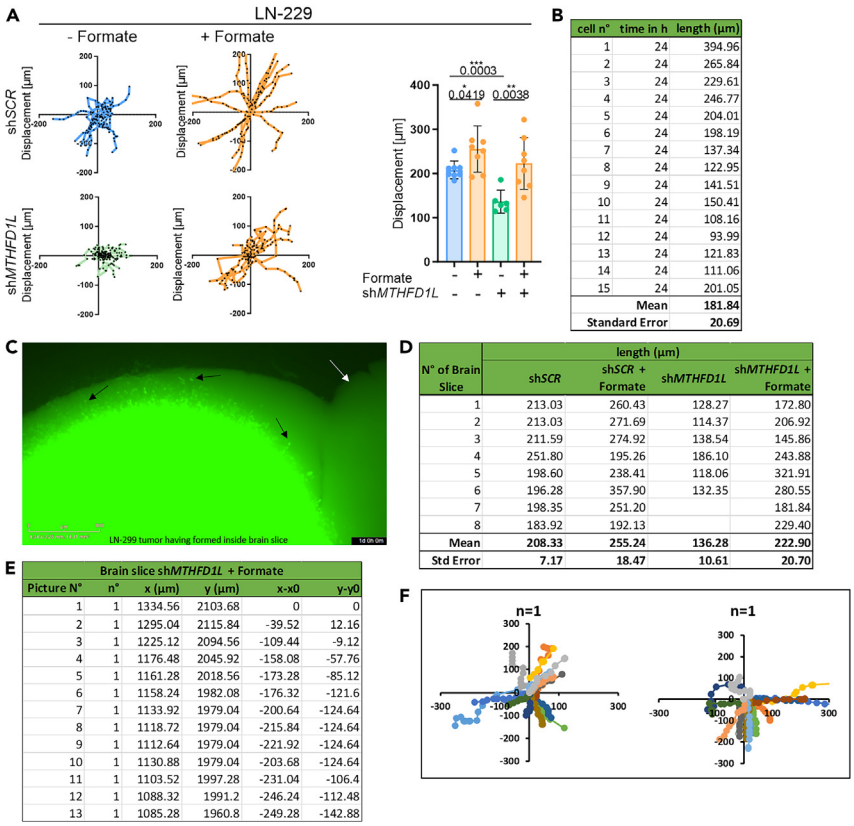

cell n°	time in h	length (µm)
1	24	394.96
2	24	265.84
3	24	229.61
4	24	246.77
5	24	204.01
6	24	198.19
7	24	137.34
8	24	122.95
9	24	141.51
10	24	150.41
11	24	108.16
12	24	93.99
13	24	121.83
14	24	111.06
15	24	201.05
	Mean	181.84
	Standard Error	20.69

N° of Brain Slice	length (µm)			
	shSCR	shSCR + Formate	shMTHFD1L	shMTHFD1L + Formate
1	213.03	260.43	128.27	172.80
2	213.03	271.69	114.37	206.92
3	211.59	274.92	138.54	145.86
4	251.80	195.26	186.10	243.88
5	198.60	238.41	118.06	321.91
6	196.28	357.90	132.35	280.55
7	198.35	251.20		181.84
8	183.92	192.13		229.40
Mean	208.33	255.24	136.28	222.90
Std Error	7.17	18.47	10.61	20.70

Brain slice shMTHFD1L + Formate					
Picture N°	n°	x (µm)	y (µm)	x-x0	y-y0
1	1	1334.56	2103.68	0	0
2	1	1295.04	2115.84	-39.52	12.16
3	1	1225.12	2094.56	-109.44	-9.12
4	1	1176.48	2045.92	-158.08	-57.76
5	1	1161.28	2018.56	-173.28	-85.12
6	1	1158.24	1982.08	-176.32	-121.6
7	1	1133.92	1979.04	-200.64	-124.64
8	1	1118.72	1979.04	-215.84	-124.64
9	1	1112.64	1979.04	-221.92	-124.64
10	1	1130.88	1979.04	-203.68	-124.64
11	1	1103.52	1997.28	-231.04	-106.4
12	1	1088.32	1991.2	-246.24	-112.48
13	1	1085.28	1960.8	-249.28	-142.88

Figure 13. Assessment of velocity of injected cells inside the mouse brain slice

(A) Displacement (in µm) (distance that cells moved) of LN-229 cells in regard to sh*SCR* vs. MTHFD1L KD cells +/− 500 µM of sodium formate. Each colored line shown in the scatter plot corresponds to the movement/displacement of one cell, with each dot showing the cell at the respective time point (every 2 h). Dots in the barplot represent mean displacement of 15 cells, n = 6–8, mean ± SEM; unpaired t-test with Welch's correction. Modified from Delbrouck et al., 2023, Cell Reports.[1]

(B) Average length (in µm) of 15 cells per brain slice and their arithmetic mean with standard deviation.

(C) Exemplary microscopy image showing bright green fluorescent LN-299 cells (exemplarily indicated by black arrows) moving inside the brain tissue (light green structure, indicated by white arrow). Image taken with IncuCyte live cell imaging system, scale bar 800 µm.

(D) Summary of the average length of monitored cells per brain slice over all experimental conditions. This table represents the raw data to depict the barplot in A.

(E) Summary of coordinates "x[µm]" and "y[µm]" for one single monitored cell in brain slice n°1 over 13 analyzed pictures. Travelled distance per image shown as values for $x\text{-}x_0$ and $y\text{-}y_0$.

(F) Displacement of monitored cells in a scatter plot. Each scatter plot shows the displacement of cells (individually colored in plot) in one brain slice (n = 1).

Note: In our experiment, we visualized the displacement of 15 analyzed LN-299 *shMTHFD1L*[1] cells per single brain slice, averaging eight individually analyzed brain slices (n = 8, except *shMTHFD1L* n = 6) as shown in Figure 13A on the left in green. Figure 13C represents exemplary microscopy image showing bright green fluorescent LN-299 cells (indicated by black arrows) moving inside the brain tissue.

58. Open another excel file and therein an additional sheet.
59. Copy paste the values resulting from the tracking of one single cell in the image from "x[µm]" and "y[µm]" into two separate columns (Figure 13E).
60. Annotate both coordinates x and y for the starting point from which the selected cell was shown to move as "0".

61. Individually subtract any later x and y coordinate respectively of this selected cell from the value at "0", so the starting position of the analyzed cell.
62. Repeat step 59–61 for every single cell monitored in the respective image set (brain slice).
63. You will end up with as many x-x_0 and y-y_0 values, as you analyzed pictures for each cell in the individual brain slice.
64. Use the values x-x_0 and y-y_0 resulting from every single cell tracking in the respective brain slice as data source to generate a scatter plot (Figure 13F).

EXPECTED OUTCOMES

The protocol allows for the assessment and quantification of cancer cell invasion in viable mouse brain slices. Monitoring of colonization of the injected tumor cells allows to characterize the process of cancer cell tumor growth and invasion in a more physiological environment compared to simple *in vitro* conditions. One rather straightforward readout of the assay focuses on the assessment of the area of colonized tumor cells. Since here the invasion area may be impacted by the proliferation rate of the tumor cells, the assessment of velocity of the single cells brings additional insights into the behavior of tumor cells in the brain. Importantly, the protocol allows to assess tumor growth and motility capacities of different cell cultures, including upon genetic engineering and treatment over several days at lower cost than *in vivo* experiments.

LIMITATIONS

The main limitation of the protocol is the need for a fluorescent labeling readout allowing to track viable tumor cells inside the mouse brain tissue structure. Injecting tumor cells without a fluorescent marker excludes follow-up over time by live-cell imaging and requires additional immunohistochemistry-based readouts at fixed time points. While assessment of the area of colonization can be performed with a basic fluorescence microscope, tracking single cells requires additional equipment allowing for live fluorescence imaging. Discrimination between tumor cell proliferation and invasion is challenging in certain tumor cell models, thus advanced single cell tracking may be required to distinguish between the two processes. Another main limitation of the protocol is the fact that with the described analysis, one cannot fully exclude that the cells being analyzed in the microscopy images and/or videos may be migrating on top or even underneath the tissue. We would here suggest a technique that will allow for acquisition of z stacks of the brain slices, to confirm the cells' integration into the mouse brain tissue. An additional limitation is linked to the finite viability of brain slices beyond 10–12 days in culture, which restricts protocols requiring longer treatment exposure times. To further assess the brain tumor structure and crosstalk with normal brain cells additional steps may involve paraffin-based fixation of the tissue followed by immunohistochemistry[4] or spatial omics-based assessment. Optionally, specific genetically engineered mice with fluorescently labeled cell populations may be applied as alternative. The co-cultures can also involve depletion and/or integration of other cell types e.g., immune cells that may integrate to brain slices over time.[5] Advanced cancer models such as tumor tissue fragments and organoids may be more difficult to integrate to brain slices *ex vivo*. Alternatively, *ex vivo* cultures can be obtained from brains with already developed xenografted tumor tissue. Since brain microenvironment is significantly altered in patient-derived orthotopic xenografts,[6,7] additional optimization of tissue cutting may be needed.

TROUBLESHOOTING

Problem 1

During the cutting process, the mouse brain tissue slices start attaching to the razor blade instead of quickly removing from the blade after being cut to remain as a whole cut brain together on the filter paper.

Potential solution

Immediately stop the cutting process to release the slice from the blade. To do so, take the tweezers and carefully remove the slice from the blade. If you manage to remove without inducing any damage to the tissue, you can still keep this slice for injection. Carefully transfer it into the Petri dish filled

with cutting solution to fully submerge it with liquid. However, if the tissue appears already damaged or with injured tissue structures, discard the respective slice. Clean off the blade from any remaining tissue using 70% EtOH and tissue paper. Verify if the brain is still in the correct position to the blade, by confirming the blade's perpendicular position to the brain. Flip the reset switch to continue with the cutting process.

Problem 2

You are facing difficulties during cutting due to the stickiness of the brain. After having stopped the cutting process within the cutting of a mouse brain, it may be difficult to restart the entire process, due to the stickiness of the tissue and the cut tissue slices.

Potential solution

To prevent difficulties to restart the process, rather focus on working with fresh mouse tissue. If you have access to additional mouse brains, proceed directly with a freshly isolated and ice-cold brain. Discard the part of the leftover brain that you will not use anymore. Keep in mind that the more time passes during the cutting of one mouse brain, the more the temperature inside the tissue increases. Such temperature increase will result in the tissue becoming stickier. Cutting of ice-cold brain tissue will be of advantage here, since the process will have to be stopped less times due to sticking of slices to the blade. If you do not have access to additional mouse brain material, you need to make a compromise in trying to use as much of the brain as you can. Make sure that the slices that you keep for further experimentation are free of any tissue damage and disrupted tissue parts.

Problem 3

You are facing difficulties during the disassembling of the single tissue slices from the cut brain and the slices do not detach when removing the single filter paper stripes.

Potential solution

Depending on personal preferences, use the tweezers, the flat spatula or two brushes and carefully separate the cut slices from each other (Figures 5B and 5C). When using tweezers, detach brain slices one by one from the whole brain using the tweezers (preferred option). When using the spatula or the two brushes, carefully "peel off" the slices from the brain. Use some magnifying glasses to ensure precise movements. It may also be helpful to use one pair of tweezers to fix the filter paper and the other pair or the flat spatula to separate the brain slices. Be extremely careful not to damage the thin tissue slices. Only keep and further process the slices that still maintain all essential structures. Ensure that the tissue slice is still intact as a whole.

Problem 4

The injection of an exact amount of cells in a rather small volume of 1 μL in ECM is challenging since you need to be sure to precisely release all cell solution from the pipette tip.

Potential solution

To ensure that the same cell number is injected, the cells of the remaining aliquot of all injections can be counted to see if the content of cells was correct. Furthermore, once having injected the 1 μL suspension containing the cells, verify that the pipette tip does not retain any liquid. If still the case, you may try other pipetting methods such as reverse pipetting to release the volume of 1 μL precisely.

Problem 5

It may be difficult to precisely inject all cells resuspended in the very small volume of 1 μL into the brain slice tissue, without encountering cells being released below or on top of the tissue. This step is very crucial to the entire protocol, since it will limit the risk of encountering false results due to cells growing on top or below the tissue slice resulting in incomparable replicates between different experimental conditions. Moreover, partial integration of cells into the brain tissue needs to be prevented.

Potential solution

To ensure that the cells are appropriately injected into the tissue and do not end up on top or below the tissue slice, ensure that once the pipette tip has punched a hole in the tissue, at the same time you release the cell suspension from the pipette tip and simultaneously you also carefully but immediately remove the pipette tip horizontally from the tissue. In case of ending up with a brain slice where cells were not completely injected into the brain slice tissue, try to remove those cells from above or below the brain with a pipette tip. You may also try to carefully flush the tissue slice with brain slice medium in order to rinse off the cells on or below the tissue. This can be considered as a washing step. Fully aspirate this medium afterwards. It may be advised to always ensure complete tissue integrity being a crucial prerequisite for correct injection of the cells. Another very helpful verification step before cell injection comprises assessment of the physical depth of the tissue slice. To do so, completely penetrate the tissue with an empty pipette tip to get a feeling of the actual thickness of the tissue. This will allow you to improve cell injection into the tissue slice.

Problem 6

Brain tissue generally presents high autofluorescence, which can be further augmented by the blood retained in the blood vessels. Thus, if fluorescent tagging of tumor cells is low or the baseline autofluorescence of the cells is rather high, it may be difficult to precisely define the area of colonization and track single cells to determine the cells' velocity. The increased background may introduce an error in the downstream image analysis and needs to be reduced.

Potential solution

Instead of directly euthanizing the mice by cervical dislocation, first perfuse the heart of the mice using at least 10 mL of ice-cold 1x PBS. Perfusion with PBS removes blood from the blood vessel in the brain, which may decrease the overall autofluorescence of the brain tissue. Importantly, only authorized personal is allowed to perform perfusion and this procedure requires terminal anesthesia. Thereafter you can isolate the brain and pursue with the cutting. This step of perfusion reduces the risk for encountering high background during fluorescence microscopy. Another alternative of reducing the background fluorescence in the brain slice may be to prolong the incubation time of the freshly cut tissue, currently set to 18–24 h (step p), in order to allow more time for passive diffusion of the blood from the tissue into the surrounding medium. Since in our setting, the incubation time of 18–24 h worked well with the cell line we used and the subsequent analysis, we did not further investigate longer incubation times in the scope of this protocol. Optionally, you can apply fixation of the brain slice tissue[4] or even enhance quality of the fluorescence microscopy images by clearance of the tissue as described by Eisemann et al., 2018.[4]

Problem 7

You are observing that the injected cells and/or your freshly isolated brain slices at the time or even at a later stage after injection of the cells do not retain their expected viability or morphology. This means that your brain slices and the injected cells do not tolerate the above described brain slice medium.

Potential solution

Test survival of tumor cells in the brain slice medium prior injection into the brain slices. You can test the survival of the tumor cells in the respective culture medium by mean of proliferation assays. Alternatively, you can also use the modified brain slice medium, a 1:1 mixture of Hibernate A-medium (Thermo Fisher Scientific, Cat. No. A1247501), 20% BIT-100 (Provitro, Cat. no. 2043100), 100 U/mL of Pen/Strep and DMEM-F12 (Thermo Fisher Scientific, Cat. no. 11320033), 20% BIT-100, 100 U/mL of Pen/Strep, 200 mM L-glutamine (Thermo Fisher Scientific, Cat. no. 25030081), 1 U/mL of heparin (Sigma, Cat.no. H3393). Store the medium in a dedicated closed container at +4°C to ensure proper cooling of the solution until the start of the experiment. Use this medium to culture your mouse brain slices in.

Problem 8

When measuring the area of colonization by means of the increase in fluorescent signal, you cannot exclusively discriminate between invasion and proliferation. You need to assess the proliferation characteristics of the respective cells to more precisely conclude on their invasion characteristics.

Potential solution

In order to have a mean for the proliferative capacities of the cells you inject into the mouse brain slices, you can, in parallel, perform proliferation assays. Retain the same experimental conditions for the cells as for the brain slices. This will give you an idea of the growth characteristics of the cells you inject into the brain slices and may hint to some *in vitro* growth differences between your tested conditions.

RESOURCE AVAILABILITY

Lead contact

Further information and requests for resources and reagents should be directed to and will be fulfilled by the lead contact, Johannes Meiser (johannes.meiser@lih.lu).

Technical contact

Technical questions on executing this protocol should be directed to and will be answered by the technical contact, Laura Neises (laura.neises@lih.lu).

Materials availability

This study did not generate new unique reagents.

Data and code availability

Original/source data for figures in the paper is available via https://doi.org/10.1016/j.celrep.2023.113034 and https://doi.org/10.1038/s41467-020-20029-y.

ACKNOWLEDGMENTS

We thank the LIH animal facility for providing the isolated mouse brains and reviewing the manuscript. We acknowledge the financial support by the Luxembourg Institute of Health, the Luxembourg National Research Fund (FNR) (ATTRACT program A18/BM/11809970, C21/BM/15718879/1cFlex, C20/BM/14646004/GLASSLUX, PRIDE15/10675146/CANBIO, and PRIDE19/14254520/i2TRON), Fondation Cancer (INVGBM), and the Televie-FNRS (ImmoGBM 7.8505.20, ImmoGBM2 7.6603.22). For the purpose of open access, and in fulfilment of the obligations arising from the FNR grant agreement, the author has applied a Creative Commons Attribution 4.0 International (CC BY 4.0) license to any Author Accepted Manuscript version arising from this submission. Figures were created with BioRender.com.

AUTHOR CONTRIBUTIONS

Conceptualization, J.M. and L.N.; methodology, L.N., C.D., A.S., M.R., K.E., C.F., A.O., S.P.N., A.G., and J.M.; software, L.N., C.D., and A.S.; validation, L.N., C.D., M.R., K.E., and J.M.; formal analysis, L.N., C.D., C.F., M.R., K.E., and J.M.; data curation, C.D., A.S., C.F., M.R., A.G., and J.M.; writing – original draft, L.N., A.G., and J.M.; writing – review and editing, all authors; visualization, C.D., A.S., M.R., L.N., and J.M.; supervision, S.P.N., A.G., and J.M.; project administration, S.P.N., A.G., and J.M.; funding acquisition, S.P.N., A.G., and J.M.

DECLARATION OF INTERESTS

The authors declare no competing interests.

SUPPLEMENTAL INFORMATION

Supplemental information can be found online at https://doi.org/10.1016/j.xpro.2024.103401.

REFERENCES

1. Delbrouck, C., Kiweler, N., Chen, O., Pozdeev, V.I., Haase, L., Neises, L., Oudin, A., Fouquier d'Hérouël, A., Shen, R., Schlicker, L., et al. (2023). Formate promotes invasion and metastasis in reliance on lipid metabolism. Cell Rep. *42*, 113034. https://doi.org/10.1016/j.celrep.2023.113034.

2. Schuster, A., Klein, E., Neirinckx, V., Knudsen, A.M., Fabian, C., Hau, A.C., Dieterle, M., Oudin, A., Nazarov, P.V., Golebiewska, A., et al. (2020). AN1-type zinc finger protein 3 (ZFAND3) is a transcriptional regulator that drives Glioblastoma invasion. Nat. Commun. *11*, 6366. https://doi.org/10.1038/s41467-020-20029-y.

3. Meiser, J., Schuster, A., Pietzke, M., Vande Voorde, J., Athineos, D., Oizel, K., Burgos-Barragan, G., Wit, N., Dhayade, S., Morton, J.P., et al. (2018). Increased formate overflow is a hallmark of oxidative cancer. Nat. Commun. *9*, 1368. https://doi.org/10.1038/s41467-018-03777-w.

4. Eisemann, T., Costa, B., Strelau, J., Mittelbronn, M., Angel, P., and Peterziel, H. (2018). An advanced glioma cell invasion assay based on organotypic brain slice cultures. BMC Cancer *18*, 103. https://doi.org/10.1186/s12885-018-4007-4.

5. Coleman, L.G., Jr., Zou, J., and Crews, F.T. (2020). Microglial depletion and repopulation in brain slice culture normalizes sensitized proinflammatory signaling. J. Neuroinflammation *17*, 27. https://doi.org/10.1186/s12974-019-1678-y.

6. Yabo, Y.A., Moreno-Sanchez, P.M., Pires-Afonso, Y., Kaoma, T., Nosirov, B., Scafidi, A., Ermini, L., Lipsa, A., Oudin, A., Kyriakis, D., et al. (2024). Glioblastoma-instructed microglia transition to heterogeneous phenotypic states with phagocytic and dendritic cell-like features in patient tumors and patient-derived orthotopic xenografts. Genome Med. *16*, 51. https://doi.org/10.1186/s13073-024-01321-8.

7. Oudin, A., Baus, V., Barthelemy, V., Fabian, C., Klein, E., Dieterle, M., Wantz, M., Hau, A.C., Dording, C., Bernard, A., et al. (2021). Protocol for derivation of organoids and patient-derived orthotopic xenografts from glioma patient tumors. STAR Protoc. *2*, 100534. https://doi.org/10.1016/j.xpro.2021.100534.